DIGITAL IMAGE-BASED COMPUTATIONAL APPROACHES FOR THREE-DIMENSIONAL MICROSTRUCTURE CHARACTERIZATION

A Dissertation
Presented to
The Academic Faculty

by

Jie Cao

In Partial Fulfillment
of the Requirements for the Degree
Doctor of Philosophy in the
School of Civil and Environmental Engineering

Georgia Institute of Technology
May 2018

DIGITAL IMAGE-BASED COMPUTATIONAL APPROACHES FOR THREE-DIMENSIONAL MICROSTRUCTURE CHARACTERIZATION

Approved by:

Dr. J. David Frost, Advisor
School of Civil and Environmental Engineering
Georgia Institute of Technology

Dr. Arun M. Gokhale
School of Materials Science and Engineering
Georgia Institute of Technology

Dr. Susan E. Burns
School of Civil and Environmental Engineering
Georgia Institute of Technology

Dr. Andrew R. Fuggle
Geotechnical Group
Golder Associates Inc.

Dr. Sheng Dai
School of Civil and Environmental Engineering
Georgia Institute of Technology

Date Approved: March 29, 2018

TO MY FAMILY

ACKNOWLEDGEMENTS

The past five years has been a long and challenging journey. The research work presented here would not have been accomplished without the support and encouragement of many people. Foremost, I would like to express my sincere appreciation to my advisor, Dr. J. David Frost for the unwavering guidance and advice. His wisdom and insights on many things, including research, career, personal development and life, inspired me deeply and helped me overcome frustrations. I am extremely grateful for his understanding and willingness to work with me on all issues.

I would like to thank my committee members, Dr. Susan Burns, Dr. Arun Gokhale, Dr. Sheng Dai and Dr. Andrew Fuggle for providing invaluable comments, suggestions and assistance. Especially, the interactions with Dr. Gokhale enabled me to learn some important methodologies in the materials science study and bring them into my research. I also want to thank Dr. Paul Mayne, Dr. Haiying Huang, Dr. Chloé Arson and Dr. Carlos Santamarina who shared with me their rich knowledge and creative visions in geotechnical engineering through teaching.

I would like to acknowledge Albert, Jackson, Fikret, Seth, Sangy, Tianlong, Mahdi, Rodrigo, Mengmeng, Yuzhi, Karie, Alejandro, Andres, Yue, Wencheng, Jiaojun, Longde, Yixuan, as well as other former and present students of Georgia Tech GeoSociety for their friendship, accompany and kind help. I really enjoyed the conversations and fun time during meetings, geoparties, tailgates and so on.

Thank Glenn and Mary for their blessing since I came to Atlanta. They always stand by my side and take care of me just like my grandparents. I will never forget those hopeful discussions about God's mercy and grace.

Lastly, I would like to thank my parents and all the other family members for their unconditional love throughout my entire life. Their support towards my pursuit of dreams has given me lots of strength. I cannot be who I am without them.

TABLE OF CONTENTS

LIST OF TABLES

LIST OF FIGURES

SUMMARY

Employing multiscale approaches provides an innovative solution to advancing the understanding of macro-geomechanical phenomena by capturing quantitative structure information of geomaterials at the particle-pore scale. In the last two decades, microstructural properties of Ottawa sands subjected to laboratory biaxial and triaxial compression testing have been analyzed at Georgia Tech so that their correlation with the mechanisms of strain localization could be explored. Extensive 2-D and some preliminary 3-D knowledge and insights into the inherent variation and evolving behavior induced by shearing in unconsolidated sand microstructures were learned. Aimed at enhancing and complementing these preceding studies, this research focuses on developing appropriate computational methods for 3-D microstructure characterization, with a particular focus on examining the geometry and topology of the highly intricate continuum pore space.

Under a proposed skeleton-based framework, the tortuous nature of pore structure is investigated through characterizing spatial variation of geometrical tortuosity using a novel, generic computational algorithm. Based on specifying and identifying pore throats from the pore skeleton, the physically representative network architecture of pore structure is established. A local sphericity algorithm and a planar surface construction algorithm are introduced to construct pore throats and extract network statistics. The effectiveness of these pore structure analysis tools is evaluated and demonstrated on two simulated idealized packing structures. For the particle phase, image-based separation and size measurements are conducted via morphological watershed processing. The topology of the particle network is represented by the distribution of force-chain tortuosity. Design-based

stereological techniques for unbiased sampling and estimation are adopted to guarantee the quantitative analyses can be performed in a scientific manner, independent of the operator.

All the developed methods and tools are applied to characterize three pairs of reconstructed 3-D digital Ottawa sand microstructures, including one pair for biaxial specimens and two for triaxial specimens. Shear-induced alternations in pore structure and particle network are examined from the comparative studies between the sheared microstructure and the unsheared counterpart of each pair, as well as inside and outside the shear zone for the sheared biaxial microstructure. Variations in the inherent structures are analyzed by comparing unsheared triaxial specimens prepared with air pluviation and moist tamping methods. In the characterization of true pore morphology, the encountered geometric complications and then high computational expense highlight the difficulty and challenge of creating a unique pore network for unconsolidated porous media systems.

CHAPTER 1. INTRODUCTION

1.1 Motivation

The discrete nature of geomaterials determines their complex macroscopic behavior under mechanical, hydraulic, or thermal conditions. Multiscale approaches have evolved to be of great interest for correlating materials information at different length scales over the past two decades. Quantitative core knowledge of heterogeneous microstructures can be characterized at particle-pore scale, and then incorporated into macroscale formulations to strengthen the understanding of macro-geomechanical phenomena, predict properties and performance, and simulate processes in materials design and development. In both laboratory and in-situ, two-dimensional (2-D) characterization accompanied the introduction and an increasing role of digital imaging techniques in microstructure analyses, involving projected size, shape, and orientation of particles as well as areal fraction of pores. However, more and more researchers have recognized the limitations of 2-D analyses in reaching a comprehensive understanding of microstructures. With the advance of imaging techniques and computing power, three-dimensional (3-D) characterization based on computer-aided microstructure reconstruction and processing has become feasible. Early adoptions of these 3-D techniques in many disciplines, such as life science and materials science, enable a fundamental routine to be established for processing digital microstructure data. Building upon a large amount of image processing theories, the main challenge of the microstructure knowledge learning lies in developing adequate 3-D microstructure analysis methods. It is therefore beneficial to extend the preceding 2-D microstructure characterization approaches for geomaterials study to 3-D.

A number of more recent experimental and numerical studies have been devoted to tracking 3-D movements of particles and quantifying particle-to-particle interactions in sheared soil masses. 3-D computational methods remain challenging but important for quantifying other key metrics including estimating geometric attributes and exploring mathematical representation of the highly intricate pore space within the soil structure.

1.2 Research Scope

Since the 1990's, considerable experimental and numerical studies have been performed on Ottawa sands at Georgia Institute of Technology to investigate the mechanisms of strain localization, which is evidenced in many laboratory and field-scale failures of geo-structure systems. Evolving microstructural behaviors due to triaxial and biaxial loadings were characterized through detailed sub-particle level analyses inside and outside the localized zones. Variations in inherent microstructure of sand specimens reconstituted from different laboratory preparation methods were also discussed. By processing high resolution optical images, a few valuable 2-D structure metrics were successfully defined and evaluated (Kuo, 1994; Jang, 1997; Park, 1999; Chen, 2000; Yang, 2002; Evans, 2005). 3-D microstructure information, however, hasn't been well captured and understood (Yang, 2005; Lu, 2010) due to the absence of appropriate computational and analysis protocols. This current study focuses on proposing microstructure analysis approaches for 3-D quantitative characterization, and in particular examining the attributes of pore structure in an unconsolidated porous media system. In an effort to demonstrate their potential utility, these approaches will be evaluated on simulated idealized packings, and then applied in quantifying reconstructed digital real sand microstructures. This study is aimed to upgrade digital characterization capabilities for geomaterials. Complementing

the previous studies, new insights into the inherent and induced microstructure properties and characteristics will be provided. An overview of the laboratory programs for generating the digital image datasets of Ottawa sands and the microstructure investigations conducted in this work is presented in Figure 1.1.

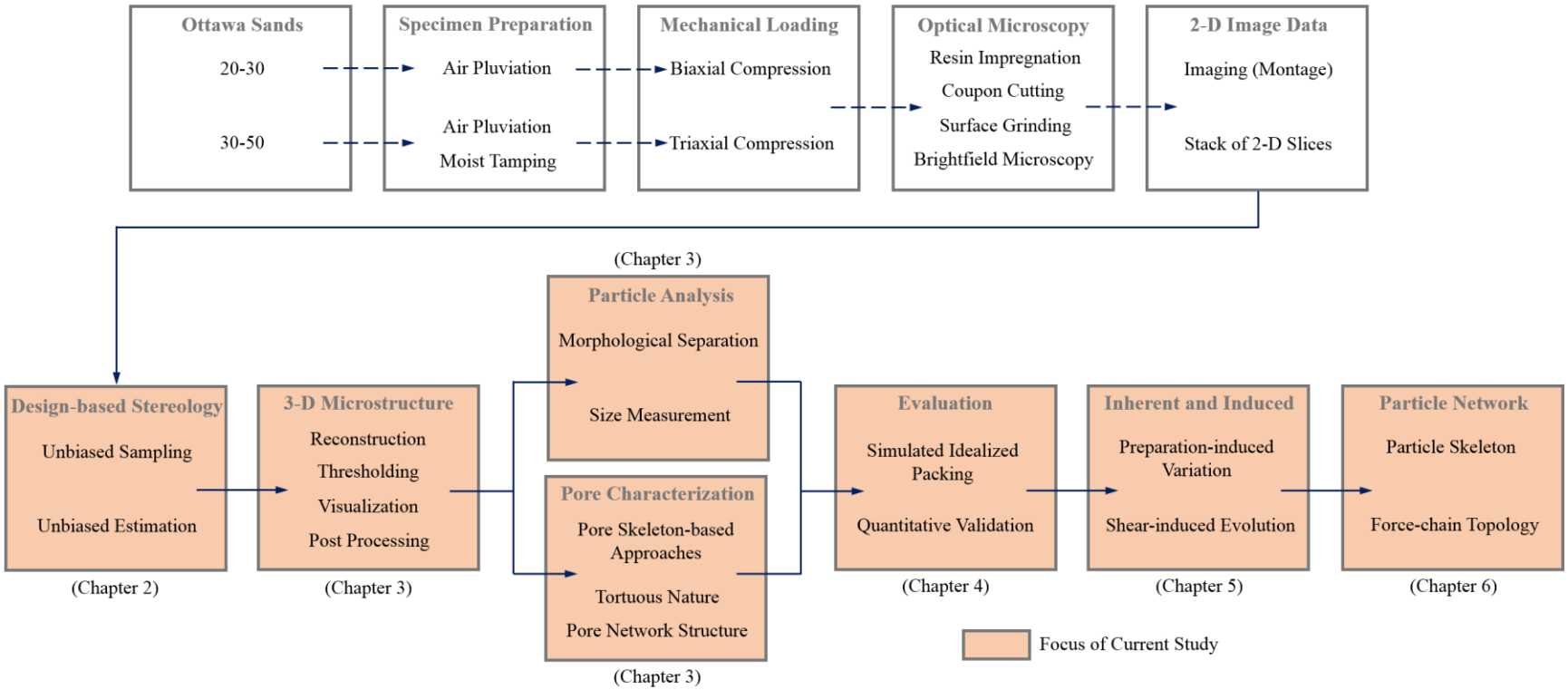

Figure 1.1 Overview of laboratory and microstructure investigations on Ottawa sands

1.3 Organization of the Dissertation

The dissertation is composed of 7 chapters. The chapters are organized as follows:

- Chapter 1 (this chapter) describes the motivation for this study and provides an overview of the thesis;
- Chapter 2 provides an overview of the evolution of three-dimensional digital imaging technology, previous work and microstructure information on laboratory specimens of Ottawa sands, pore structure studies from other researchers, and design-based stereology for unbiased quantitative microstructure characterization;
- Chapter 3 presents the basic workflow for image-based characterization on digital sand microstructures, methods for particle separation and analyses, and skeleton-based computational tools proposed for 3-D pore structure descriptions;
- Chapter 4 presents the evaluation of the pore structure analysis tools on two simulated idealized packing structures;
- Chapter 5 presents studies on the reconstructed Ottawa sand microstructures to characterize pore structure alternations induced by mechanical loadings, and pore-scale variations introduced by different laboratory specimen preparation methods;
- Chapter 6 includes an exploratory analysis on the topology of particle networks through a skeleton-based approach;
- Chapter 7 summarizes the present study and provides some recommendations for future work.

CHAPTER 2. BACKGROUND AND LITERATURE REVIEW

2.1 Three-Dimensional Digital Imaging

Rapid evolution of digital imaging technology renders multiple solutions to acquiring 3-D microstructure digital data at a wide range of resolutions. Specific disciplines may indicate their own prevalent technique by taking into account both functionality and cost affordability. For example, Magnetic Resonance Imaging (MRI), forming a magnetic field around the targeted area to generate images, is prominently used in biomedical research and diagnostic medicine (Amunts et al., 2013), and is being implemented for studying plant biology recently (Metzner et al., 2014). Scanning electron microscopy (SEM) or focus ion beam scanning electron microscopy (FIB-SEM) can achieve resolution down to the sub-nanometer range, and is commonly utilized in the field of material science for surface topology and composition analysis, nano-fabrication, failure analysis, or serial sectioning for delicate measurement such as in fuel cells (Cecen et al., 2012), etc.

In geotechnical engineering and geomechanics, digital image correlation (DIC) has been used to measure two- and three-dimensional surface displacements by correlating continuous images recorded throughout experiments. Using DIC, mechanisms of shear localization in sands were studied from the perspectives of local displacement fields and kinematics at particle-scale (Rechenmacher and Finno, 2004; Rechenmacher, 2005; Rechenmacher et al., 2010). With the advent of X-ray computed tomography (CT) and later X-ray micro-CT, 3-D structure models can be reconstructed through mapping the distribution of X-ray attenuation that reflects density variations within the objects, and internal microstructure information can be collected accordingly. Particle-to-particle

interactions including orientation, contacts and rotations, and their correlation with shear band formation and stress-strain behavior have been reported (Oda et al., 2004; Hasan and Alshibli, 2010; Higo et al., 2011; and Tagliaferri et al., 2011 amongst others). The combination of X-ray micro-CT and DIC were also used in understanding strain localization in geomaterials (Viggiani and Hall, 2008; Hall et al., 2010; Higo et al., 2013). Although high resolution micro-CT is more accessible than before, scanning artifacts (e.g. beam hardening, ring artifacts, or partial-volume effects) as well as trade-offs between image resolution and imaging volume still draw nontrivial concerns. Another well-established method to generate 3-D digital microstructure of geomaterials is optical microscopy based serial sectioning. The experimental procedure to obtain stacks of 2-D images usually consists of resin impregnation, coupon cutting and mounting, surface grinding and polishing, and imaging using bright-field microscopy based on montage technique. Considering the destructive nature and tedious repetition required in building up the image stacks, a decline in popularity is seen today compared to the X-ray micro-CT technique. At the same time, advantages in terms of high affordability, and capability of easily satisfying the needs of large total imaging area with high local resolution, are desirable to many researchers in studying geomaterials. Lately, the emergence of new techniques like laser scanning confocal microscopy can offer non-contact evaluation of nanometer-level surface profiles.

2.2 Laboratory Investigation Programs

This study continues the previous microstructure studies on laboratory specimens of Ottawa sands, and specifically expands on the 2-D characterization methods. Some of those early acquired images serve as important inputs in developing the proposed 3-D

computational approaches. Accordingly, the scope and findings of those studies are summarized below.

2.2.1 Specimen Preparation and Preservation

To study the shear behavior of sands, laboratory tests are commonly performed on reconstituted specimens given that obtaining undisturbed granular samples is rarely possible. Three major methods - air pluviation, moist tamping and water deposition - have been developed and employed to prepare specimens of Ottawa sand similar to its natural deposition. An air pluviation system (Figure 2.1) was designed by Jang (1997) and Park (1999) to prepare specimens through raining sand particles through air into a membrane lined split mold. Kinetic energy of the sand articles controls specimen density primarily through adjusting flow rate (pluviation intensity) and fall height (deposition velocity) of sand particles. Moist tamping (Figure 2.2) was used to compact specimens in seven layers of sand with equal thickness to predetermined densities using a tamping disc (Park, 1999). An under-compaction technique was applied to increase uniformity in density over the height of the specimen. Water-deposited specimens were prepared from allowing sand particles to fall and deposit in water using the apparatus developed by Chen (2000) shown in Figure 2.3. Post-placement densification by pneumatic vibration was then performed. Previous research has shown that different preparation methods would result in different initial structures of the sand specimens reconstituted to the same global void ratio, which would affect the subsequent shear behaviors under the same confining stress (Jang, 1997; Park, 1999; Chen, 2000; Yang, 2005; Frost et al., 2018). Air pluviation and water deposition methods were stated to be reliable in simulating soil fabric in natural alluvial and fluvial environments. Moist tamping simulated field compaction by vertical tamping.

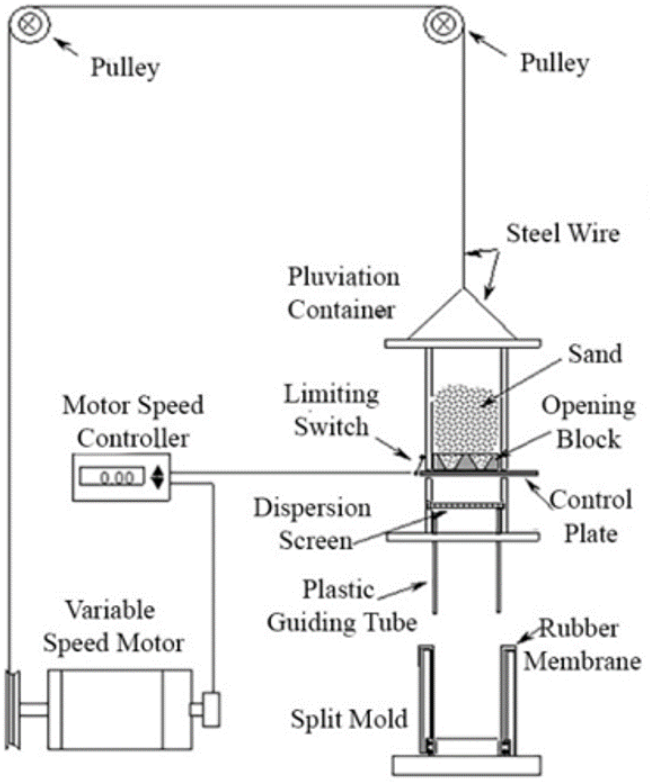

Figure 2.1 Schematic view of automated air pluviation system (Jang, 1997)

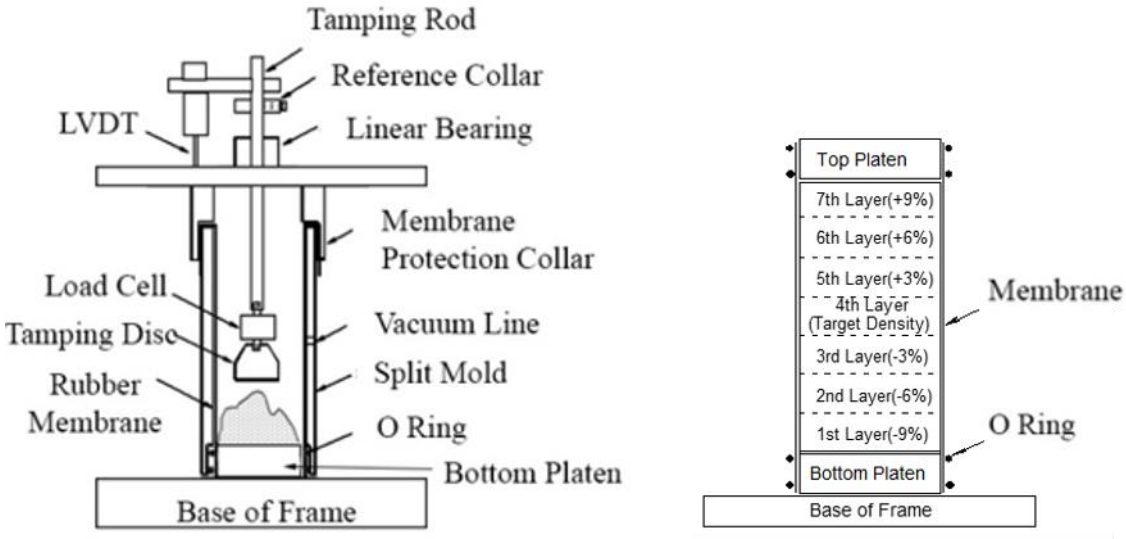

Figure 2.2 Schematic view of moist tamping system and under-compaction technique (Park, 1999)

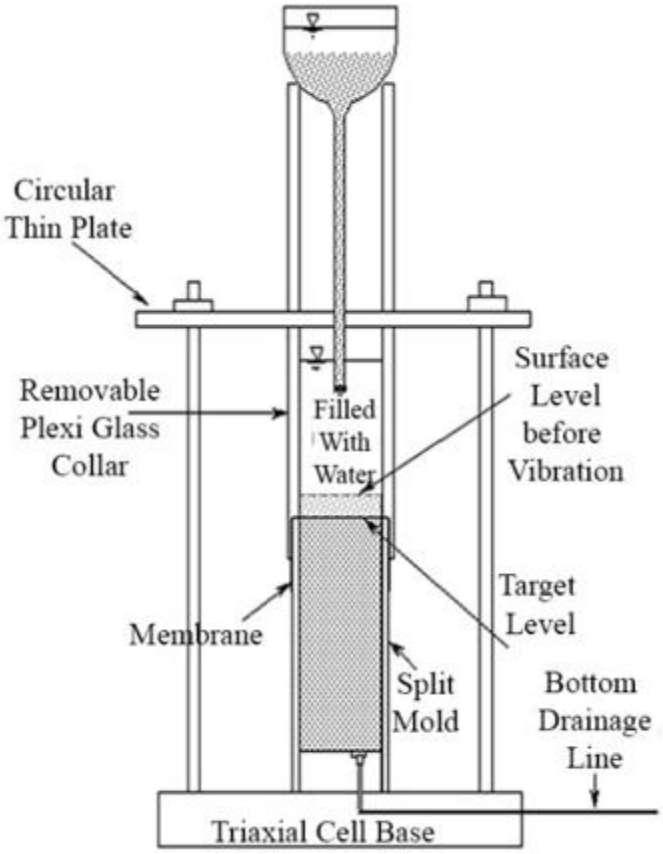

Figure 2.3 Schematic view of water deposition system (Chen, 2000)

Preserving the actual state of the sand specimen is fundamental to microstructure imaging and characterization. Multiple specimens need to be prepared and preserved if the microstructures corresponding to different strain levels are analyzed. EPO-TEK 301, an epoxy resin manufactured by Epoxy Technology Inc., was impregnated into those sand specimens followed by less than 24-hour curing at room temperature. The epoxy resin was low viscosity, low shrinkage and optically transparent, and was proven to create high bonding strength and medium hardness while causing minimum disturbance to the structure. The cured specimens were then subjected to the workflow of serial sectioning for imaging.

2.2.2 Analysis of Sand Microstructures

Microstructures of the reconstituted sand specimens described above consist of two phases - particles and pores. Efforts have been made for characterizing both phases to convey microstructure information (Kuo, 1994; Jang, 1997; Park, 1999; Chen, 2000; Yang, 2002; Evans, 2005; Yang, 2005; Lu, 2010). A trend of methodological improvement could be observed for characterization that was performed by measuring images captured at selected locations on a few representative horizontal and vertical surfaces to quantifying a stack of 2-D images successively, and even further to the volumetric quantification of a reconstructed digital specimen.

For the particle phase, two particle orientation metrics were computed in 2-D through functions built in a Cambridge Instruments Quantimet Q570 image analysis system manufactured by Leica Microsystems (Park, 1999). One was defined as a single "anisotropy" index on image level by calculating the ratio between number of horizontal intercept lines to number of vertical lines. Strong horizontal, strong vertical, or random orientation was interpreted from comparing the "anisotropy" value to 1.0. The other one involved analysis at the particle level. Orientation of projected longest axis, namely the maximum Feret diameter of each particle with respect to a reference direction, was measured. Distribution of particle orientation could thus be characterized and demonstrated graphically. Sand particles in air-pluviated and water-deposited specimens were noted to lie more horizontally. It was also argued that defining a true orientation of long axes of particles or contact normal in 3-D was difficult. Besides particle orientation, a proposed quasi-3-D image analysis approach permitted fast measurements of particle shape from orthogonal projections (Kuo et al., 1996). The long, intermediate, and short particle

dimensions were captured as essential information to derive other morphological features including elongation, flatness, sphericity, and shape factor.

Characterization of pore phase depicts the relative arrangement of pores and particles. Local void ratio distribution was deemed as an insightful descriptor of soil fabric in 2-D. It was first proposed by Oda (1976) and developed into an automated algorithm by Kuo and Frost (1996) through stereology and mathematical morphology operations. The basis of local void ratio was to measure the void ratio of a polygon formed by joining the particle centers. Solid (particle phase) area weighted frequency distribution of local void ratio, its statistical mean and standard deviation, as well as other associated parameters including skewness, kurtosis, and entropy were evaluated for Ottawa sand specimens. Moist tamping method was found to produce the least uniform specimen among the three; and larger local void ratios were more likely to appear in water-deposited specimen, implying it would be more suitable to reconstitute loose sand specimens (Chen, 2000). Further, to determine the extent of shear banding, spatial averaging of void ratio was analyzed along pre-determined inclined strips parallel to the observed shear band orientation (Evans, 2005). Stack of slices were processed in 2-D, while voxel counting in prismatic strips in 3-D could generate more accurate results (Lu, 2010). By plotting incremental void ratio together with cumulative void ratio against the distance along a transect that is normal to the shear band, identification of three distinct zones - shear zone, transition zone, and non-dilatant zone - was accomplished. This enabled in-depth studies of particle-pore structure changes linked to the presence of shear zones. A model consisting of two primary rigid blocks separated by a secondary shear block was suggested (Evans and Frost, 2010). In additional to the concept of void ratio which was embraced by the

established pore metrics to exercise pixel or voxel counting, other descriptive methods are necessary to characterize the complicated pore structure. Preliminary study to quantify pore geometry was performed by Yang (2005). In 3-D, it was achieved with the help of a research software package 3DMA, but limitations were recognized when applying it to sand microstructures which are unconsolidated media with higher porosity than consolidated systems and few contracts existing between particles. Details of 3DMA will be presented in Section 2.3. Moreover, a 2-D algorithm was suggested for pore and throat size analyses, but manifested itself as being quite limited to represent the real interconnectivity of a 3-D porous medium.

2.2.3 Structure Information under Study

Three pairs of digital sand microstructures are involved in this research. Two pairs were reconstructed from specimens that were subjected to triaxial loading by Yang (2005), and the remaining one was from biaxial specimens (Evans, 2005; Lu, 2010). The tested geomaterials were poorly graded, sub-rounded Ottawa sands that are primarily composed of silicon dioxide (quartz). Table 2.1 summarizes the index properties of Ottawa 30-50 sands used for triaxial tests and Ottawa 20-30 sands used for biaxial tests. All specimens have a target initial relative density of 75%, and thus are dense specimens.

The triaxial specimens were prepared using air pluviation (AP) method through the previously mentioned mechanical system and moist tamping (MT) method to a similar initial void ratio. The nominal dimension of the specimens were 70 mm in diameter and 140 mm in height. One of the two specimens prepared using the same method was sheared to 14% global axial strain state under a confining pressure of 50 kPa, while the other one was preserved at its initial unsheared state (0% global axial strain) for comparison. The

stress-strain responses are shown in Figure 2.4 and Figure 2.5. The air-pluviated specimen yielded a higher peak stress and peak strain but a lower initial modulus than the moist-tamped specimen. The biaxial device allowed a plain strain compression on the prismatic specimens with a nominal dimension of 140 mm × 80 mm × 40mm. The plain strain configuration is favorable to produce the dominant strain-localization failure pattern. The biaxial specimens were prepared using a manual air pluviator, and the sheared one reached a state of 10% global axial strain under a confining stress of 69 kPa. The stress-strain response is presented in Figure 2.6.

If shear banding was observed during loading which was the case for the sheared biaxial specimen and the sheared moist-tamped triaxial specimen, coupons for digital imaging were cut to encompass the localized zone; and otherwise they were cut from the specimen center. It should be noted that a highly dilated bulging deformation was observed in the middle portion of the sheared air-pluviated triaxial specimen. It was suggested (Park, 1999; Frost and Park, 2003; Frost et al., 2018) that the moist- tamped triaxial specimens were more likely to develop shear planes because they underwent some degree of pre-shearing by the vertical tamping force applied during specimen preparation.

Table 2.1 Index properties of Ottawa sands (based on Yang, 2005; Evans, 2005)

Material Property	30-50	20-30
Median Grain Size, D_{50} (mm)	0.35	0.74
Coefficient of Uniformity, C_u	1.65	1.12
Coefficient of Curvature, C_c	1.06	1.00
Specific Gravity, G_s	2.67	2.65
Maximum Void Ratio, e_{max}	0.82	0.74
Minimum Void Ratio, e_{min}	0.50	0.50

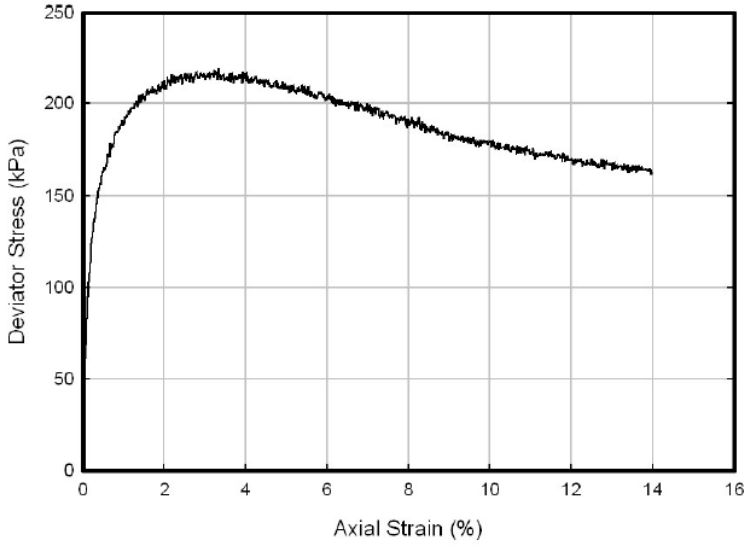

Figure 2.4 Stress-strain plot for air-pluviated triaxial specimen (Yang, 2005)

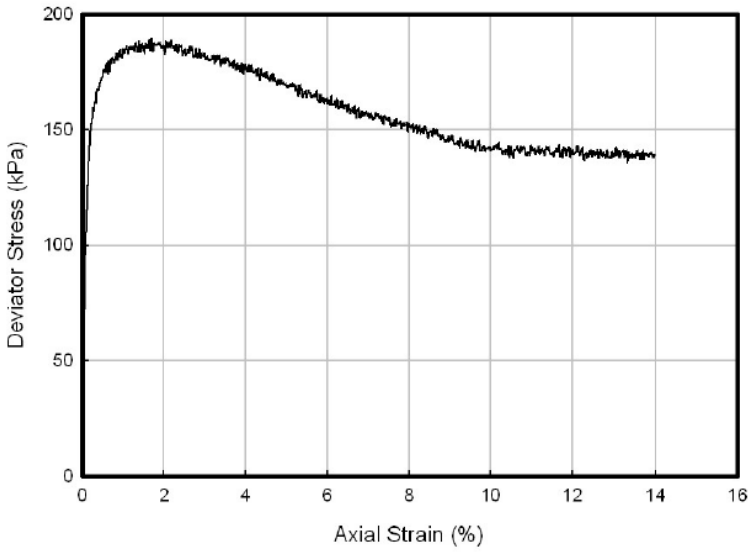

Figure 2.5 Stress-strain plot for moist-tamped triaxial specimen (Yang, 2005)

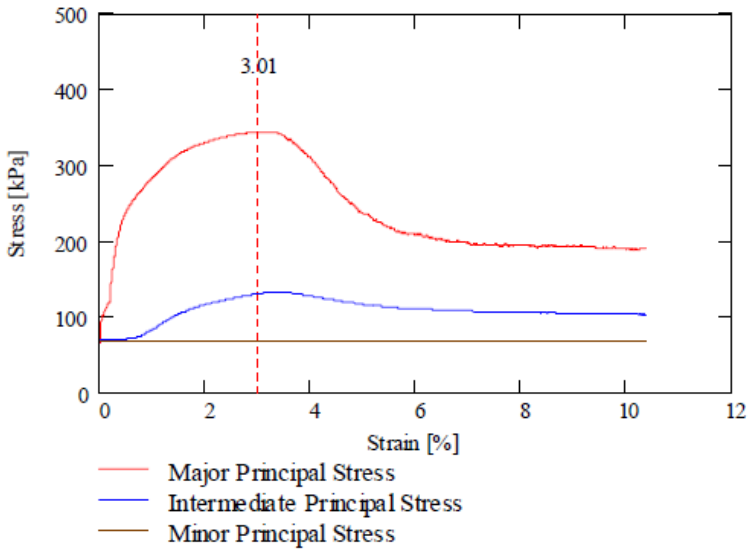

Figure 2.6 Stress-strain plot for biaxial specimen (Evans, 2005)

Using a Leica DM4000 microscope, 600 slices with a pixel of side approximately 8 μm and total image area of 1800 × 1100 pixels were generate from the triaxial specimens AP0, AP14, MT0, and MT14. The designations indicate preparation methods and global axial strain states. Similarly, 430 slices and 600 slices with a resolution of 14 μm/pixel and total image area of 1300 × 800 pixels were acquired from the unsheared (designated as BT0) and the sheared (designated as BT10) biaxial specimen, respectively. Information on all these sand structures is given in Table 2.2.

Table 2.2 Information on digital sand structures (based on Yang, 2005; Lu, 2010)

ID	Test	Initial Void Ratio	Resolution/ slice spacing	Dimension (mm^3)
AP0	Triaxial	0.582	8 μm	14.4 × 8.8 × 4.8
AP14		0.579		
MT0		0.580		
MT14		0.583		
BT0	Biaxial	0.570	14 μm	18.2 × 11.2 × 6.0
BT10		0.560		18.2 × 11.2 × 8.4

2.3 3-D Pore Network Extraction

The geometry and topology of the pore space, as the complementary phase of the grain space, control fluid transport, thermal conductance, electrical and acoustic properties of geomaterials. Heterogeneity and anisotropy of these properties within the pore structure underscore the significance of microstructure analysis for obtaining comprehensive knowledge. In studying the mechanical behavior of geomaterials, pore characterization is integral to fully understanding structural alternations under loading as well as pore-scale discrepancy introduced by different laboratory preparation methods. Numerous parameters to describe pore structure exist, including standard ones such as porosity, surface area and connected components. Regarding the quantification of other more advanced pore metrics, however, developing efficient computational protocols is rather challenging. Inadequacy of rigorous definitions that arise from intrinsic structural complexity and irregular shapes of the pore space is the major reason. High computational expense of processing large 3-D digital image datasets is another impediment.

Many research efforts have been dedicated to delineate and represent the pore structure as a 2-D or 3-D network architecture. This network structure is proposed to be a simplified, topologically equivalent, parameterized representation of the pore system. Based on mapping the real pore structure onto a network, pore-scale modeling has become a powerful tool to better understand the fundamental behavior of physical processes and phenomena. In the fields of petroleum engineering, chemical engineering and hydrology, for example, single-phase and multiphase flow processes have been widely studied. Transport properties like absolute and/or relative permeability, capillary pressure hysteresis, and capillary pressure-saturation were predicted in different porous media

systems. Two components of a pore network model are the pore body or larger pore space opening and the pore throat or the narrow opening connecting pore bodies. The number, size, and distribution of pore throats plays a dominant role on many of the pore-scale characteristics of a porous medium (Kim et al., 2013). Therefore, identifying and quantifying the pore throats has always been pivotal in pore structure characterization, and as a primary focus in the vast literature on network extraction. Considering the complexity of true pore morphology, making simplifying assumptions is unavoidable in specifying distinct pore throats and pore bodies. Herein, two representative methods, medial-axis transformation and maximal balls, that build pore networks from arbitrary 3-D digital image data as well as one process-based method termed as grain recognition method are briefly described.

Medial-axis based method transforms pore structure into a centrally-located skeleton that preserves its topological information by an iterative erosion or a so-called "burning" procedure (Baldwin et al., 1996; Lindquist and Lee, 1996; Liang et al., 2000; Al-Raoush et al., 2003; Al-Raoush and Willson, 2005; Al-Raoush and Willson, 2005; Jiang et al., 2007). The attraction of medial axis method is its ability to realize a dimensional reduction of pore structure which is easier to analyze. Having the medial axis serve as a searchable structure, pore throats can be located through different algorithms. 3DMA, a research software package developed by Lindquist (1999) and updated until 2005, proposed three throat finding algorithms: Dijkstra shortest path based algorithm (Lindquist and Venkatarangan, 1999); "wedge finding" algorithm (Shin et al., 2005); and sub-sectioning Dijkstra based algorithm (Prodanović et al., 2006). A pore throat was perceived as a non-planar surface of local minimum cross-section area in the pore network. The

underlying logic was to locate the bounding perimeter of a throat surface and subsequently span the perimeter loop into a triangulated surface. The software was designed and primarily applied to characterize the pore structure in consolidated systems such as rocks where pores are mostly disconnected, and particles were presumed to be largely connected. From previous use of 3DMA to study pore structure in the aforementioned laboratory sand specimens, it was not possible to resolve the throat construction properly in those unconsolidated geomaterials (Yang, 2005). Morphological dilatation was applied to the images to create more contacts between particles prior to implementing the throat finding algorithm at the expense of accuracy. Generally, 3DMA could be quite restrictive for the unconsolidated porous media with porosities exceeding 20%. With regard to computing medial-axis in most cases, the sensitivity of the algorithms to image noise and the irregularity at pore-particle surfaces demanded significant manual clean-up efforts.

Maximal ball method (Silin and Patzek, 2003; Silin and Patzek, 2006; Al-Kharusi and Blunt, 2007; Dong and Blunt, 2009) represented pore space by maximal balls (MB) constructed from computing discrete, largest inscribed spheres centered at each pore voxel touching the pore-particle boundary. The sphere that was not fully enclosed by others defined a maximal ball. Identified maximal balls were hierarchized to form pore-throat chains through a process of cluster search and family-tree affiliation. A pore throat was denoted to be the "common child" belonging to two families, while a pore body to be the "ancestor" of each family (Dong and Blunt, 2009). This ancestor-child was analogous to a master-slave classification in other occasions (Silin and Patzek, 2006). No image thinning was needed in this method, but instead the pore-throat chains composed of maximal balls portrayed the skeleton. A pore network in the form of pore bodies connected by cylindrical

channels was produced. Nonetheless, throat computations would be practically more difficult because clusters of equal balls or multiple pore-throat chains may appear between pore bodies (Al-Kharusi and Blunt, 2007). In segmenting the whole pore space, it was also subjective to determine where a pore body ended and a connecting channel began.

In contrast with the former two methods, the grain recognition method started from simulating grain packings involving geological sedimentation, compaction and diagenesis (Bryant et al., 1993; Bakke and Øren, 1997; Øren and Bakke, 2002; Øren and Bakke, 2003). The pore network was characterized from its complementary particle network through image analyses. With the known particle locations, Voronoi polyhedra were formed around particle centers. The pore skeleton was composed of voxels along edges of these polyhedra, and pore body centers were indicated by their vertices. The sizes of pore bodies were calculated with a planar rotational vector to find the pore body walls, and the sizes of pore throats were measured similarly. This method was distinctive by trying to account for the fact that pore structure often resulted from geological history, and taking advantage of the prior particle knowledge. However, generating the numerical model required a significant amount of additional work, and accessing 3-D particle information might not be straightforward and easy in an arbitrary, realistic packed structure.

Other pore network extraction methods based on 3-D thinning of the flow velocity field (Dong et al., 2008) or distance function combined with watershed segmentation (Rabbani et al., 2014) were proposed as well but were not considered further in this study.

2.4 Implications from Design-Based Stereology

To perform quantitative analyses of materials in a scientific manner, a methodology with a high degree of objectivity and rigor is required. Design-based stereology is one such approach for providing practical solutions to quantitative characterization of anisotropic and heterogeneous microstructures in microscopy. It has a strict theoretical basis and is completely generalized with extensive applications (Baddely et al., 1986; Gokhale, 1990; Fiala and Harris, 2001; Mouton et al., 2002; Weibel et al., 2007; Segal et al., 2009), particularly having gained increasing popularity in biological and biomedical research. The principles concerning the unbiased facets of the stereological approach are reviewed in this section, and will be referred to later in characterizing the digital sand microstructures.

Stereology is the science of capturing quantitative information about a 3-D microstructure from measurements performed on the lower dimensional manifolds like 2-D planar sections. Design-based stereology, as the most modern stereology, is free of any restrictive assumptions (size, shape, spatial orientation and spatial distribution) of the geometrical features to be investigated, permitting the collection of accurate data. Possible bias for quantitative analyses is embedded in both the sampling and estimation stages. Design-based stereology addresses these two sources of bias through designing robust sampling schemes and choosing correct measurement tools, respectively.

2.4.1 Unbiased Sampling Technique

In all microstructure studies, examining the object of interest as a whole cannot be practical, and a sample needs to be taken out of the large 3-D domain. Unbiased sampling requires that every part of the 3-D domain has the same chance of being contained in the

sample. Therefore, randomizing the sampling should be employed throughout all of the hierarchical levels in quantitative microstructure characterization. When random sampling holds true, random sampling error can be estimated statistically, and will decrease to a desired level as the sample size approaches the whole 3-D domain size.

Two unbiased sampling techniques are uniform random sampling, also called "independent random" sampling, and systematic random sampling. The first one is the simplest but not very efficient when repeated random sampling is needed to acquire much more information. Redundancy in the information acquired happens because there is a tendency for uniform random samples to cluster together mathematically (Howard and Reed, 2004). A superior technique is systematic random sampling that is much easier to execute practically and also provides smaller sampling error than uniform random sampling under the same sampling efforts (Gunderson and Jensen, 1987). It is composed of a random component and a systematic component. The sampling starts with selecting the location of the first sample at random and then takes other samples by following a systematic pattern spatially. In the application of stereology, geometrical test probes (e.g. planes, lines, points, cycloids etc.) are randomized in a systematic random way to estimate geometric attributes of microstructures unbiasedly. It is worth mentioning that if the microstructure being sampled presents natural periodicity, systematic random sampling can be potentially biased if a coincidence in periodicity exists between the systematic pattern and the microstructure.

2.4.2 Unbiased Estimation Technique

Once random samples have been generated out of the 3-D microstructure, an unbiased estimator must be utilized to gather quantitative information from the samples. Biased estimators will cause systematic bias. Unlike random sampling error, systematic error depends on microstructure characteristics and the nature of the estimation technique, and hence cannot be evaluated. Supposing the estimator is unbiased, the sample mean value regarding a geometric attribute of a 3-D microstructure will approach the true mean value as the sample size increases. Otherwise, increasing sample size can merely contribute to the convergence of the sample mean to a value other than the true mean value, and the deviation from the true mean value indicates the existence of systematic bias.

Quantifying the number density, N_v, of microstructure features (e.g. particles, pores, inclusions, cells etc.) within a 3-D microstructure is of significant scientific interest, and is correlated closely with the quantification of size or shape distribution. When performing the number density estimation on the sampled microstructure (denoted as the "counting domain") that has a smaller field of view than the whole domain, "edge effect" occurs because some profiles being quantified intersect the boundaries of that counting domain. Systematic bias in the estimation can arise from inappropriate treatment of the edge effect. Gundersen (1977) did pioneering work by proposing an unbiased counting frame to estimate number density in a 2-D section. As shown in Figure 2.7, the counting frame is an asymmetrical intersecting stereology probe consisting of dashed lines termed as "acceptance lines", and solid lines extending to infinity termed as "forbidden lines". The counting rule states that a feature is counted if it lies entirely within the frame or if it intersects the acceptance lines without touching any forbidden line. This counting frame

guarantees that each feature of interest is counted in one and only one frame. Compared with 2-D estimation, reliable quantification of number density in 3-D is more challenging due to the fact that a three-dimensional probe is required.

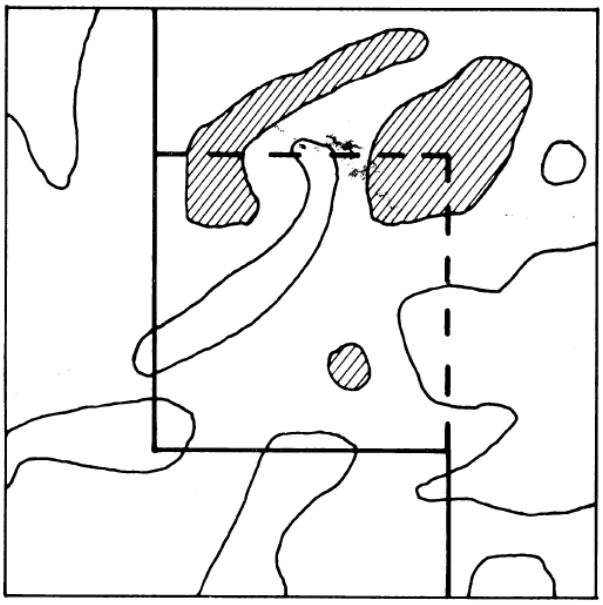

Figure 2.7 A field of view superposed by a counting frame (Gundersen, 1977)

Sterio (1984) presented the "disector" involving two parallel planar sections separated by a small distance, which are sometimes called "reference section" and 'lookup section". In counting, an unbiased counting frame can be placed on the reference section, and the features sampled by this section are counted if they are not present in the lookup section. Alternatively, an unbiased counting frame can be placed on the lookup section to count the features sampled by this section that are not present in the reference section. Or both of the above two counts are taken and averaged in practice. The idea of optical disector was also suggested to make observations on consecutive focal planes at different depths through transparent biological microstructures (Gundersen, 1986). As for opaque microstructures in most other applications, a large-area disector (LAD) was created by

Tewari and Gokhale (2000) using montage technique. The high resolution, large area disector planes can yield a much larger feature count than the conventional disector.

Apart from section-to-section estimation, an unbiased brick counting rule and a formal proof of its unbiased nature was given by Howard et al. (1985). The unbiased brick is an extension of the counting frame into three-dimensional space. The brick has a central volume bounded by three "acceptance surfaces", and five "forbidden surfaces" as shaded planar surfaces shown in Figure 2.8. The brick counting rule is: a feature is counted if it is completely inside the brick or if it intersects the brick but not any of the forbidden surfaces. Obviously, this brick counting demands 3-D information, and its applicability has been broadened since imaging and computing techniques for reconstruction of 3-D microstructures became available.

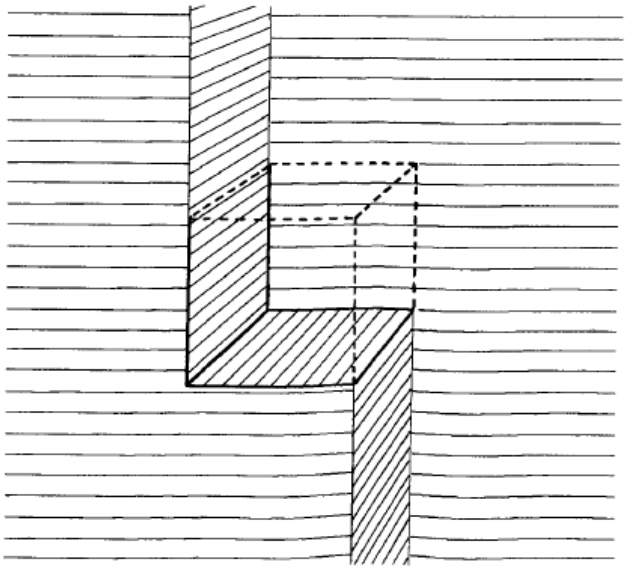

Figure 2.8 A typical rectangular counting brick in 3-D space (Howard et al., 1985)

There is another "edge effect" concerning the relative size or location of the counting domain against the whole microstructure domain, or the "edge effect" of the

whole domain. It is implied in the unbiased counting methods that features intersecting the counting domain are important. Therefore, it is always necessary to have a "guard area" in 2-D or a "guard volume" in 3-D at the sides of the counting domain so that every feature that intersects this domain can be fully observed in the whole microstructure domain. More detailed discussion regarding the "guard volume" will be presented in the next chapter.

Furthermore, the unbiased estimation of number density can be easily adapted to quantify distribution of feature size (e.g. length, volume, or radius), shape or some other geometric attributes. Taking a sampled microstructure volume as an example, the counting brick rule can be used to select the features awaiting characterization followed by performing a specific geometrical measurement such as voxel counting for volume.

2.5 Summary and Conclusions

Different digital imaging techniques are becoming widely available to reconstruct three-dimensional microstructures. Optical microscopy based serial sectioning has been well adopted in the previous triaxial and biaxial related studies on Ottawa sands prepared by air pluviation, moist tamping, or water deposition approaches. Particle orientations, and local void ratio distribution were measured on selected 2-D image slices. Particle shape was quantified from three characteristic dimensions. Spatial averaging of void ratio facilitated the identification of shear zones, transition zones, and non-dilatant zones within a sheared structure. Some of the 2-D characterization results indicated that varying soil fabrics prepared using different laboratory methods led to different microstructural behaviors and macroscale mechanical shearing behaviors. Basic information was reviewed on the digital Ottawa sand microstructures to be investigated in the current study. Index

properties of the Ottawa sands, stress-strain responses during experimental compression tests, as well as digital imaging details were provided.

Characterization of the pore phase in 3-D porous media systems plays a preeminent role in capturing and evaluating spatial variations of many fundamental structure-related properties governed by pore-scale physical processes. However, ambiguous definitions of pore parameters, and expensive computations concerning both underlying high structural complexity and size of the digital microstructure data are major challenges for pore structure characterization. Pore network architecture was normally constructed to retain the true morphology of pore structure based on different geometrical simplifying assumptions. Pore skeleton has been acknowledged in almost all of the preceding computational algorithms to embody not only visual but quantitative information and to be fairly critical for the identification of pore throats and pore bodies. Further exploration of the role of pore skeleton should be valuable and help in establishing a framework of knowledge regarding pore structure in geomaterials.

Design-based stereology allows rigorous, scientific quantitative characterization of 3-D microstructures in numerous disciplines including geology, petrology, metallurgy, cell biology, and neurobiology amongst others. To generate accurate information, sampling bias and systematic bias must be avoided effectively. Systematic random sampling scheme manifests itself as a robust, unbiased and much more efficient sampling technique compared with uniform random sampling. Random sampling error decreases as the sample size increases. Systematic bias originates from the use of biased estimation tools, and the induced systematic error is difficult to predict. In the quantification of topological microstructural properties such as number density, as well as size and shape distributions,

edge effects can lead to serious systematic bias. Practical solutions emerged and evolved from 2-D unbiased counting frame to disector and large-area disector (LAD). Unbiased brick, an important 3-D stereology probe, refers to the volume produced by sweeping a 2-D unbiased counting frame down through 3-D space. Aided by the 3-D microstructure reconstruction, quantitative analyses of the digital sand microstructures in this study will benefit from these significant insights provided by stereological methods.

CHAPTER 3. COMPUTATIONAL APPROACHES FOR MICROSTRUCTURE CHARACTERIZATION

3.1 Introduction

To extend previous insights gained from 2-D and preliminary 3-D studies, an image-based workflow for characterizing the digital Ottawa sand microstructures in 3-D is undertaken with the aid of the commercial software Avizo from Thermo Fisher Scientific. Avizo is a leading 3-D visualization and analysis application, and offers abundant image data processing, exploration and quantification solutions for scientific and industrial data. It contains graphical user interface and customized scripting (e.g. Tcl, Python, and link to MATLAB). A marker-based morphological watershed algorithm is implemented for 3-D particle separation and analysis. Having recognized the significance of pore skeleton in preserving the true pore morphology, skeleton-based computational analysis tools are developed and utilized in order to establish a mathematical, geometrical representation of pore structure in the unconsolidated porous media systems under study. These computational approaches could strengthen the preceding characterization capacity at pore-scale by facilitating the study of the tortuous nature of pore, as well as pore network structure and its statistics. The unbiased stereological techniques reviewed in Chapter 2 are adopted to capture quantitative information from both particle and pore phases.

3.2 Reconstruction and Visualization

Analyzing digital microstructures incorporates image processing (i.e. image enhancement, segmentation, and morphological operations), visualization, and exploration

(e.g. surface generation, phase measurement, and macroscopic property simulation). Because the 2-D images of the Ottawa sand microstructures have very good quality, it is unnecessary to perform pre-segmentation enhancement.

3.2.1 Threshold Segmentation and 3-D Visualization

Regarding the two-phase Ottawa sand microstructures, binary images are created from the grayscale images by interactively choosing a global threshold. An example of binarized 2-D slice stacking is displayed in Figure 3.1. Voxels corresponding to pore phase are set to 1 and shown in blue, while voxels for particles are set to 0.

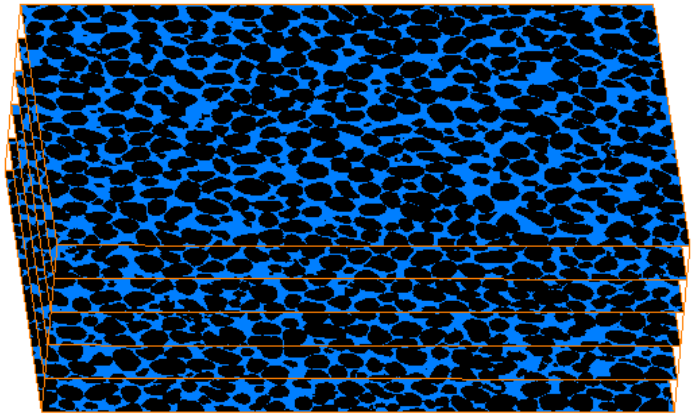

Figure 3.1 A stack of binarized 2-D images

To render the 3-D volume, Avizo features a real-time visualization model according to the emission and absorption of light that pertains to every voxel in the image data. In Figure 3.2, the reconstructed BT0 structure is presented with sand particles illustrated in grey and pores in blue. Internal structure can be visualized by removing a portion of the original volume. As will be discussed in details later, use of the representative elementary volume (REV) is essential for multiscale modelling. REV is a small sub-volume sampled from the original microstructure domain, and hence allows for speedy execution of any

computational algorithm. Identification of the REV for each sand microstructure will be presented in Section 5.5. In this Chapter, a sub-volume of 200 × 200 × 200 voxels extracted from BT0, designated as BT0_SUB, will be employed mostly for the demonstration of the newly developed computational tools. Figure 3.3 visualizes BT0_SUB in the form of continuum, particles and pores.

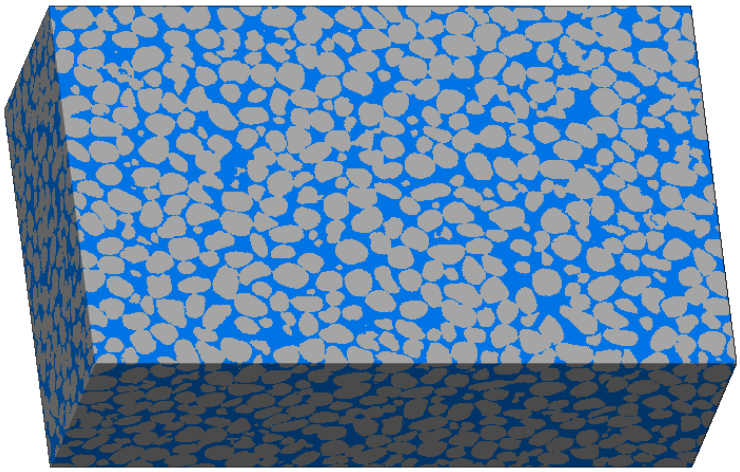

(a)

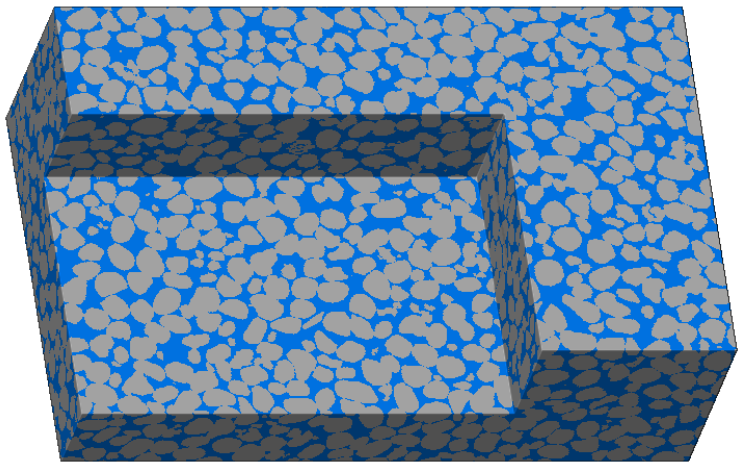

(b)

Figure 3.2 3-D reconstructed structure of BT0 (grey: sand particles; blue: pores): (a) a surface view; (b) an inside view

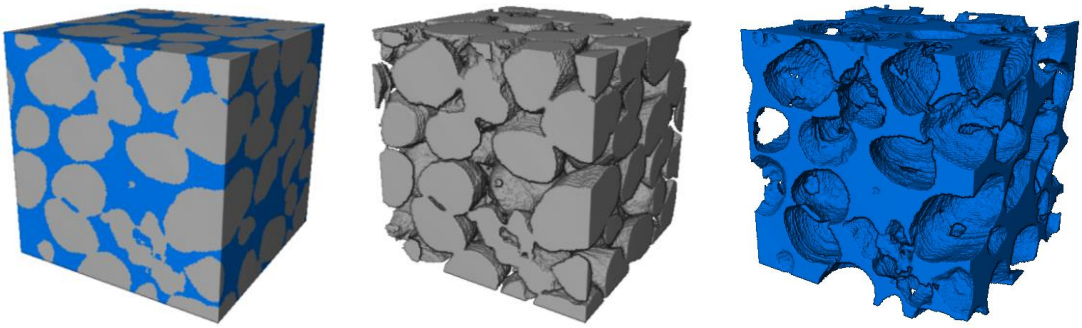

Figure 3.3 Visualization of a sub-volume BT0_SUB

3.2.2 Basic Fabric Characterization

A 3-D digital microstructure that consists of discrete voxels is equivalent to a 3-D matrix. At a resolution of 14 μm/pixel, for example, a voxel has a dimension of 14 × 14 × 14 μm. There are three possible connectivity types considered in processing adjacent voxels. 6-connectivity refers to as two voxels having one common face; 18-connectivity refers to two voxels having at least one common edge; and 26-connectivity refers to two voxels having at least one common corner. In a 2-D configuration, 4- and 8-connectivity are defined alike. 26-connectivity is set to be the default one for its completeness in 3-D processing unless otherwise specified.

As an initial step in characterizing standard structure metrics in a 3-D digital microstructure, phase-specific volume fraction (e.g. porosity) is computed by voxel counting. 3-D void ratio, measuring the relative volume in a two-phase structure, is estimated as the total number of pore voxels divided by the total number of particle voxels. The total surface area is defined as the interstitial surface area of pores and particles, while specific surface area is the total surface area per unit bulk volume of the analyzed microstructure. Applying matrix shifting, particle-pore boundaries are detected in both positive and negative directions of the orthogonal axes, *X*, *Y*, and *Z*. The number of all

boundary voxels, which can be identified from the six principal directions, are multiplied by the surface area of one voxel face to compute total surface area. This particle-pore boundary detection can be discerned as a 6-connectivity (face-to-face) check between a pore voxel and its potential neighboring particle voxels. Additionally, suppose *S* represents a subset of voxels in a 3-D microstructure. If a path that is composed exclusively of voxels in *S* exists between two voxels, the two voxels are connected in *S*. For any voxel *p* in *S*, the set of voxels that are connected to it in *S* is termed as a connected component of *S*. Connected components can be computed and labelled for each phase.

3.2.3 Post Segmentation Processing

In current practice, a procedure of post segmentation processing is proposed to improve the binary images and prepare them for effective computational characterization. Firstly, particle-pore boundaries are smoothed by applying a modified 3-D Gaussian filter in Avizo's *Smooth Labels* tool. Small irregularities at the particle-pore boundaries as a result of digitization/segmentation artifacts negatively impact particle separation and pore skeleton analysis, and hence need to be corrected. After the smoothing operation, a *Fill Holes* module is used to remove very small, isolated particles that are fully embedded in the pore phase through a region filling process combining complementation, dilation and intersection. The isolated particles intersecting the volume borders are not removed. Most of those removed particles are less than 10 voxels in volume and negligible for particle analysis, but can be detrimental to the computation of pore skeleton. Based on comparing the standard structure metrics before and after post segmentation processing, the influence of the above two clean-up operations is minimal. For BT0 structure, for example, change

in void ratio is only about 0.6% while surface area is 8%. Effects of polishing binarized images on pore structure analysis will be further illustrated in Section 3.5.2.

3.3 Unbiased 3-D Quantification Rule

As introduced in Section 2.4.2, an unbiased counting technique prevents systematic bias due to the edge effect in quantifying topological microstructural properties including number density, size and shape distribution. In 3-D, an unbiased counting brick can help in selecting the features to be characterized. The schematic view of a typical counting brick is redrawn in Figure 3.4 over the whole domain of BT0 showing the central brick volume in red, three "acceptance surfaces", and five "forbidden surfaces" that are shaded planes in blue and extending to infinity. The brick counting rule states that a feature is selected if it totally inside the brick or if it intersects the brick but not any of the forbidden surfaces. In the Cartesian coordinate system *XYZ* (Figure 3.4), let *P* be a feature consisting of a set of voxels, and (x, y, z) be an arbitrary voxel in *P*. The corners of a brick *B* can be (x_1, y_1, z_1), (x_2, y_1, z_1), (x_2, y_2, z_1), (x_1, y_2, z_1), (x_1, y_1, z_2), (x_2, y_1, z_2), (x_2, y_2, z_2), and (x_1, y_2, z_2) given that $x_1 < x_2$, $y_1 < y_2$ and $z_1 < z_2$. Note that $x, y, z, x_1, x_2, y_1, y_2, z_1$ and z_2 should all be integers. *P* will be selected in *B* if (a) any voxel in *P* satisfies $x_1 \le x \le x_2$, $y_1 \le y \le y_2$, and $z_1 \le z \le z_2$, or (b) *P* intersects *B* with conditions: (1) there is no voxel (x, y, z) such that $z > z_2$; (2) there is no voxel such that $z_1 < z \le z_2$ and $x < x_1$; (3) there is no voxel such that $z_1 < z \le z_2$, $x_1 \le x < x_2$, and $y > y_2$. There is a special scenario that all voxels in *P* lie on the boundary surfaces of the central brick volume while criterion (a) is satisfied. This rarely happens, but when it does, *P* will be selected if it is not located on the forbidden surfaces. By following the above rule, it is guaranteed that each feature is selected by one and only one brick.

Another requirement in practice concerns the size and location of the counting brick with respect to the whole microstructure domain. All features intersecting the 3-D brick must be able to be inspected at the full extent. Considering many features of interest that intersect the borders of the whole domain haven't been imaged completely, the 3-D brick cannot be as large as this domain. The "guard volume" is therefore introduced to be located at the sides of the central brick volume that should be large enough to avoid miscounting. Dimensions of the "guard volume" are commonly defined based upon the characteristic size of the features to be quantified. Specification of the "guard volume" for particle characterization will be presented in Section 3.4.3 and for pore characterization will be presented in Section 3.5.6.

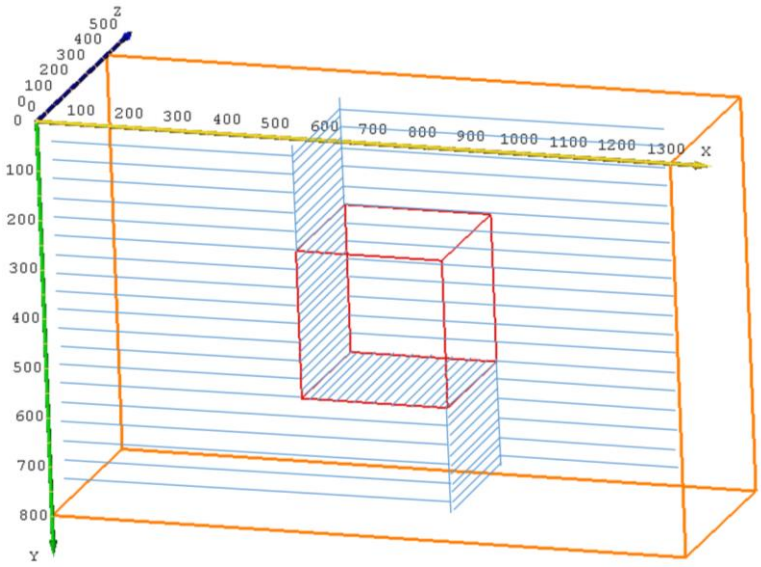

Figure 3.4 Schematic view of a counting brick placed over the domain of BT0

3.4 3-D Particle Characterization

Particles that are individually accessible and measurable are desired for quantitative characterization. From observing the datasets under study, many particles appear to be

touching, and separation is needed. This can be accomplished using a marker-based family of morphological watershed as it was previously stated to defend against over-segmentation and over-sensitivity to noise (Beucher, 1992).

3.4.1 Marker-Based Morphological Watershed

A greyscale image is a topographic surface involving spatial coordinates and grey levels. A watershed algorithm defines catchment basins and watershed lines by means of a flooding process beginning around local minima of the topographic surface. Catchment basins are regions that contain the local minima, while watershed lines (or watershed surfaces in 3-D) are continuous boundaries where distinct basins are merging. Particles are separated by subtracting voxels on the watershed lines from the particle phase in binary images. Figure 3.5 gives a best illustration in 1-D.

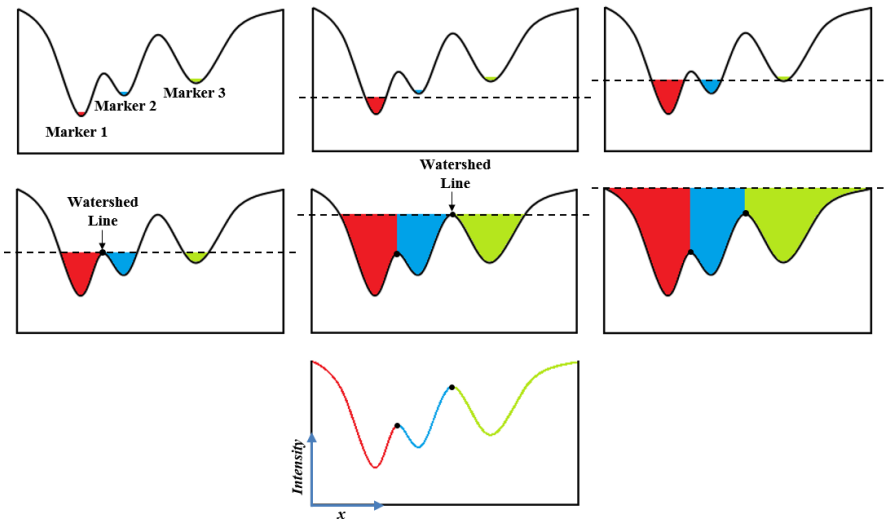

Figure 3.5 Illustration of marker-based morphological watershed in 1-D

A marker-based watershed algorithm depends on two inputs: markers and separation function (i.e. topographic surface). A "marker" is constructed as a connected

region around local minima and definitely inside a single particle. Markers are used as seeds for the flooding, and the number of them is directly corresponding to the number of separated particles. In this study, markers are constructed through distance transform followed by local maxima merging. Euclidean distance map (EDM) on the segmented particle phase is calculated, and each particle voxel on the EDM has a value representing its minimum Euclidean distance to the pore phase. So the interior regions of the particle are associated with a bigger value than that at the particle-pore boundaries. Then Avizo's *H-Maxima* module is applied so that local maxima in the distance map are merged within the contrast variation controlled by a coefficient *h*. Assuming a local maximum has a value *m* on EDM, the set of voxels adjacent to it having a value greater or equal to *m-h* will be merged to form one marker. Through the merging, one marker may include several local maxima to avoid over-segmentation. Figure 3.6 illustrates this marker generation process on one 2-D slice (300 × 300 pixels) of BT0.

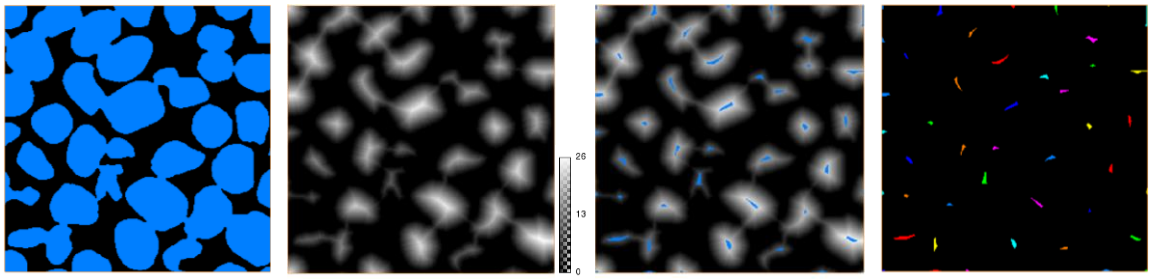

(a) (b) (c) (d)

Figure 3.6 A 2-D illustration of marker generation on one slice in BT0: (a) binary image; (b) Euclidean distance map (unit: voxel); (c) markers (h = 1); (d) labelled markers

It was previously proven that the above marker generation method could be very successful for spherical particles (Ando, 2013). In images of the natural, sub-rounded sands studied in this work, however, perfectly generating markers in each particle is difficult and errors can occur, such as situations shown in Figure 3.7. Incorrect markers will lead to

over-separation or under-separation. The former usually occurs if the object of interest has a non-convex shape or small cavities inside, while the latter one when two objects are considered as one from the standpoint of local maxima on distance map owing to irregular particle shape or contacts. Contrast coefficient *h* can be tuned to change the number of separated particles, but errors are hard to resolve completely (Figure 3.8).

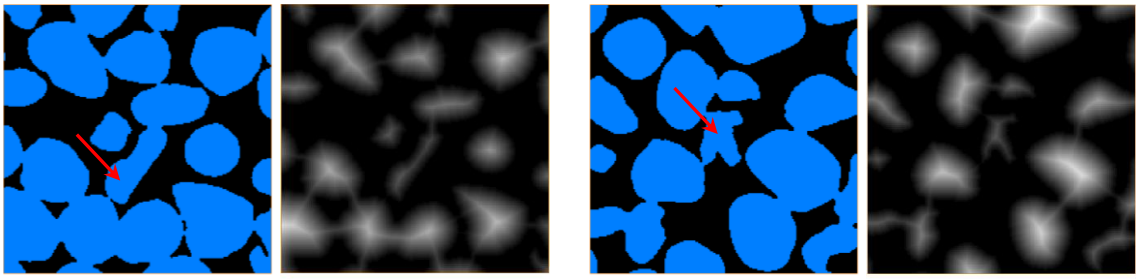

(a) (b)

Figure 3.7 Possible situations where markers may be generated incorrectly: (a) two markers in one elongated particle; (b) one marker for irregularly contacted particles

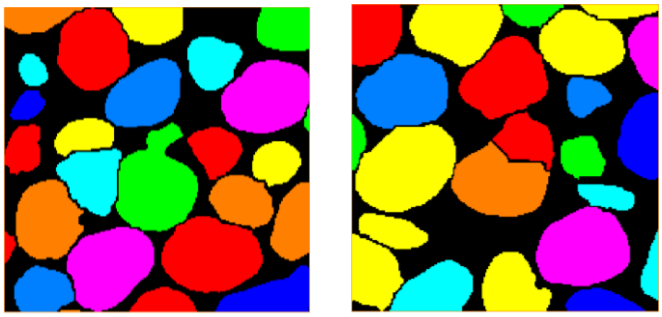

(a) (b)

Figure 3.8 Examples of errors observed from 3-D particle separation in BT0: (a) under-separation; (b) over-separation

Separation function, on the other hand, controls the flooding progression and eventually the locations of watershed separations. A qualified separation function should have troughs around the markers, and peaks where particles are touching each other. Inverted distance map, grayscale image, and gradient of the grayscale image are three possible candidates. Both grayscale image and gradient image can present peaks at particle-

pore boundaries, but not necessarily at particle-particle contacts especially when grayscale intensity is fairly homogeneous across the particle phase. Inverted distance map relies on geometry of particles and proves itself valid by having the demanded trough-peak features, as shown in Figure 3.9 in which it is computed through multiplying EDM by negative one.

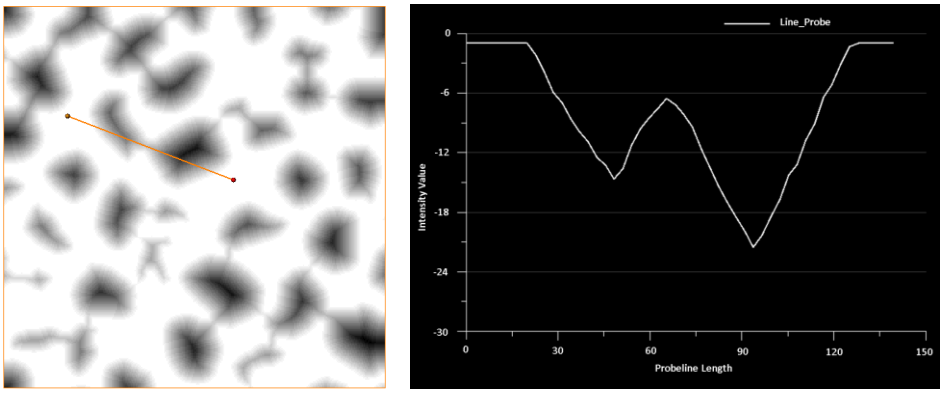

Figure 3.9 Inverted EDM (Figure 3.6(b)) and intensity distribution along a line segment

3.4.2 Particle Separation

Avizo's *Marker-Based Watershed* module iteratively grows the markers towards increasing values of the separation function. Figure 3.10 shows a 2-D separation result, and watershed lines possess a thickness of unit voxel. The separated particles in structure BT0 are shown in Figure 3.11. Individual particles are labelled based on connected components analysis, and are displayed using an 8-color cyclic colormap. Uniquely labelled particles can be examined singly as well.

As mentioned earlier, some separation errors cannot be avoided for configurations such as irregular particle shapes and particle-particle contacts. The current computational procedure indicates that parameterization controlling the separation concentrates in the marker generation step. Trials can be performed by varying contrast coefficient *h*, and assessment can be made by visual comparison regarding whether the separated particles

can represent the physical reality of particles or not. It is observed that the marker-induced separation errors do occur occasionally, but the quality of the 3-D separation is considered to be sufficient for measurement in this work.

Admittedly, there is possibility for improving particle separation in future research. When a structure contains a limited number of particles, manually generating markers becomes feasible. If priori information on particles morphology is able to be known, adding or modifying certain parameters locally may help correct some errors in marker generation. More complex approaches such as the level set-based method (Vlahinić et al., 2014) have been suggested to deal with the challenge of identifying irregular particle-particle contacts.

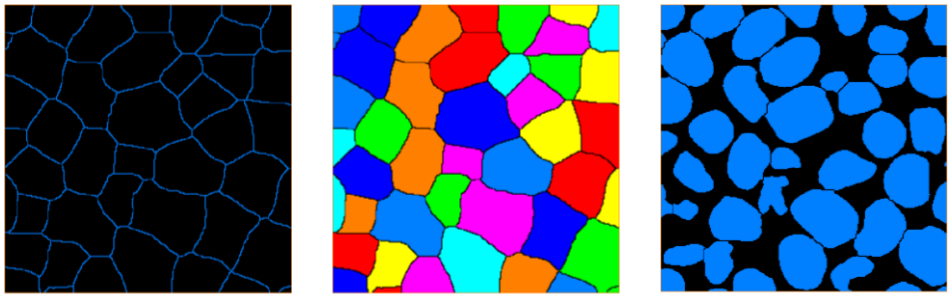

(a) (b) (c)

Figure 3.10 2-D particle separation on one slice (same as that in Figure 3.6) in BT0: (a) watershed lines; (b) catchment basins; (c) separated particles

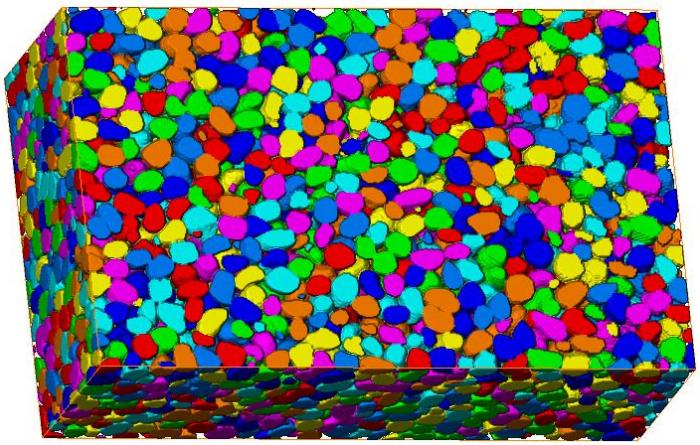

Figure 3.11 3-D particle separation in structure BT0 showing labelled particles

3.4.3 3-D Measurement of Particle Size

Quantitative analyses on particles cannot be performed directly on the separated particles shown in Figure 3.11 because many particles intersect the microstructure domain borders. A large unbiased 3-D brick is placed by specifying the "guard volume" at each side of the central volume that has a characteristic length of D_{50} of the Ottawa sands. As for BT0, D_{50} of Ottawa 20-30 sands is 0.74 mm, and is equivalent to about 55 voxels at an image resolution of 14 μm/pixel. So, the central volume of the 3-D brick has a dimension of 1190 × 690 × 320 voxels (see Figure 3.12), and it is concentric to the whole domain (1300 × 800 × 430 voxels). The distance between each surface of the central brick volume and its parallel domain surface is 55 voxels. Figure 3.13 shows the particles selected in BT0 structure following the unbiased counting rule. Out of 4210 separated particles, 1872 particles are considered for measurement. In Figure 3.12 and Figure 3.13, domain of the central brick volume is presented in green solid line and the whole domain in orange.

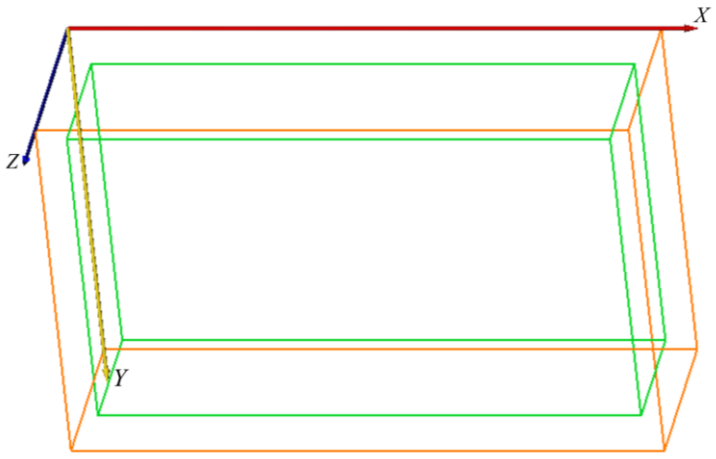

Figure 3.12 Central volume domain of the 3-D unbiased counting brick

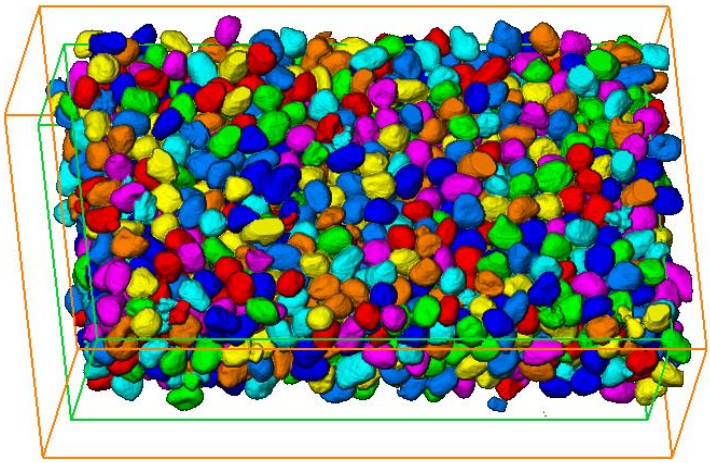

Figure 3.13 Selected particles for measure using 3-D unbiased counting brick in BT0

Particle size can be defined in several ways for irregular particles depending on the measurement method. One of the concepts is "volume equivalent diameter" that quantifies the diameter of a sphere with the same volume of the particle. Besides, since "sieve size" measured from sieve analysis has been utilized by soil classification systems for decades of geotechnical engineering practice, it is worthwhile to compare image-based particle size with that. Ohm and Hryciw (2013) derived an equivalent sieve opening size d_e from image analysis using translucent segregation table (TST) test as Eq. (1), in which particles are idealized to be ellipsoidal with $d_1 > d_2 > d_3$.

$$d_e = \sqrt{(d_2^2 + d_3^2)/2} \tag{1}$$

For each separated particle in Figure 3.13, ellipsoidal dimensions are calculated based on finding principal axes of moments of inertia. Comparison can be made between image-based particle size distribution and sieving result. Figure 3.14 plots two image-based particle size distributions in BT0 and the sieving result conformed to ASTM D422-63 on Ottawa 20-30 sands of the biaxial specimen (Evans, 2005). In general, agreement between

image-based measure and sieving is very good. An improvement as to matching the sieving data can be seen in using the sieve equivalent size.

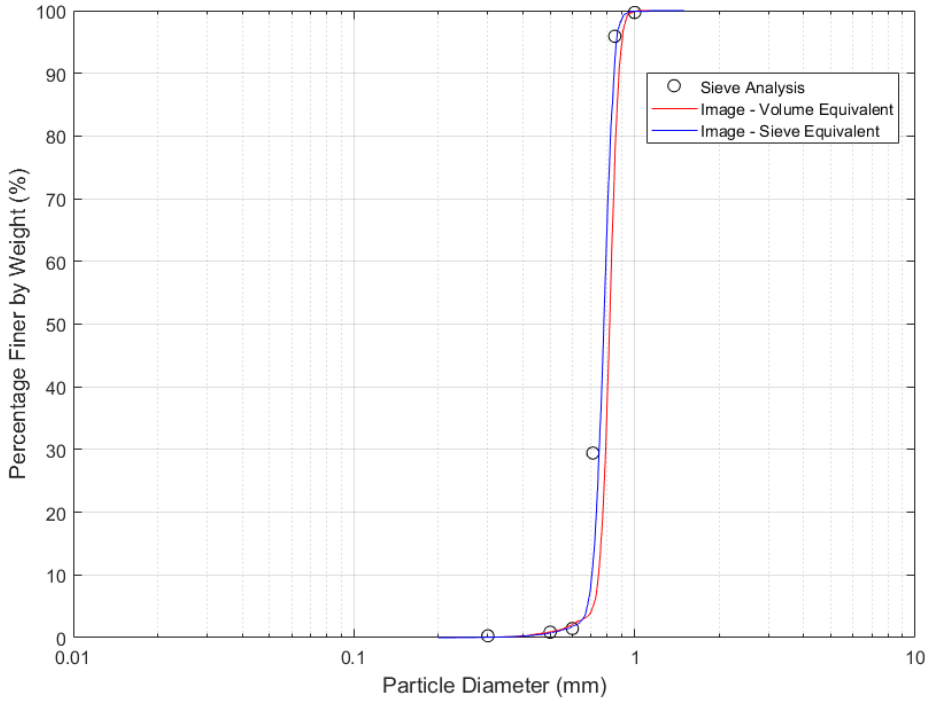

Figure 3.14 Comparison of image-based particle sizes in BT0 with sieving result of Ottawa 20-30 sands

3.5 3-D Pore Structure Characterization

This section presents the proposed skeleton-based algorithms for quantitative characterization of the complex pore structure in unconsolidated porous media like the Ottawa sand microstructures studied. Both the tortuous attribute as well as the physically representative pore network architecture are investigated. Exploration of preparation-induced variations in inherent structures and mechanical shearing-induced evolution at pore-scale will benefit from the enhanced computational characterization capacity.

3.5.1 Research Framework

Inspired by medial-axis transformation, pore skeleton is computed using an adaptation of Distance Ordered Homotopic Thinning (DOHT) method as a discrete representation of the continuum pore space. It is a hybrid algorithm that combines distance map and morphological thinning to ensure a homotopic, thin, and centered skeleton (Fouard et al., 2006). Initially developed for microvascular network study, this algorithm applies a Chamfer distance transform to guide the iterative process of eliminating voxels towards an object's center. Chamfer distance (Borgefors, 1984) is an approximation of Euclidean distance based on a 3 × 3 × 3 mask in 3-D, and consequently realizes faster computation while being accurate enough in most applications. Avizo has it built in the *Auto Skeleton* module.

Pore skeleton is initially extracted in the form of "voxel skeleton". It is a binary representation with voxels on the skeleton having a labelled value of 1 and non-skeleton voxels being 0. Geometrical tortuosity of the pore structure is evaluated on the voxel skeleton through developing a novel, generic analysis tool. A second way of representing the pore skeleton is "spatial graph" that simplifies the voxel skeleton into a network of curved 3-D lines. This is not the pore network architecture yet, but is fundamental to analyze pore network properties. Performing search on the spatial graph, two algorithms are introduced to locate pore throats. A local sphericity algorithm enables the extraction of all important parameters in the pore network, and permits a mathematical model to be established. Planar surface construction algorithm, in comparison, aims to geometrically partition the entire pore space into pore bodies bounded by declared pore throat surfaces. As will be deliberated later, throat finding using the planar construction algorithm is much

more challenging than the local sphericity algorithm owing to the presence of geometric complications in the porous media of concern. The 3-D spatial distribution of pore throats and pore bodies, size distribution of pore throats and pore bodies, pore body-throat connectivity, and pore channel length can be estimated. Spatial size correlation within the network can be examined preliminarily too. Figure 3.15 presents a research framework for pore structure characterization. All the algorithms for computing the above-mentioned pore-scale metrics are developed and coded in MATLAB by MathWorks. Illustration is continued mostly on the structure BT0_SUB shown in Figure 3.3.

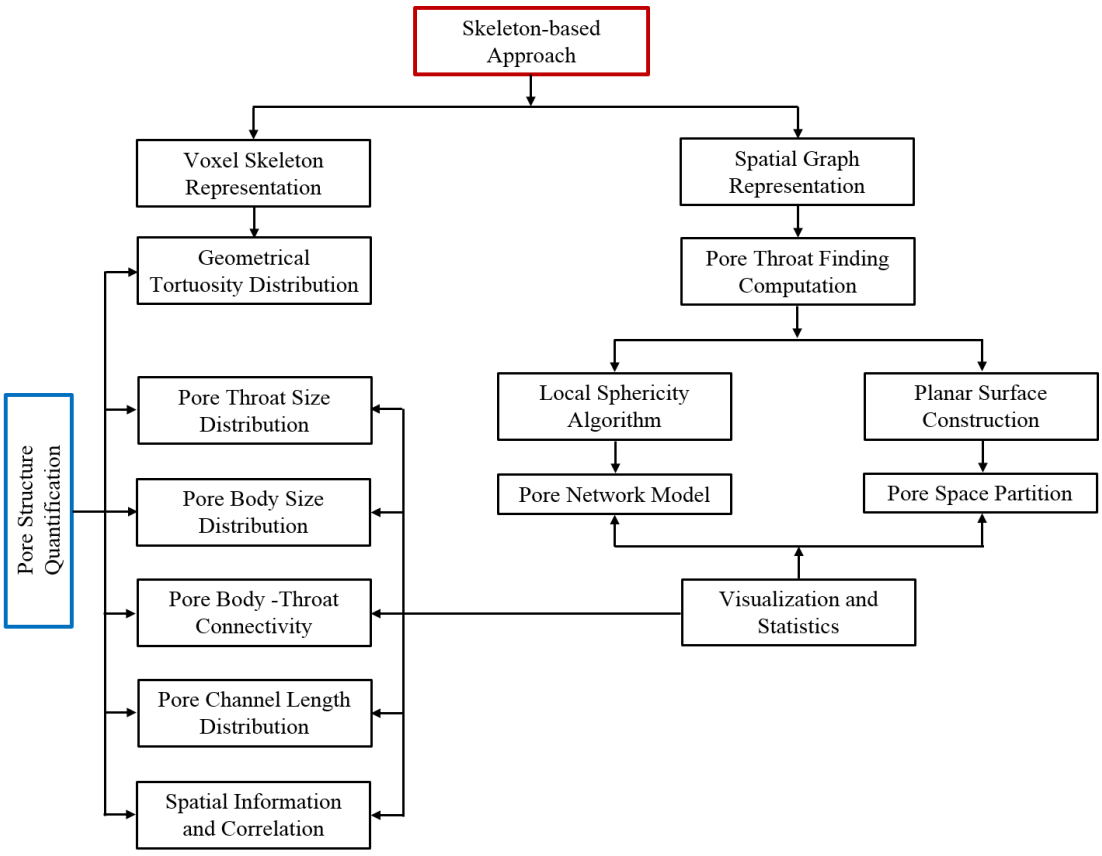

Figure 3.15 Framework for pore structure characterization

3.5.2 Voxel Skeleton and Geometrical Tortuosity

A 2-D example of pore skeleton extraction is shown in Figure 3.16 for an intuitive visualization, and the slice is from BT0_SUB. One-voxel thickness skeleton is located along the distance map maxima, suggesting an equidistance to particle-pore boundaries. Voxel skeleton is visualized in 3-D, and can be seen to be improved effectively by the post segmentation processing noted earlier in Figure 3.17. Closed "surface", resulting from very small isolated particles or irregularities at particle-pore interfaces, surrounds those regions and algorithmically complicates the skeleton-based analyses. Post segmentation processing can succeed in over 90% removal of these closed surfaces.

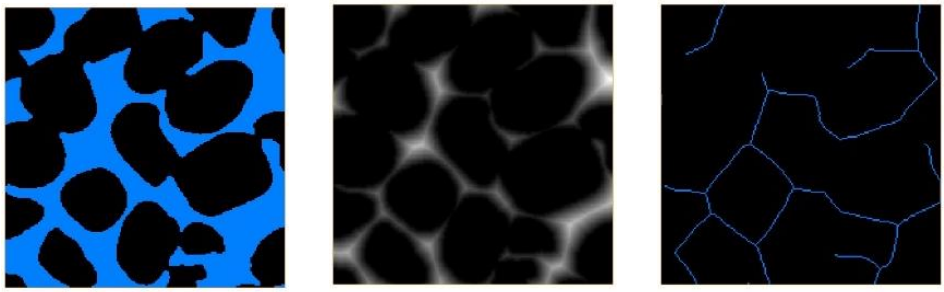

(a) (b) (c)

Figure 3.16 Pore skeleton computation in 2-D from segmented pore phase of BT0_SUB: (a) segmented pore; (b) Chamfer distance; (c) voxel skeleton

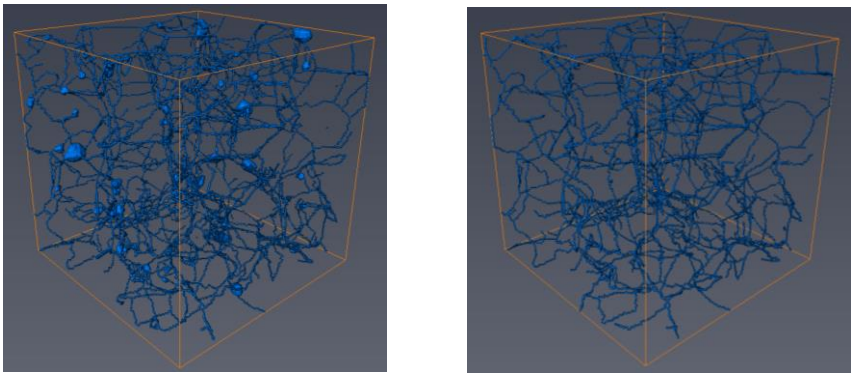

(a) (b)

Figure 3.17 Improved skeleton from post segmentation processing on BT0_SUB: (a) before processing; (b) after processing

In 3-D pore structures, a geometrical tortuous path is defined as the shortest path that starts at any surface voxel on one side of the microstructure volume and reaches the opposite side while always remaining in the pore skeleton network. A geometrical tortuosity measure is computed as the ratio of the actual tortuous path length to the characteristic distance between the opposing surfaces. It is an important structural metric characterizing the convoluted pathways of fluid diffusion and electrical conduction through porous media. Conventionally, tortuosity is resolved by use of semi-empirical correlations, for instance, relation of effective diffusivity coefficient and tortuosity (Ostadi et al., 2010; Iwai et al, 2010; Haussener et al., 2010), and is reported as a single value averaging over the microstructure volume. Provided that internal structure of the pore space is highly complex and heterogeneous, however, defining a single tortuosity value can be restrictive in capturing the comprehensive knowledge of the structural topologies associated with every tortuous path. A more appropriate approach would be to examine the spatial variation of geometrical tortuosity in order to better predict the variation of relevant transport properties within the microstructure. In this work, a pure voxel-based algorithm is developed for a direct quantification of the tortuosity distribution in 3-D without involving semi-empirical approximations.

3.5.2.1 Graph Theory and Shortest-Path Searching

The fundamental theory behind the tortuosity analysis tool is graph algorithms. A graph $G = (V, E)$ is made up of vertices, V, connected by edges, E. There are two types of graphs: directed and undirected. In a directed graph, edges are directed from one vertex to another; while in an undirected graph, no distinction is present between the two vertices corresponding to each edge. Figure 3.18 shows pictorial examples of both graphs.

Adjacency information for each $u \in V$ can be generated to represent a graph in a list or a matrix. The adjacency-matrix form is capable of quickly determining whether a given edge is present in the graph, but at the cost of consuming more memory. If each edge has an associated weight function w, the graph is a weighted graph such that the edge $(u, v) \in E$ stores the weight $w(u, v)$. And this weight can be stored as the entry in row u and column v of the adjacency matrix.

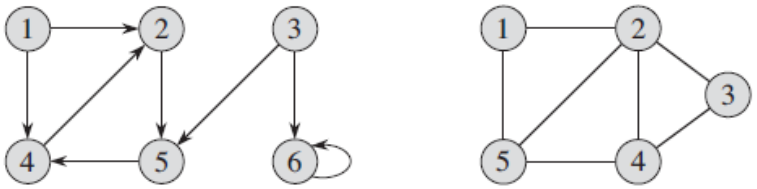

Figure 3.18 Example of directed and undirected graphs (Cormen, 2009): (a) a directed graph with 6 vertices and 8 edges; (b) an undirected graph with 5 vertices and 7 edges

Graphs can be utilized to model many practical problems in physical, biological, social and information systems. Some of the significant ones include the computation of a minimum-weight spanning tree, shortest paths, or a maximum flow of material in a flow network. In a shortest-path problem for a given weighted, directed graph $G = (V, E)$ with weight function w, the weight $w(p)$ of the path p is the sum of the weights of its constituent edges. The shortest-path weight $\delta(u, v)$ from u to v is defined as $\min\{ w(p): u \xrightarrow{p} v \}$ if there is a path from u to v; otherwise ∞ (Cormen, 2009). A shortest path from u to v is then identified as any path p with weight $w(p) = \delta(u, v)$. That is to say, it is the problem of finding a path between two vertices in a graph so that the sum of the weights of those edges comprising the path is minimized. Many algorithms exist such as Dijkstra's algorithm, Bellman-Ford algorithm, A* search algorithm and so on. The most basic shortest-path problem is the single-source problem, which is to search for a shortest path from a given

source vertex to each vertex in the graph. Its variants involve single-destination shortest-path problem, single-pair problem, and all-pairs problem.

3.5.2.2 A Pure Voxel-Based Algorithm

The algorithm identifies all tortuous paths existing in the 3-D pore skeleton by calculating the shortest path for every single skeleton voxel on an entry surface of interest. A 3-D voxel skeleton structure is the original input to this algorithm, and has the same size as the microstructure volume from which it is computed. The voxels corresponding to the skeleton can be denoted as V_s that have a labelled value of 1. In the context of graph theory, the voxel skeleton needs to be transformed into a 2-D mathematical graph, and a shortest-path search is then performed on that graph. To implement the method, a 2-D adjacency matrix is constructed as a computational representation of the graph by recognizing the physical connectivity for voxels within the voxel skeleton structure. Importantly, it is a large but sparse matrix since non-zero weights are exclusively reserved for the connections between every two voxels on the skeleton, in other words, V_i -to-V_j (V_i, $V_j \in V_s$, $i \neq j$) connections. Zero values mean no connection, and it is guaranteed that tortuous paths will be computed along the skeleton. In graph $G = (V, E)$, subsets of vertices V are V_s, and subsets of edges E are E_s having positive numerical values stored that specify the Euclidean distances for connected V_i -to-V_j pairs. So, 1 is stored for face-to-face type of V_i -to-V_j connection, $\sqrt{2}$ for edge-to-edge, and $\sqrt{3}$ for corner-to-corner. Graph G is undirected considering V_i -to-V_j and V_j -to-V_i represent an identical edge. To account for every skeleton voxel on the entry surface, designated as V_{entry}, a source vertex s is fictitiously added beyond the exit surface (i.e. the opposite side) with an equal distance to every voxel on that surface (see Figure 3.19). Setting the distances to be equal prevents any favoritism in the

shortest-path searching among voxels on the exit surface. That distance will be subtracted when computing tortuosity. Accordingly, the problem of searching for the shortest paths to s from V_{entry} is reduced to a single-source problem starting from s. By incorporating s into the graph, the adjacency matrix is finalized to be in a dimension of $|V|+1 \times |V|+1$. Dijkstra's algorithm searches on the weighted, undirected graph for the shortest paths.

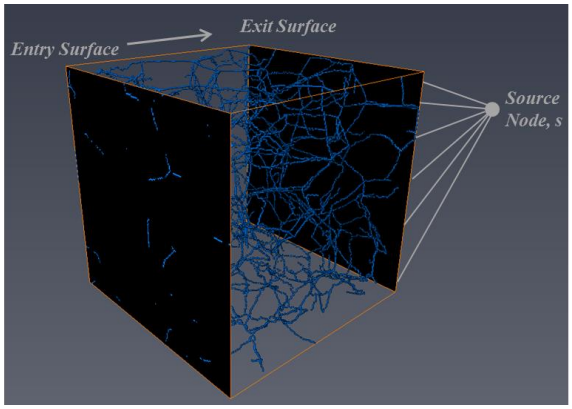

Figure 3.19 Creation of a single-source shortest-path problem

It is worthwhile to state that the objective of the present approach is to identify a complete set of existing pathways available for transport within the microstructure. It is formulated to find shortest paths from every voxel on the entry surface to the entire exit surface rather than every voxel on it. Tortuosity herein is a directional metric. In creating the adjacency matrix, travelling from one skeleton voxel to another is assumed to be based on 26-connectivity, i.e. 26 probable directions locally. This tool is generic and applicable to any 3-D microstructure data, and even without having skeleton extraction as a requisite. From the obtained tortuosity distribution, statistics can be collected. It allows for gaining a deeper insight into the tortuous nature of pore structure, its variation due to mechanical shearing, as well as the role it has in affecting the transport properties. As to a specific

transport-related problem, the preferable pathways from those computed shortest paths would need to be determined depending on a proper physical model.

3.5.3 Pore Skeleton Trimming

3.5.3.1 Spatial Graph Representation

Spatial graph represents the pore skeleton using a network of 3-D curved lines consisting of three structural elements: *Point*, *Node*, and *Segment*. A *Node* is either a branching voxel with equal to or over three neighbours, or an end voxel with only one neighbour. A *Segment* is a discrete line connecting *Node*s, and consists of *Point*s that have exactly two neighbours. *Point*s are specified by their spatial coordinates. If more than one branching voxel is connected to each other forming a cluster, which is not uncommon, a *Node* will be located at the barycentre of the cluster to maintain equivalence topologically. Spatial graph is generated using the *Trace Lines* module in Avizo. By zooming in on a small portion of a pore skeleton, conversion from the voxel skeleton representation into the spatial graph representation is shown in Figure 3.20. For each *Point* in the spatial graph, an important geometrical attribute termed as "local sphericity" can be calculated through mapping the distance map onto it. The "local sphericity" estimates a radius of the local maximal sphere centered at a *Point* that completely fits into the pore space. This piece of quantitative information is critical to the pore skeleton trimming process and pore network construction. Figure 3.21 presents the spatial graph of pore skeleton structure in BT0_SUB in a basic format of *Node*s connected by *Segment*s, and in colormap implying the local sphericity attributes. With a *Node-Segment* structure, spatial graph is more advantageous than voxel skeleton in building the pore network architecture.

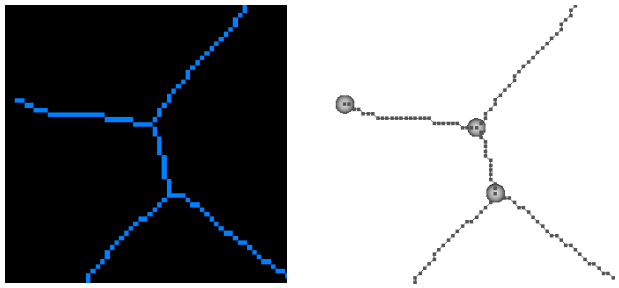

(a) (b)

Figure 3.20 Illustration of conversion from voxel skeleton into spatial graph: (a) voxel skeleton form; (b) spatial graph form

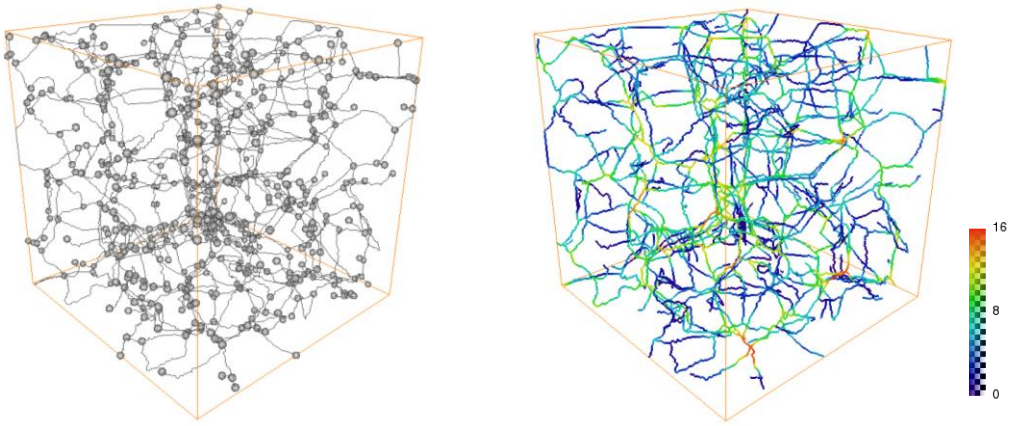

(a) (b)

Figure 3.21 Spatial graph representation of pore skeleton in BT0_SUB: (a) basic format; (b) colored by local sphericity attribute (unit: voxel)

3.5.3.2 Significant Pore Paths Identification

One conceptual model in characterizing pore morphology is pore bodies, the larger pore space openings, connected by pore pathways. Each pore pathway is likely a candidate to contain a pore throat as the narrow pore opening. Pore pathways are usually described by a single curved path, while pore bodies are described by a collection of branching voxels and paths. Although each pore pathway has its corresponding *Segment* on the spatial graph, not each *Segment* essentially corresponds to a pore pathway. Likewise, several *Node*s may belong to the same pore body. Through identifying "Significant Pore Path", which is

designated as *SPP*, a one-to-one correspondence among these geometrical components is expected to be established.

Delineated by a skeleton trimming process, *SPP*s will characterize the *Segment*s that exclusively describe pore pathways. The main purpose of skeleton trimming is to concentrate the pore network analysis on the flow-accessible portion of the skeleton. It should be clarified first that coordination number (*CN*) of a *Node* is the number of incident neighbors it has. Connection feature of a *Segment* is determined by *CN*s of its two end *Node*s. The original value of *CN* for every *Node* before trimming is easily extracted from the spatial graph. A procedure for identifying *SPP*s is proposed as follows:

1. Identify *Segment*s that intersect the boundary surfaces of the microstructure domain being imaged, and record them as *SEG_Incomplete* instead of *SPP*. Considering these *Segment*s contain incomplete pore structure information, *SEG_Incomplete* will be employed to deal with the edge effect in the quantification of pore structure (see Section 3.5.6).
2. "Loop" *Segment*s are eliminated unless closed pore paths are acknowledged. For each identified "loop", *CN* of that same *Node* at both ends is reduced by 2.
3. Skeleton components that do not support pore-scale transports, or saying non-percolating, are removed. Isolated single skeleton voxel, isolated *Segment*s (both ends with $CN = 1$), and interior dead-end *Segment*s (one end with $CN = 1$) are included. Isolated *Segment*s are more often seen in 2-D as an artifact; nonetheless, a fewer number appear in 3-D terminating the domain boundaries that should have been recorded in *SEG_Incomplete*. As to either isolated or dead-end *Segment*s, the

end *Node*s with $CN = 1$ are simultaneously eliminated. For dead-end *Segment*s, *CN* of the remaining end *Node* is reduced by 1.

4. *Node*s and their connecting *Segment*s that entirely lie in one pore body are "merged" into a *Node Cluster*. "Merging" is achieved by a dynamic distance measure test (see Figure 3.22). Suppose length of a *Segment* is L, and let R_1 and R_2 denote local sphericity attributes of the two end *Node*s, N_1 and N_2. If $L < R_1 + R_2$, the *Segment* is deemed as a pore-internal path, and "merged" into a *Node Cluster* together with N_1 and N_2. As a *Node* can be perceived as the "center" of a potential pore body, local sphericity attribute at the *Node* should reasonably correspond to a radius measure of that pore body. This "merging" criterion thus states that if two pore bodies overlap, the two *Node*s representing them and the *Segment* joining them are considered part of a same pore body with a bigger size. Iterating the "merging" will lead to the possibility that more than two *Node*s are absorbed by a *Node Cluster*. "Merging" does not mean to change the skeleton, but rather marks and records the information. All the identified pore-internal paths are not included in *SPP*s. In computing *CN* of a *Node Cluster*, *CN*s of the "merged" *Node*s as well as the number of pore-internal paths belong to that cluster are taken into account.
5. After step 4, repeating step 2 to eliminate the newly produced "loop" *Segment*s. There might be a scenario that the two ends of a *Segment* are "merged" into one pore body with an identical *Node Cluster* information. This *Segment* is turned into a closed path by the "merging".

Besides, the presence of duplicated pore pathways in the skeleton requires being aware of this in the skeleton trimming process. It refers to multiple *Segment*s connected to one same

Node or *Node Cluster* at one end while to another same *Node* or *Node Cluster* at the other end. Because these are meaningful pore pathways, trimming is not performed but *CN* for each end is reinterpreted. Another key fact to mention is that the "merging" criterion applied in defining pore-internal paths is not a convention, and individual decisions can then result in discrepancies in the end results. Recognition of additional pore-internal paths during throat finding will be discussed in Section 3.5.4.

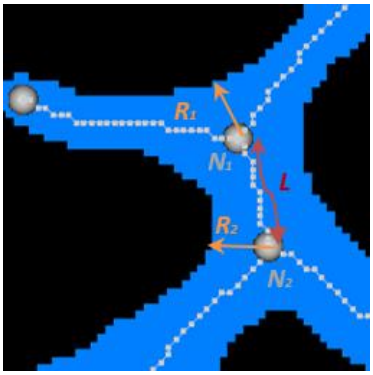

Figure 3.22 2-D illustration of the distance measure test

After pore skeleton trimming, the remaining *SPP*s and *Node*s or *Node Cluster*s in the spatial graph are in one-to-one correspondence with pore pathways and pore bodies. Though, whether these pore pathways are actual pore channels containing pore throats still remains to be investigated. In view of the essential role of pore throats in characterizing pore network, efforts have been devoted into developing algorithms to locate pore throats. Having pore throats identified, then pore bodies, pore body-throat connectivity, and pore channels can be quantitatively characterized.

3.5.4 Throat Finding Methods

All preceding research have demonstrated that the determination of pore throat from 3-D intricate, irregular pore structure is a challenging task, and creating a unique pore

network architecture is difficult to achieve. A rigorous definition of pore throat is absent, while the shape of it was stated to be possibly nonplanar (Lindquist and Venkatarangan, 1999; Shin et al., 2005; Prodanović et al., 2006; Kim et al., 2013). However, oftentimes assumptions are made to simplify its geometry and quantification is also approximated somehow because of computational difficulties. In this section, two algorithms involving distinct simplifications are proposed. Identified significant pore paths, percolating from one pore body to another, serve as the searching structure for throat computation.

Pore throat here is a geometric quantity, and is defined as a position corresponding to local minimum restriction in the pore network. More importantly, only the "primary" local minimum, or in other words, the global minimum restriction on each *SPP*, will be located due to its predominant influence on pore-scale behavior. Furthermore, it is ensured in both algorithms that a computed throat does not entirely lie in a pore body represented by a *Node* or *Node Cluster* on the significant pore paths. Finally, in the pore network, one throat should separate exactly two different pore bodies.

3.5.4.1 Local Sphericity Algorithm

Using the local sphericity attribute, pore throats and pore bodies are simplified as spherical shape. The local sphericity algorithm for throat finding consists of three steps.

Step 1: Along every identified *SPP*, the radius of the maximal inscribed sphere centered at every voxel on the *SPP* excluding its two ends is stored in a list. The radius of the candidate throat for this *SPP* is determined to be the smallest radius by sorting the list. If multiple skeleton voxels on a single *SPP* have the same radius value, one is randomly assigned as the candidate throat location. A condition is applied in generating the *SPP* list.

Let *v* be a voxel on one *SPP*, and distance from *v* to each of the two ends along the path be l_1 and l_2, respectively. Only if the estimated radius r_v at *v* is not larger than $\min(l_1, l_2)$, the chance of finding a throat at *v* is accepted. Otherwise (i.e. $r_v > \min(l_1, l_2)$), it is reliably argued that this computed throat is enclosed fully within a pore body. The $\min(l_1, l_2)$ can be defined as the critical radius r_{cr} for checking against the computed throat radius. Enforcing this check, a scenario might happen that all voxels on a *SPP* being ignored in the throat finding because the *SPP* lies in sole pore body. Accordingly, candidate throats will not exist on a portion of the *SPP*s within a microstructure volume under study.

Step 2: Those *SPP*s without candidate throats are identified as new pore-internal paths, and "merging" of *Node*s or *Node Cluster*s is implemented again as in the skeleton trimming process. New "loop" paths connecting to the same *Node Cluster*, if there is any, and their contained candidate throats are eliminated after the "merging". Since every remaining candidate throat correctly separates two distinct pore bodies, it is identified as a throat formally. At the end of this step, each identified throat is labelled uniquely while its size and location are stored.

Step 3: Pore bodies are identified as follows. On the binary image representing pore skeleton where the skeleton voxels are labelled with a value 1, each voxel corresponding to an identified throat is turned into value 0. Through connected component analysis, pore skeleton is classified into separated groups belonging to different pore bodies. Only the pore bodies that associate with *SPP*s portraying the connected, flow-accessible part of the pore skeleton are identified. Isolated pore space is not considered. Once identified pore bodies are labelled, the radius of a pore body is estimated to be the largest local sphericity measure for each group. This computation searches for all voxels in each group, and

topological equivalence between voxel skeleton and spatial graph is well exploited. In practice, owing to the fact that each skeleton group always contains a *Node* or a *Node Cluster*, spatial information of an identified pore body can be recorded or extracted using that of the embedded *Node* or *Node Cluster*.

To give a visual illustration of this algorithm, throat finding is implemented on a 2-D pore skeleton considering that a 3-D skeleton will be too complicated to view clearly. A section of the extracted pore skeleton is presented in both spatial graph and voxel skeleton formats (see Figure 3.23). In the image, particles are shown in black and pore space in white. Identified *SPP*s through skeleton trimming are colored in red. As can be noticed, some pore-internal paths have been determined such that a couple of *Node Cluster*s are formed and recorded. It is demonstrated that no modifications are required in the skeleton for "merging" *Node*s into *Node Cluster*s. At the completion of step 2, Figure 3.24 shows that the skeleton voxels corresponding to the identified pore throats are marked in red while other normal skeleton voxels are in blue. A closer examination is provided by zooming in a small area on the image. Labelled separated skeleton groups are rendered in Figure 3.25 from which radii of pore bodies are computed. Topological characteristics of distinct pore bodies are successfully retained in those classified skeleton groups.

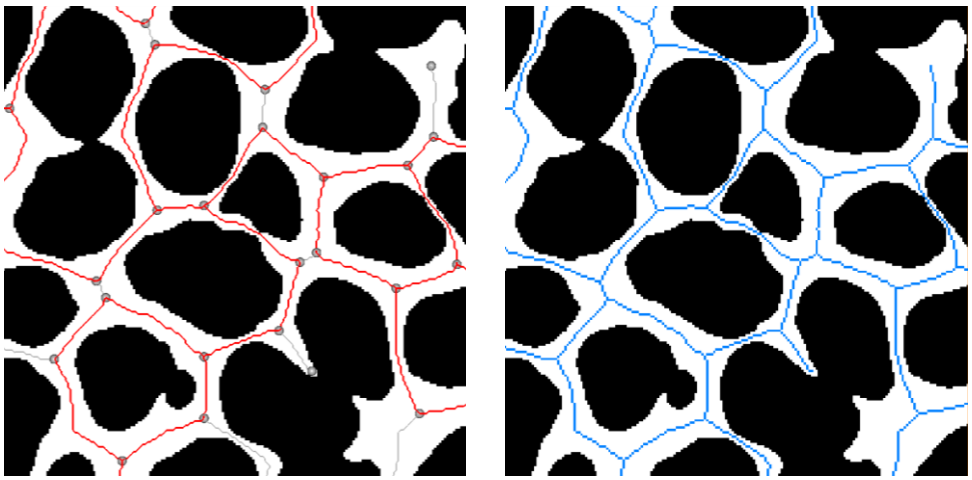

(a) (b)

Figure 3.23 A 2-D example of pore skeleton presented in two forms: (a) spatial graph with significant pore paths emphasized; (b) voxel skeleton

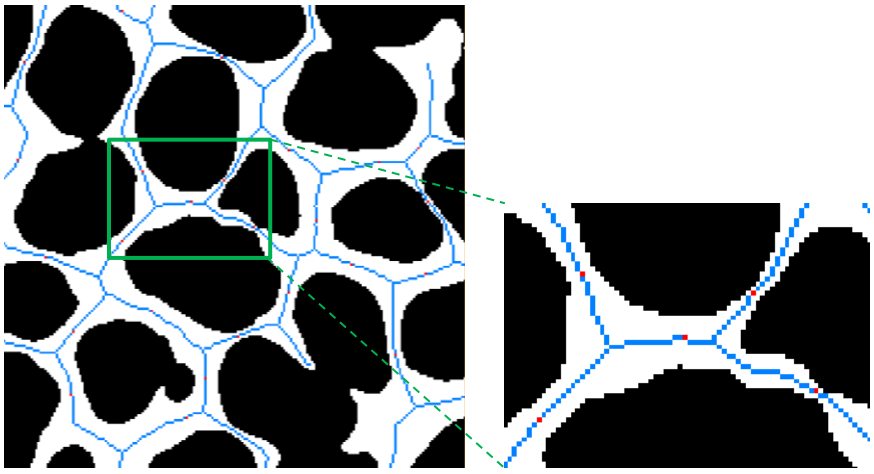

Figure 3.24 2-D illustration on marked locations of identified throats

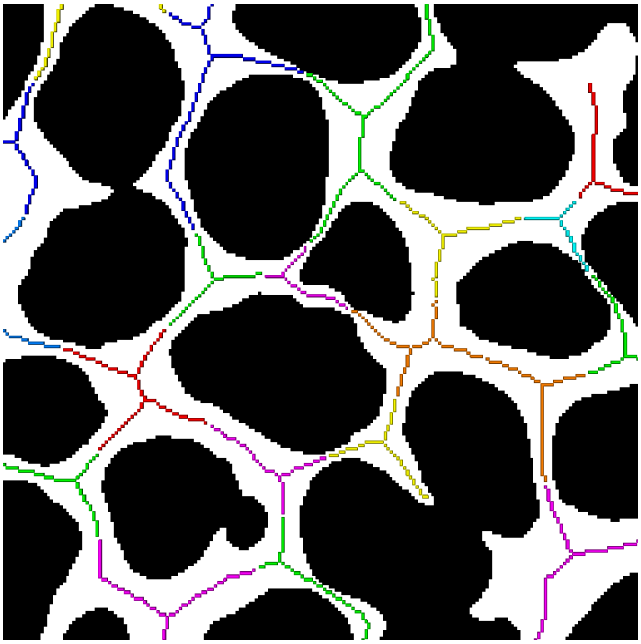

Figure 3.25 2-D illustration on labelled separated skeleton groups representing different pore bodies

3.5.4.2 Planar Surface Construction Algorithm

For further upgrading of the pore structure characterization, this algorithm aims to realize an actual, geometrical separation of pore space into individual pore body volumes. Rather than simplifying a pore throat as a sphere, it is prescribed as a planar surface having the local minimum cross-section area in the pore network but with zero volume. Recalling that only the "primary" local minimum will be considered, so each *SPP* will possibly contain at most one pore throat representing the global minimum cross-section area for that path. Approximating the pore throat surface as a planar one, though it may have curvature, is for computational feasibility.

The core methodology of constructing a planar cross-section for every voxel on a *SPP* is to compute an assembly of face-to-face connected pore voxels, which are termed as a "barrier". These pore voxels constituting the barrier are called "barrier voxels" through

which a planar surface passes. The face-to-face connectivity (i.e. 6-connectivity) property of barrier voxels assures an effective partition of pore structure, with a 26-connectivity in 3-D, by blocking the pore pathway. As discussed in Section 2.3, some existing algorithms such as those in the research package 3DMA have revealed that successful throat finding and pore partition in 3-D can be especially difficult in relatively high porosity (> 20%), unconsolidated porous media. All the Ottawa sand microstructures studied in this research have a porosity exceeding 33% and up to 42%. Consequently, complicated geometric scenarios in terms of not only failure in throat finding but also that throats may cross each other are diagnosed in developing and testing this new algorithm. Efforts are made on improving the algorithm to address those issues. This algorithm is composed of two major parts: (1) independent candidate throat construction; and (2) alternate throat identification and construction. Computational procedure is explained in detail as follows, and the attempts for improvements are emphasized.

Part (1): independent candidate throat construction. Suppose there are *M SPP*s determined from the pore skeleton in the microstructure for analysis. Let S_0 be one random *SPP* which consists of *N Point*s (i.e. voxels). Starting from an arbitrary voxel *v* on S_0, a candidate throat is to be computed. "Independent" indicates that candidate throat computation at any one voxel is not influenced by those computed at others already.

Firstly, the local tangent direction at *v* to the path S_0 is determined by a nonlinear least-squares fitting through *v* and its adjacent six voxels on S_0, and the directional vector is $\vec{t}$. *Second*, a normal vector $\vec{n}$ is introduced which is normal to the cross-section plane *P* representing the candidate throat surface. For now, let $\vec{n} = \vec{t}$. *Third*, using plane *P* as a

searching plane in 3-D, the candidate throat barrier is constructed through v by a dilation searching process to identify pore voxels that intersect with P. The dilation searching is initiated from v, and the searching range is defined by a 26-connectivity mask (a $3 \times 3 \times 3$ matrix) created around v. For each pore voxel v_p in the 3-D binary image within that searching range, inner products are calculated between the vectors from the center of v to the eight corners of v_p and $\vec{n}$. Then an intersecting test is performed to determine whether P passes through v_p. If there is at least one positive inner product value and in the meantime at least one negative value, v_p intersects with P and v_p is a barrier voxel. If at least one inner product equals to zero while the others are all positive, v_p is a barrier voxel too. The intersecting test fulfils the 6-connectivity requirement of barrier voxels. As a side note, the latter intersecting condition is interchangeable to the one stating that at least one inner product is zero while the others are all negative. However, allowing both will produce redundant barrier voxels. Positive and negative inner product can be perceived as the corner of v_p locating above and below plane P, respectively. To speed up the searching process, each pore voxel that has been searched will be classified as either a barrier voxel B or a non-barrier voxel NB in the binary image. The next iteration of dilation searching will begin with the Bs and only test those unclassified pore voxels. Dilation searching is terminated when a barrier voxel can no longer be found. Because of the independence of throat finding in this part, the classification on pore voxels won't be in effect once the computation is finished at this particular voxel. *Fourth*, area of the candidate throat surface is quantified by summing the intersecting areas of plane P with every barrier voxel in the constructed candidate throat barrier. A 3-D planar polygon is formed when plane P intersects with a barrier voxel, and a standard formula (Goldman, 1991) is referred to in calculating its area.

It involves resolving intersection points of P with each edge of a barrier voxel to identify vertices of the polygon, and then sorting the vertices into a counter clockwise orientation. At the completion of this step, a candidate throat at a single voxel v on S_0 is determined, along with its barrier and surface area. Figure 3.26 presents a 2-D illustration.

Practically, a condition analogous to the one enforced in the local sphericity based candidate throat finding is implemented to guarantee that a qualified candidate throat won't lie within a pore body. The radius of the computed candidate throat can be taken as the one of a circle with the same area, i.e. $r_{\text{throat}} = \sqrt{A/\pi}$, where A is the candidate throat surface area. The critical radius of a throat at voxel v still applies, that is $r_{cr} = \min(l_1, l_2)$, where l_1 and l_2 are the distances from v to the two ends along path S_0, respectively. Then, the requirement of a qualified candidate throat is stated as $r_{\text{throat}} \leq r_{cr}$. Having this condition taken into consideration, it is more pertinent to exercise it during dilation searching than after the candidate throat surface has been obtained from dilation searching. The initial value of A is the intersecting area of plane P with voxel v, and the added value of A is the sum of intersecting areas of P with newly determined barrier voxels after each iteration of dilation searching. As the value of A keeps increasing, r_{throat} is calculated and compared with r_{cr} to make sure the candidate throat under computation remains qualified. If not, terminate the iteration and set A = NaN (not a number) to indicate that no candidate throat can be constructed at v. An instant decision-making is realized from this, and a lot of computational time can be saved.

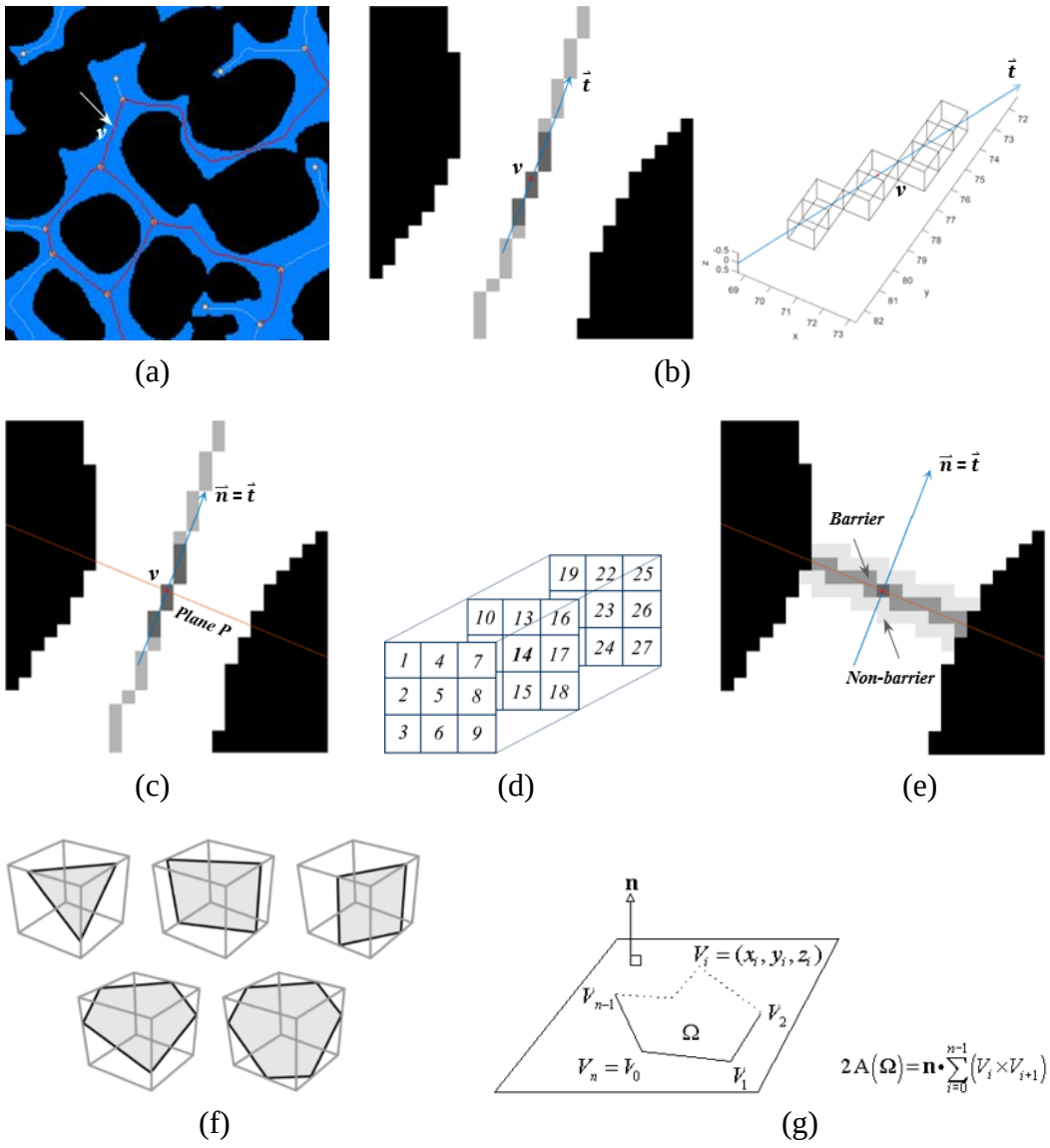

Figure 3.26 A 2-D illustration of independent candidate throat construction at one arbitrary voxel using the planar surface construction algorithm: (a) a voxel *v* on a *SPP* S_0; (b) compute local tangent direction; (c) identify searching plane (let its normal direction be the local tangent direction here); (d) 26-connectivity mask for dilation searching; (e) construct candidate throat barrier by an intersecting test; (f) intersecting polygon scenarios; (g) formula to compute 3-D planar polygon area

Repeating the above procedure for the *N* voxels on path S_0, a candidate throat list *LIST_SPP* can be created containing information of every skeleton voxel v_i (i = 1, 2, …, *N*), candidate throat area (A_{v1}, A_{v2}, …, A_{vN}) and candidate throat barrier through it. Then the list is sorted by the value of candidate throat areas, and the smallest one is the temporary

throat for the *SPP* designated as A_{SPP}. A *SPP* can have no temporary throat, i.e. A_{SPP} = NaN, when A_{v1}, A_{v2}, …, and A_{vN} are all non-existent. Next, a candidate throat list *LIST* for the microstructure under analysis can be generated storing information of the *M SPP*s, *LIST_SPP* and the determined temporary throat for every *SPP*. Out of the *M SPP*s, percentage of *SPP*s having temporary throat found is defined as "throat-finding rate".

Before introducing the second part of this algorithm, structure BT0 is analyzed to demonstrate the result of independent candidate throat finding. From the extracted skeleton in the whole microstructure, a spatial graph is built that consists of 30563 *Node*s and 42351 *Segment*s involving 763532 *Point*s. Trimming the skeleton, 22367 *SPP*s are identified and 518519 *Point*s are involved. It is not computationally practical to construct candidate throats on this large amount of data, pore network exploration using the present algorithm has to be accomplished on the REV. The REV for BT0 is a cubic sub-volume with an edge length of 300 voxels, and its determination will be explained in Section 5.5. A sub-volume BT0_Center is sampled from the center of BT0 (see Figure 3.27), with the region of interest (ROI) shown together with the spatial graph. There is an issue regarding pore skeleton extraction, spatial graph and throat computation caused by the edge effect of any sub-volume under study. Herein, out of the total 22367 *SPP*s for BT0, a subset of *SPP*s is selected as the relevant *SPP*s to BT0_Center and investigated for throat finding. Besides, the dilation searching process is performed on the entire pore structure rather than only on the pore structure of BT0_Center. A detailed discussion about the influence of the edge effect on pore structure characterization is in Section 3.5.6. The relevant *SPP*s can be briefed as "*R-SPP*s", and there are 2411 *R-SPP*s for BT0_Center containing 58193 *Point*s. Running part (1) with the premise $\vec{n} = \vec{t}$, the throat-finding rate of BT0_Center is 42.1%

with 1014 temporary throats found (i.e. $A_{SPP} \neq$ NaN). Figure 3.28 shows the temporary throat barriers. Deleting the barrier voxels from the pore space, different pore bodies can be separated out. Considering the pore space is highly continuous and only a small sub-volume is involved in the analysis, a very large portion of the pore space surrounding the sub-volume is not separated yet, and hence becomes the largest connected pore component. It is filtered in a close examination of the separated pore bodies pertaining to BT0_Center. In Figure 3.29, the number of distinct pore bodies is quite low, and the remaining volumetric part of pore structure is still one part of that largest connected pore component. Those labelled pore bodies, very small in volume, are disconnected pore space and will be ignored in the quantitative characterization.

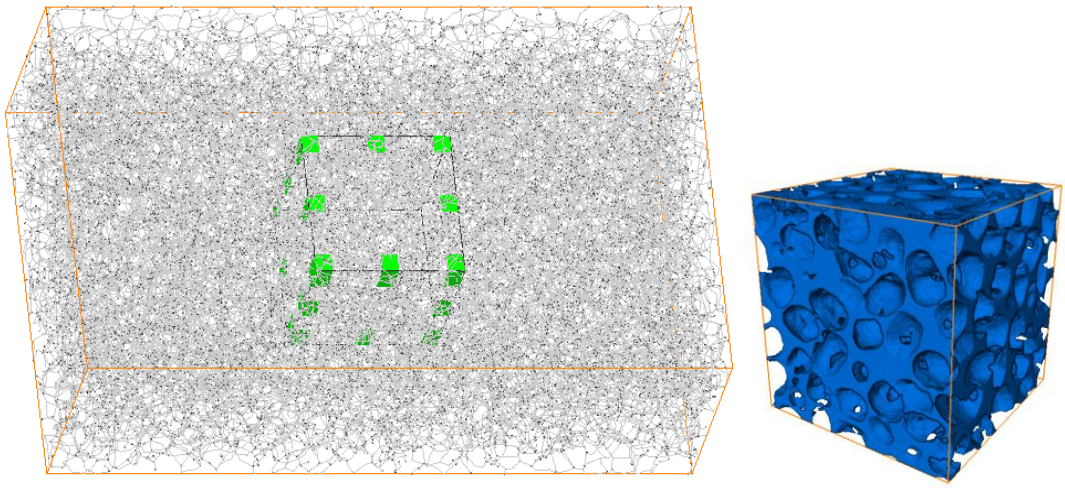

Figure 3.27 Sampling a sub-volume BT0_Center from structure BT0 for planar surface construction algorithm based throat finding

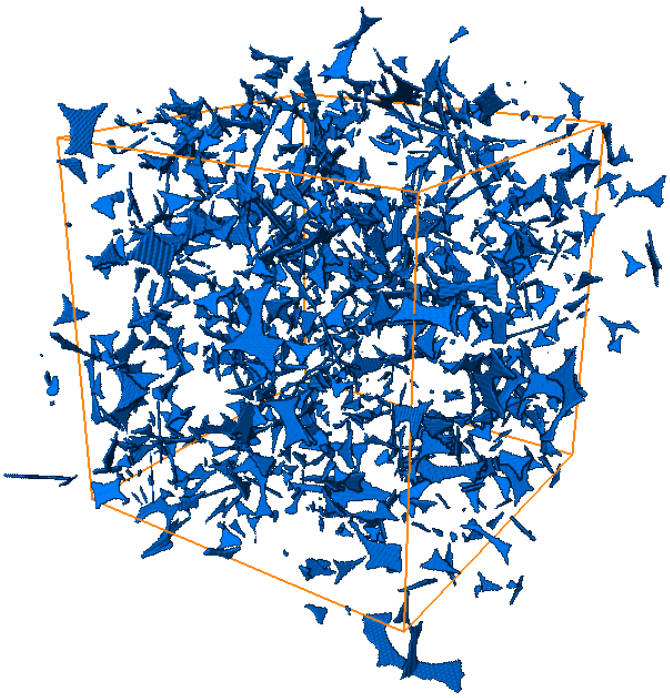

Figure 3.28 Temporary throat barriers independently computed ($\vec{n} = \vec{t}$) on *R-SPP*s in BT0_Center

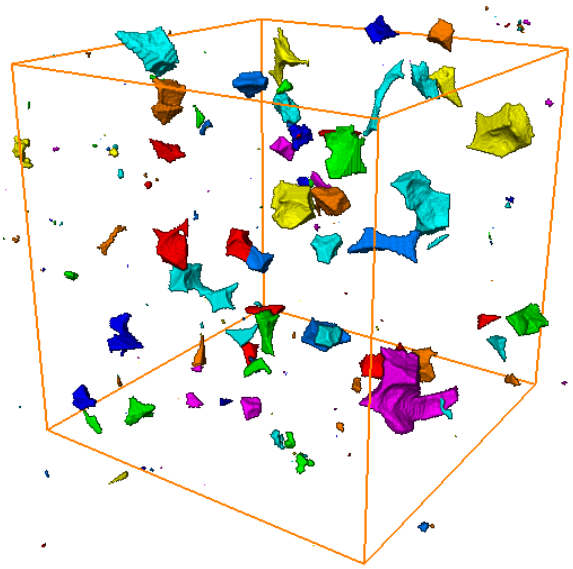

Figure 3.29 Labelled pore bodies pertaining to BT0_Center after temporary throats computation ($\vec{n} = \vec{t}$)

A less than 45.0% throat-finding rate in BT0_Center (porosity is 33.6%) confirms the difficulty of throat construction in the unconsolidated sand microstructures. When the

porosity is high such that particles do not have enough contacts, finding the connected boundary particle voxels circling a pore path to define a throat perimeter can often be problematic. Therefore, a candidate throat barrier can possibly keep expanding over a large region in the dilation searching, and the condition $r_{\text{throat}} \leq r_{cr}$ cannot be met.

One major improvement is attempted for this part of the algorithm concerning orientation of the cross-section plane *P*. Instead of imposing $\vec{n} = \vec{t}$ to presume that flow will strictly follow the local tangent direction of pore skeleton and a throat surface must be perpendicular to that direction, a small discrepancy is allowed for $\vec{n}$ with respect to $\vec{t}$. $\vec{n}$ is defined in the following way: establish a local spherical coordinate system with the skeleton voxel *v* as the origin and $\vec{t}$ as the zenith direction, $\vec{n}$ has a polar angle θ measured from the zenith axis and an azimuth angle φ measured on the plane orthogonal to the zenith. Now plane *P* is determined by the normal vector $\vec{n}(\theta, \varphi)$. The expression of $\vec{n}(\theta, \varphi)$ in the Cartesian coordinate system containing the digital microstructure can be derived through coordinate system conversion as well as elemental rotation in 3-D. The discrete combinations of (θ, φ) produce different cases of *P* around which candidate throats will be constructed at *v*. In this study, θ ranges from 5° to 30° in an increment of 5° such that generally the directional discrepancy between $\vec{n}$ and $\vec{t}$ is arguably small. φ ranges from 0° to 315° in an increment of 45°. So, including the case $\theta = \varphi = 0°$ for $\vec{n} = \vec{t}$, 49 cases of plane *P* totally are accounted for. Candidate throats at *v* are constructed for these 49 cases, and candidate throat areas are stored in a list $\boldsymbol{A}(\boldsymbol{\theta}, \boldsymbol{\varphi})$. The smallest candidate throat area ($A_v = \min(\boldsymbol{A}(\boldsymbol{\theta}, \boldsymbol{\varphi}))$) and its corresponding barrier will appear in the aforestated candidate throat list *LIST_SPP* for the path S_0. Workflow for the candidate throat construction at each voxel is presented in Figure 3.30. With this enhancement, throat-finding rate for part (1)

increases to 57.4% with 1383 temporary throats found out of the 2411 *R-SPP*s in BT0_Center. Figure 3.31 and Figure 3.32 visualize the temporary throat barriers and the labelled distinct pore bodies pertaining to BT0_Center, respectively. More pore bodies are separated out from the pore space compared to that shown in Figure 3.29. It needs to mention that Figure 3.31 does not simply contain 369 more throat barriers than Figure 3.28, but instead the preceding 1014 throat barriers will change when A_v is not optimized at the cross-section plane orientation defined by $\theta = \varphi = 0°$.

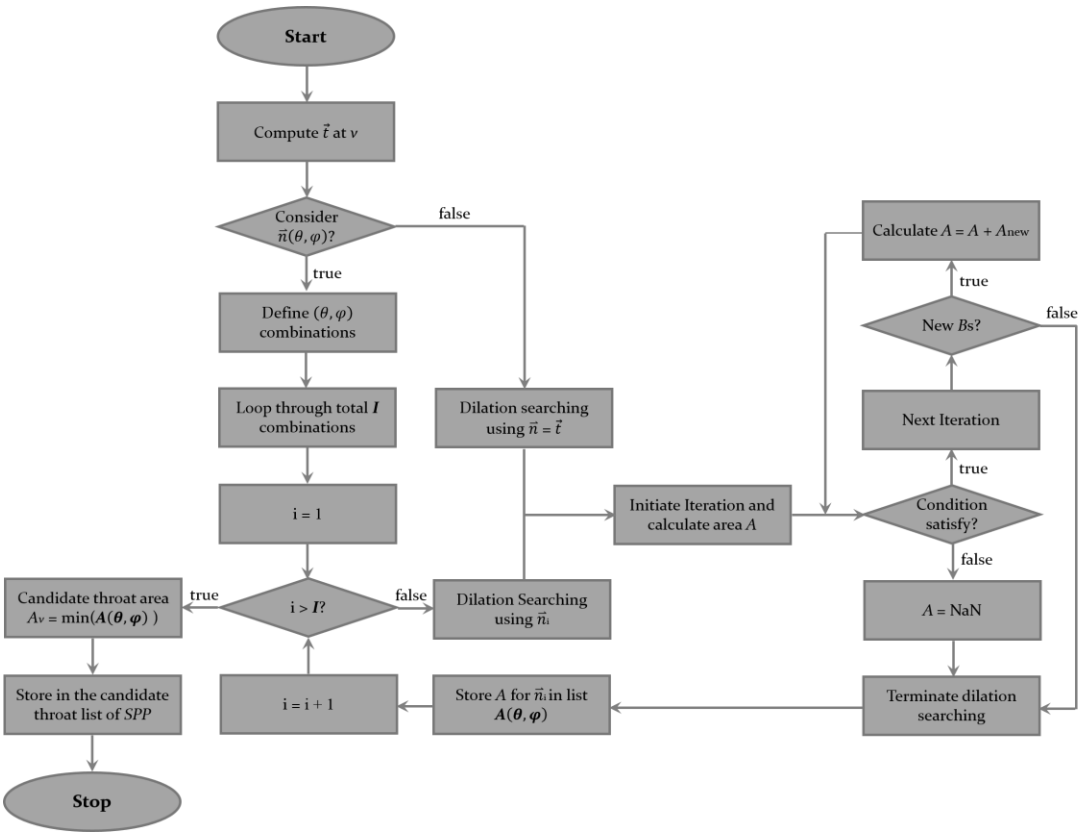

Figure 3.30 Flowchart for candidate throat construction at an arbitrary voxel *v* on the pore skeleton

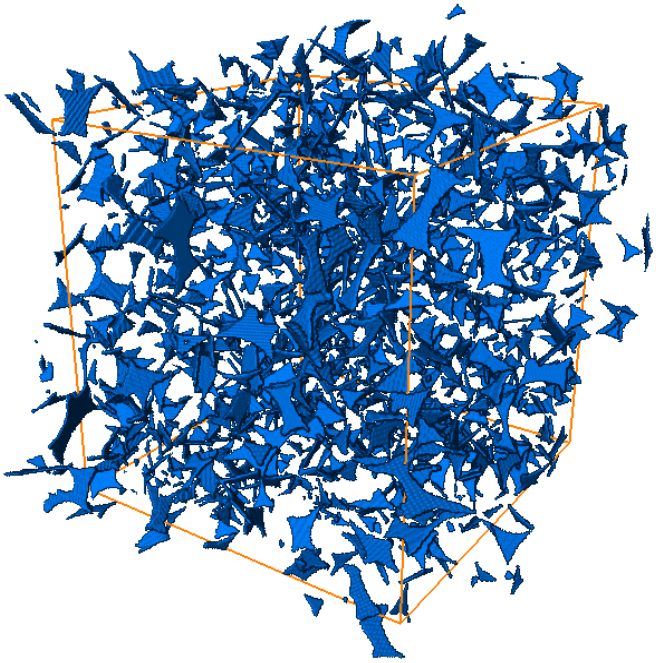

Figure 3.31 Temporary throat barriers independently computed ($\vec{n}(\theta, \varphi)$) on *R-SPP*s in BT0_Center

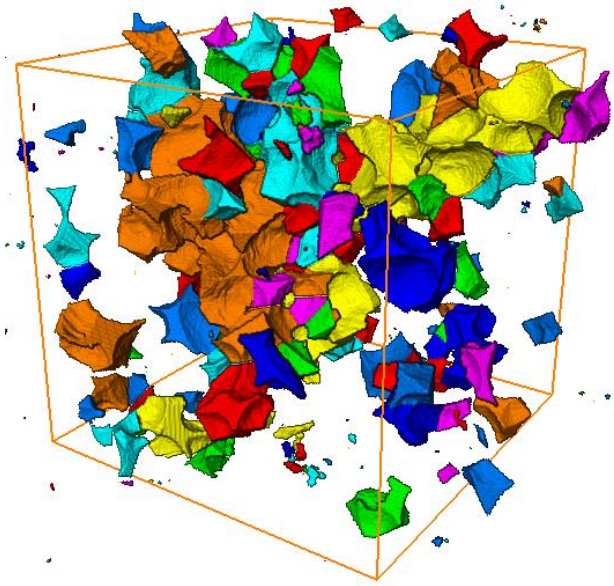

Figure 3.32 Labelled pore bodies pertaining to BT0_Center after temporary throats computation ($\vec{n}(\theta, \varphi)$)

Taking into account 49 cases for candidate throat construction at every single voxel demands significant computation power. Parallel computing is thus realized in MATLAB.

Despite this, running part (1) on BT0_Center using several computers with an either 4-core or 8-core CPU takes about 7 days. It would be prohibitive to consider more additional (θ, φ) combinations, for example adding 24 cases with maximum θ value reaches 45°, or adopting a finer discretization for both θ and φ. This is left for the future work.

Part (2): alternate throat identification and construction. Observing the results from part (1), it is found that the constructed throats may cross each other. Two examples of crossing-throat barriers are given in Figure 3.33(a) and (b), in which surfaces of the two temporary throats pass through each other or common barrier voxels are shared by the two barriers. The existence of crossing-throat will lead to ambiguity in specifying pore bodies and pore body-throat connectivity. This part deals with this issue and identifies throats from the temporary throats constructed on the *SPP*s.

Once the candidate throat list *LIST* is generated for the microstructure under study, it is sorted by the value of temporary throat areas ($A_{SPP1}, A_{SPP2}, \ldots, A_{SPPM}$) from the smallest to the largest. *LIST* is classified into two groups: *LIST_G1* and *LIST_G2*, and *LIST_G2* includes A_{SPP} = NaN exclusively. *SPP*s are classified into two groups accordingly: *SPP_G1* and *SPP_G2*. *SPP_G1* stores the information of those *SPP*s that have temporary throat found, and *LIST_G1* is the corresponding candidate throat list. *SPP_G2* stores the rest of information. Three inputs for throat identification are: *LIST_G1*, *SPP_G1*, *THROAT*, and binary image of the entire 3-D microstructure (termed as "*Alpha*") marked with the identified throat barriers (termed as "*Alpha_THROAT*"). The list *THROAT* is for storing the information of identified throats: identity of the *SPP* it belongs to, throat area, and throat barrier voxels. As there are no identified throats yet, *THROAT* is empty for now. *Alpha_THROAT* is initiated to be exactly the binary microstructure image *Alpha*. The

general rule is identifying the throat having a smaller area first, and that non-crossing one is preferred to the crossing-throat. The computational procedure for the throat identification component of part (2) is explained as below.

Because the first temporary throat in *LIST_G1* has the smallest area, it is directly identified as a throat and stored in *THROAT*. *Alpha_THROAT* is updated by marking the corresponding barrier voxels. Then proceed to the second *SPP* in *LIST_G1*. Rather than solely examining the temporary throat on this *SPP*, the candidate throats having an area that is slightly different from the temporary throat area are also taken into consideration. *LIST_SPP* is utilized to define a threshold of the candidate throat area: $A_{thresh} = A_{temp} + (A_{max} - A_{temp}) \times 5\%$, where A_{temp} is the temporary throat area, i.e. the smallest candidate throat area, and A_{max} is the largest candidate throat area computed from the path. If the area of a candidate throat is not larger than A_{thresh}, its barrier is selected for examination. Among all the candidate throats that meet this selection criterion, the one with the smallest area and meanwhile its barrier does not intersect the barrier of the first identified throat is identified as the throat on this path. Further, it is categorized as a non-crossing throat. If every selected candidate barrier on the path intersects with that identified one, on the other hand, this path contains a crossing-throat. To deal with this, the throat constructing procedure is performed again at the skeleton voxels associated with those selected barriers. *Alpha_THROAT* is applied in the dilation searching. Different from part (1), the throat surface will be terminated by not only particle voxels but also the identified barrier voxels. From the reconstructed candidate throats, the one with the smallest area is identified as a throat. Looping through each subsequent element in *LIST_G1*, a similar selective crossing-throat test is implemented and the barriers corresponding to the throats that have been identified

earlier will be checked against. Likewise, candidate throat reconstruction is implemented right after a crossing-throat is determined. *Alpha_THROAT* is updated whenever a throat is identified. When the loop ends, output *THROAT* and *Alpha_THROAT*. Figure 3.33(c) and (d) shows two examples of the reconstructed barriers. The comparison between the barrier before and after reconstruction demonstrates that only the throat having a smaller area is retained if two throats cross each other.

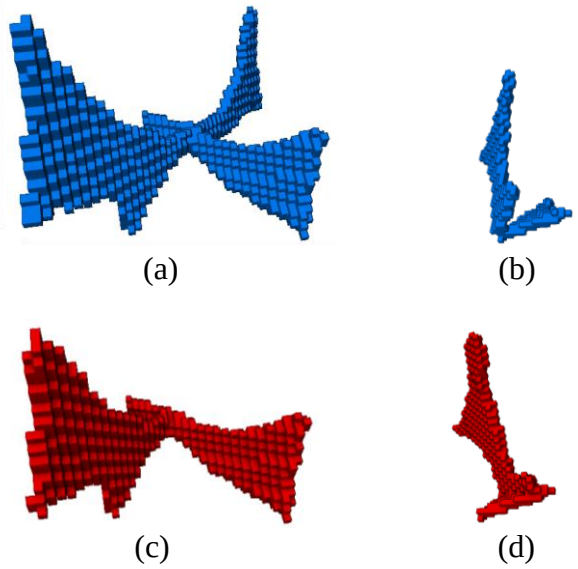

Figure 3.33 Examples of barriers of crossing-throat and barriers after reconstruction: (a) and (b): crossing-throat barriers; (c) barriers reconstructed from (a); (d) barriers reconstructed from (b)

After the completion of throat identification, performing an independent candidate throat computation on the *SPP*s in *SPP_G2*. The same computational workflow as in part (1) is followed, except that *Alpha_THROAT* is being searched instead of *Alpha*. It means that the throat surface construction at this stage will be affected by the identified throats. An updated candidate throat list *LIST* is generated.

Sorting and classifying *LIST* in the same manner as the beginning of part (2) to renew *LIST_G1* and *LIST_G2*, as well as *SPP_G1* and *SPP_G2*. Next, the proposed throat identification procedure is re-run, list *THROAT* is expanded as newly identified throats are stored, and *Alpha_THROAT* is kept updating. Then, candidate throats are computed on the *SPP*s in *SPP_G2*. Alternating between throat identification and candidate throat computation is iterated until no more temporary throats can be found (i.e. *LIST_G1* and *SPP_G1* are empty). *THROAT* and *Alpha_THROAT* are finalized.

Figure 3.34 presents the workflow combining part (1) and part (2) of this algorithm, focusing on the latter part. The final throat-finding rate can be defined as the percentage of *SPP*s having an identified throat out of the *M SPP*s being considered.

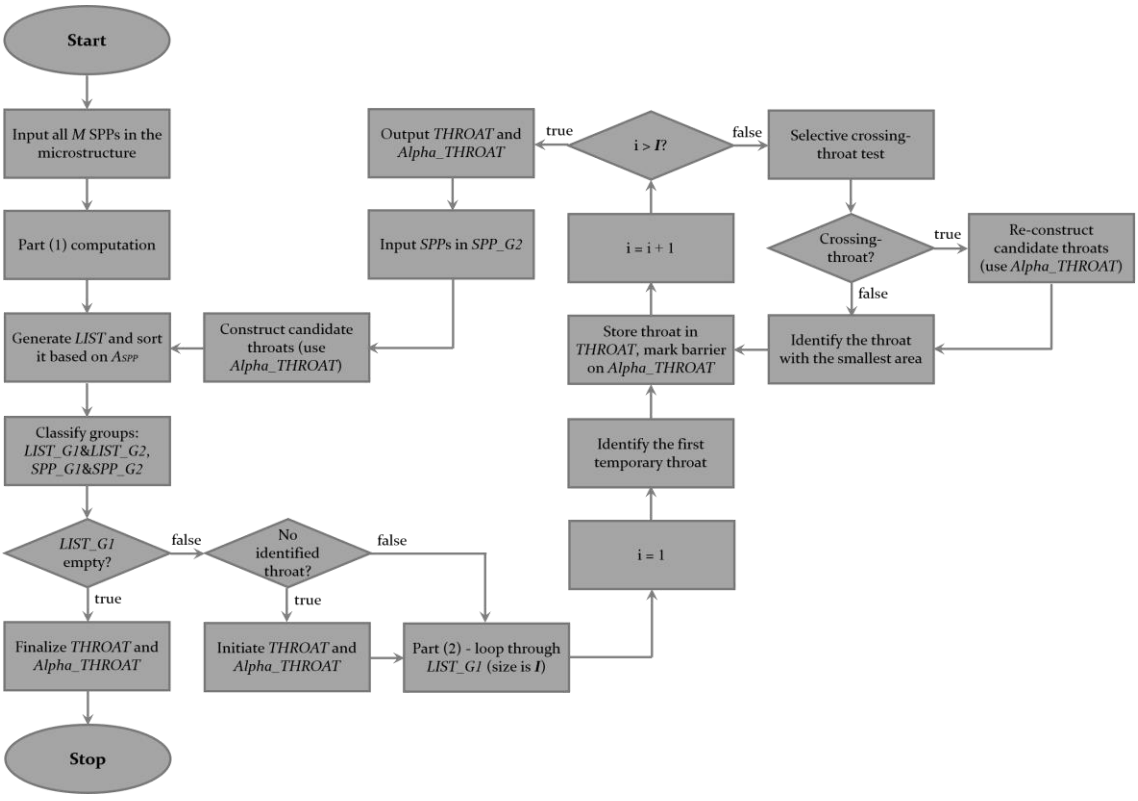

Figure 3.34 Flowchart for planar surface construction based throat finding with a focus on part (2) of the algorithm

Throat finding for BT0_Center is continued. Running part (2) on the constructed temporary throats, alternate throat identification and construction are completed after 6 iterations. After the initial throat identification in which reconstruction is implemented for crossing-throats, 1383 identified throats are shown in Figure 3.35(a) and the quantity remains the same as the temporary throats shown in Figure 3.31. 101 out of these 1383 throats, at a percentage of over 7%, are crossing-throats. When the iteration is finished, 165 additional throats are constructed and identified (Figure 3.35(b)). The final throat-finding rate for BT0_Center is 64.2%, and identified throats are visualized in Figure 3.35(c). The total percentage of crossing-throats closes to 18% which is impressive. A larger amount of pore bodies are separated out from the continuum pore space as presented in Figure 3.36.

We can name the procedures of part (1) with $\vec{n} = \vec{t}$ and part (1) with $\vec{n}(\theta, \varphi)$ as *BASIC* and *ADV*, respectively, and the full procedure of this algorithm as *FINAL*. The results of throat finding on the 2411 *R-SPP*s in BT0_Center are compared in Table 3.1 and Figure 3.37. The enhancements are evident from *BASIC* to *ADV*, and then from *ADV* to *FINAL*. The major efforts put into tackling with the geometric complications encountered in throat finding for unconsolidated porous media are demonstrated. Besides, a separated pore body bounded by its neighboring throats is well presented in Figure 3.37.

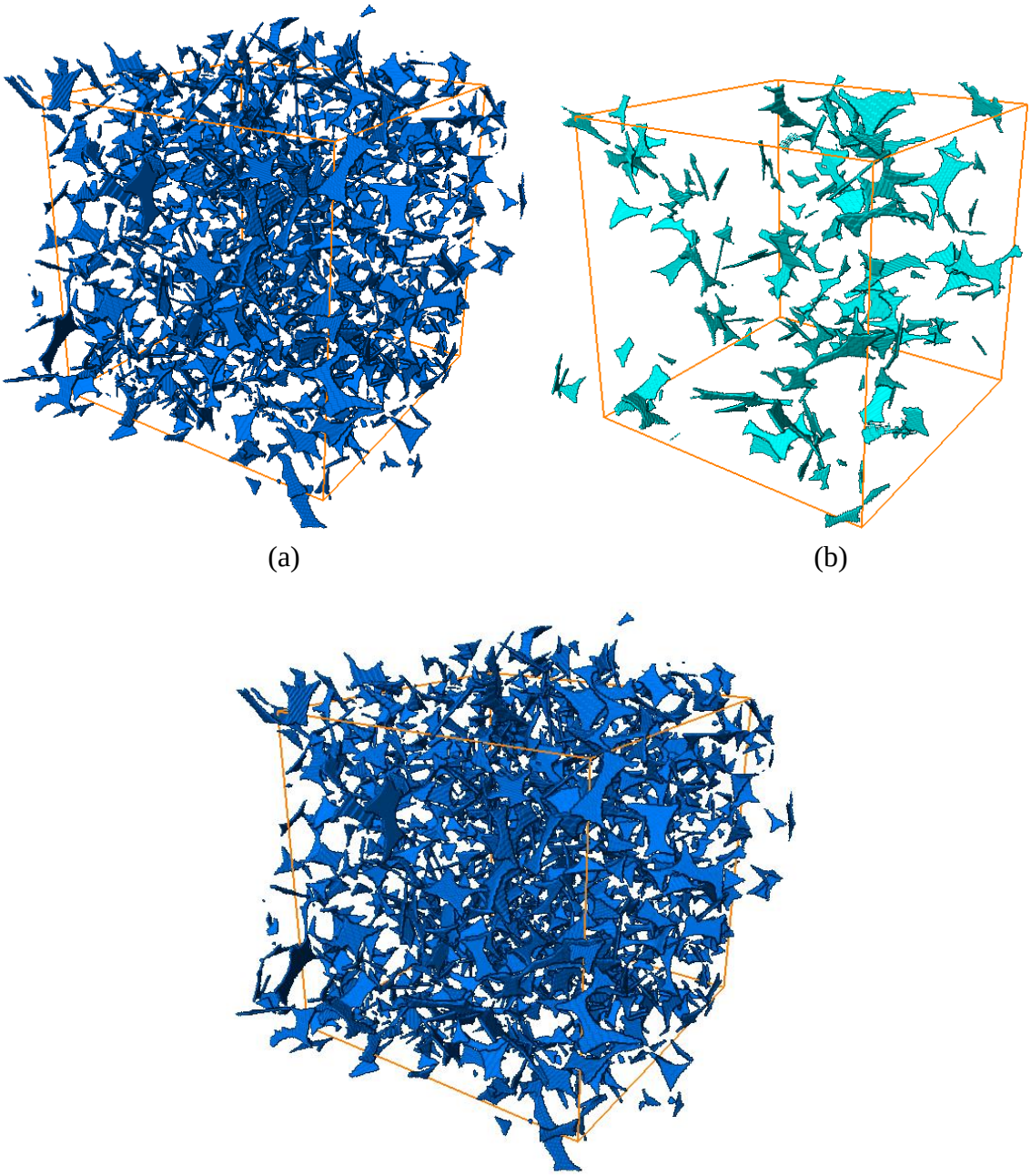

Figure 3.35 Identified throats obtained from running part (2) of the algorithm: (a) after initial throat identification; (b) total added identified throats to (a) when iteration is finished; (c) all identified throats in BT0_Center

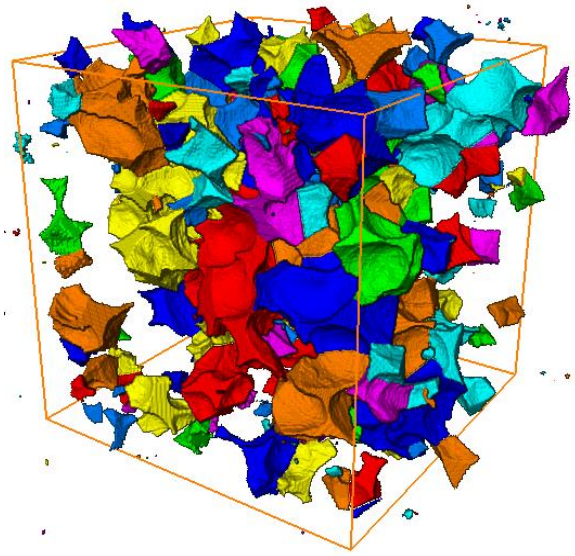

Figure 3.36 Labelled pore bodies pertaining to BT0_Center after running part (2) of the algorithm

Table 3.1 Results of throat finding for BT0_Center

	No. *R-SPP*s	No. Throats	Throat-finding Rate	No. Crossing-throats
BASIC	2411	1014	42.1%	n/a
ADV	2411	1383	57.4%	n/a
FINAL	2411	1548	64.2%	266

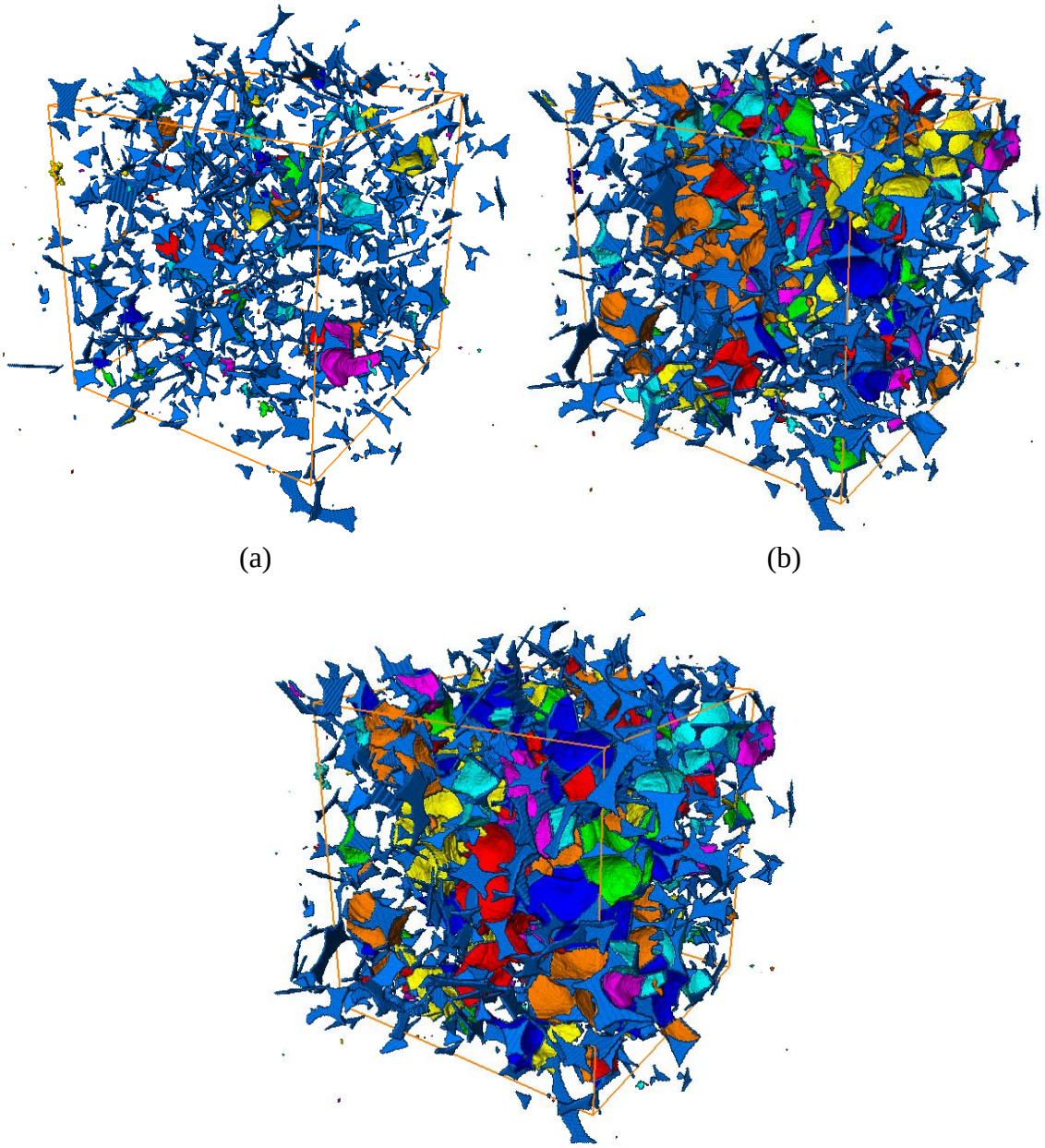

Figure 3.37 Pore throats and labelled pore bodies pertaining to BT0_Center: (a) *BASIC*; (b) *ADV*; (c) *FINAL*

Another potential direction for improvement is to enhance the identification process of *R-SPP*s on which throats are computed. As shown in Figure 3.36 and Figure 3.37(c), some volumetric parts of the pore structure near the REV domain borders that haven't been labelled remain connecting to the largest connected pore component outside the domain.

The underlying reason is that not enough throats are found on the *R-SPP*s near the borders; otherwise, more pore bodies can be identified as intersecting the domain, and importantly, some of them will be counted for characterization according to the unbiased counting rule. Therefore, the current throat-finding rate limits the unbiased quantification of pore bodies. Details about the design logic in identifying the *R-SPP*s is explained in Section 3.5.6. The idea here is to increase the number of *SPP*s located outside but still close to the domain borders being involved for throat finding. To be specific, after obtaining the candidate throats from the above *ADV* procedure, any *SPP* without a temporary throat are identified as an interim pore-internal path since no candidate throats constructed from that *SPP* pass the qualified throat condition. An interim skeleton trimming and "merging" follows. From the modified *Nodes* or *Node Cluster*s, the *R-SPP*s for the sub-volume are re-identified. A few added *R-SPP*s that haven't been included in the original *R-SPP*s are captured, and subjected to part (1) of the algorithm. This process is named as *1st Expand*.

Implementing *1st Expand* process for BT0_Center, 520 *R-SPP*s are added to the existing 2411 *R-SPP*s. Figure 3.38 presents 280 newly constructed temporary throats. The result from part (1) thus renders a throat-finding rate of 56.7%. The final throat-finding rate is 63.9% after running part (2), and information about the results of throat finding is listed in Table 3.2. Figure 3.39 visualizes the separated pore bodies pertaining to BT0_Center. Comparing the result from *FINAL_1st Expand* to *FINAL* (Figure 3.36), more pore bodies intersecting the sub-domain borders are able to be captured.

The *R-SPP*s can be further expanded outward from the sub-domain, and we can have *2nd Expand*, *3rd Expand, and 4th Expand* and so on. Although change in the throat-finding rate is minor, it is possible to capture all available pore bodies intersecting the sub-

domain borders such that the unbiased counting technique can achieve its desired objective. This can be explored in the future work.

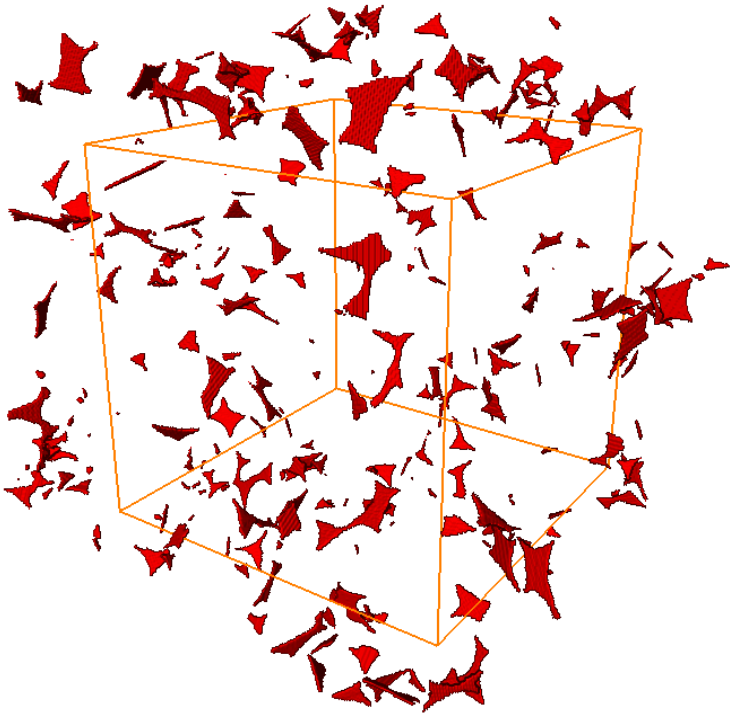

Figure 3.38 Added temporary throat barriers for the added *R-SPP*s on the basis of that from *ADV* in BT0_Center

Table 3.2 Comparison of throat finding results with and without *1st Expand* process

	No. *R-SPP*s	No. Throats	Throat-finding Rate	No. Crossing-throats
ADV	2411	1383	57.4%	n/a
ADV_1st Expand	2931	1663	56.7%	n/a
FINAL	2411	1548	64.2%	266
FINAL_1st Expand	2931	1872	63.9%	318

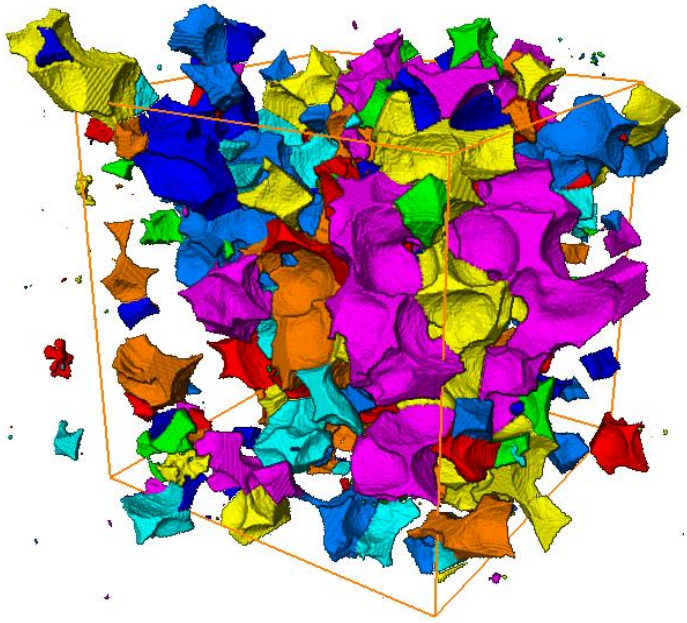

Figure 3.39 Labelled pore bodies pertaining to BT0_Center for *FINAL_1st Expand*

3.5.4.3 Comparison between Two Methods

Searching on the *SPP*s in pore skeleton, local sphericity (LS) algorithm and planar surface construction (PSC) algorithm have been introduced to identify pore throats. Some primary differences between the two algorithms are summarized in Table 3.3. The LS algorithm idealizes pore throats and pore bodies as sphere inscribed onto the pore surface, and obtains size measure directly. This simplification brings about great superiority in terms of computational expense. Geometrically, pore space partition cannot be accomplished using this algorithm. In comparison, the PSC algorithm strives for characterizing the real geometry of pore structure through pore space partition. A much more complicated procedure is undertaken, and thus a markedly higher computational expense is demanded in constructing candidate throat surfaces and identifying throats. It obtains the area measure for pore throats and volume measure for pore bodies. In unconsolidated, usually high porosity porous media systems, throat-finding rate from the

PSC algorithm is less satisfying than that from the LS algorithm. The first rate is computed after running part (2) of the PSC algorithm, and the latter one is after Step 2 of the LS algorithm. Take BT0_Center for example again, the PSC algorithm provides a final throat-finding rate of 64.2% while the LS algorithm results in a rate of 98.1% for the same set of *R-SPP*s. On the other hand, the LS algorithm tends to yield a smaller size measure of pore throats and pore bodies than the PSC algorithm considering the fact that cross-sections along the skeleton are irregular. Commonly, both algorithms can acquire the 3-D spatial distribution (i.e. coordinates) of pore throats and pore bodies at the end.

Table 3.3 Comparison of two throat finding algorithms

	Local Sphericity (LS)	Planar Surface Construction (PSC)
Assumption on Throats	sphere	planar surface
Assumption on Pore Bodies	sphere	bounded by planar surface
Pore Geometrical Partition	no	yes
Direct Throat Statistics	size (diameter)	area
Direct Pore Body Statistics	size (diameter)	volume
Computational Complexity	low	very high
Computational Expense	low	very high
Throat-finding rate	high	low

With respect to algorithm implementation, different strategies are managed in the characterization of the sand microstructures under study. Taking advantage of the high

computational efficiency, the LS algorithm is run for throat finding on the *SPP*s identified from the whole microstructure volume. Pore network statistics that will be described in the next section can be extracted after pore throats and pore bodies are identified spatially. For the PSC algorithm, however, throat finding is limited to the REV domain and its relevant *SPP*s considering computational feasibility. Therefore, the LS algorithm enables a higher flexibility in quantitatively characterizing the pore structure. Unbiased 3-D counting brick can be placed as needed to generate result for a sub-volume of interest.

3.5.5 Pore Network Statistics

3.5.5.1 Local Sphericity Algorithm

Accomplishing specification and identification of pore throats from this algorithm, a comprehensive set of statistics for describing the pore network characteristics can be extracted. Primary statistics include pore throat size distribution, pore body size distribution, pore body-throat connectivity, and pore channel length distribution. Additional statistics include size correlation between neighboring pore bodies, size correlation between neighboring pore throats and pore bodies, as well as pore throat/pore body aspect ratio.

The size of a pore throat or a pore body is its diameter measure that simply doubles the estimated radius in throat finding. Pore body-throat connectivity can be characterized by the distribution of coordination number of pore bodies. Coordination number of every pore body can be obtained by counting the number of pore throats that directly connect that pore body to its neighboring pore bodies. In the LS algorithm, every pore body can be cross-indexed with its connecting throats using the *SPP* information. Based on this data,

cross-index of every pore body with its neighboring pore bodies can be created, so does every pore throat with its connecting pore bodies.

Geometrically defining where a pore body ends and a pore channel begins is ambiguous. A pore channel is defined here as a *SPP* connecting two different pore bodies. In other words, a pore channel contains an identified pore throat. After pore skeleton trimming in Section 3.5.3, the *SPP*s represent the pore pathways. Considering the list of *SPP*s is finalized through the throat finding (Step 3), pore channels are a subset of the pore pathways. So, pore channel lengths in the pore network are characterized by the distribution of lengths of those *SPP*s.

Based on the quantitative information up to now, including spatial coordinates of pore throats and pore bodies, size distribution of pore throats and pore bodies, pore body-throat connectivity, as well as distribution of pore channel lengths, a 3-D pore network model (PNM) can be built mathematically. The PNM is composed of spherical pore bodies connected by cylindrical tubes of each having a constant diameter. Spherical pore bodies have already been captured from the algorithm. Considering the cylindrical tubes, some prior research discussed the concept of equivalent throat length (Youssef et al., 2007). An equivalent throat length was derived through replacing a pore channel by a series of elementary cylinders of variable radii, and assuming the fluid flow complying with the Hagen-Poiseuille law. For each elementary cylinder, however, the diameter is noticeably larger than its length. Under this circumstance, use of the Hagen-Poiseuille law would be in question. Other research introduced the pore-throat segmentation coefficient to decide the lengths of the tubes (Dong and Blunt, 2009). In the absence of solid calibration on the pore-throat segmentation coefficient, the cylinder tubes are characterized by pore throat

size as the cross-section diameter and the pore channel length as the longitudinal dimension in the present study. Creating the PNM like this emphasizes the governing role of pore throats play on the pore-scale physical processes. Now that the 3-D PNM accommodates all the extracted information of the pore structure, it can be utilized for pore network simulations to predict transport properties. In the simulation of hydraulic conductance, for instance, a spatial lattice can be generated with pore bodies as the nodes and pore channels as the connecting tubes where the conductance is located. When a macroscopic fluid pressure gradient is applied across the whole network, a distribution of pressures at nodes and flow rates through the tubes will be induced. A linear system under the Hagen-Poiseuille law and principle of mass conservation can be solved. The pore network simulation is not the focus of this study, but could be considered in the future.

There is other topological information to be explored regarding the size correlation between pore bodies or between pore throats and pore bodies. For each pore body, the average size of its neighboring pore bodies can be calculated and plotted against its size. For each pore throat, the average size of its two neighboring pore bodies can be plotted against its size. Also, the ratio of that throat size to the calculated average pore body size can be presented in a distribution, that is, the distribution of throat/pore body aspect ratio.

3.5.5.2 Planar Surface Construction Algorithm

From the identified pore throats, volume of the pore space is partitioned into pore body volumes enclosed by throat surfaces which have no volume but planar area. Distinct pore bodies are labelled through calculating connected components. The volume of a pore body is measured by voxel counting except for the voxels passed through by the throat

surfaces (i.e. throat barrier voxels). For geometric simplicity, half of the total volume of the throat barrier corresponding to a throat is distributed to each of the two pore bodies separated by the throat. This ensures that summation of the volumes of distinct pore bodies equals the entire pore volume in the microstructure.

However, as a result of crossing-throats, it is likely that a throat surface bounds more than two pore bodies. Throats of this kind typically served as the terminating ones during part (2) of the algorithm. In compliance with the principle that a throat should separate exactly two different pore bodies, a modification on those throats is considered for extracting network statistics. Through a 26-connectivity analysis, the barrier voxels adjacent to more than two pore bodies are marked and used to divide the throat. Each of the divided throats is assigned a partial area accordingly, and that partial area is approximated for simplicity. For instance, it is very common that the barrier voxels of one throat barrier are adjacent to three pore bodies, the throat is thus divided into two parts, and half of the original throat area is assigned to each for approximation. Each of the two barriers is reconfigured from the barrier-pore body adjacency information. Figure 3.40 provides a simple illustration. Some barrier voxels of Throat *A* that are located at the intersection of Throat *A* and Throat *B* border three pore bodies (labelled in red, purple and green). Therefore, all the barrier voxels will be segregated into three groups through adjacency analysis: (a) those that only border the pore bodies labelled in red and purple; (b) those that only border the pore bodies labelled in red and green; (c) and those that border the three. The barrier voxels in group (c) will be distributed to both (a) and (b) without splitting one single voxel. It has to be mentioned that limited by the current throat-finding rate, an identified pore throat might not bound any separated pore body but the largest,

unpartitioned pore component. For now, these throats are simply retained without any modification.

Once the modification have been completed, throat size is derived as an "area equivalent diameter" from the computed throat area. The "volume equivalent diameter" computed from the pore body volume is taken as the pore body size. Distribution of throat area (size), pore body volume (size) as well as pore body-throat connectivity are calculated as the major network parameters from this algorithm. As stated earlier, any isolated pore body without connecting throats will be disregarded in the pore network analysis.

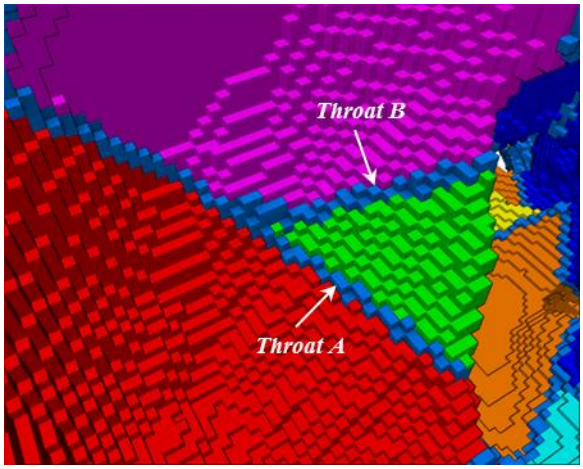

Figure 3.40 Example of a throat (*Throat A*) bounding three different pore bodies in BT0_Center

3.5.6 Unbiased 3-D Sampling and Quantification

Generally, sampling sub-volumes like the REV is necessary for the skeleton-based 3-D pore structure characterization. Domain borders of a sub-volume have an influence on the pore skeleton computation using the adapted DOHT method. To illustrate this edge effect, two different approaches to compute pore skeleton on a sub-volume sampled from

structure BT0 are exercised and compared. Moreover, a 2-D comparison is supplemented for a more intuitive visualization through sampling a sub-area from one slice in BT0.

Approach 1: sample the sub-volume or sub-area first, followed by skeleton computation. Figure 3.41 presents the 2-D pore skeleton, and the sub-domain is marked in orange solid lines. The spatial graph is created from the voxel skeleton. Approach 2: compute skeleton on the whole pore structure, and then sample the sub-volume or sub-area. Figure 3.42 superimposes the sub-domain on both the voxel skeleton and spatial graph of the whole domain. It implies that the voxel skeleton of the sub-domain can be obtained by extracting directly from the voxel skeleton of the whole domain. A comparison on the voxel skeleton obtained from both approaches is conducted in Figure 3.43 in which the two sets of voxel skeleton are displayed together. In 2-D, the divergence near the sub-domain borders is highlighted using red circles. That divergence can be recognized in 3-D as well, especially when the orthogonal boundary surfaces are viewed (see Figure 3.44). The edge effect cannot assure that the essential properties of skeleton concerning homotopy and medialness are preserved on the borders when processing the sub-domain independently. This raises problems in characterizing geometrical tortuosity as the number and position of skeleton voxels on both entry and exist surfaces are distorted. Therefore, approach 2 is the preferred approach to access to the voxel skeleton of a sub-domain.

As for the spatial graph, a straight conversion from the voxel skeleton within the sub-domain into a spatial graph is at the expense of losing the interconnectivity information of pore structure. *Node*s are incorrectly created, and the coordination relations among them are misrepresented. However, it is not achievable to break down the continuous *Segment*s to extract a spatial graph for a sub-domain. Also, a valid skeleton trimming should

definitely be performed with respect to the real spatial graph created from the skeleton of the entire pore structure. Otherwise, several *Segment*s that appear to be dead-end near the sub-domain borders such as those in Figure 3.41 will be trimmed, disregarding their existing connections to the *Segment*s outside the sub-domain.

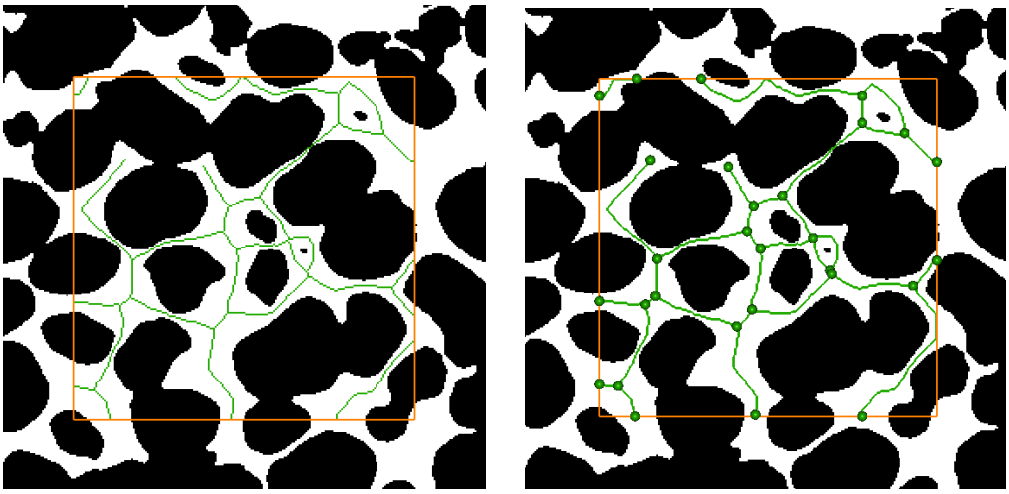

Figure 3.41 2-D illustration on pore skeleton of approach 1

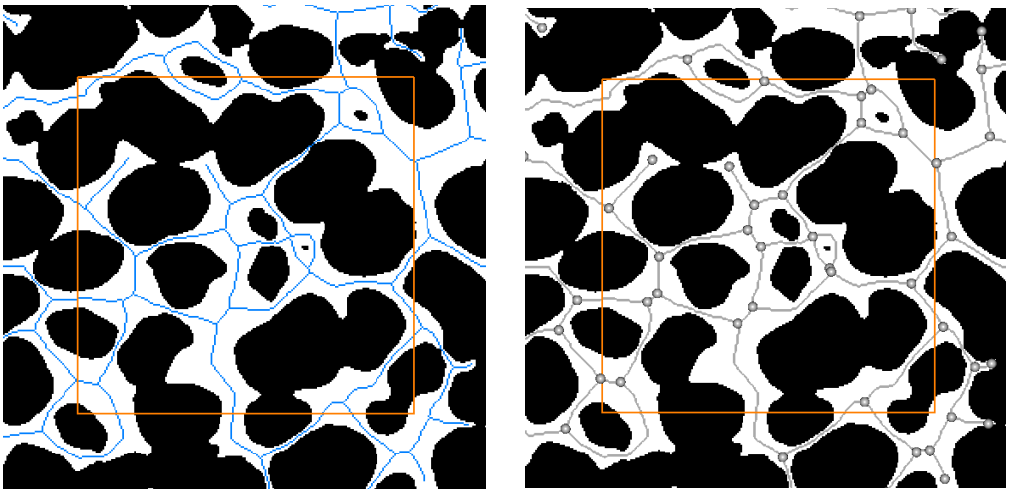

Figure 3.42 2-D illustration on pore skeleton of approach 2

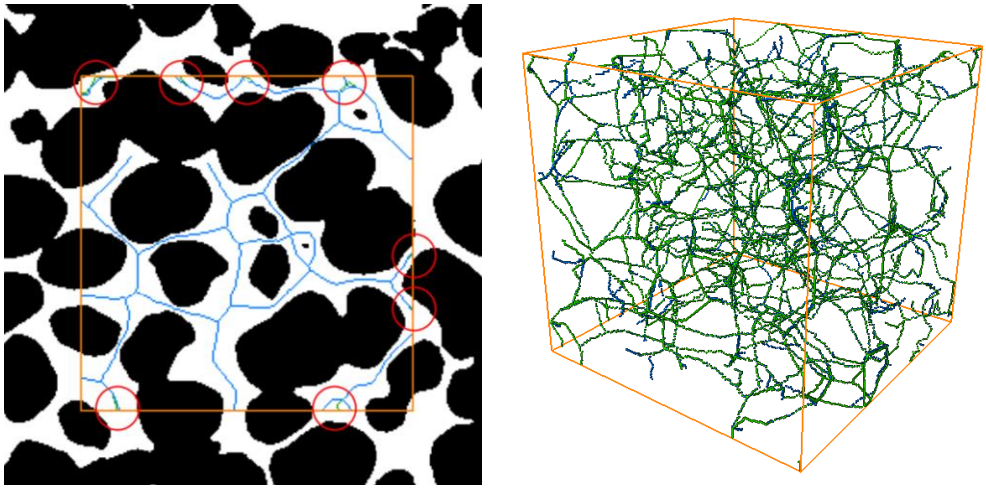

Figure 3.43 Visualization of the voxel skeleton from both approaches

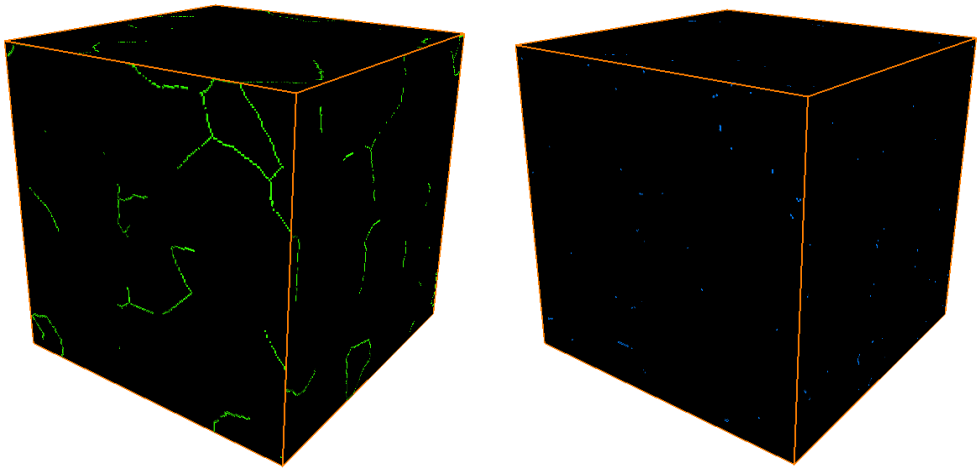

(a) (b)

Figure 3.44 Comparison of 3-D extracted voxel skeleton between two approaches: (a) approach 1; (b) approach 2

In addition to the edge effect emerged from sub-volume sampling, the whole domain contains incomplete pore structure information in the vicinity of its borders as mentioned in Section 3.5.3.2. Discretion needs to be taken in analyzing the pore skeleton there too. In this research, bias due to the edge effects is resolved in the following manner:

Step 1: Employ pore skeleton computation on the whole microstructure domain.

Step 2: Establish the spatial graph, and perform skeleton trimming to identify *SPP*s according to the procedure described in Section 3.5.3.

Step 3: Define a largest analysis volume (LAV) domain on the basis of specifying the "guard volume" at each side of the LAV. Characteristic length of the "guard volume" is taken to be at least the average length of those *Segment*s stored in *SEG_Incomplete*. *SEG_Incomplete* was generated at the first step of skeleton trimming, and contains information of the *Segment*s intersecting the borders of the whole microstructure domain. For example, *SEG_Incomplete* for structure BT0 stores the *Segment*s with an average length of about 40 voxels. Distance from the surface of the LAV from its parallel domain surface is thus 40 voxels. This renders the LAV for BT0 to be 1220 × 720 × 350 voxels in dimension and being concentric to the whole domain (1300 × 800 × 430 voxels). Sub-volume sampling and all quantitative characterizations of the pore structure must be carried out within the LAV domain. When the quantification is on the LAV, such as pore topology based on the local sphericity method, the LAV plays the role of a large central brick volume and the unbiased brick counting rule (see Section 3.3) is applied.

Step 4: For geometrical tortuosity analysis, voxel skeleton of any sampled sub-volume will be extracted directly from that obtained in Step 1. For pore network property characterization, especially pore topology analysis based on the planar surface construction method, the *SPP*s that are relevant to the sub-volume of interest need to be identified so that the continuity of a *Segment* and the realistic network connectivity won't be impaired. To select the *R-SPP*s, those *SPP*s that interact with the sub-volume are determined in the first place. "Interact" means that at least one *Point* on the *SPP* is within the sub-domain range including its borders. Figure 3.45(a) gives a 2-D example and marks these *SPP*s in

red. Non-marked *Segment*s shown in grey are either non-*SPP*s or not satisfying the "interact" criterion. Then, an extension is implemented to identify the *SPP*s that connect with those "interact" *SPP*s through a shared *Node* or *Node Cluster*. Combining the "interact" *SPP*s and its extension produces the *R-SPP*s (see Figure 3.45(b)). The *R-SPP*s are mainly used in throat finding for a sampled sub-volume, and this identification design is motivated by the unbiased brick counting rule. When the pore structure is quantified on the sub-volume, the sub-volume serves as the central brick volume. According to the counting rule, features such as pore throats or pore bodies intersecting the brick are examined in spite of locating partially outside the brick. Identifying the *R-SPP*s, particularly the extension process, is expected to realize unbiased quantification of pore network parameters. Although the algorithm is run on the selected *R-SPP*s, the 3-D binary microstructure image data of the whole domain rather than the sub-volume is engaged in throat finding as the intact pore structure is considered.

It's worth pointing out that this design for identifying *R-SPP*s is benchmarked on more idealized porous media. In those systems, a high throat-finding rate enables all distinct pore bodies that would intersect the sub-domain borders to be separated out from the pore space, so quantification of pore bodies is unbiased. As for pore throats, by contrast, any throat as long as it exists can always be correctly counted for characterization by this design. Above all, regardless of throat-finding rate, the utilization of *R-SPP*s for pore topology analysis on sub-volumes is adequate.

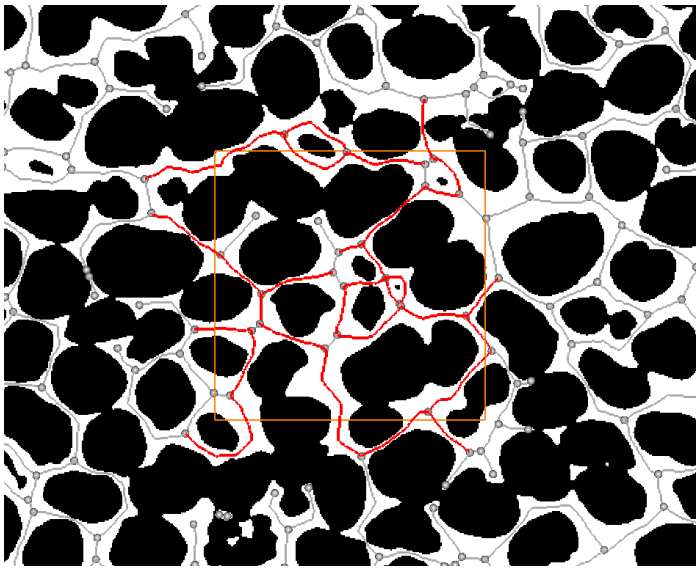

(a)

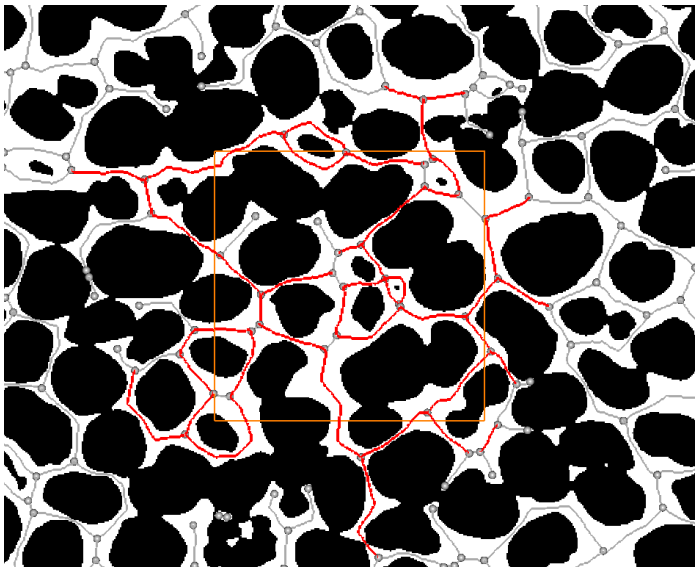

(b)

Figure 3.45 2-D illustration on the identification of *SPP*s relevant to a sub-domain (marked in red): (a) *SPP*s interacting with the sub-domain; (b) identified *R-SPP*s after an extension from (a)

3.6 Summary and Conclusions

The digital Ottawa sand microstructures can be processed through threshold segmentation, visualization, and post segmentation procedures. 3-D porosity (or void

ratio), specific surface area, and connected components are the representative standard structure metrics. The 3-D bricking rule was expressed mathematically in the Cartesian coordinate system along with specification of "guard volume" for unbiased quantification.

Particle separation is a weak link in micro-to-meso scale image analysis concerning the characterization of particles and particle-particle contacts. The maker-based watershed algorithm applied in this work provided a relatively high separation quality and flexibility to some extent through well-defined procedures. To rectify the observed separation errors, improvements in marker generation and separation function would need further attention.

Pore skeleton was computed as a discrete representation of the pore space. Tortuous attribute of the pore structure can be characterized spatially by an algorithm developed using graph theory. Presenting the skeleton as a spatial graph object, a skeleton trimming process was designed to establish a one-to-one correspondence of significant pore paths (*SPP*s) and *Node*s or *Node Cluster*s with pore pathways and pore bodies. Starting from the *SPP*s, pore network architecture was investigated. Two algorithms, built on different assumptions about simplifying the complex pore geometry, were proposed to compute pore throats. A pore throat was defined as the global minimum restriction on a *SPP* and uniquely connects two pore bodies.

The local sphericity (LS) algorithm located a throat as the position with the smallest local sphericity measure, and identified pore bodies by classifying skeleton into groups separated from the throats. A pore network model (PNM) consisting of spherical pore bodies connected by cylindrical tubes can be created capturing all the essential descriptive parameters. Owing to a high computational efficiency, this algorithm can be directly

implemented for throat finding on the whole microstructure volume. The second algorithm, planar surface construction (PSC) algorithm, advanced the pore structure characterization by constructing approximated throat surfaces with definite area in 3-D. However, throat construction was found to be especially difficult in the unconsolidated porous media under study which have porosities higher than 30%. Major attempts to improve the algorithm included introducing discrete optimization on the orientations of a throat surface, identifying crossing-throats, and proposing throat reconstruction. Future work needs to enhance the separation and identification of pore bodies intersecting the borders of a domain being analyzed. This algorithm consumes notable computation power, and thus is only applicable to throat finding on small sub-volumes like the representative elementary volume (REV) used in the current study.

Edge effects were revealed in the extraction of pore skeleton. To address the bias induced by edge effects, a scheme was suggested for 3-D unbiased sub-volume sampling and quantification. Specifically, it was necessary to compute the skeleton for the pore structure of the whole microstructure volume. Based on the skeleton trimming, a largest analysis volume (LAV) was defined to specify the appropriate domain for sampling and quantitative characterization. As for the pore topology study using the PSC algorithm in particular, an idea of identifying the relevant significant pore paths (*R-SPP*s) to retain the realistic pore structure interconnectivity was illustrated.

CHAPTER 4. 3-D PORE STRUCTURE CHARACTERIZATION OF SIMULATED MICROSTRUCTURES

4.1 Introduction

To evaluate the performance of the skeleton-based computational analysis tools introduced in Chapter 3, two idealized packing structures with monosized spheres: Simple Cubic packing (SCP) and Face-Centered Cubic packing (FCP) are generated and studied. The 3-D pore structure is characterized quantitatively involving geometrical tortuosity along the pore skeleton and throat finding based pore topology representation. The results for all pore metrics of interest rendered by the computational approaches are compared with the theoretical values.

4.2 Pore Structure Analysis on Simple Cubic Packing

4.2.1 Structure Information

The Simple Cubic packing (SCP) has a cubic unit cell that consists of eight 1/8 spheres located at the corners of the cube. The spheres correspond to the particle phase and are digitized with a radius of 25 voxels. The digitization process is achieved by specifying the center of each sphere in the packing followed by a slice dissectioning in MATLAB. The unit cell structure with a dimension of 50 × 50 × 50 voxels is shown in Figure 4.1. By replicating the unit cell, a cubic structure containing 6 × 6 × 6 cells with an edge length of 300 voxels is created and shown in Figure 4.2.

The representative elementary volume (REV) of the SCP structure is one unit cell and thus characterization is conducted on its pore structure. Besides, a larger sub-volume of 4 × 4 × 4 cells (Figure 4.3) is extracted from the structure center for pore structure characterization as well. Table 4.1 lists the structure information. It is straightforward geometry to derive the theoretical values of some key pore metrics of interest, and Table 4.2 provides their values or expressions as the function of sphere radius r.

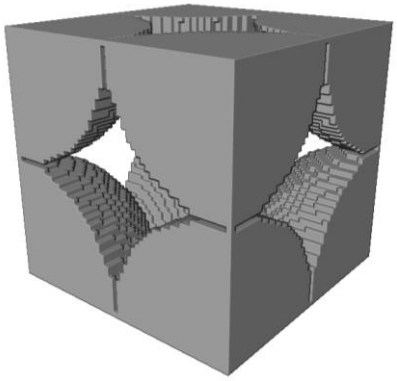

Figure 4.1 Digitized unit cell structure (particle phase) of SCP

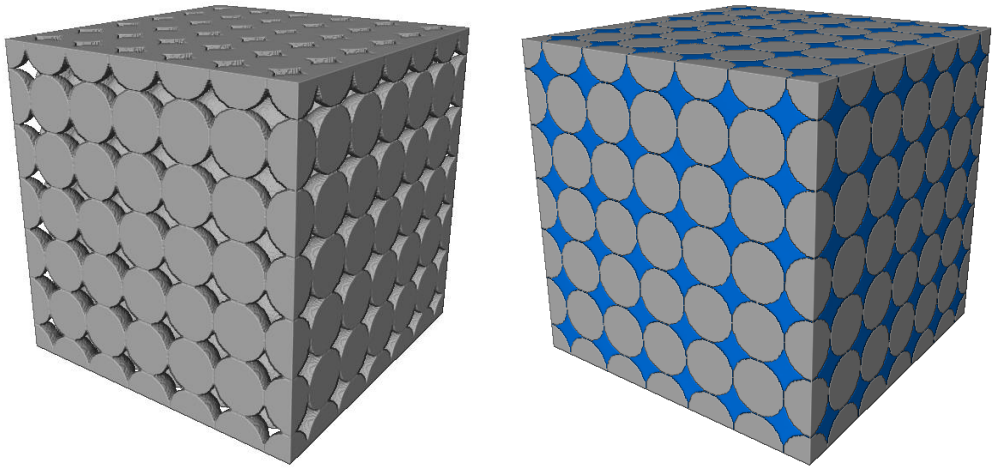

(a) (b)

Figure 4.2 Digitized SCP structure: (a) particle phase; (b) particle and pore phases (grey: particles; blue: pore space)

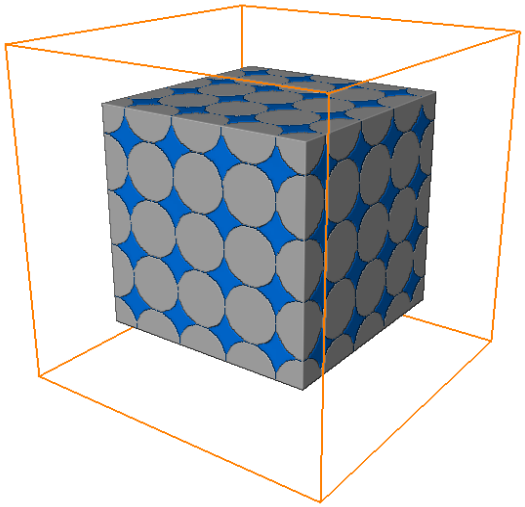

Figure 4.3 A larger sub-volume structure of SCP for pore structure characterization

Table 4.1 Information of structure SCP (unit: voxel)

Sphere Radius	25
Sphere Volume	65450
Packing Volume	300 × 300 × 300
Unit Cell	50 × 50 × 50
Sub-volume	200 × 200 × 200

Table 4.2 Theoretical value of selected pore metrics of structure SCP

Porosity	$1 - \pi/6$
Tortuosity (*X*, *Y*, or *Z*)	1
Throat Area	$(4 - \pi)\ r^2$
Pore Body Volume	$(8 - 4\pi/3)\ r^3$
Pore Channel Length	2 r

Note: r - sphere radius in the structure

4.2.2 Skeleton Analysis

According to the scheme of unbiased 3-D pore structure quantification suggested in Section 3.5.6, pore skeleton is computed on the entire pore space in the SCP. Figure 4.4

presents the skeleton in voxel skeleton and spatial graph forms. The spatial graph is composed of 432 *Node*s, 756 *Segment*s and 31860 *Point*s. Performing skeleton trimming on the spatial graph, 540 *SPP*s totally are identified. *Segment*s in the list *SEG_Incomplete* have a length of 25 voxels, and therefore the dimension of the largest analysis volume (LAV) is 250 × 250 × 250 voxels, which is bigger than the dimension of the unit cell and the sub-volume involved for characterization. It is also guaranteed that the extraction of either the unit cell or the sub-volume will be within the LAV domain.

Geometrical tortuosity is quantified along *X*, *Y*, *Z* axes on the voxel skeleton extracted for the sub-volume. Computed tortuous paths along positive *Z* direction in the sub-volume are highlighted in Figure 4.5. There are 16 tortuous paths with an identical tortuosity value of 1.000.

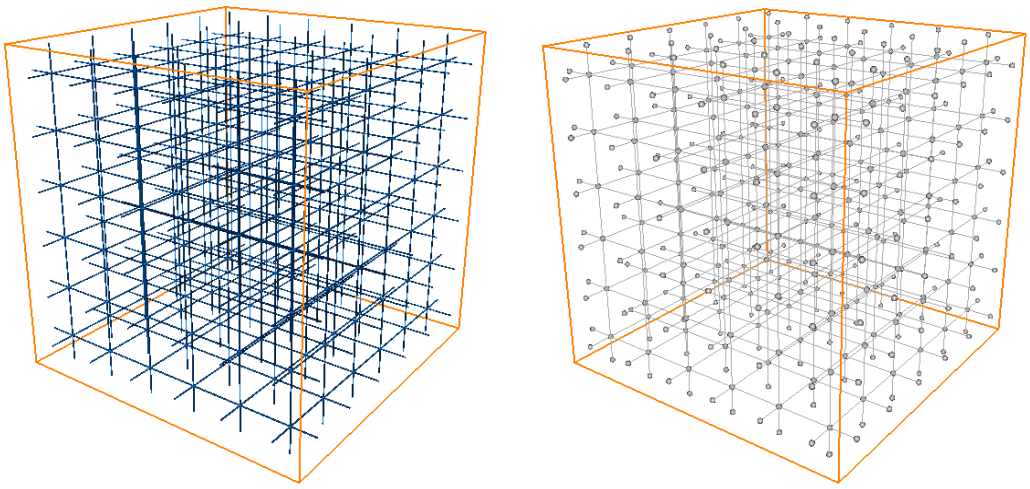

(a) (b)

Figure 4.4 Skeleton of the SCP pore structure: (a) voxel skeleton representation; (b) spatial graph representation

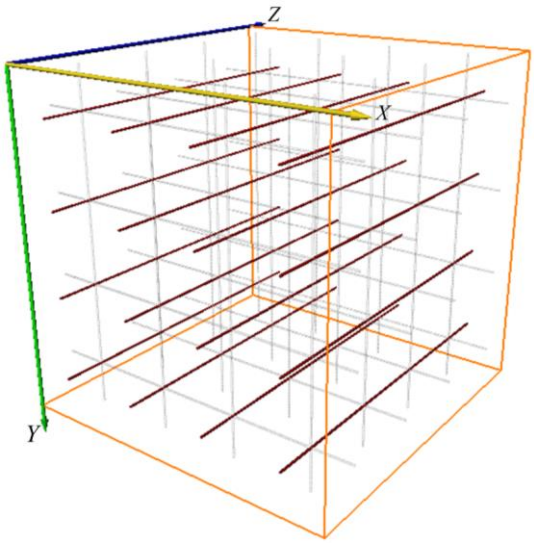

Figure 4.5 Tortuous paths computed along positive *Z* direction in the SCP sub-volume

4.2.3 Pore Topology Quantification

Figure 4.6 presents the local sphericity measures on the pore skeleton spatially using a "rainbow" color scale. Red represents a larger local inscribed sphere radius while purple represents a smaller radius.

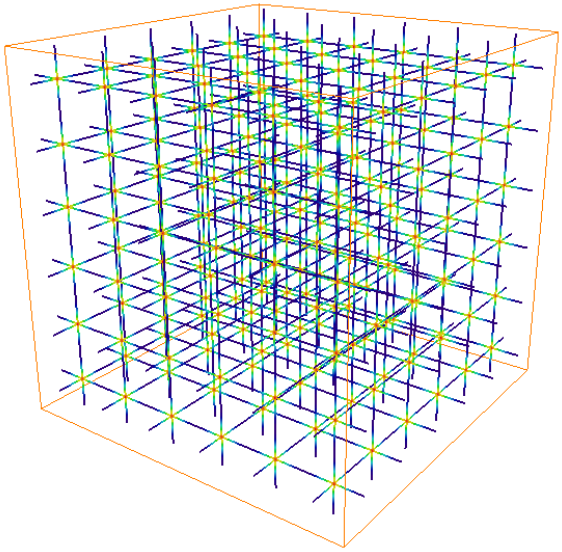

Figure 4.6 Spatial graph colored by local sphericity attribute in the SCP structure

Implementing the local sphericity (LS) algorithm to identify pore throats from the *SPP*s in the whole SCP structure, throat size is estimated to be 18.7 voxels. Different pore bodies are labelled through classifying skeleton into separated groups in Figure 4.7.

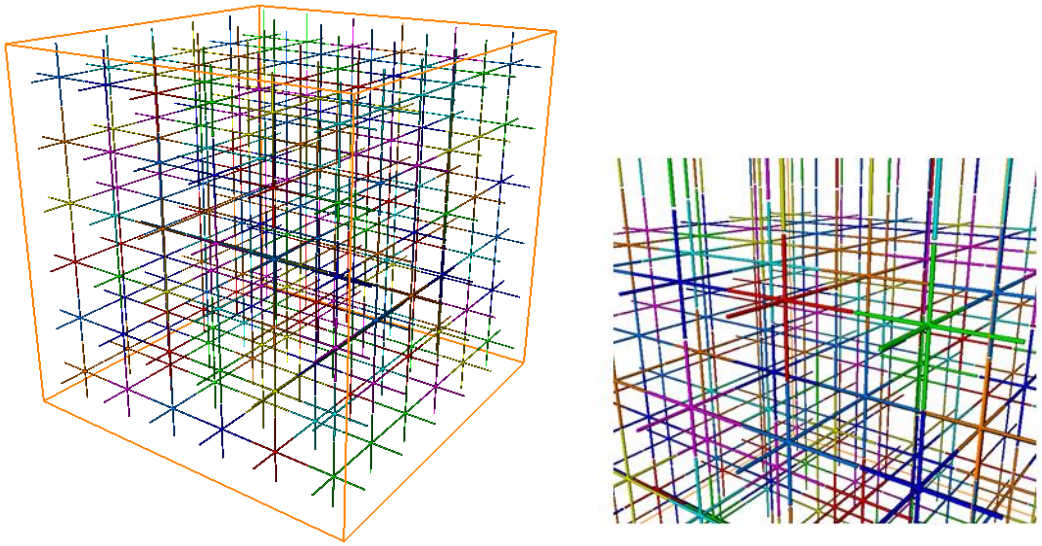

(a) (b)

Figure 4.7 Labelled separated skeleton groups representing different pore bodies in the SCP structure: (a) a whole structure view; (b) a zoom-in view

The planar surface construction (PSC) algorithm based throat finding is first implemented on the unit cell structure domain. With the ROI defined (Figure 4.8 (a)), 36 *R-SPP*s are determined in place and marked (Figure 4.8 (b)). Figure 4.8 (c) displays the 36 constructed throat barriers. Pore space in the SCP structure is partitioned by these barriers. Ignoring the largest pore component outside the unit cell, 7 pore bodies pertaining to the structure are visualized in Figure 4.9. To generate pore network statistics for the unit cell, take it as the 3-D central brick volume. Applying the unbiased quantification rule in the Cartesian coordinate system *XYZ*, only three throats intersecting with the "acceptance surfaces" (see Figure 3.4) are counted, and one pore body completely inside the domain is counted as shown in Figure 4.10. Theoretically, each identified throat surface is shared

between the unit cell itself and its neighboring cell, and thus half of the six surfaces belong to the unit cell. This is the case in counting the number of pore channels too.

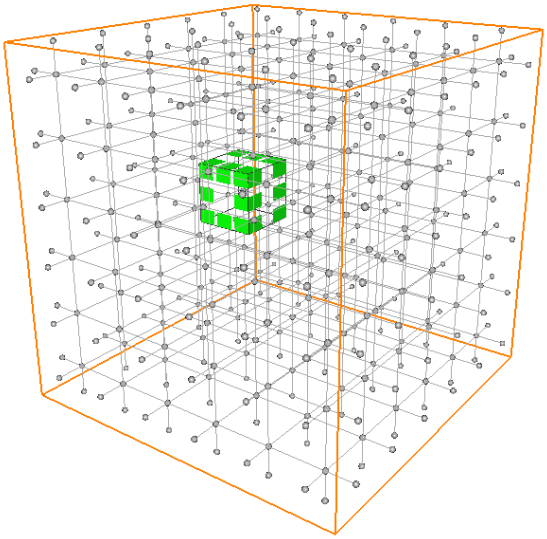

(a)

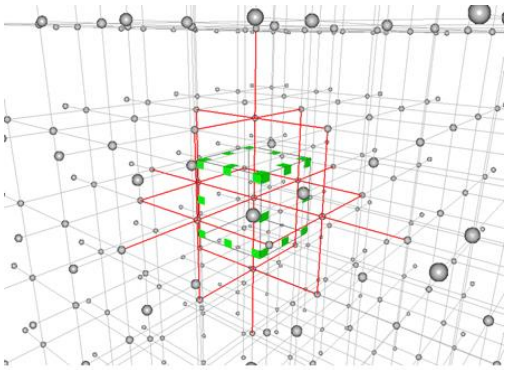

(b)

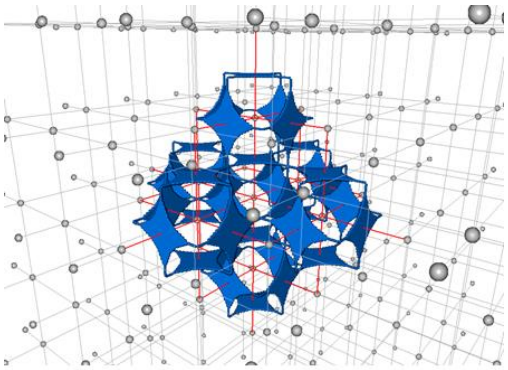

(c)

Figure 4.8 Implementation of the PSC algorithm for throat finding on the SCP unit cell: (a) location of the unit cell structure; (b) *R-SPP*s; (c) constructed throat barriers

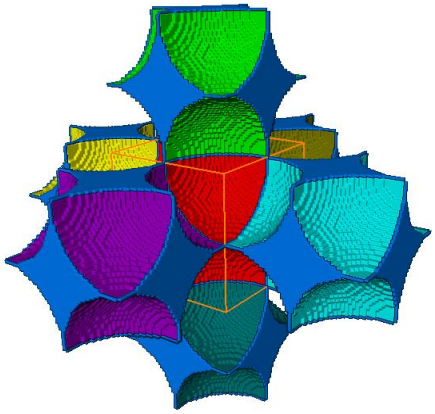

Figure 4.9 Pore throats and pore bodies pertaining to the SCP unit cell structure

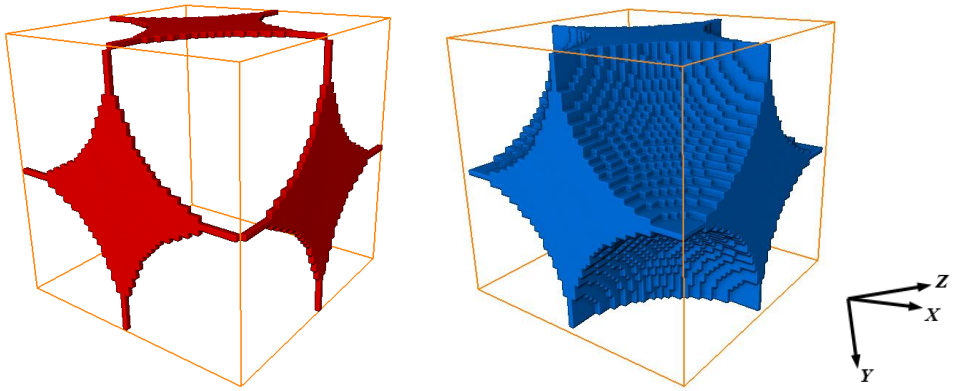

(a) (b)

Figure 4.10 Counted pore network components for the SCP unit cell structure: (a) pore throat barriers; (b) pore body

A comparison of the computational results with the theoretical values is presented in Table 4.3. Because the throat has an irregular shape, throat size obtained theoretically or from the PSC algorithm is an "area equivalent diameter" that quantifies the diameter of a circle with the same area. Likewise, pore body size is a "volume equivalent diameter" derived from the computed pore body volume. The LS algorithm is not capable of obtaining throat area and pore body volume. It is to be noted that the tortuosity algorithm works very well, and the PSC algorithm renders a much higher accuracy in characterizing pore throats and pore bodies. Both algorithms give a good prediction on pore connectivity. The small

deviations of the computational values based on the PSC algorithm from the corresponding theoretical ones stem from the pixelization of the original spheres in the structure. The finite size of a voxel leads to digitization error in representing the smooth surface of spheres. As for the LS algorithm, on the other hand, a computational error of about 30% is found in estimating sizes of throats and pore bodies. Besides, the results prove the argument made in Section 3.5.4.3 that the LS algorithm typically underestimates pore throats and pore bodies due to the spherical assumptions made about their shapes. Considering the computational expense, it took more than 10 hours for throat finding on the *36 R-SPP*s by the PSC algorithm while negligible time by the LS algorithm using a 4-core CPU.

Table 4.3 Comparison between the computational and theoretical results on SCP unit cell

Metrics	Theoretical		Computational		Relative Error
	Value	Quantity	Value	Quantity	
Porosity	0.476	n/a	0.463	n/a	2.7%
Tortuosity (*x*, *y*, or *z*)	1.000	1	1.000	1	0
Throat Area	536.5	3	541.0[b]	3[b]	0.8%[b]
Throat Size	26.1	3	18.7[a]; 26.2[b]	3[a,b]	28.4%[a]; 0.4%[b]
Pore Body Volume	59550.2	1	59736.0[b]	1[b]	0.3%[b]
Pore Body Size	48.5	1	33.3[a]; 48.5[b]	1[a,b]	31.3%[a]; 0.1%[b]
Pore Body *CN*s	6	1	6[a,b]	1[a,b]	0[a,b]
Pore Channel Length	50.0	3	50.0[a]	3[a]	0[a]

Note: a - Local Sphericity algorithm; b - Planar Surface Construction algorithm

Regarding the sub-volume structure, 480 *R-SPP*s are determined and a 100% throat-finding rate enables 480 pore throats to be identified. Using the unbiased estimation, 196 throats and 64 pore bodies, having the same size measures as those given in Table 4.3, belong to the sub-volume. Figure 4.11 visualizes the counted throats and pore bodies.

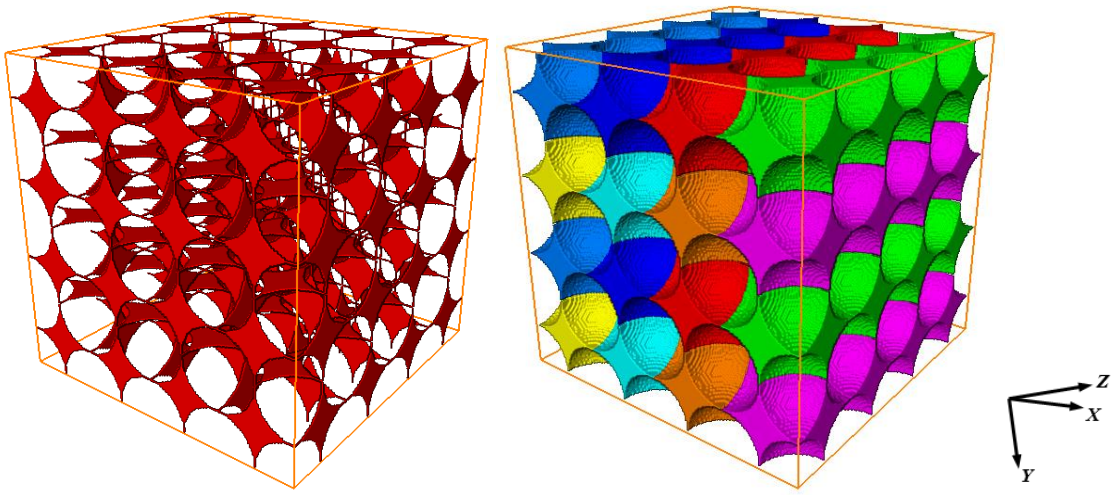

(a) (b)

Figure 4.11 Counted pore network components for the SCP sub-volume structure: (a) pore throat barriers; (b) pore bodies

4.3 Pore Structure Analysis on Face-Centered Cubic Packing

4.3.1 Structure Information

The Face-Centered Cubic packing (FCP) has a unit cell composed of 1/2 spheres located in the center of each face in addition to 1/8 spheres at each corner of the cube. In the digitization process, spheres (particle phase) are generated to have a radius of $25\sqrt{2}$ voxels to avoid specifying the coordinates of each sphere center as float numbers. In this way, the FCP structure is symmetrical. Additionally, to resemble the point contact between the smooth spheres in the packing, a delta value of 0.02 voxel is added to the sphere radius. Figure 4.12 shows the unit cell structure and its dimension is 100 × 100 × 100 voxels. By replicating the unit cell, a cubic structure containing 5 × 5 × 5 cells with an edge length of 500 voxels is created and shown in Figure 4.13.

Pore structure characterization is performed on one unit cell as the REV of the FCP structure, and a sub-volume of 3 × 3 × 3 cells (Figure 4.14) sampled from the structure

center. The structure information is summarized in Table 4.4. Theoretical values of the important pore metrics are derived and provided in Table 4.5. It is more complicated geometrically in calculating the theoretical values of pore throats and pore bodies, and two different sizes of pore bodies are recognized. Knowledge of spherical trigonometry is exploited in the derivation.

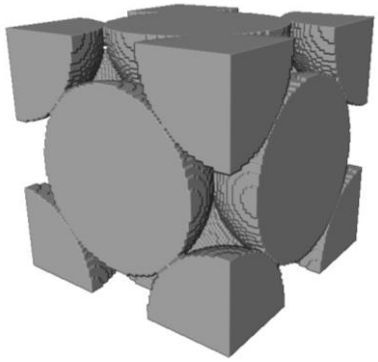

Figure 4.12 Digitized unit cell structure (particle phase) of FCP

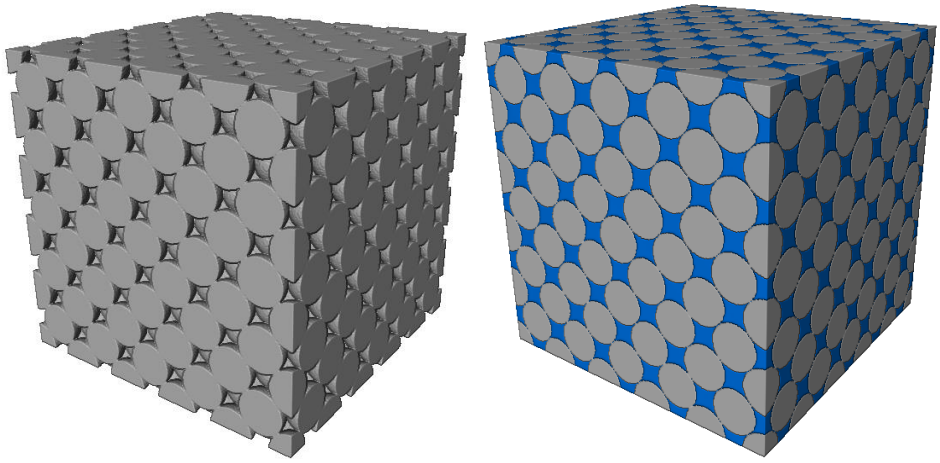

(a) (b)

Figure 4.13 Digitized FCP structure: (a) particle phase; (b) particle and pore phases (grey: particles; blue: pore space)

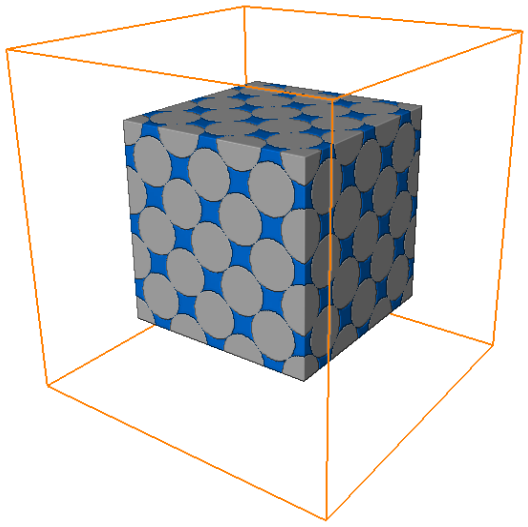

Figure 4.14 A larger sub-volume structure of FCP for pore structure characterization

Table 4.4 Information of structure FCP (unit: voxel)

Sphere Radius	$25\sqrt{2}$
Sphere Volume	185120
Packing Volume	500 × 500 × 500
Unit Cell	100 × 100 × 100
Sub-volume	300 × 300 × 300

Table 4.5 Theoretical value of selected pore metrics of structure FCP

Porosity	$1 - \sqrt{2}\,\pi/6$
Tortuosity (*X*, *Y*, or *Z*)	$\sqrt{3}$
Throat Area	$(\sqrt{3} - \pi/2)\ r^2$
Pore Body I Volume	$[2\sqrt{2}/3 - 4(3\cos^{-1}(\frac{1}{3}) - \pi)/3]\ r^3$
Pore Body II Volume	$(8\sqrt{2}/3 + 8\cos^{-1}(\frac{1}{3}) - 4\pi)\ r^3$
Pore Channel Length	$\sqrt{6}/2\ r$

Note: r - sphere radius in the structure

4.3.2 Skeleton Analysis

Pore skeleton is computed for the pore structure in the FCP, and its voxel skeleton and spatial graph representations are presented in Figure 4.15. The spatial graph consists of 1605 *Node*s, 3940 *Segment*s and 103940 *Point*s. After skeleton trimming, 2920 *SPP*s are identified. Length of the *Segment*s in the list *SEG_Incomplete* is approximately 87 voxels, resulting in the LAV with a dimension of around 325 × 325 × 325 voxels. The unit cell and the sub-volume for pore structure analyses are extracted within this LAV domain.

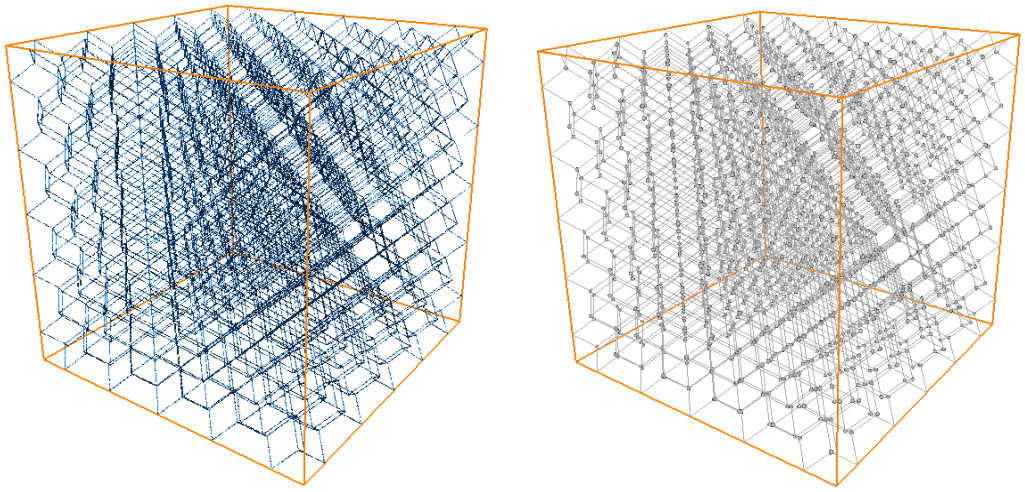

(a) (b)

Figure 4.15 Skeleton of the FCP pore structure: (a) voxel skeleton representation; (b) spatial graph representation

From the voxel skeleton for the unit cell structure displayed in Figure 4.16(a), 12 rhombuses can be observed and each of them has a side length of $\sqrt{6}/2$ r that is 43.3 voxels. In quantifying the geometrical tortuosity, every tortuous path has an identical length equals to four times the side length. So, an arbitrary decision is involved when determining how a tortuous path passes through the skeleton along a specified direction. As can be seen from Figure 4.16(b), the highlighted 4 tortuous paths computed along positive *Z* direction do not

follow the same pattern. With respect to the sub-volume structure, 24 tortuous paths altogether along positive *Z* direction are determined and shown in Figure 4.17. All these tortuous paths contribute to a tortuosity value of $\sqrt{3}$ (≈1.732).

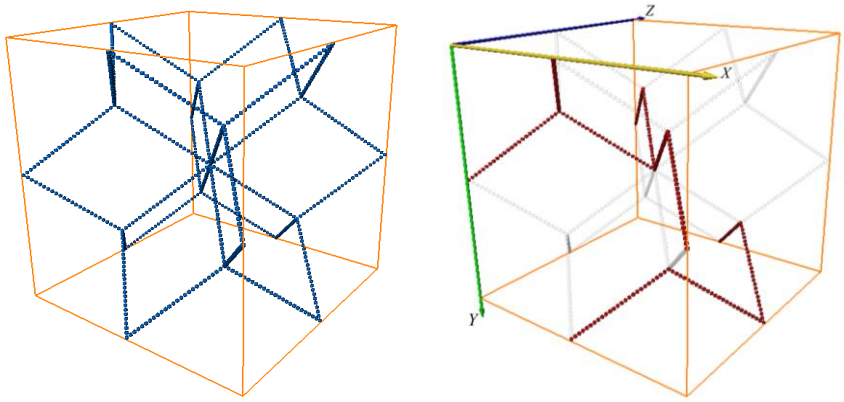

(a) (b)

Figure 4.16 Pore skeleton and computed tortuous paths in the FCP unit cell structure: (a) voxel skeleton; (b) tortuous paths along positive *Z* direction

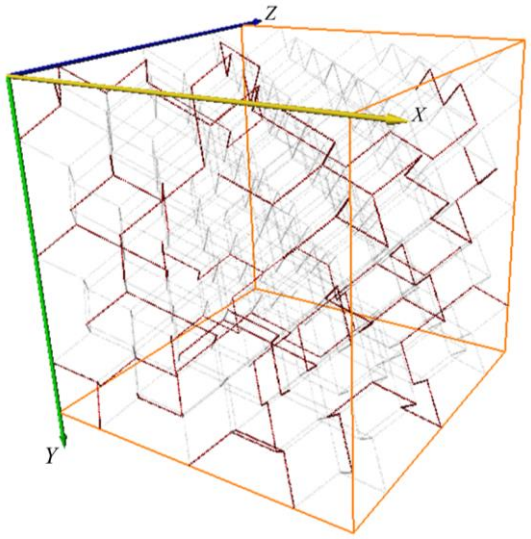

Figure 4.17 Tortuous paths computed along positive *Z* direction in the FCP sub-volume

4.3.3 Pore Topology Quantification

Spatial distribution of the local sphericity measures on the pore skeleton of the FCP structure is presented in Figure 4.18 with that of the unit cell structure displayed separately. Again, the larger local inscribed sphere radius is in red and the smaller one in purple.

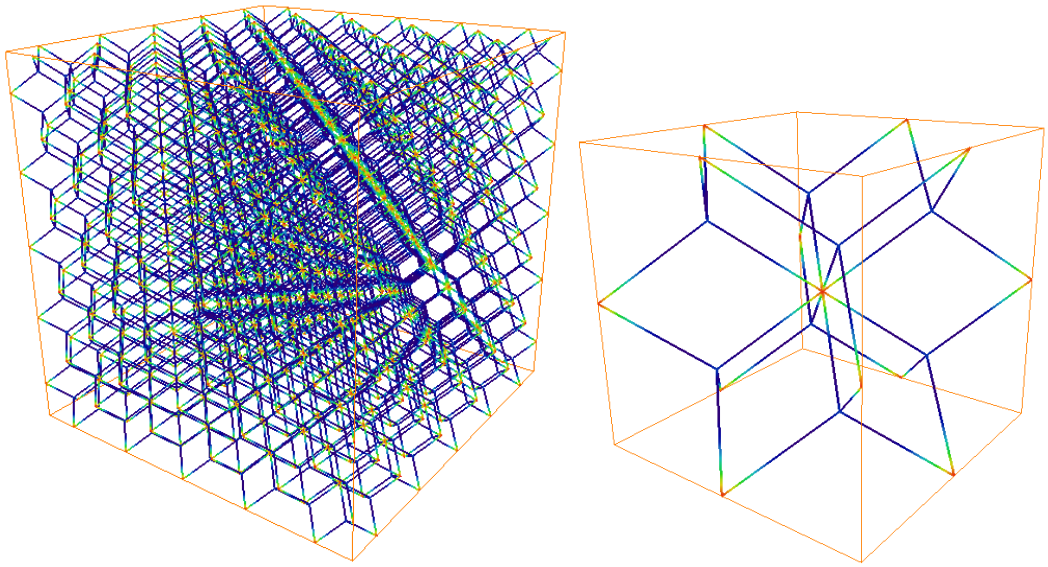

(a) (b)

Figure 4.18 Spatial graph colored by local sphericity attribute in the FCP structure: (a) whole pore structure; (b) unit cell pore structure

Pore skeleton is separated into different groups through identifying pore throats based on the LS algorithm, and shown in Figure 4.19, Size of the pore throat is estimated to be 9.3 voxels. Two sizes for pore bodies are found: 13.3 voxels and 28.7 voxels. Pore bodies of the bigger size can be termed as “pore body I” having a coordination number of 8, and those of the smaller size termed as “pore body II” with a coordination number of 4.

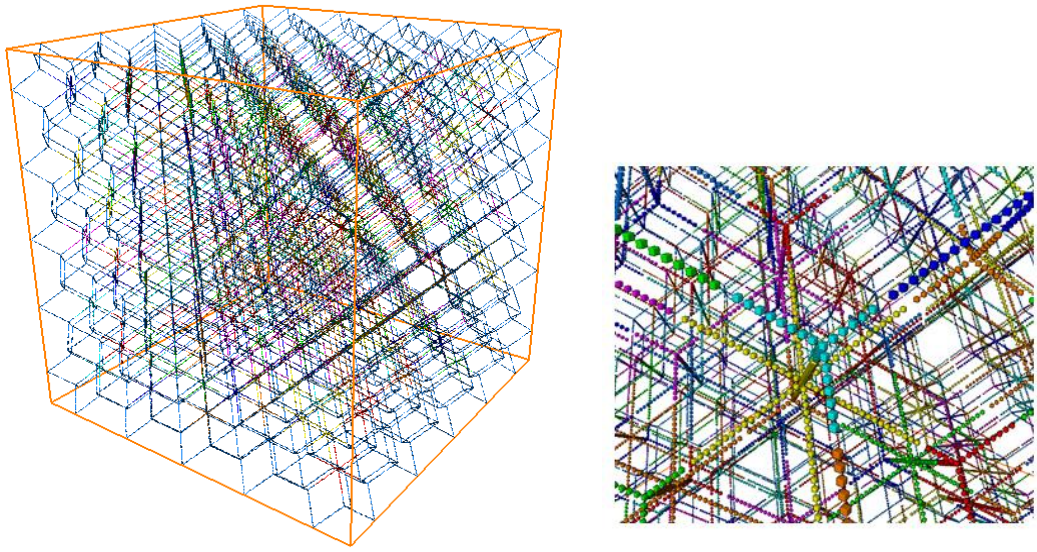

(a) (b)

Figure 4.19 Labelled separated skeleton groups representing different pore bodies in the FCP structure: (a) a whole structure view; (b) a zoom-in view

When running the PSC algorithm for throat finding on the unit cell pore structure, 224 throats are constructed and identified related to the ROI (Figure 4.20). Accordingly, 13 “pore body I” and 56 “pore body II” pertaining to the unit cell are separated out and visualized in Figure 4.21. Taking the unit cell as the central volume of the unbiased 3-D brick in extracting pore network statistics, only 32 throats that locate completely inside the domain are counted, 4 “pore body I” and 8 “pore body II” are counted (Figure 4.22). Among the 4 “pore body I”, 3 pore bodies intersect with the “acceptance surfaces” of the counting brick. If the scheme of unbiased 3-D pore structure quantification is not followed, in other words, the PSC algorithm is run on the pore structure of the unit cell and the *SPP*s inside it are considered alone, quantification of the pore bodies is incorrect. Although the pore structure in the unit cell is separated, “pore body I” cannot be fully captured at the domain borders. As presented in Figure 4.23, each edge has only 1/4 “pore body I”. Therefore, pore bodies will be falsely identified to have three different sizes: “pore body

I", "pore body II", and a quarter of "pore body I". In fact, every "pore body I" centered at the 12 edges of the unit cell is shared with 3 other neighboring cells, and thus each unit cell contains 4 "pore body I" including the one in the middle.

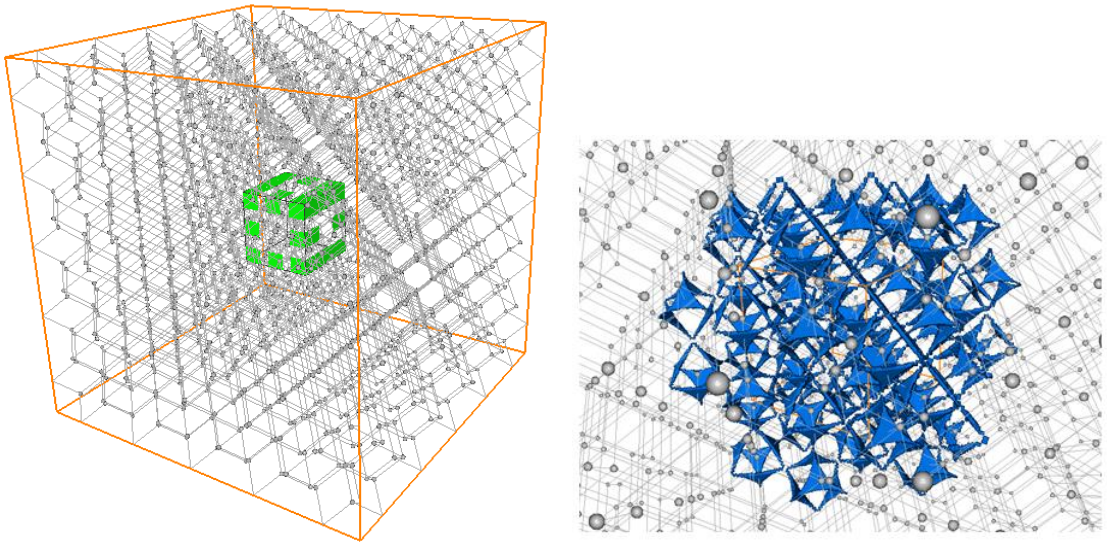

(a) (b)

Figure 4.20 Implementation of the PSC algorithm for throat finding on the FCP unit cell: (a) location of the unit cell structure; (b) constructed throat barriers

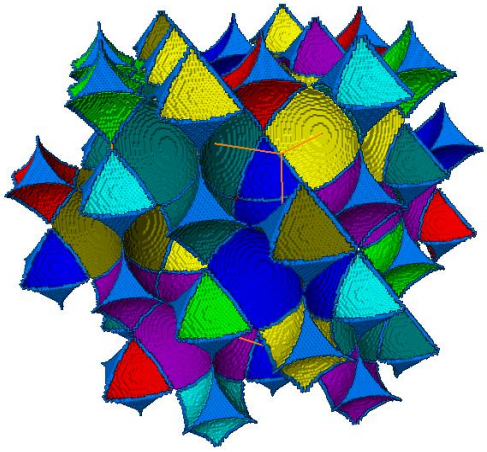

Figure 4.21 Pore throats and pore bodies pertaining to the FCP unit cell structure

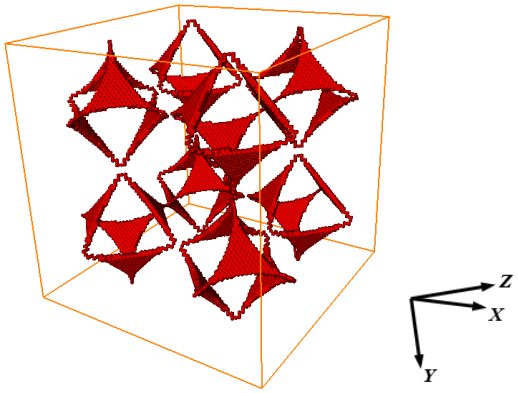

(a)

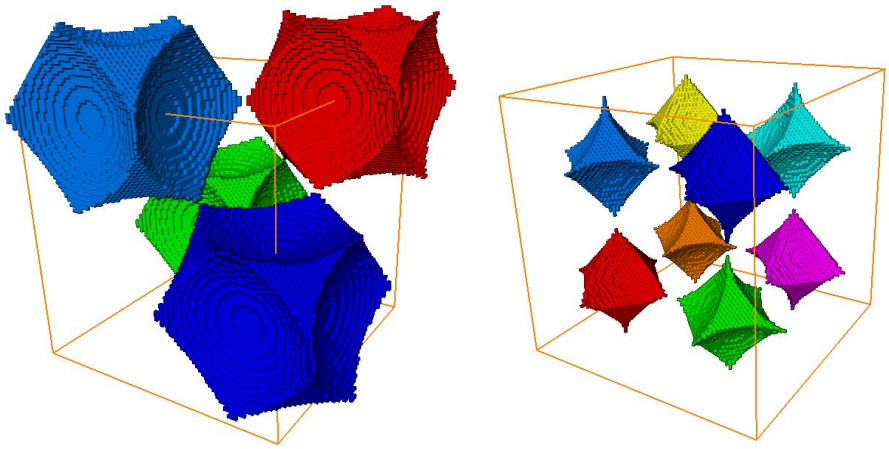

(b)

Figure 4.22 Counted pore network components for the FCP unit cell structure: (a) pore throat barriers; (b) pore bodies

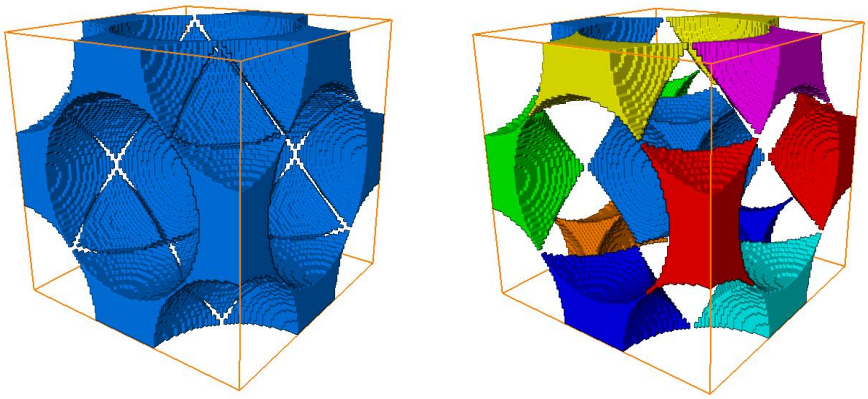

Figure 4.23 Biased quantification of pore bodies for the FCP unit cell structure

Table 4.6 lists the comparative information between the computational results and the theoretical values. Similar to the findings in the pore structure characterization of the SCP structure, the PSC algorithm provides a better estimation on the sizes of pore throats and pore bodies than the LS algorithm, though a much higher computational expense is demanded. Using a 4-core CPU, the PSC algorithm took about 70 hours for throat finding on the 224 *R-SPP*s. Estimation error of the PSC algorithm results from both the digitization error as well as the delta value introduced in creating the sphere-to-sphere point contact. By contrast, the LS algorithm underestimates the sizes of pore throats and pore bodies by almost 40% ~ 50% while it is efficient computationally.

Table 4.6 Comparison between the computational and theoretical results on FCP unit cell

Metrics	Theoretical		Computational		Relative Error
	Value	Quantity	Value	Quantity	
Porosity	0.260	n/a	0.257	n/a	1.0%
Tortuosity (*x*, *y*, or *z*)	1.732	4	1.732	4	0
Throat Area	201.6	32	197.5[b]	32[b]	2.0%[b]
Throat Size	16.0	32	9.3[a]; 15.9[b]	32[a,b]	41.8%[a]; 0.6%[b]
Pore Body I Volume	46516.2	4	47149.0[b]	4[b]	1.4%b
Pore Body I Size	44.6	4	28.7[a]; 44.8[b]	4[a,b]	35.7%[a]; 0.4%[b]
Pore Body I *CN*s	8	4	8[a,b]	4[a,b]	0[a,b]
Pore Body II Volume	9181.9	8	8669.0[b]	8[b]	5.6%[b]
Pore Body II Size	26.0	8	13.3[a]; 25.5[b]	8[a,b]	48.8%[a]; 1.9%[b]
Pore Body II *CN*s	4	8	4[a,b]	8[a,b]	0[a,b]
Pore Channel Length	43.3	32	43.3[a]	32[a]	0[a]

Note: a - Local Sphericity algorithm; b - Planar Surface Construction algorithm

For the FCP sub-volume structure, 2016 pore throats are constructed and identified from the 2016 *R-SPP*s. 864 throats, 108 “pore body I” and 216 “pore body II” are included in the pore network statistics of the sub-volume. Visualization of the throat barriers and

pore bodies is presented in Figure 4.24. Above all, it has been demonstrated that the selection of *R-SPP*s for running the PSC algorithm is suitable and sufficient for pore space partition and analysis for both the SCP structure and this FCP structure.

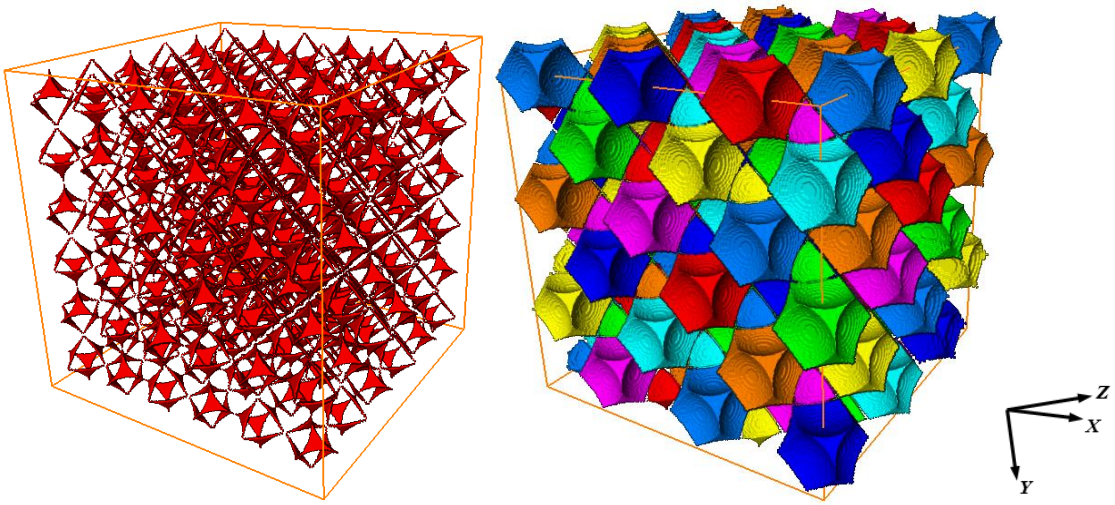

(a) (b)

Figure 4.24 Counted pore network components for the FCP sub-volume structure: (a) pore throat barriers; (b) pore bodies

4.4 Summary and Conclusions

The computational analysis tools developed in the current study can effectively characterize the 3-D pore structure of the two idealized packings. Algorithm for the geometrical tortuosity analysis permitted an accurate spatial quantification of the tortuous nature of the pore structure. Both algorithms for finding pore throats achieved a 100% throat-finding rate. The PSC algorithm worked better in capturing the true geometry of pore throats and pore bodies, and thus offered a very good estimation of their sizes. In comparison, it was shown that the LS algorithm underestimated the sizes of pore throats and pore bodies due to the simplifying assumptions built into its design. However, the LS algorithm could be more applicable when taking the computational efficiency into account.

In executing the throat finding algorithm and generating the distribution statistics of various pore metrics, the scheme of unbiased 3-D sampling and quantification was employed, and confirmed to be adequate and important.

CHAPTER 5. 3-D CHARACTERIZATION OF INHERENT AND INDUCED DIGITAL SAND MICROSTRUCTURES

5.1 Introduction

Three pairs of digital Ottawa sand microstructures (BT0 and BT10, AP0 and AP14, MT0 and MT14) are characterized in 3-D using the analysis tools introduced in Chapter 3. Visualization and basic fabric of these microstructures are presented. As for the particle phase, image-based particle measurement is compared with the laboratory sieving result. In characterizing the pore phase, existence and determination of the representative elementary volume (REV) for each microstructure are discussed in details. On the basis of defining the largest analysis volume (LAV) and the REV, shear-induced pore structure changes are investigated by comparative studies conducted between unsheared and sheared pore structures. Preparation-induced pore-scale variation is explored through quantifying unsheared microstructures reconstituted using different laboratory specimen preparation methods. Spatial information of geometrical tortuosity and pore topology characteristics are examined. The unbiased stereology continues to serve as the scientific characterization guideline in 3-D sampling and estimation.

5.2 Visualization and Standard Pore Metrics

Figure 5.1 presents the rendered 3-D microstructures for specimens BT0 and BT10. The microstructure for BT0 is 18.2 mm × 11.2 mm × 6.0 mm in dimension and contains 1300 × 800 × 430 voxels of side approximately 14 μm. The two phases are illustrated with grey for sand particles and blue for pores. The microstructure for BT10 has a dimension of

18.2 mm × 11.2 mm × 8.4 mm and contains 1300 × 800 × 600 voxels. A shear band, referred to as the region of deformation localization, was observed in the laboratory test and captured in BT10. Further, the shear band was found to include a shear zone and two transition zones (Evans and Frost, 2010). With an approximate 61° inclination, the width of the full shear band was determined to be 10.5 mm (14.2 × D_{50}) through a 3-D strip analysis (Lu, 2010). The extent of the shear zone along the direction perpendicular to the shear zone was estimated to be 5.6 mm, which is marked by a pair of red solid lines in Figure 5.1(b). The lateral extent of the transition zone on the left was about 2.1 mm and that on the right was about 2.8 mm. Regions outside the two transition zones were identified as non-dilatant zones where shear-induced dilation was basically negligible. The shear zone where shear-induced volumetric dilation occurred can be visually distinguished from the non-dilatant zones by larger pore space and/or looser particle packing. Affected substantially by the shear zone, a gradual transition from low void ratios (the non-dilatant zones) to high void ratios (the shear zone) was observed in the transition zones.

Figure 5.2 shows the 3-D microstructures for specimens AP0 and AP14 and each microstructure is 14.4 mm × 8.8 mm × 4.8 mm containing 1800 × 1100 × 600 voxels of side approximately 8 μm. In the triaxial loading, a barrel-like failure pattern was observed in the sheared air-pluviated specimen. Because the microstructure for AP14 was extracted from the bulging region in the middle of that specimen, it should capture a more global dilation. By visual comparison, particles in AP14 are in a looser packing than those in AP0. The reconstructed 3-D microstructures for MT0 and MT14 are presented in Figure 5.3, and have the same dimension as AP0 and AP14. Formation of a prominent shear plane was reported in the sheared moist-tamped specimen, and the microstructure for MT14 was

intended to encompass those regions. However, the extent of the shear band wasn't clearly identified and reported (Yang, 2005) due to the complex nature of shear banding with detected curvature. Nevertheless, particles are observed to be more loosely packed in MT14 (Figure 5.3(b)) globally than in MT0 (Figure 5.3(a)).

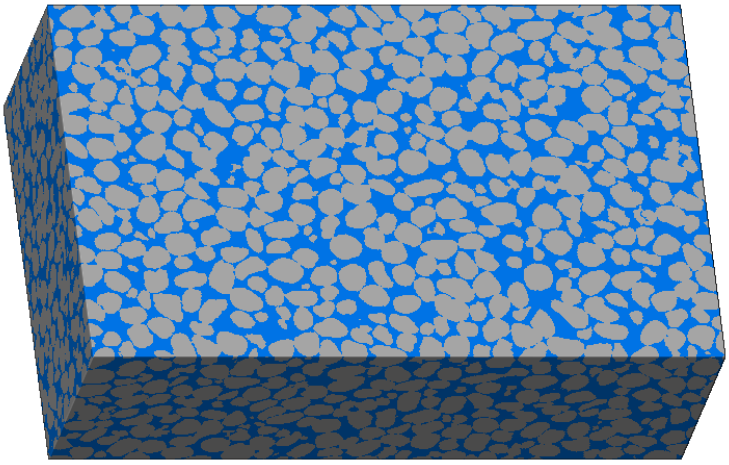

(a)

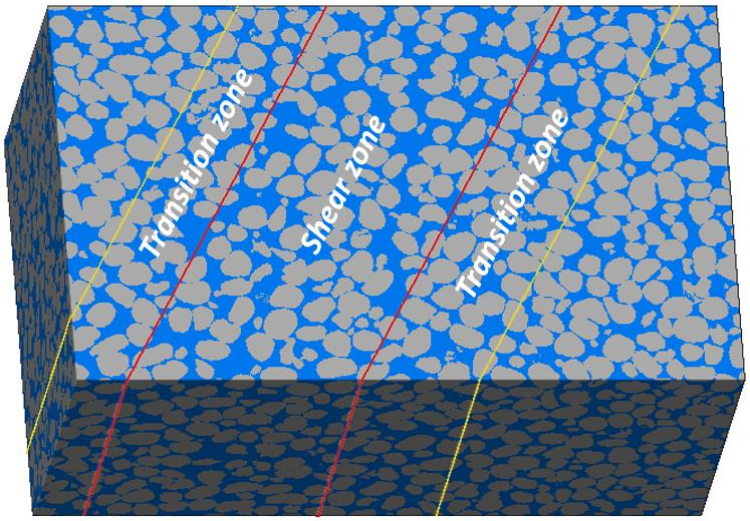

(b)

Figure 5.1 3-D reconstructed structures of BT0 and BT10 (grey: sand particles; blue: pore space): (a) BT0; (b) BT10

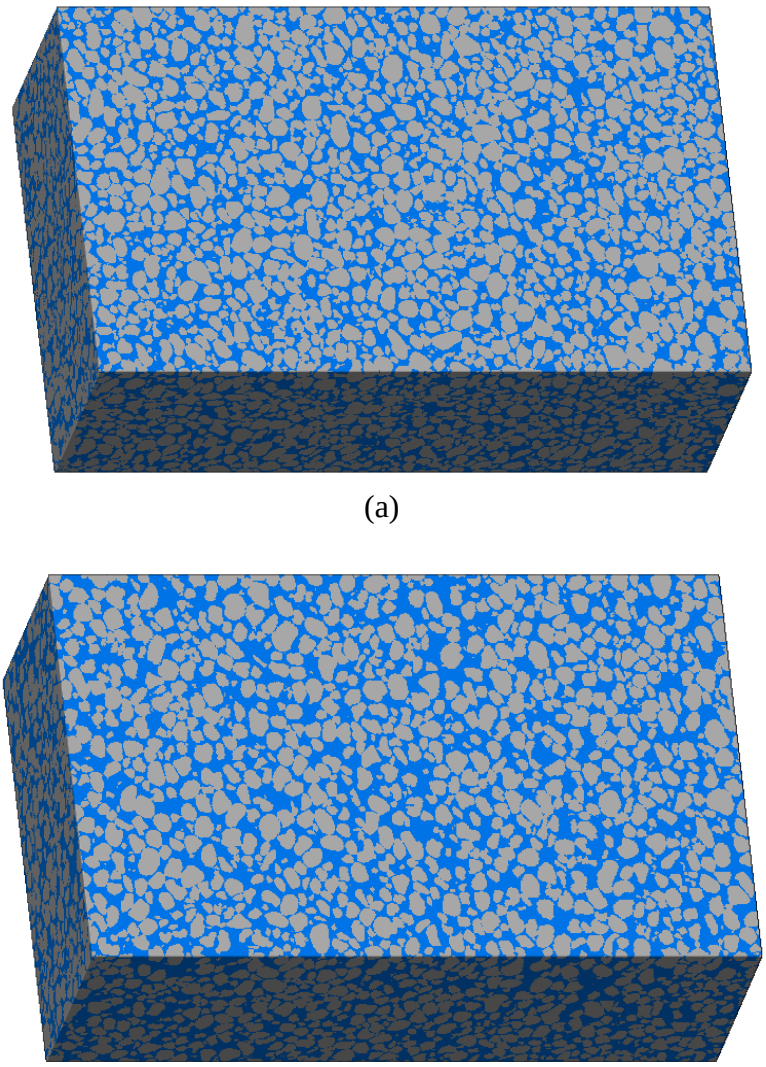

(a)

(b)

Figure 5.2 3-D reconstructed structures of AP0 and AP14 (grey: sand particles; blue: pore space): (a) AP0; (b) AP14

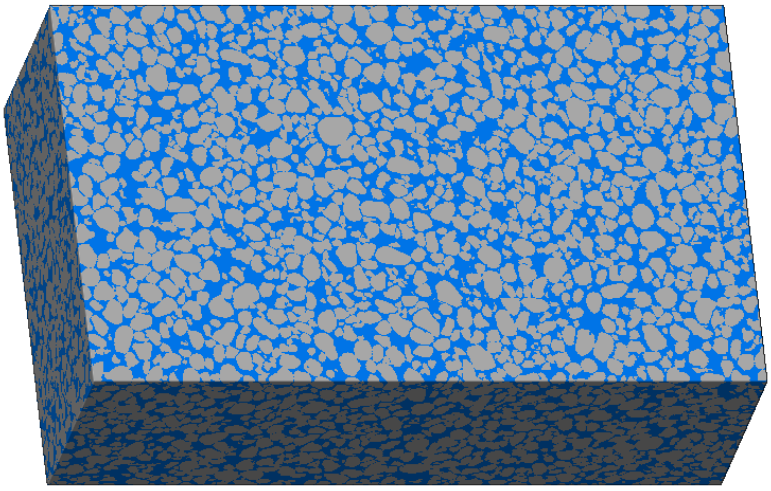

(a)

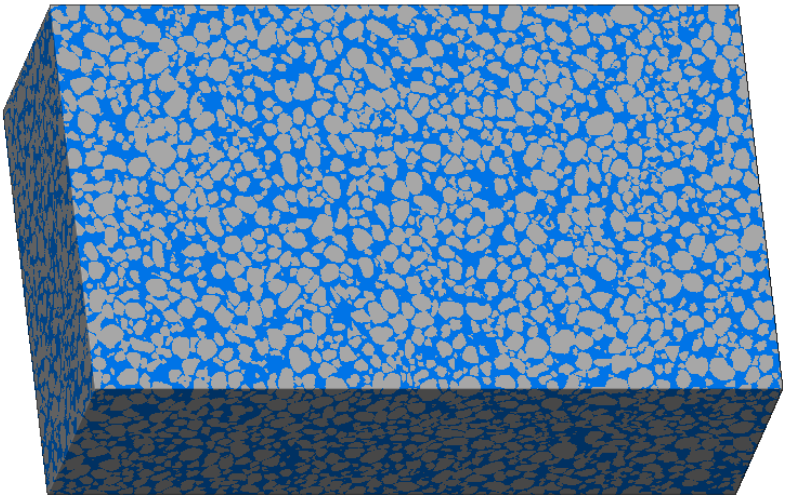

(b)

Figure 5.3 3-D reconstructed structures of MT0 and MT14 (grey: sand particles; blue: pore space): (a) MT0; (b) MT14

3-D porosity and void ratio are estimated on the six digital sand microstructures. As suggested in Section 3.2.3, a post segmentation processing procedure was designed to reduce digitization/segmentation artifacts and eliminate very small, isolated particles that could harm pore structure analyses. By comparing the results before and after this processing shown in Table 5.1, it only introduces a less than 0.6% change in porosity and 0.9% change in void ratio. These post-processed microstructures will be studied.

Table 5.1 3-D porosity and void ratio of digital sand microstructures

ID	Threshold Segmentation		Post Segmentation Process	
	Porosity	Void Ratio	Porosity	Void Ratio
BT0	33.8%	0.510	33.6%	0.507
BT10	36.2%	0.567	36.1%	0.564
AP0	36.5%	0.575	36.5%	0.575
AP14	41.7%	0.716	41.7%	0.716
MT0	35.9%	0.560	35.7%	0.555
MT14	41.3%	0.704	41.4%	0.705

It is noted that each digital volume of AP0, AP14, MT0, and MT14 contains approximately 1.2 billion voxels, which is significantly more than BT14 (less than 0.7 billion voxels) and BT0 (less than 0.5 billion voxels). The pore skeleton is extracted from each of them, and information about the created spatial graph is shown in Table 5.2. All triaxial microstructures have 2 to 3 times as many *Node*s, *Segment*s, and *Point*s as BT10, leading to quite expensive computations in the skeleton-based pore structure analyses. So, volumes of AP0, AP14, MT0, and MT14 are reduced by re-defining the region of interest for pore structure characterization.

Since the microstructures for AP0 and AP14 were prepared by cutting from the specimen center, and no evident shear planes aside from bulging deformation was observed in AP14, volume AP0a and AP14a having the same dimension as BT10 are cut from the center of AP0 and AP14, respectively. As for MT14, spatial void ratio distribution is examined to prevent the shear banding zone from being chopped off. The 3-D volume is divided into a grid of sub-volumes with each having 100 × 100 × 600 voxels. Figure 5.4 and Figure 5.5 plot the spatial void ratio of MT0 and MT14 in a planar view separately. Each grid on the *XY* plane (100 × 100 voxels) in the plot is around 2 × D_{50} square of the

Ottawa 30-50 sands. It is apparent that 3-D void ratios do not vary greatly within the unsheared volume. In the sheared volume MT14, however, void ratios increase markedly. Localized shear roughly appears in the diagonal region from top right to bottom left as evident from the higher void ratios. Therefore, a smaller volume MT14a is cut from the region indicated by the red dashed lines in MT14, and MT0a is cut correspondingly from MT0. Considering the lateral limits of shear band are not obvious in MT14a, the characterizations later are performed without distinguishing inside and outside shear zones. From the results of pore skeleton in AP0a, AP14a, MT0a, and MT14a (Table 5.2), it can be seen that the number of *Node*s, *Segment*s, and *Point*s are nearly decreased by half. In this chapter, 3-D microstructure characterizations will be performed on BT0, BT10, AP0a, AP14a, MT0a, and MT14a.

Table 5.2 Pore skeleton information of digital sand microstructures

ID	Dimension (voxels)	Spatial Graph		
		*Node*s	*Segment*s	*Point*s
BT0	1300 × 800 × 430	30563	42351	763532
BT10	1300 × 800 × 600	48176	61963	1066242
AP0	1800 × 1100 × 600	141296	208408	3177760
AP14	1800 × 1100 × 600	104945	141400	2422580
MT0	1800 × 1100 × 600	136692	205371	3159641
MT14	1800 × 1100 × 600	134288	189124	2986620
AP0a	1300 × 800 × 600	74392	109514	1677365
AP14a	1300 × 800 × 600	54578	73300	1266729
MT0a	1300 × 800 × 600	72299	108822	1673537
MT14a	1300 × 800 × 600	71352	100355	1584008

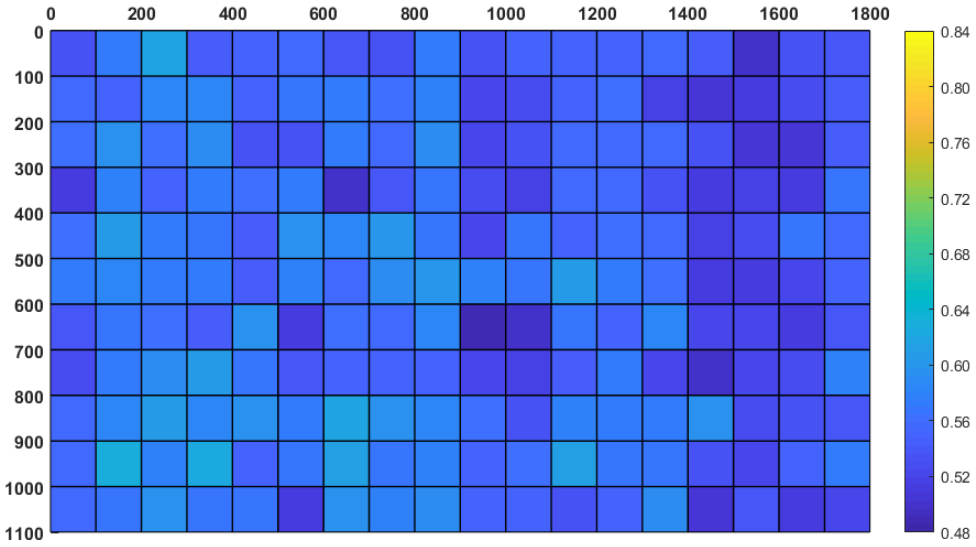

Figure 5.4 Spatial void ratio distribution in structure MT0

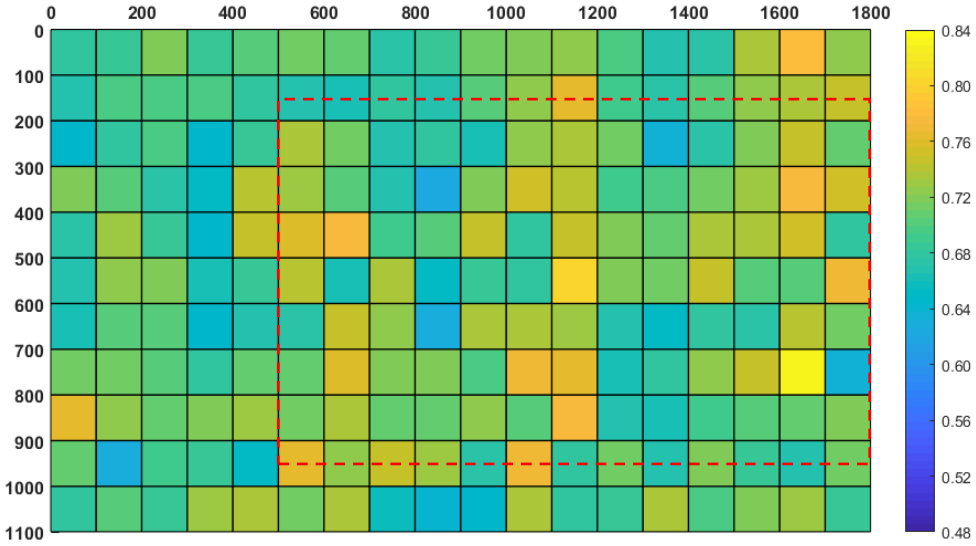

Figure 5.5 Spatial void ratio distribution in structure MT14

5.3 Image-Based Particle Characterization

Separation of particles is realized using the marker-based morphological watershed method. Based on D_{50} of the sand particles and image resolution, the "guard volume" has a characteristic length of 55 voxels for structures BT0 and BT10 containing Ottawa 20-30 sands, and of 45 voxels for structures AP0a, AP14a, MT0a, and MT14a containing Ottawa

30-50 sands. Dimension of the 3-D unbiased counting brick centered at each microstructure volume is defined accordingly (see Table 5.3). Selection of particles for size measurement is achieved by implementing the 3-D unbiased counting rule. As the selected particles in BT0 was previously shown in Figure 3.13, Figure 5.6 - Figure 5.8 visualize the selected particles in the remaining five microstructures under study. The microstructure domain is labelled in orange line and domain of the central brick volume is in green line. Table 5.3 also summarizes the information about the number of separated particles and selected particles for measurement.

Table 5.3 Information for particle characterization

	Central Volume of Counting Brick (voxels)	No. Particles	No. Counted Particles
BT0	1190 × 690 × 320	4210	1872
BT10	1190 × 690 × 490	5557	2687
AP0a	1210 × 710 × 510	11314	6747
AP14a		7931	4283
MT0a		10870	5923
MT14a		12179	7008

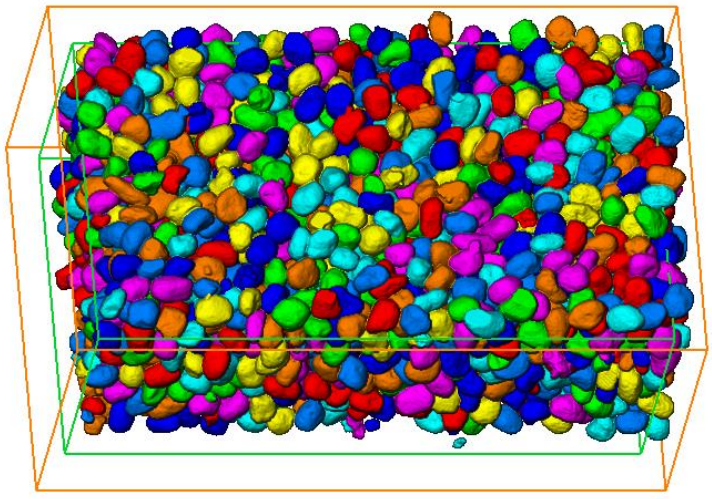

Figure 5.6 Selected particles for measure using 3-D unbiased counting brick in BT10

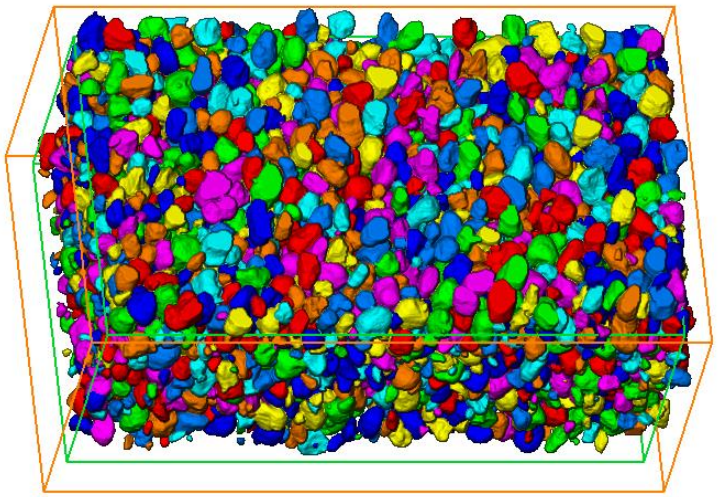

(a)

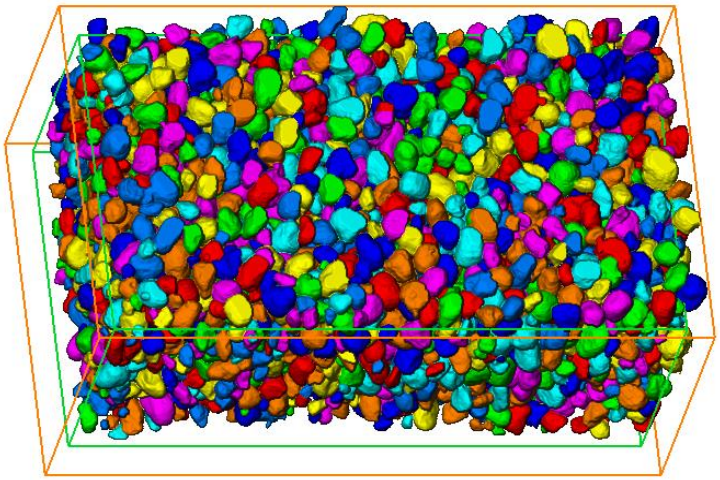

(b)

Figure 5.7 Selected particles for measure using 3-D unbiased counting brick in air-pluviated microstructures: (a) AP0a; (b) AP14a

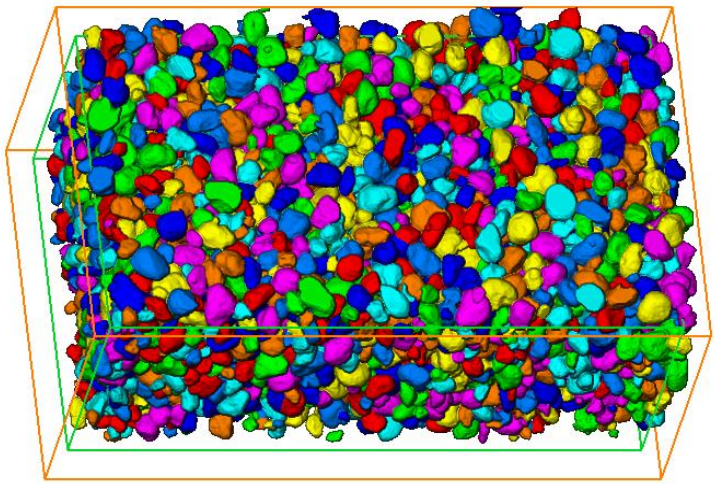

(a)

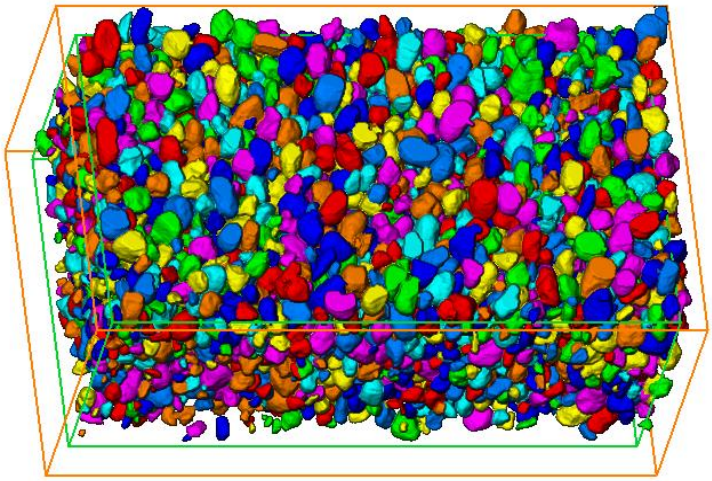

(b)

Figure 5.8 Selected particles for measure using 3-D unbiased counting brick in moist-tamped microstructures: (a) MT0a; (b) MT14a

Comparison of particle size distribution between image-based and sieving methods are conducted. Sieving results are reported from Evans (2005) for BT0 and BT10 on Ottawa 20-30 sands, and from Yang (2005) for AP0, AP14, MT0, and MT14 on Ottawa 30-50 sands. Both "volume equivalent" size and "sieve equivalent" size that were defined in section 3.4.3 are calculated. Figure 5.9 and Figure 5.10 show that the image-based sizes agree with the corresponding sieve size well. The "sieve equivalent" particle size appears

to better match the sieve data. It is noted that the curve for “sieve equivalent” size shifts slightly to the left (finer) than the curve for “volume equivalent” size.

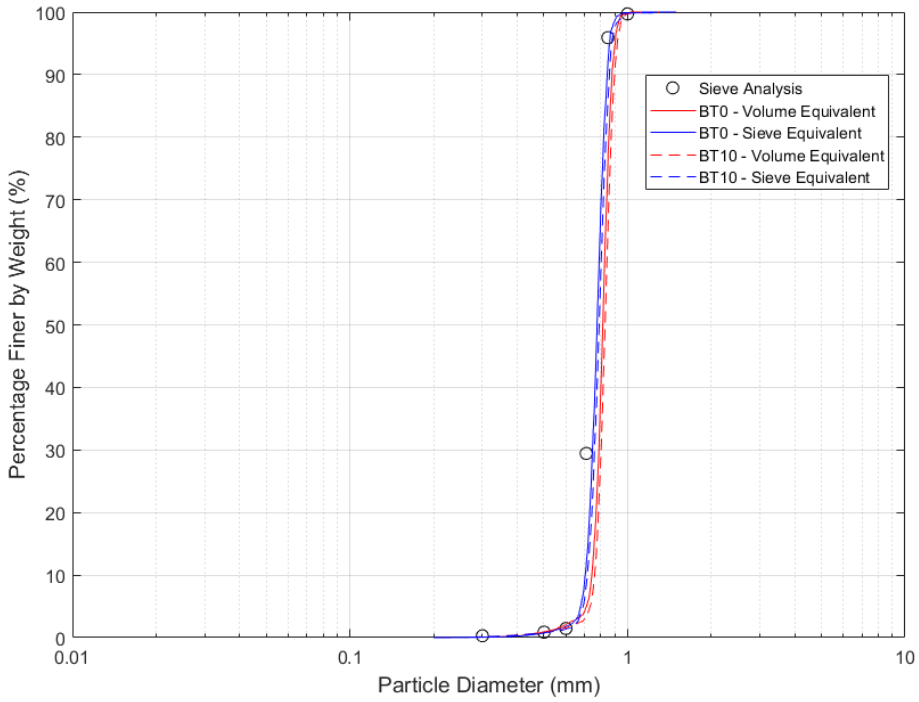

Figure 5.9 Comparison of image-based particle size in BT0 and BT10 with sieving result of Ottawa 20-30 sands

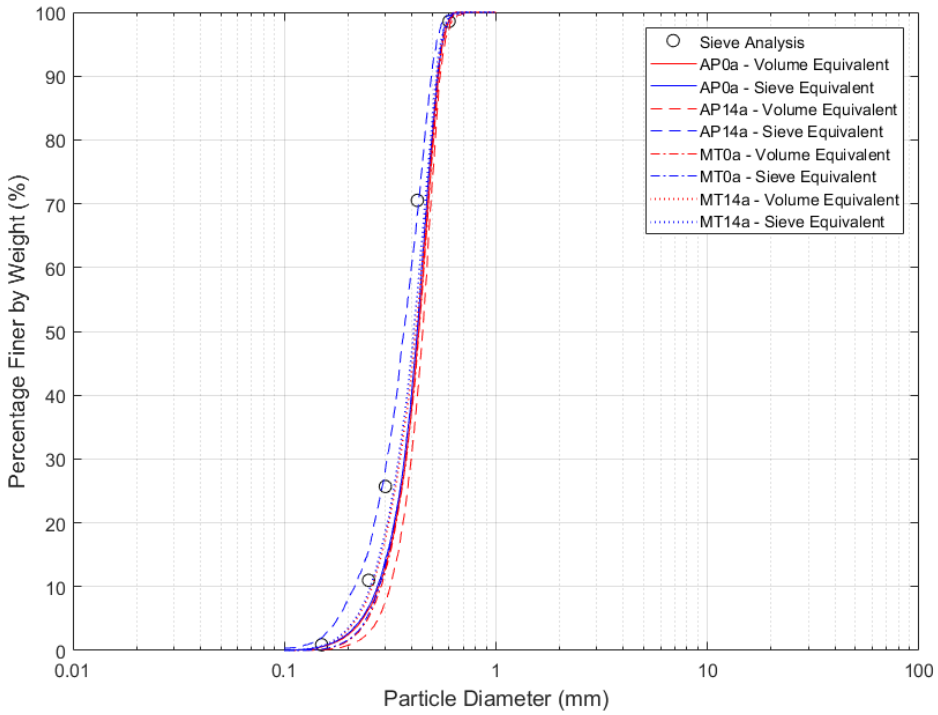

Figure 5.10 Comparison of image-based particle size in AP0a, AP14a, MT0a and MT14a with sieving result of Ottawa 30-50 sands

5.4 Determination of the Largest Analysis Volume

According to the scheme of unbiased 3-D sampling and quantification discussed in section 3.5.6, a largest analysis volume (LAV) domain needs to be defined such that the edge effect with respect to the whole microstructure domain can be properly resolved.

From the computed pore skeleton (see Table 5.2), significant pore paths (*SPP*s) are identified through the trimming process. At the borders of each microstructure volume, incomplete information of the pore structure topology was captured in *SEG_Incomplete* containing the skeletons that intersect the boundary surfaces. Average length of those *Segments* in *SEG_Incomplete* provides a desirable approximation for the characteristic dimension of the "guard volume" at the sides of the LAV. Table 5.4 presents the information of identified *SPP*s, characteristic length of the "guard volume" (termed as

l_guard), as well as the dimension of LAV for the six microstructures. The LAV domain is concentric to the microstructure volume, and prescribes volumetric range for sampling sub-volumes and all the following quantitative characterizations of pore network related metrics. It serves as the largest central brick volume in the unbiased 3-D brick counting if demanded. It can be seen that quantity of *SPP*s, which are in correspondence with pore pathways, is still considerable, particularly the number of *Point*s involved.

Table 5.4 Information of identified *SPP*s and defined LAV dimension

ID	Significant Pore Paths			*l_guard* (voxels)	LAV (voxels)
	*Node*s	*Segment*s	*Point*s		
BT0	12461	22367	518519	40	1220 × 720 × 350
BT10	16244	27962	640249	40	1220 × 720 × 520
AP0a	34848	66398	1257370	30	1240 × 740 × 540
AP14a	18194	34012	794047	35	1230 × 730 × 530
MT0a	35098	67757	1265051	30	1240 × 740 × 540
MT14a	28126	53640	1092527	30	1240 × 740 × 540

5.5 Representative Elementary Volume (REV)

Multiscale investigation invokes the concept of a representative elementary volume (REV), or also called representative volume element (RVE). The REV concept allows the scale-bridging for studies of any materials phenomenon of interest to become computationally practical, and all of the salient characteristics in the microstructures are effectively captured. Non-identical definitions of REV exist in the literature. Classically, REV can be defined as the minimum volume over which a measurement performed can render a result representative of the whole structure (Hill, 1963). With respect to the length scales, it typically requires $l_{micro} \leq l_{REV} \leq l_{macro}$, where l_{micro}, l_{REV}, and l_{macro} denote

the characteristic lengths corresponding to the microscale, the representativity, and the macroscale, respectively (Rozenbaum and Roscoat, 2014). Strategies for determining REV fall into two general categories: one is based on macroscale material parameters (e.g. elastic modulus, conductivity, coefficient of thermal expansion), and is widely seen in continuum mechanics field (Gusev, 1997; Kanit et al., 2003); and the second one is based on micro-to-meso scale parameters like porosity in studying porous media (Razavi et al., 2006; Fernandes et al., 2012; Yang et al., 2015; Mukunoki et al., 2016). Determining the REV is usually not a trivial task and some complications have been disclosed from the perspective of macroscale simulation or microscale characterization. It was stated that the REV size varies for different properties of concern, and thus an adequate methodology was to identify the REV according to their respective distributions over different sampled volumes (Al-Raoush and Papadopoulos, 2010). Besides, computational procedure of identifying the REV could be either "deterministic" or "statistical". The "deterministic" procedure performs sampling at a specified location to evaluate the volume size over which a property of interest remains constant. On the contrary, the "statistical" REV is the volume size beyond which the mean of a property is almost constant while a desired accuracy has been satisfied. The "statistical" procedure would definitely require a larger amount of sampling efforts. Some published research using this procedure considered that the REV could be dependent of the property studied, the desired accuracy, and the number of samples taken (Gusev, 1997; Kanit et al., 2003; Rozenbaum and Roscoat, 2014).

In the current characterization study, executing the developed algorithms for tortuosity estimation and planar surface construction based throat finding on the full dimension of our digital sand microstructures is limited by computational capacity. REV,

therefore, will play a central role on capturing quantitative information of pore structure, and then correlating the information at very different length scales. In the following paragraphs, existence and size of REV will be explored by focusing on realizing its representativeness for pore-scale properties, and incorporating both deterministic and statistical manners. This means that not only different sizes but also different locations are taken into account when sampling. The main motivation is the expectation that an REV that already acquires the major pore-scale characteristics in the sand microstructure will automatically capture all of the pore structure relevant macroscopic properties.

5.5.1 REV Determination Approach

3-D pore-scale characteristics being investigated include porosity, void ratio and specific surface area as standard metrics, as well as geometrical tortuosity, throat size, pore body size, pore body-throat connectivity (i.e. coordination number of pore bodies), and pore channel lengths as five advanced metrics. Throat finding and pore network construction are accomplished using local sphericity (LS) algorithm. To vary sampling locations, a systematic random sampling scheme specifying the centers of the sampled sub-volumes is employed over the microstructure volume. If possible, overlapping of the sub-volumes will be prevented so that a significantly large region out of the whole domain can be considered and sampling efficiency is maximized. At each location, concentric cubic sub-volumes are analyzed with an incrementally increasing edge length: 50 voxels, 70 voxels, 100 voxels, 120 voxels, 150 voxels, 170 voxels, 200 voxels, 220 voxels, 250 voxels, 270 voxels, 300 voxels, 320 voxels, 350 voxels, 370 voxels and 400 voxels. Physical size of a sub-volume is the cubic edge length multiplied by the image resolution.

Because quantifications of the advance pore metrics need to be performed within the range of LAV, the systematic random sampling is designed based on the LAV domain. In this case, the edge length of the sub-volumes may not be able to reach 400 voxels when non-overlapping is strictly enforced in computing the advanced pore metrics. In computing the standard metrics, however, the edge length is increased till reaching 400 voxels where a small overlapping of the sub-volumes can possibly occur. For porosity, void ratio, and specific surface area, a sub-volume is the binary 3-D image data containing pore phase and particle phase; and for tortuosity, a sub-volume is the voxel skeleton data of the pore phase. These are quantified directly on the extracted sub-volumes. For the remaining pore network related metrics, on the other hand, a sub-volume represents the central volume of a 3-D unbiased counting brick. After identifying pore network related features on the whole microstructure by the LS algorithm, the 3-D brick counting rule decides whether a specific profile (throats, pore bodies, or pore channels) is selected to yield a distribution pertaining to that sub-volume.

Each sub-volume will generate one single value for porosity, void ratio or specific surface area, and a distribution for each of the five advanced pore metrics. Consequently, relationships between the value of a standard metric and the sub-volume size are examined. Variation of the statistical parameters of any distribution of the advanced metrics with change of the sub-volume size is explored. Moreover, for the purpose of better describing a distribution, entropy of a distribution histogram H_v (Chen, 2000) is utilized:

$$H_v = -\sum_{i=1}^{n} P_i \log_n(P_i) \tag{2}$$

where n is the number of bins in the histogram and P_i is the probability of the i^{th} bin. If P_i is zero (logarithm is undefined but multiplied by zero), the entire term $P_i \log_n(P_i)$ is taken to be zero. Entropy is a measure of disorder in a system, and its range is between 0 and 1. If a metric is equally distributed among all bins in a histogram, H_v is equal to 1; and if a metric is in a single bin, H_v will be 0. Having the same parametric setting in plotting histograms, entropy enables a better comparison regarding the shape of histograms.

The convergence criteria to validate the REV are considered as follows:

1. Porosity, void ratio, or specific surface area converges to the reference value that is estimated from the whole 3-D microstructure volume, and remains nearly constant beyond the REV size. Also, values among the sub-volumes sampled from different locations converge to each other.
2. For the distribution of throat size, pore size, coordination number of pore bodies, or pore channel length, statistical parameters including mean, standard deviation, coefficient of variation (CV) and entropy that are estimated on the LAV are the reference values. As size of the sampled sub-volumes increases, these statistical parameters converge to their respective reference values, and become nearly constant beyond the REV size. Relative variation among different sampling locations decreases, and converging is finally realized.
3. For the distribution of geometrical tortuosity, computation based on the developed pure voxel-based algorithm requires high RAM to store the big adjacency matrix. So its computation on the voxel skeleton of the LAV is not practical currently, and the reference value is not estimated. However, values of the statistical parameters

used in criterion 2, as well as their relative variation among different sampling locations still need to show a tendency of convergence beyond the REV size.

4. After applying criteria 1 - 3 on the systematic randomly sampled sub-volumes, sub-volumes are sampled from three additional locations over the microstructure volume. The distribution histograms are generated for the advanced pore metrics. At any location, histograms should demonstrate a converging trend as size of the sub-volumes increases. And beyond the REV size, histogram should demonstrate limited divergence among different locations. Since histogram itself contains richer information than examining the above statistical parameters solely, this criterion is a post-validation step.

5.5.2 REV of Digital Sand Microstructures

BT0 microstructure is taken as an example to illustrate the application of the above criteria for its REV determination. Over the LAV, six locations are selected to generate the concentric cubic sub-volumes. As shown in Figure 5.11(a), the determined LAV domain only allows the cubic edge length up to 350 voxels for a sub-volume in computing the advanced pore metrics. By expanding the sub-volumes further until the cubic edge length reaches 400 voxels, small overlapping of those sub-volumes in computing the standard pore metrics is shown in Figure 5.11(b). In the figure, within the whole microstructure domain (orange solid line), the LAV domain is labelled in red solid line and the sub-volume domains are in green solid line with the six different regions denoted as (I) - (VI). The concentric sub-volumes of varying edge lengths are depicted at region (IV). Figure 5.12 and Figure 5.13 visualize pore structure and voxel skeleton of the sub-volumes at this region, respectively. Note that Figure 5.13 does not show the pore skeleton of the sub-

volume with an edge length of 400 voxels, and results of the five advanced metrics for the sub-volumes of this size are not included in the discussions below.

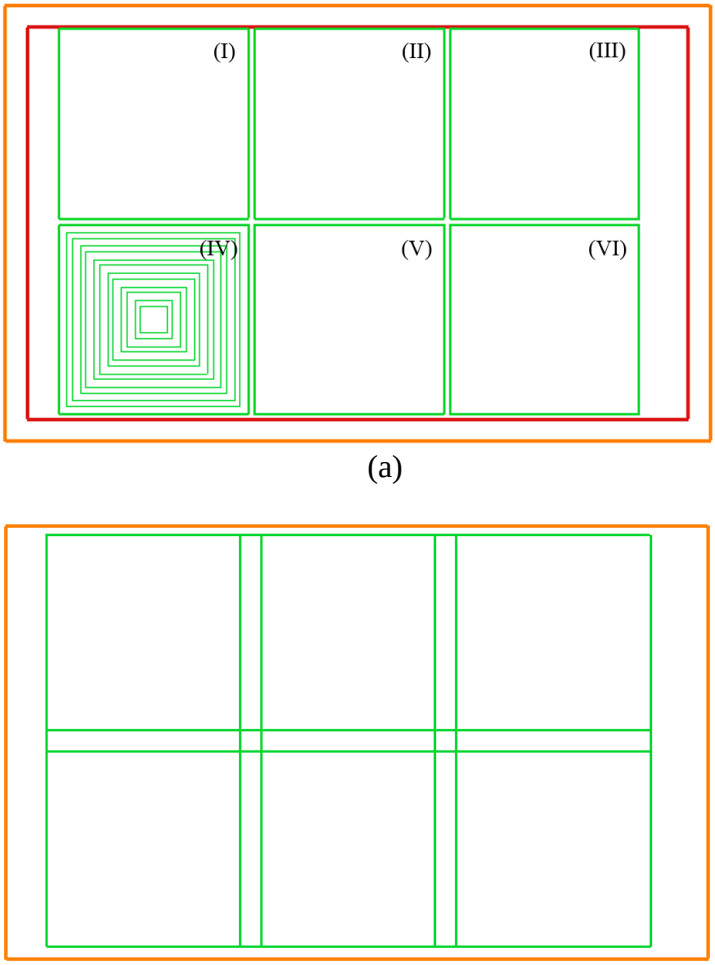

Figure 5.11 A planar view of the systematic random sampling scheme showing the largest sub-volumes: (a) non-overlapping sub-volumes for advanced pore metrics within the LAV; (b) partial overlapping sub-volumes for standard pore metrics

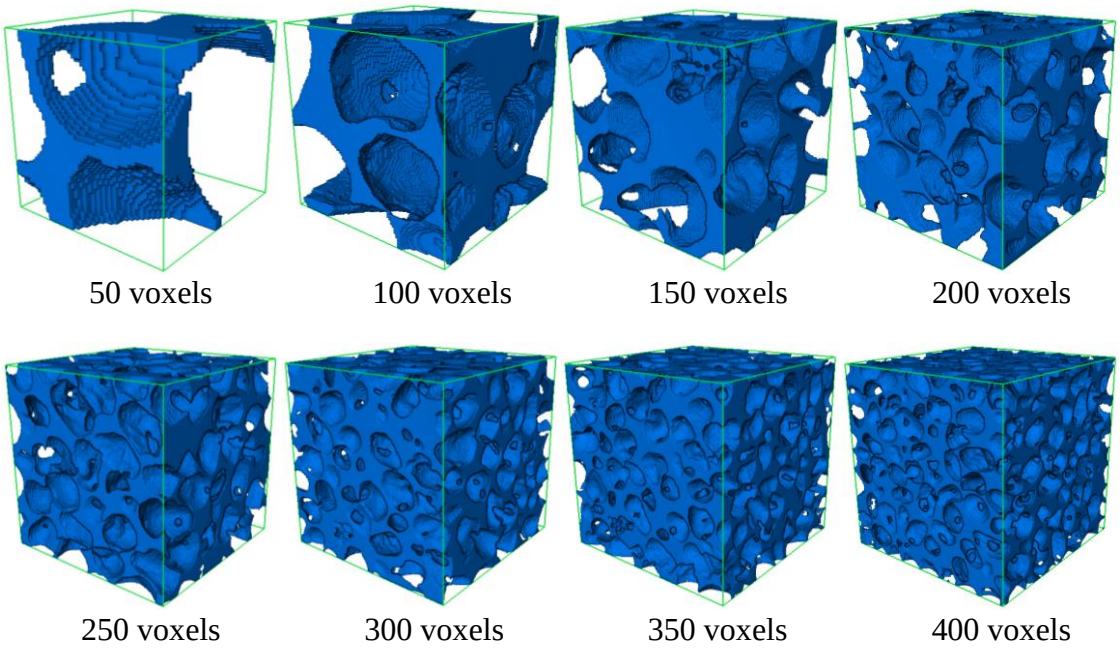

Figure 5.12 3-D images of pore structure for a sequence of concentric cubic sub-volumes with varying edge lengths

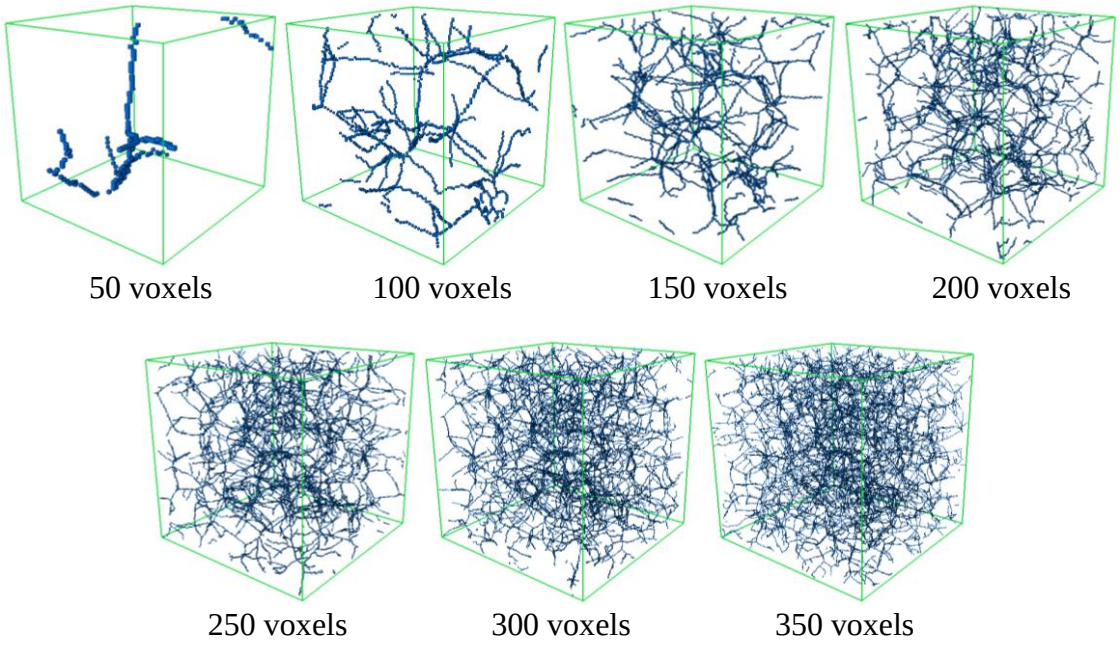

Figure 5.13 3-D images of voxel skeleton for a sequence of concentric cubic sub-volumes with varying edge lengths

Figure 5.14 presents the analyzed porosity, void ratio and specific surface area from the six locations for various sub-volume sizes. The results are plotted in red or blue solid,

dashed and dotted lines representing the different sampling regions. The reference value computed on the whole 3-D microstructure volume is indicated with the horizontal green dashed line. The starting value of any metric varies a lot among different locations. But it is convergent to the reference value upon growth of the sub-volume size, and the relative difference has a trend to decrease. Based on the convergence criteria, REV exists for these pore metrics, but the REV sizes are different. It is indicated that the cubic edge length of REV for porosity is 250 voxels, for void ratio is 270 voxels, and for specific surface area is 220 voxels. For advanced pore metrics, Figure 5.15 and Figure 5.16 show the changes of major statistical parameters of their distributions as the sub-volume size increases. All plots use the same legend as that annotated in Figure 5.14 for the results at different locations. A tendency of convergence towards the reference value can be observed for each of the pore network related metrics, and a clear decreasing trend in the relative difference among different locations. Considering the four statistical parameters inclusively, REV for throat size is a cubic length of 250 voxels, for pore body size is 250 voxels, for pore body-throat connectivity is 220 voxels, and pore channel length is 250 voxels. On the contrary, the tendency of convergence regarding tortuosity is not very clear. Fluctuation in the statistical parameters describing the tortuosity distribution, and their relative variations among different locations can be observed noticeably, especially in the distribution entropy. Therefore, the existence of an REV for tortuosity at least up to the sub-volumes with an edge length of 350 voxels in the present study is in doubt. Further studies on larger sub-volumes are recommended for future.

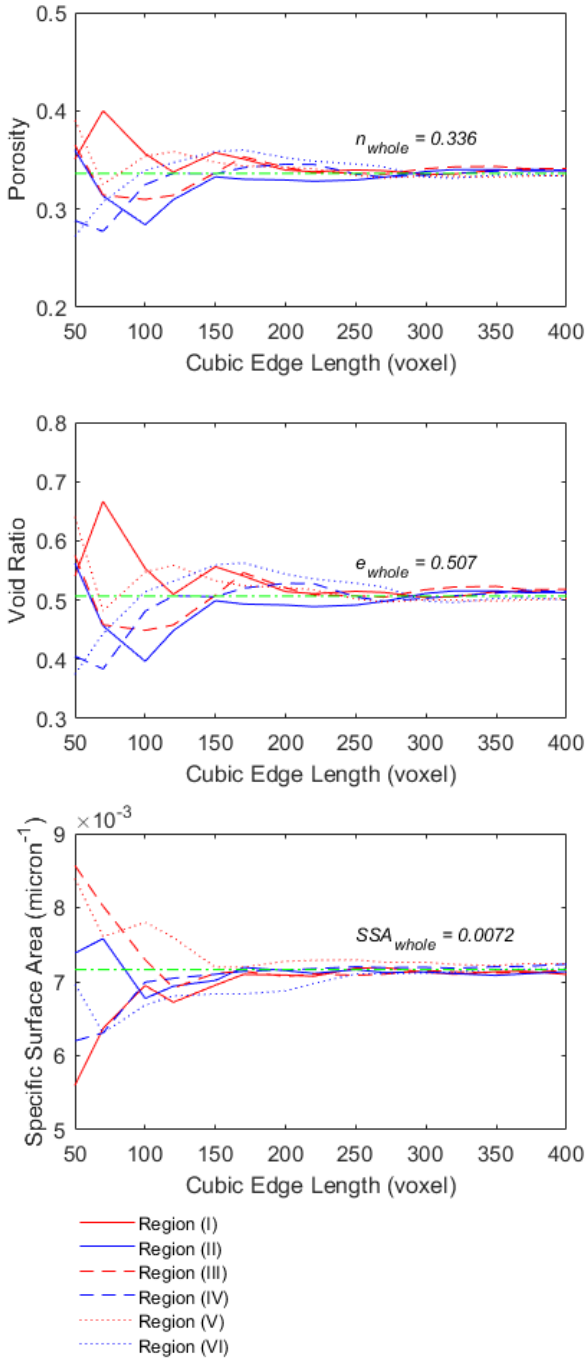

Figure 5.14 Variation of standard pore metrics with change of sub-volume size in different regions of BT0

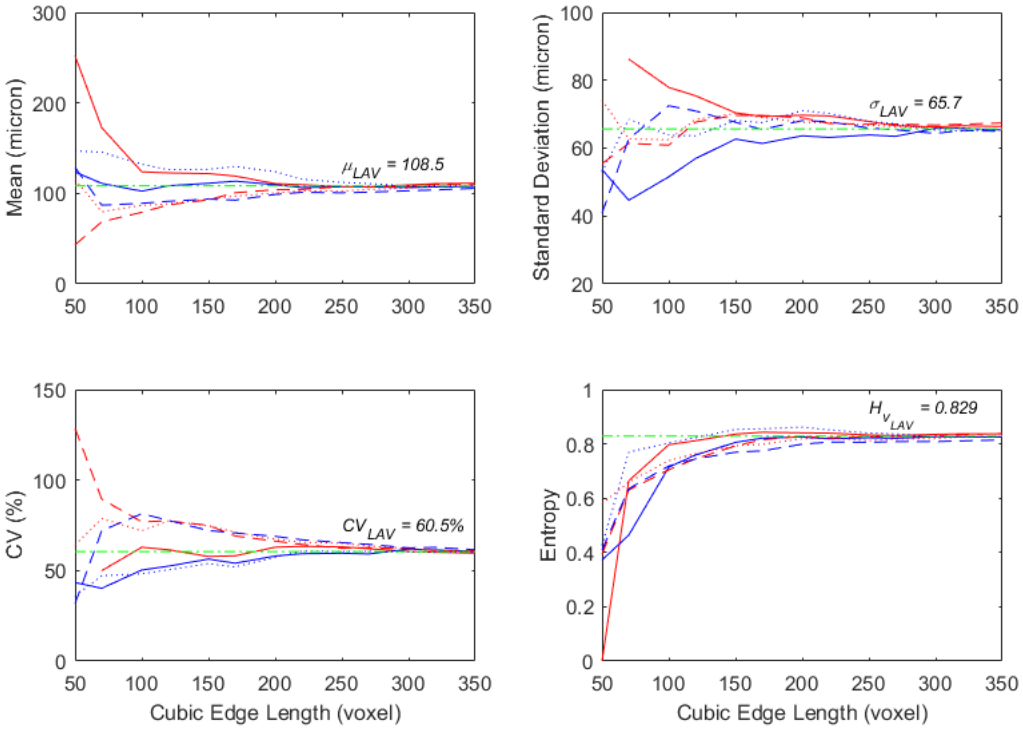
Mean (micron)
μ_{LAV} = 108.5
Standard Deviation (micron)
σ_{LAV} = 65.7
CV (%)
CV_{LAV} = 60.5%
Entropy
$H_{v_{LAV}}$ = 0.829
Cubic Edge Length (voxel)
Cubic Edge Length (voxel)

(a)

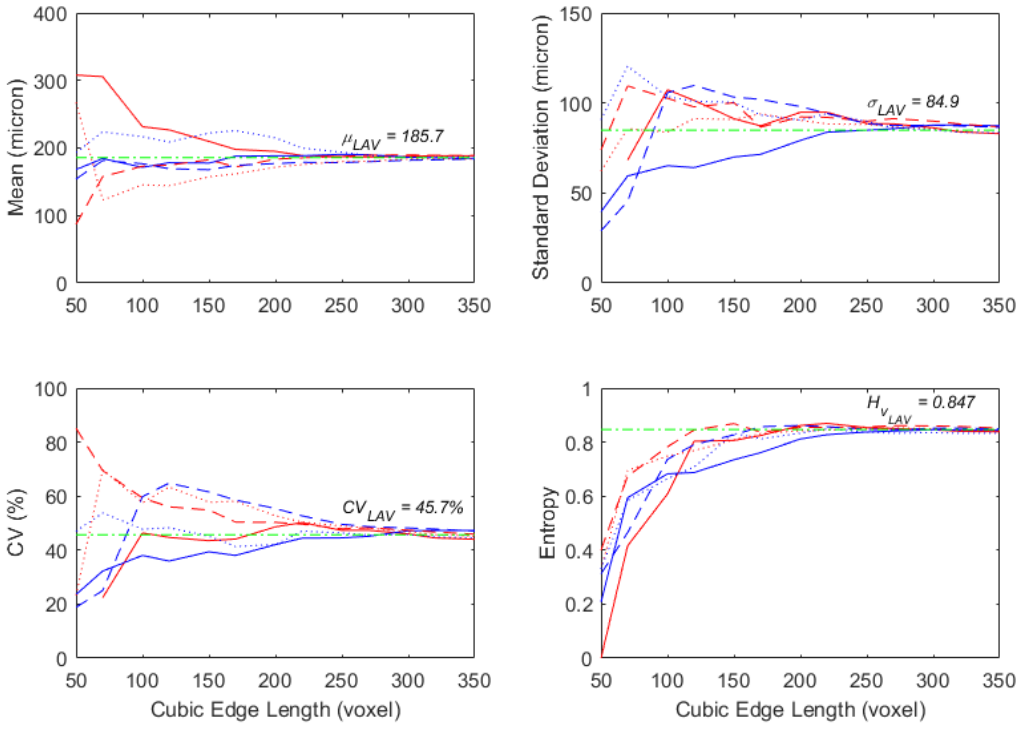
Mean (micron)
μ_{LAV} = 185.7
Standard Deviation (micron)
σ_{LAV} = 84.9
CV (%)
CV_{LAV} = 45.7%
Entropy
$H_{v_{LAV}}$ = 0.847
Cubic Edge Length (voxel)
Cubic Edge Length (voxel)

(b)

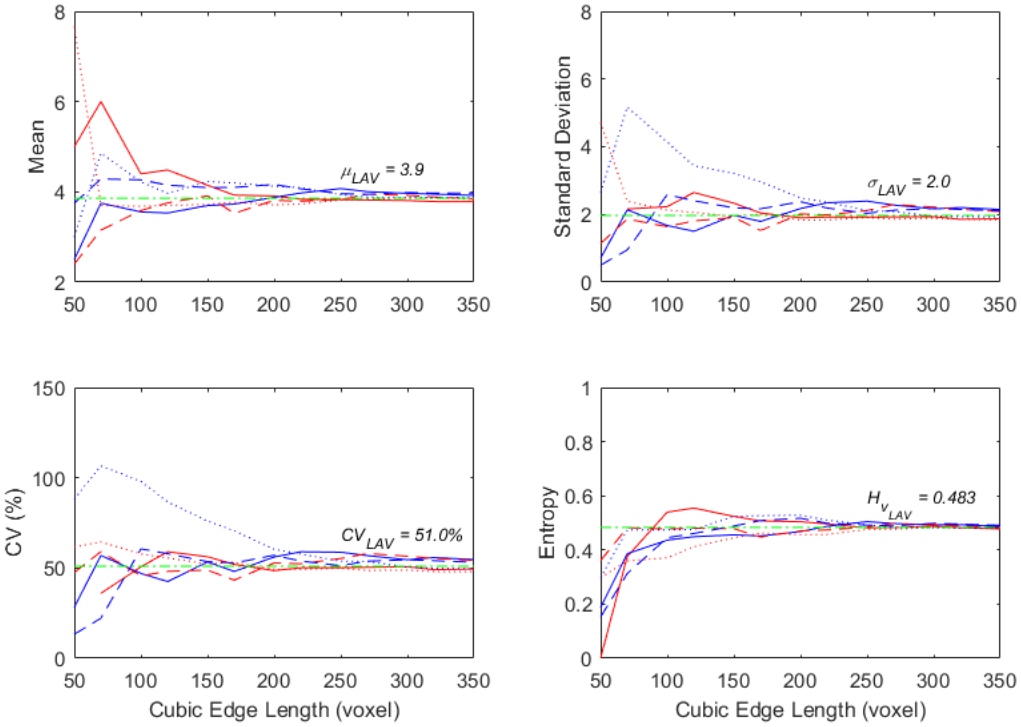

(c)

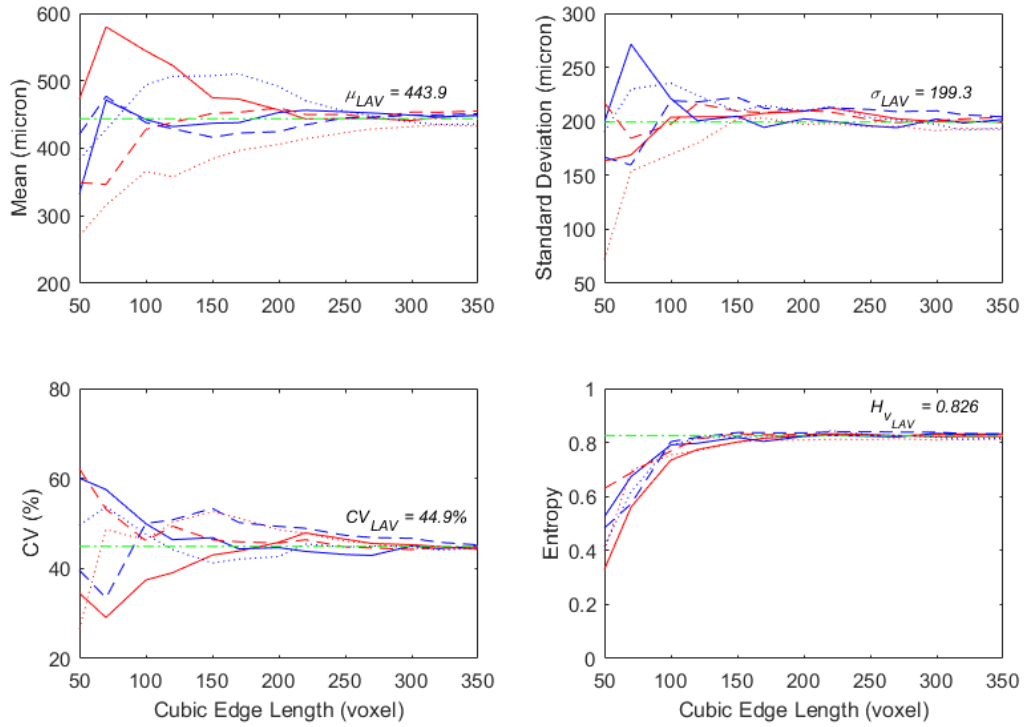

(d)

Figure 5.15 Variation of descriptive parameters for distributions of pore network related metrics with change of sub-volume size in different regions of BT0: (a) throat size; (b) pore body size; (c) coordination number of pore bodies; (d) pore channel length

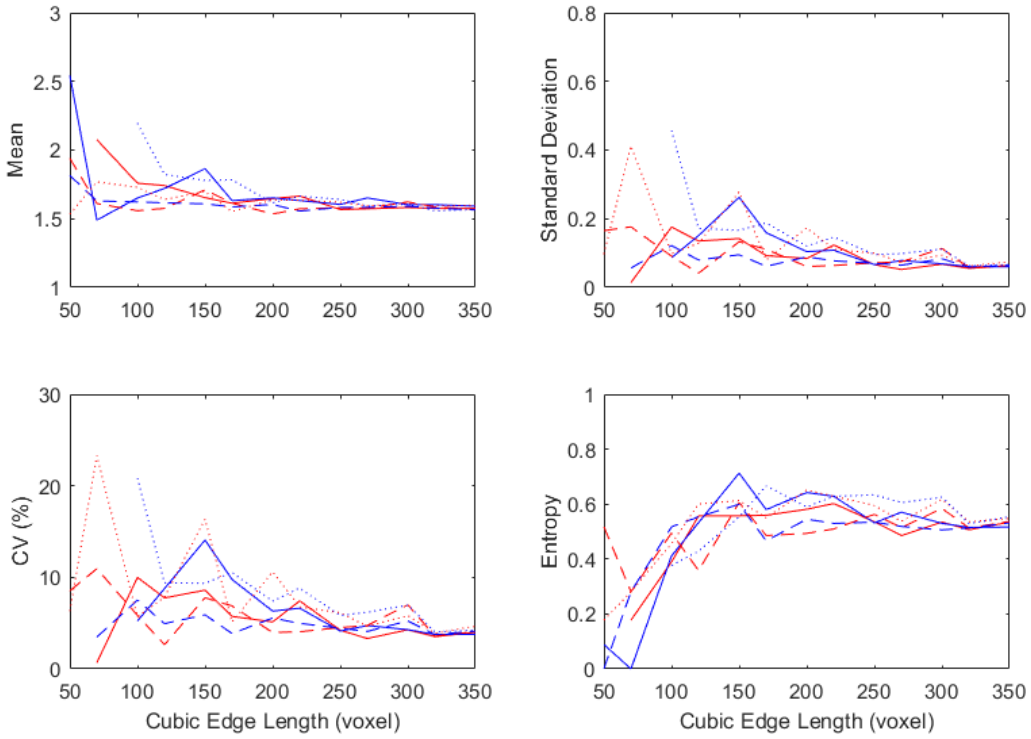
Mean
Standard Deviation
CV (%)
Entropy
Cubic Edge Length (voxel)
Cubic Edge Length (voxel)

(a)

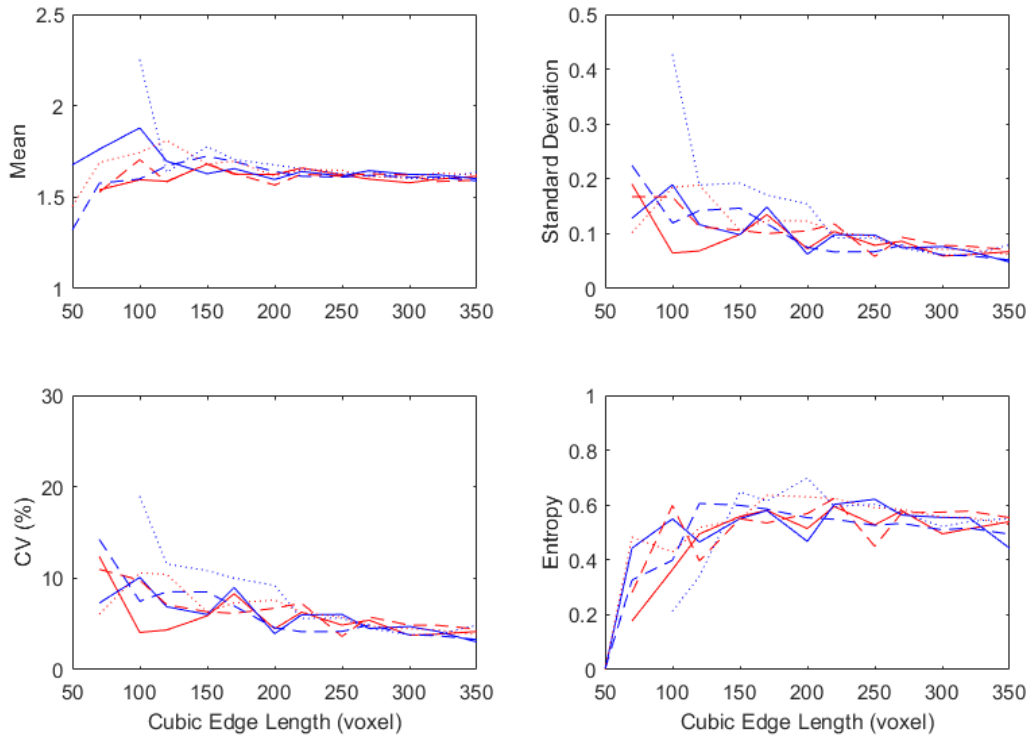
Mean
Standard Deviation
CV (%)
Entropy
Cubic Edge Length (voxel)
Cubic Edge Length (voxel)

(b)

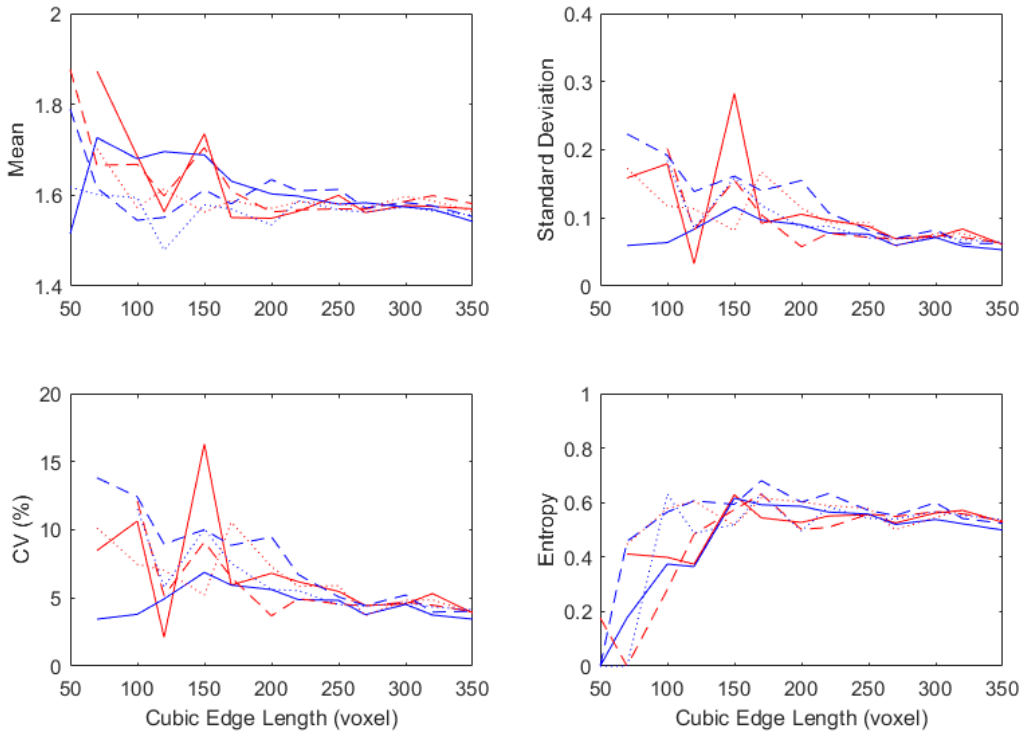

(c)

Figure 5.16 Variation of descriptive parameter for tortuosity distribution with change of sub-volume size in different regions of BT0: (a) Tortuosity along positive *X* direction; (b) Tortuosity along positive *Y* direction; (c) Tortuosity along positive *Z* direction

Existence of REV and REV size identified above for the advanced pore metrics are verified by sampling sub-volumes from three additional locations (Figure 5.17), which can be simply designated as "Left", "Center", and "Right". Distributions of the advanced pore metrics are plotted for different sub-volume sizes at the "Center" location in Figure 5.18 - Figure 5.24. Histograms of throat size, pore size, coordination number of pore bodies, and pore channel length suggest the convergent trend specifically after the cubic edge length increases to 250 voxels, which is approximately consistent with the REV size determined from examining the variations of the statistical parameters. Figure 5.25 - Figure 5.28 demonstrate the high similarity in the distributions among the three locations when the edge length of the sub-volumes is 300 voxels. On the other hand, no convergent trend is

found in the histograms of tortuosity when the sub-volume size increases in Figure 5.22 - Figure 5.24, and divergence at different locations is also well discerned in Figure 5.29. Besides the analyzing results for the statistical parameters of tortuosity distribution, this implies again that it is not able to select an adequate REV for geometrical tortuosity in the present study.

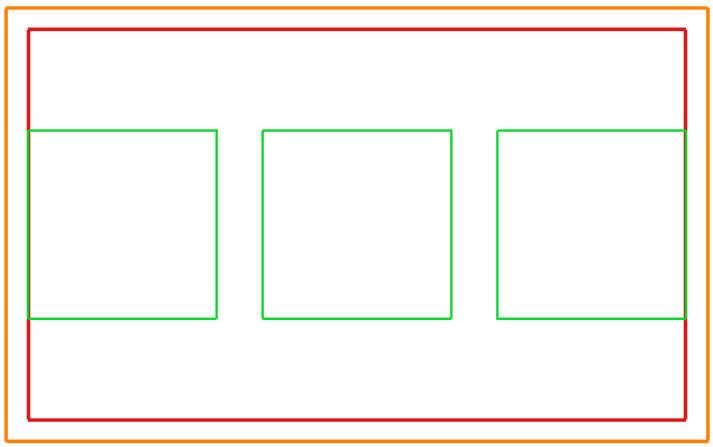

Figure 5.17 A planar view of the largest sub-volumes sampled from three additional locations within the LAV

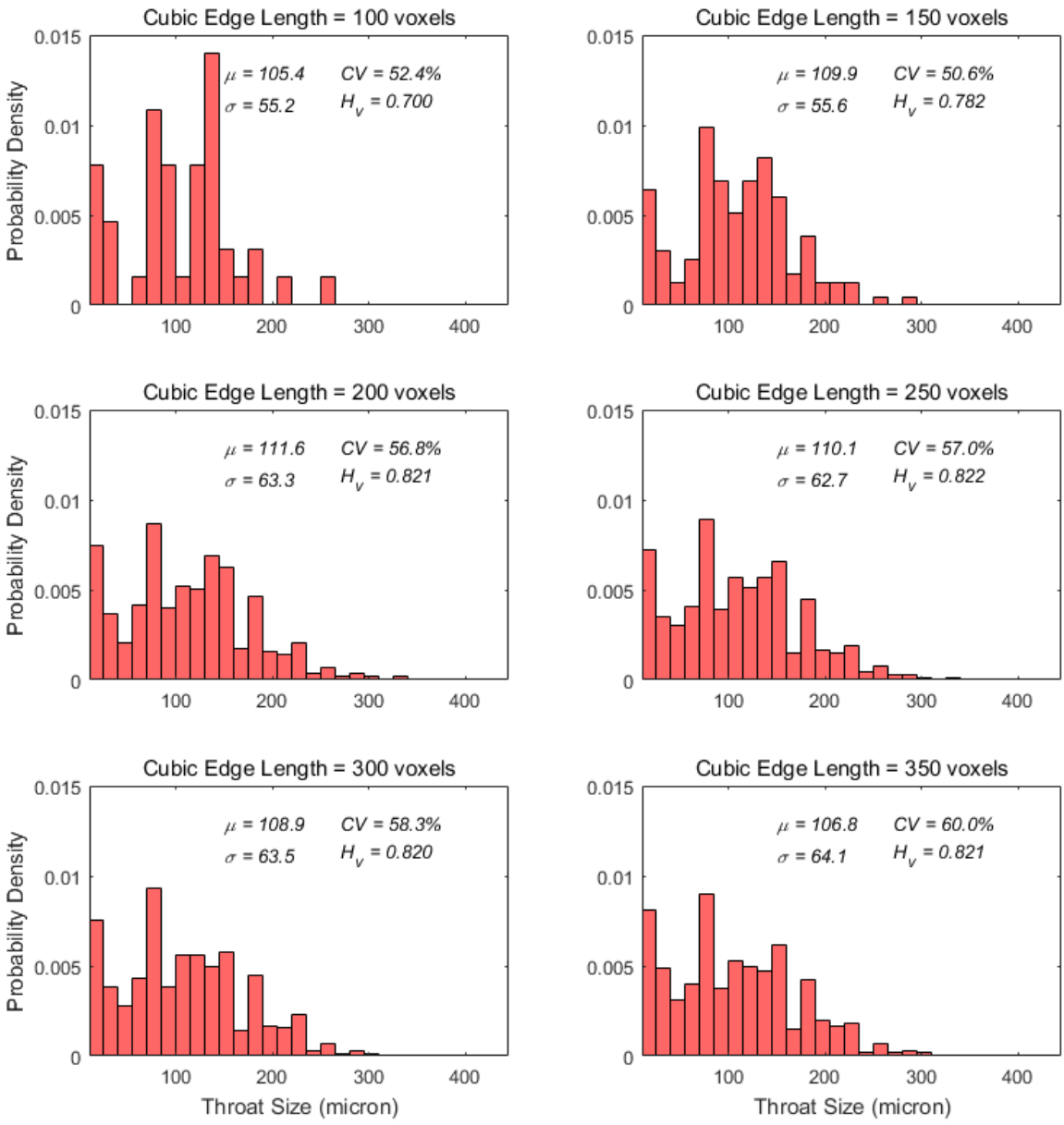

Figure 5.18 Distribution of throat size for sub-volumes at the “Center” location

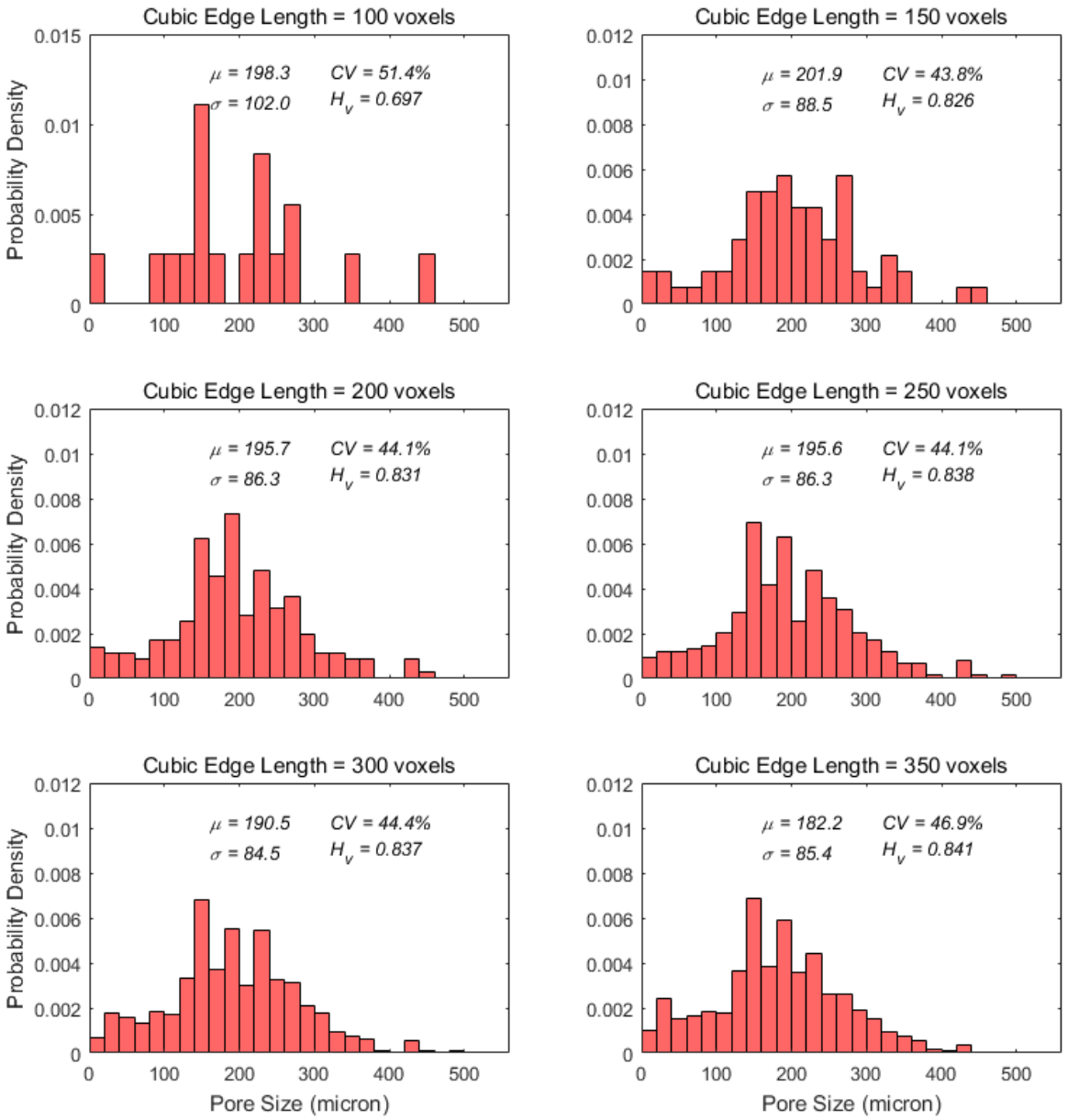

Figure 5.19 Distribution of pore body size for sub-volumes at the “Center” location

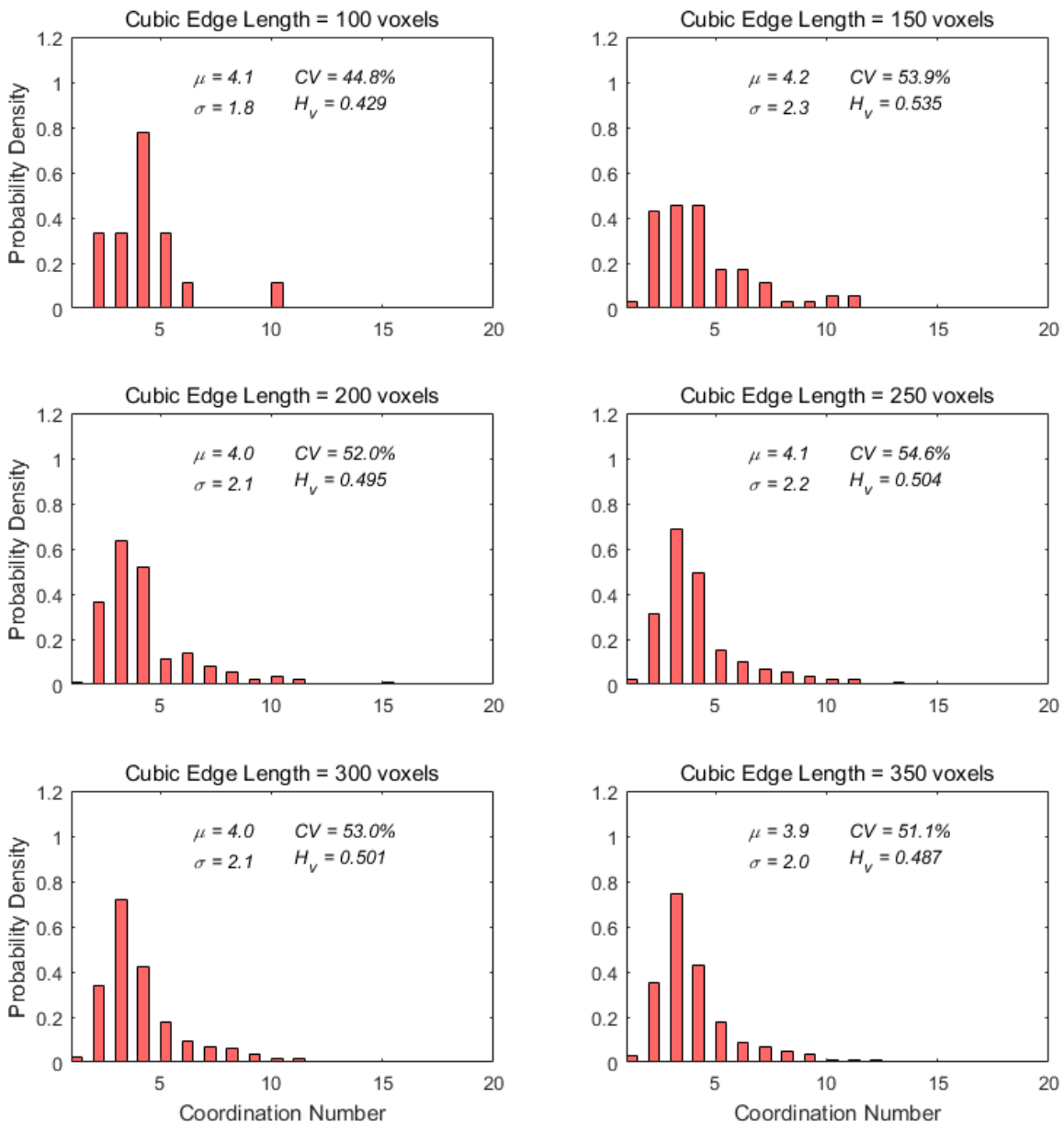

Figure 5.20 Distribution of coordination number of pore bodies for sub-volumes at the "Center" location

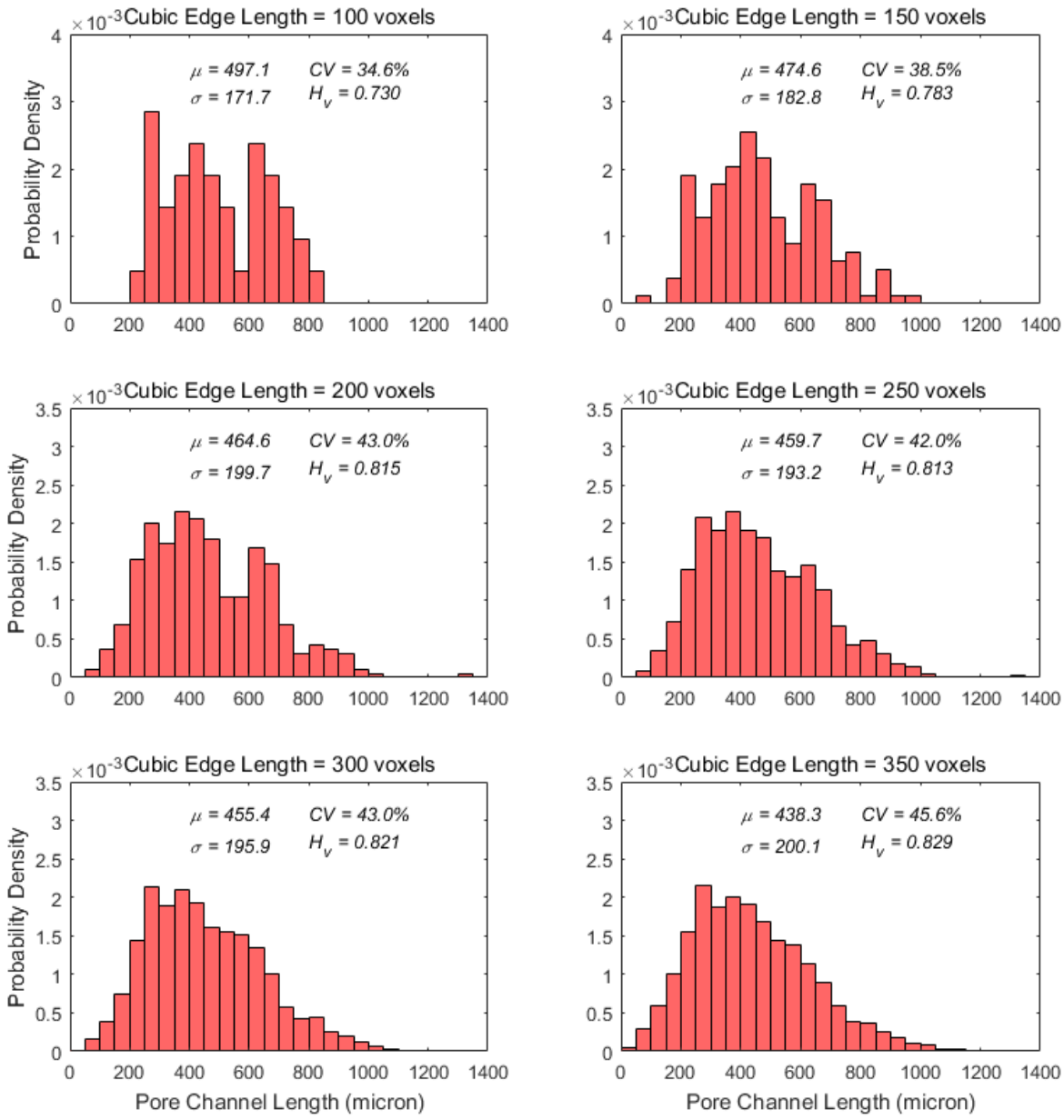

Figure 5.21 Distribution of pore channel length for sub-volumes at the “Center” location

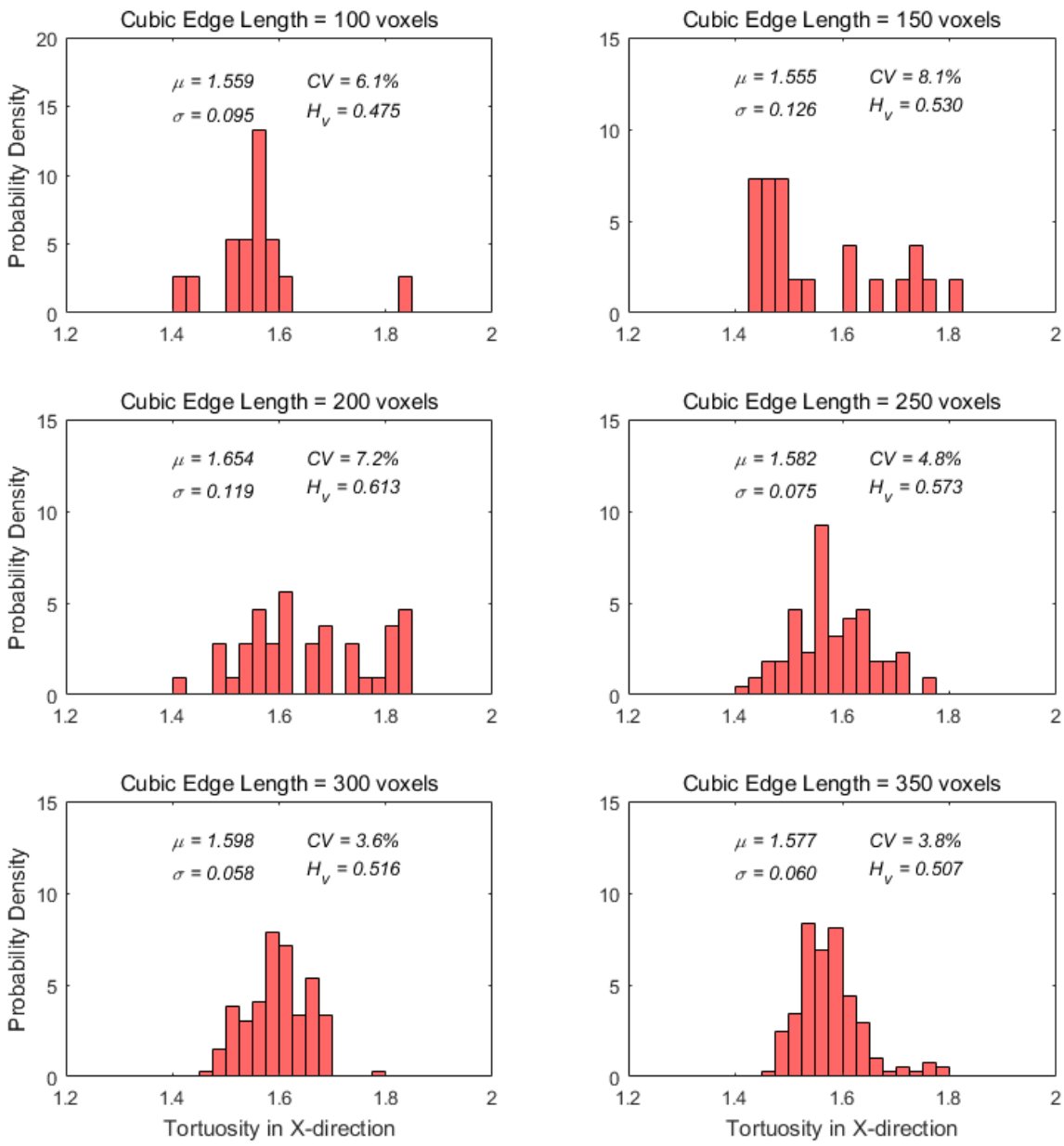

Figure 5.22 Distribution of tortuosity along positive *X* direction for sub-volumes at the "Center" location

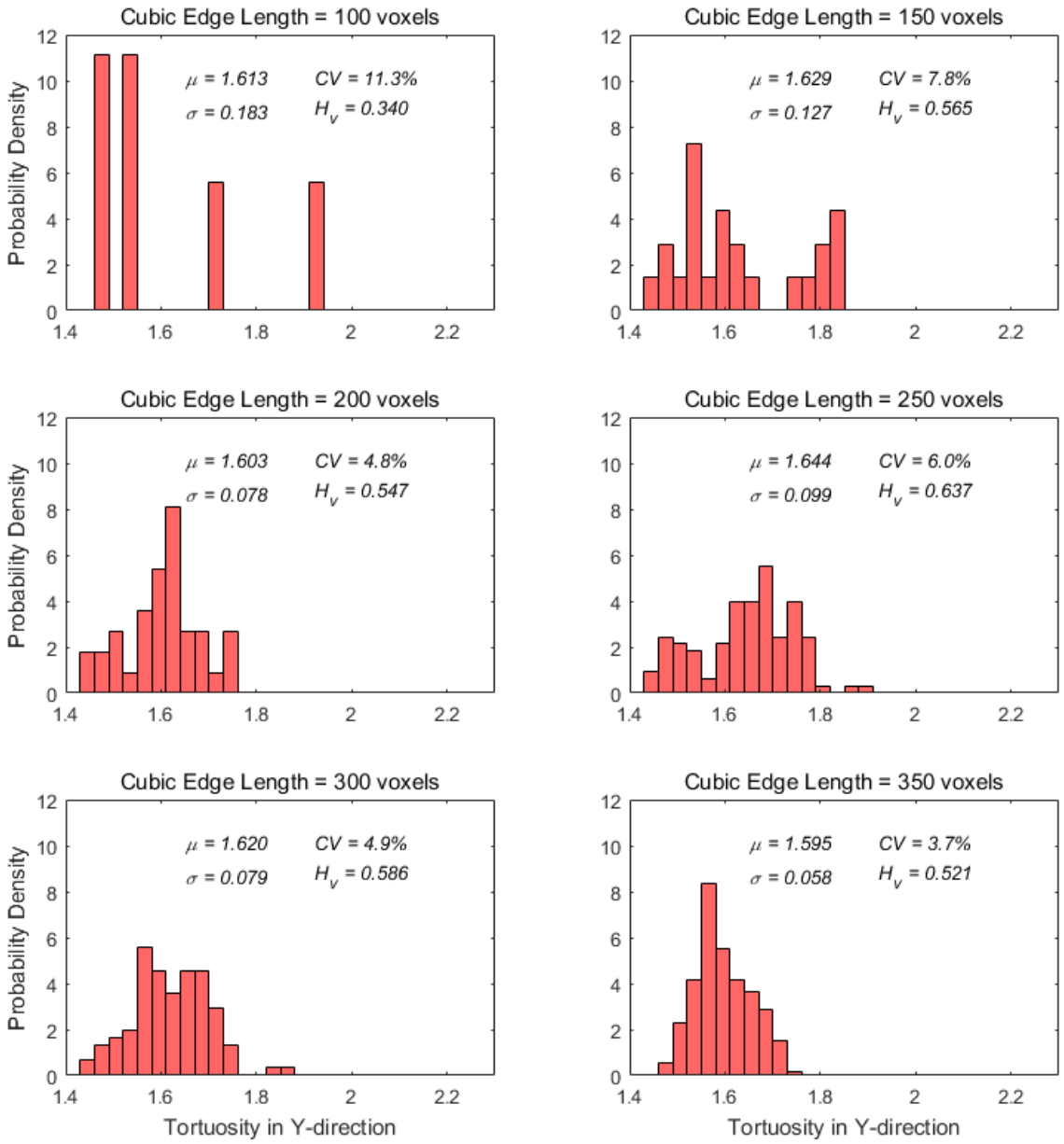

Figure 5.23 Distribution of tortuosity along positive *Y* direction for sub-volumes at the "Center" location

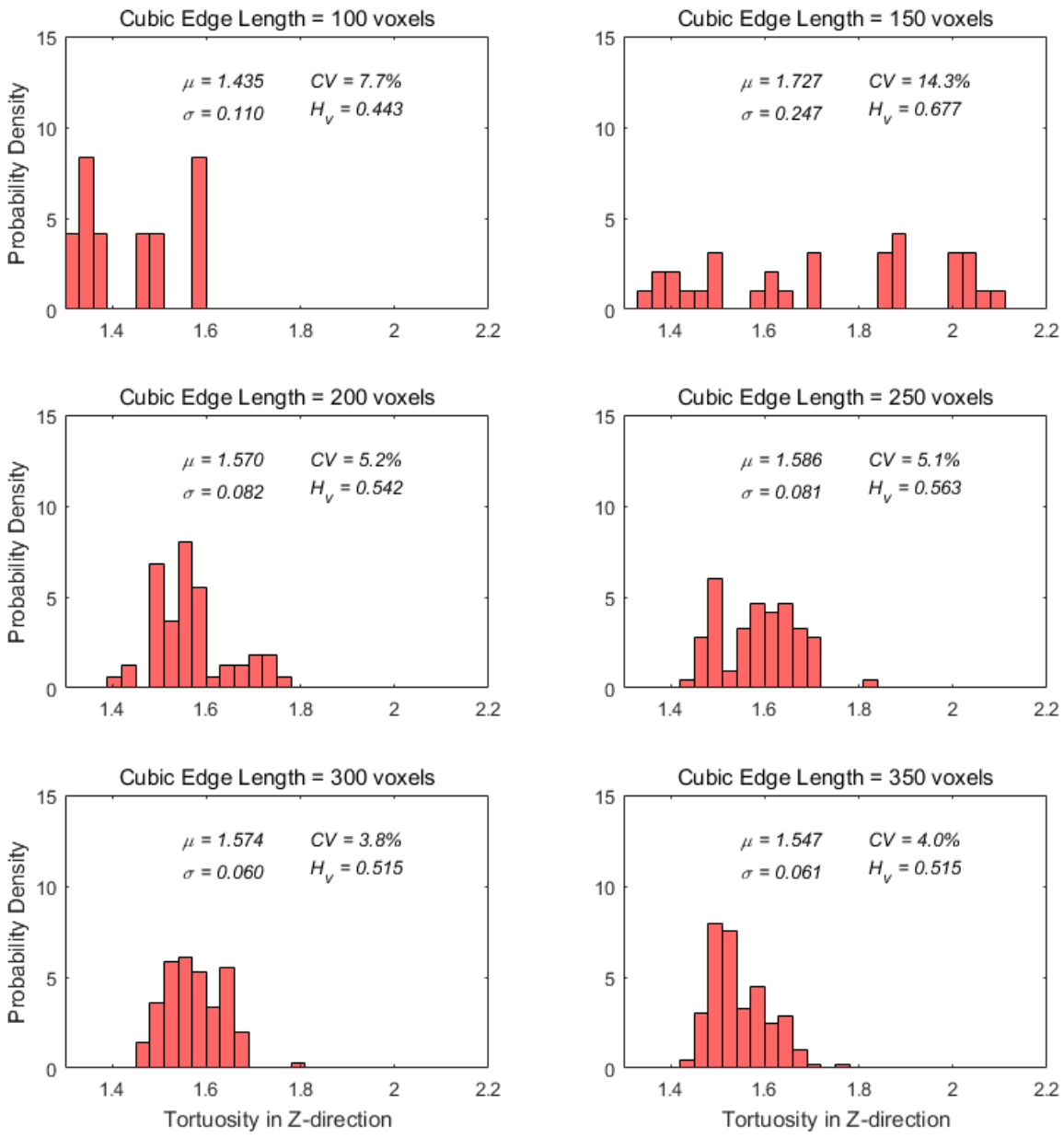

Figure 5.24 Distribution of tortuosity along positive *Z* direction for sub-volumes at the "Center" location

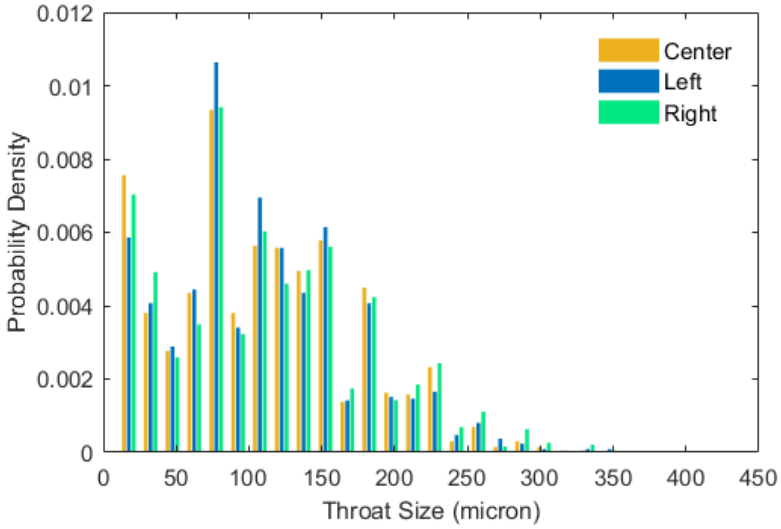

Figure 5.25 Distributions of throat size for sub-volumes with edge length of 300 voxels

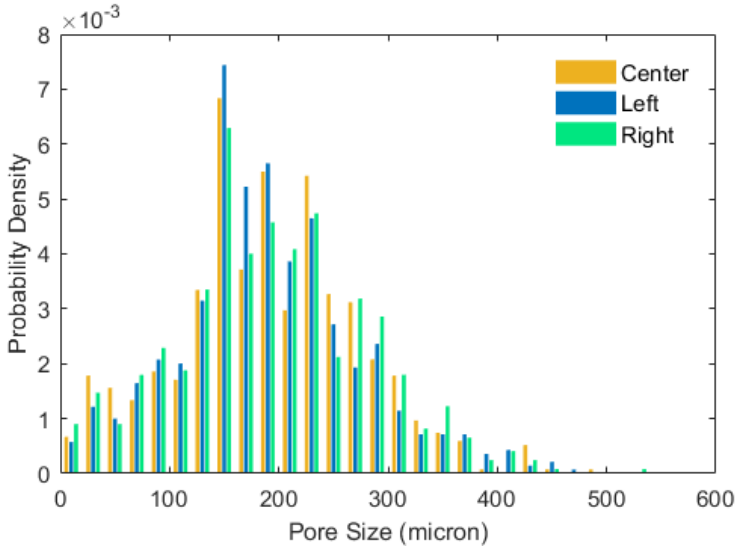

Figure 5.26 Distributions of pore body size for sub-volumes with edge length of 300 voxels

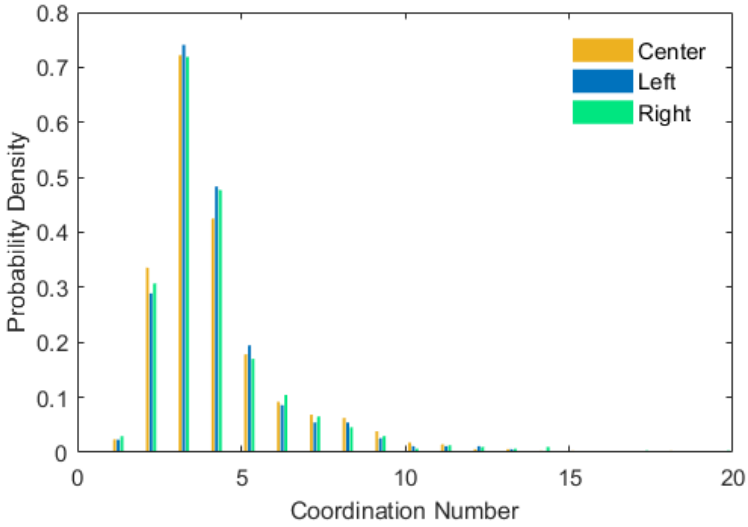

Figure 5.27 Distributions of coordination number of pore bodies for sub-volumes with edge length of 300 voxels

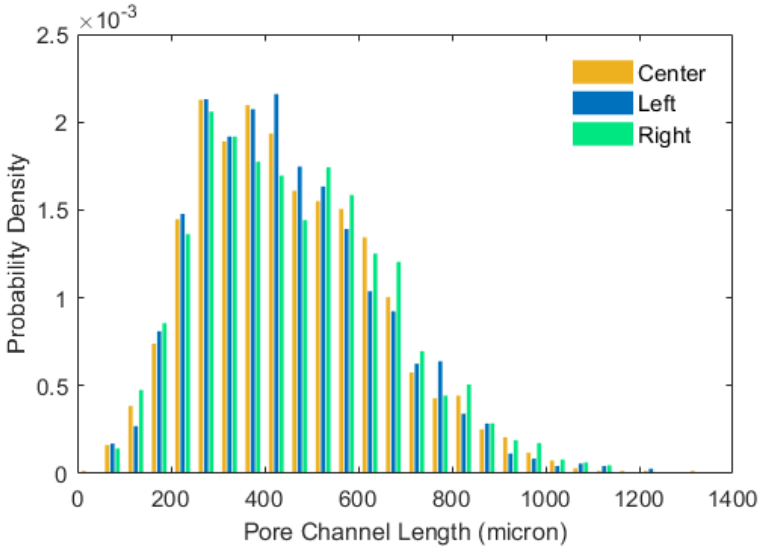

Figure 5.28 Distributions of pore channel length for sub-volumes with edge length of 300 voxels

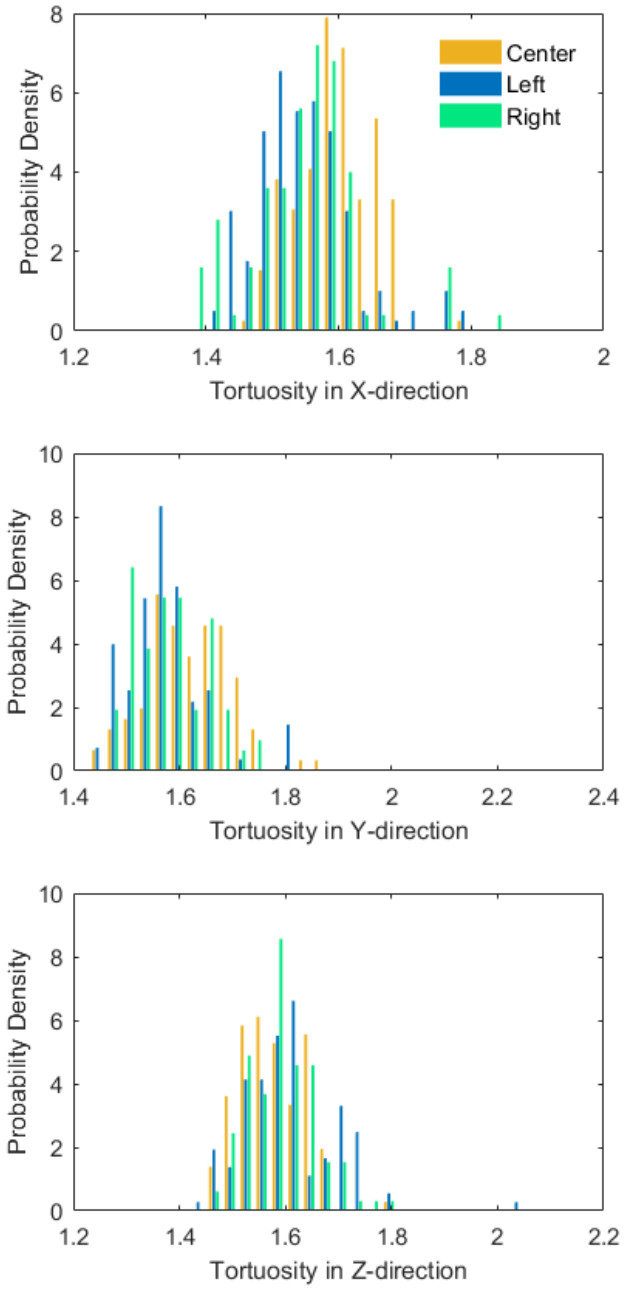

Figure 5.29 Distributions of tortuosity for sub-volumes with edge length of 300 voxels

This REV study proves that REV indeed depends on the considered properties of the porous media. Combing the results, a cubic sub-volume with an edge length of 300 voxels can be deemed as an overall REV for structure BT0 to evaluate most pore structure characteristics except geometrical tortuosity. Because tortuosity is computed by searching on a graph constructed from the pore skeleton structure, size and location of the sub-volumes can have significant influence on the pore skeleton structures being examined as those shown in Figure 5.13, and consequently adjacency feature of voxels on the skeleton, graph construction, as well as the shortest path search. Figure 5.30 visualizes the tortuous paths along positive *Z* direction searched from the voxel skeleton structures in Figure 5.13. The starting voxels on the entry/exit surfaces change, and so do the tortuous paths. So, instead of estimating the tortuosity through extracting one well-defined REV, a statistical way can be considered by taking several measurements on small, randomly sampled sub-volumes. Detailed discussions will be provided in the next section.

As presented above, REV size can be expressed as the edge length of the representative cubic sub-volume. Using the same procedure, REV can be investigated on AP0a and MT0a. Table 5.5 provides determined REV for the Ottawa sand microstructures under study, including its size for every individual pore metric and an adequate overall size without taking tortuosity into consideration. For BT0, the ratio of its REV size to D_{50} of Ottawa 20-30 sands is about 5.68. REV size for the pore-scale characteristics in AP0a is estimated to be 250 voxels, approximately 5.71 times D_{50} of Ottawa 30-50 sands. REV size of MT0a is taken to be the same as that of AP0a. The REV, determined from the unsheared microstructure, will be applied in analyzing the sheared counterpart in each pair.

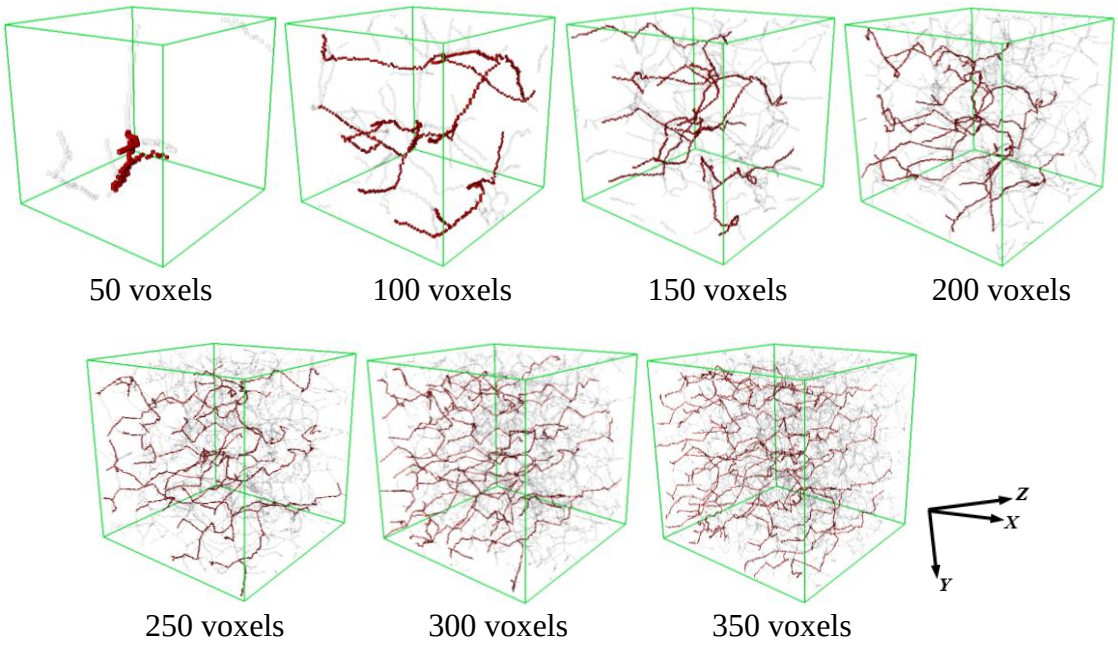

Figure 5.30 Computed tortuous paths along positive *Z* direction from the voxel skeleton structures shown in Figure 5.13

Table 5.5 Results of the REV determination

Items	BT0	AP0a	MT0a
	REV (voxel)	REV (voxel)	REV (voxel)
Porosity	250	220	220
Void Ratio	270	220	250
Specific Surface Area	220	220	200
Tortuosity (positive *X*)	n/a	n/a	n/a
Tortuosity (positive *Y*)	n/a	n/a	n/a
Tortuosity (positive *Z*)	n/a	n/a	n/a
Throat Size	250	220	220
Pore Body Size	250	220	220
Pore Body-Throat Connectivity	220	170	220
Pore Channel Length	250	170	200
Overall	300	250	250

5.6 Shear-Induced Pore Structure Evolution

5.6.1 Characterization of Biaxial Sand Structures

Comparative studies between the unsheared and the sheared biaxial microstructures concentrate on analyzing spatial distribution of geometrical tortuosity and characteristics of pore network. Shear band observed in structure BT10 was shown in Figure 5.1(b). Because an adequate REV size for tortuosity was difficult to identify according to the discussion in Section 5.5.2, tortuosity computation is performed on sets of random small sub-volumes sampled from the voxel skeleton within the LAV domain (see Table 5.4).

Characterizing pore structures from the pore network perspective involves both local sphericity (LS) method and planar surface construction (PSC) method based throat finding and pore topology investigations. LS method concerns the LAV as well as the REV. A cubic sub-volume with an edge length of 300 voxels is sampled from the center of BT0 (BT0_Center), inside the shear zone of BT10 (BT10_Inside), and outside the shear zone of BT10 (BT10_Outside), respectively. A planar view of the two sampled sub-volumes in BT10 is presented in Figure 5.31. On the contrary, PSC method limits the discussions on BT0_Center and BT10_Inside for computational feasibility.

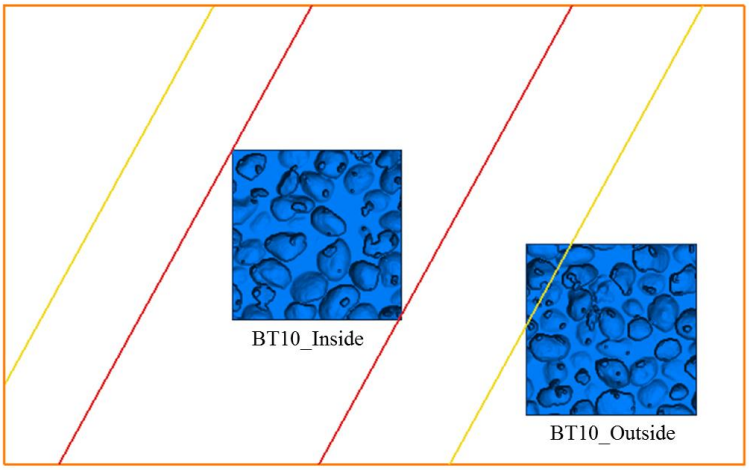

Figure 5.31 Planar view of the sub-volumes sampled from structure BT10

5.6.1.1 Geometrical Tortuosity Distribution

Sub-volumes (each 200 × 200 × 200 voxels) with the size smaller than the REV size, are randomly selected to explore the spatial information of geometrical tortuosity. Choosing relatively small sub-volumes allows for faster execution of the computational algorithm. To ensure the sampling is sufficient, different groups of datasets consisting of varying number of sub-volumes are generated. Changes in the estimated standard pore metrics (porosity, void ratio, and specific surface area) are assessed accordingly. Table 5.6 and Table 5.7 display the results using mean and standard deviation of the metrics obtained from BT0 and BT10, respectively. As the number of random sub-volumes accounted varies, very small change in the estimated values can be seen. Also, the values estimated from the sub-volumes agree well with that from the whole microstructure, given that BT0 has a porosity of 0.336, void ratio of 0.507, and specific surface area of 0.0072 μm^{-1}; while structure BT10 has a porosity of 0.361, void ratio of 0.564, and specific surface area of 0.0071 μm^{-1}. These imply that the microstructure is adequately sampled. Considering that

more information of the microstructure is contained in the group of 300 random sub-volumes, this dataset is selected for tortuosity analysis.

Table 5.6 Standard metrics computed using different groups of sub-volumes in BT0

No. Sub-volumes	Metrics		
	Porosity	Void Ratio	Specific Surface Area (μm^{-1})
40	0.335±0.011	0.505±0.024	0.0071±0.0001
60	0.335±0.010	0.504±0.023	0.0071±0.0001
80	0.335±0.010	0.504±0.022	0.0071±0.0001
100	0.335±0.010	0.503±0.022	0.0071±0.0001
200	0.334±0.010	0.501±0.022	0.0071±0.0001
300	0.335±0.010	0.504±0.022	0.0071±0.0001

Table 5.7 Standard metrics computed using different groups of sub-volumes in BT10

No. Sub-volumes	Metrics		
	Porosity	Void Ratio	Specific Surface Area (μm^{-1})
40	0.368±0.028	0.584±0.068	0.0069±0.0003
60	0.366±0.029	0.580±0.071	0.0069±0.0003
80	0.366±0.029	0.581±0.072	0.0069±0.0003
100	0.367±0.028	0.584±0.070	0.0069±0.0003
200	0.369±0.027	0.588±0.067	0.0069±0.0003
300	0.369±0.027	0.587±0.067	0.0069±0.0003

Running the voxel-based shortest-path algorithm introduced in Section 3.5.2.2, tortuosity distribution is computed for each of the sampled 300 sub-volumes along the three orthogonal axes *X*, *Y* and *Z*. Three representative values - average, minimum, and maximum - of tortuosity are determined from the distribution and summarized in Table 5.8 and Table 5.9. Figure 5.32 presents overall tortuosity distribution for the 300 sub-volumes on the left and distribution of average tortuosity on the right. In the plots on the left, the number of tortuous paths computed, mean and standard deviation of the distribution are

listed. Difference among the tortuosity distributions along different directions indicates spatial anisotropy in the tortuous attributes within the pore structure. Besides, the pore structure accommodates a broad range of tortuous paths with various lengths. For instance, the computed tortuosity values along *Z* axis range from 1.431 to 1.850 with an average value of 1.605 in BT0 (see Table 5.8). Variation in the tortuosity reveals the existence of different convoluted paths that are closely correlated with the complicated pore-scale transport processes and properties. This suggests that using a "single" tortuous value alone may misrepresent the tortuous pore structure, and in contrast, using the distribution with peaks and trend can permit a thorough prediction of the transport characteristics.

As for the comparison between BT0 and BT10, BT10 has fewer computed tortuous paths (3.3% ~ 7.5% less), larger values of both statistical mean and standard deviation. A right shifting trend and a flatter shape can be observed in the histograms of BT10 (see Figure 5.32). This conveys the information that shearing tends to produce lower density of pore skeleton distributed within the defined volumes, which in turn renders a smaller number of tortuous paths computed from those curved skeletons. Shearing also tends to cause higher dispersion in terms of the length of tortuous paths, and to induce more longer paths and fewer shorter paths.

Table 5.8 Calculated average, minimum, and maximum tortuosity from 300 random sub-volumes for structure BT0 along three orthogonal axes

Metrics	Average	Minimum	Maximum
Tortuosity in *X*-direction	1.615±0.043	1.436±0.040	1.864±0.124
Tortuosity in *Y*-direction	1.647±0.043	1.457±0.042	1.893±0.116
Tortuosity in *Z*-direction	1.605±0.038	1.431±0.040	1.850±0.119

Table 5.9 Calculated average, minimum, and maximum tortuosity from 300 random sub-volumes for structure BT10 along three orthogonal axes

Metrics	Average	Minimum	Maximum
Tortuosity in *X*-direction	1.652±0.050	1.454±0.048	1.925±0.127
Tortuosity in *Y*-direction	1.675±0.052	1.466±0.050	1.959±0.120
Tortuosity in *Z*-direction	1.667±0.058	1.460±0.057	1.956±0.133

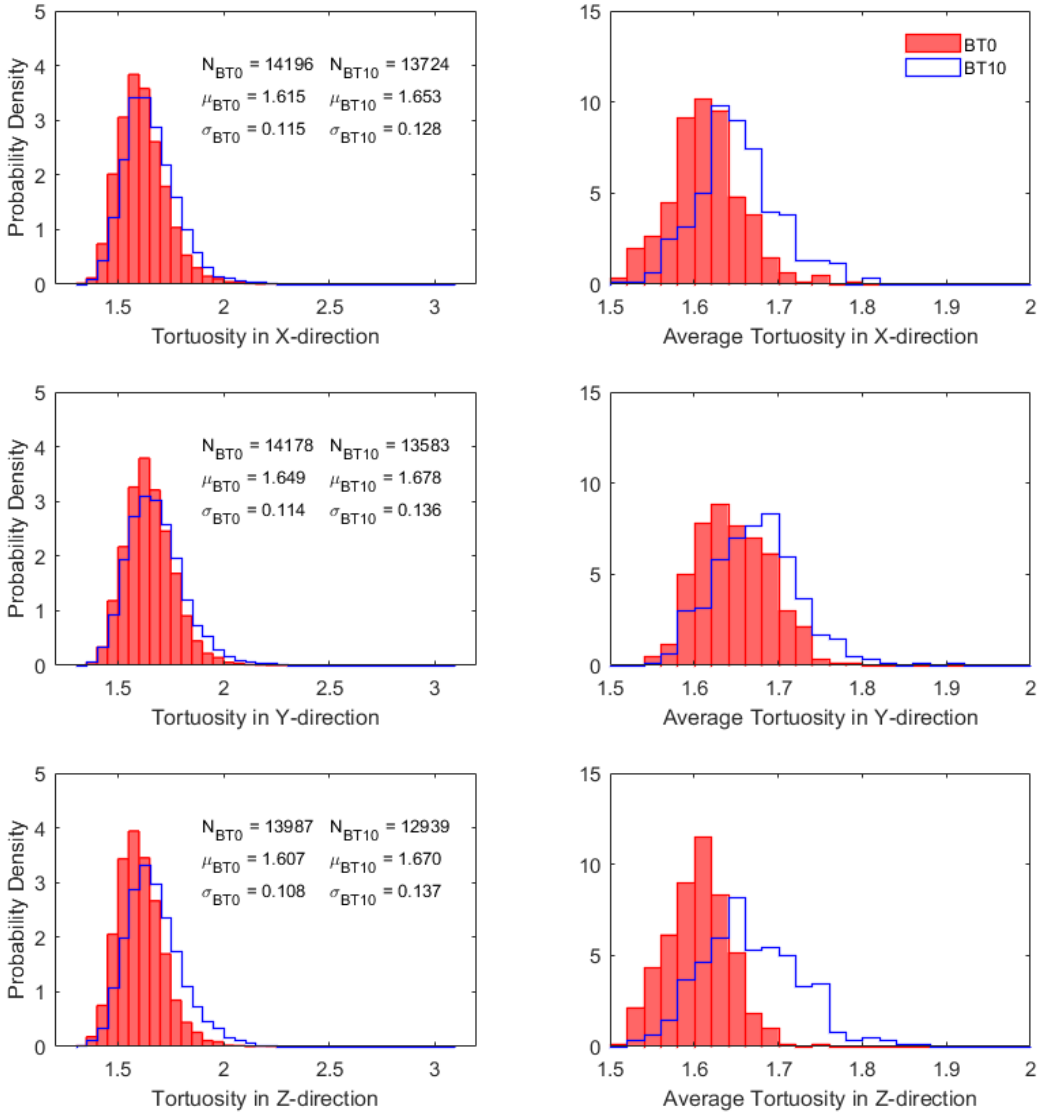

Figure 5.32 Distribution of tortuosity computed from 300 random sub-volumes and comparison between BT0 and BT10

To perform a closer inspection on shearing related distinctive tortuous structures, 200 random sub-volumes are generated for both inside and outside shear zone in BT10. The 200 sub-volumes located outside the shear zone comprises 100 sub-volumes located entirely in the non-dilatant zones (denoted as "ND"), which are the upper-left region and the lower-right region bounded by the two yellow lines as shown in Figure 5.1(b), as well as the other 100 sub-volumes that intersect the transition zones (denoted as "T").

Estimated values for the standard metrics are presented in Table 5.10. There is a gradual decrease in porosity and void ratio from inside the shear zone to the transition zones and then to the non-dilatant zones. In Figure 5.33, the left three plots compare the distribution of tortuosity inside and outside the shear zone. Inside the shear zone, fewer tortuous paths are obtained, and the histogram shows lower peak and flattens with a higher standard deviation. Except for the tortuosity along *Y* axis, the mean value of tortuosity is slightly higher (about 1.0%) inside the shear zone than outside the shear zone. The right three plots in Figure 5.33 further examine the regions outside the shear zone. Histogram for the sub-volumes intersecting the transition zones, with higher mean and standard deviation, slightly shifts to the right of that for the non-dilatant zones. The results presented here suggest that high porosity (or void ratio) does not necessarily mean that the pore structure is less tortuous, particularly when the tortuous attribute is represented by the distribution of tortuosity rather than a single value averaging over the entire pore structure. Spatially, the tortuous attribute should be influenced by porosity (or void ratio), size of pore openings and more importantly, connectivity of pore network.

Table 5.10 Standard metrics computed for sub-volumes in different zones of BT10

		Metrics		
		Porosity	Void Ratio	Specific Surface Area (μm^{-1})
Inside Shear Zone		0.399±0.012	0.665±0.034	0.0066±0.0002
Outside Shear Zone	"T"	0.336±0.012	0.506±0.026	0.0073±0.0001
	"ND"	0.321±0.005	0.472±0.012	0.0074±0.0001
	Combined	0.328±0.012	0.489±0.026	0.0074±0.0001

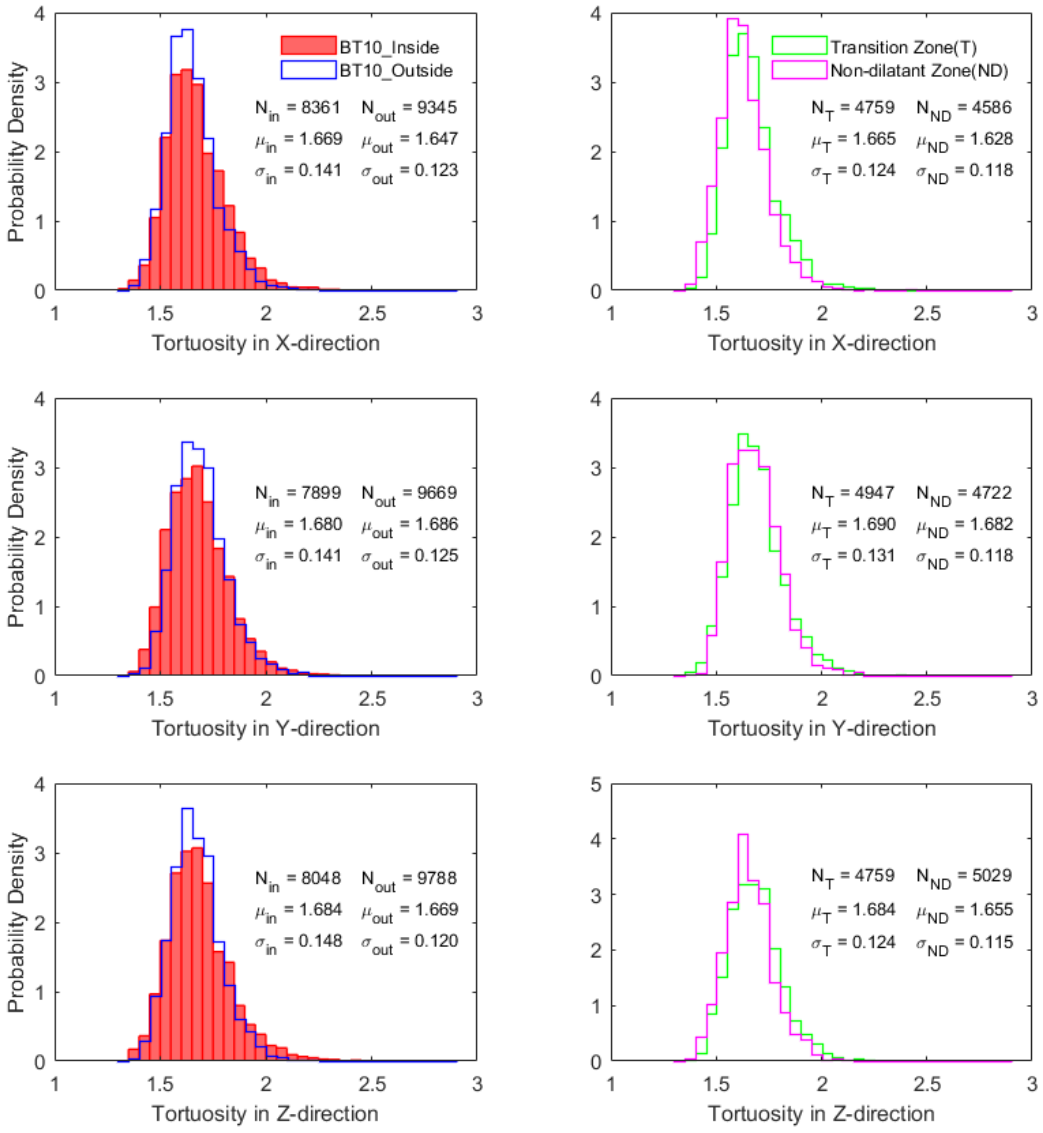

Figure 5.33 Comparison of tortuosity distribution among different zones for BT10

5.6.1.2 Pore Topology Based on Local Sphericity Method

In the analysis of pore topology using the local sphericity (LS) algorithm, throat finding is executed on the *SPP*s identified for the whole microstructure volume. Out of the 22367 *SPP*s in BT0 and the 27962 *SPP*s in BT10 (see Table 5.4), 21930 and 27323 pore throats are identified. The extraction of pore network statistics conforms to the unbiased quantification rule by taking either the LAV or the sampled sub-volume as the central volume of the 3-D counting brick.

Distributions of pore throat size, pore body size, pore body-throat connectivity, and pore channel length are compared between the LAV of BT0 and BT10 in Figure 5.34. Statistical mean, standard deviation, coefficient of variation, as well as entropy of all distributions are calculated and listed in Table 5.11. The LAV volume of BT0 is thinner than BT10, so the amount of these metrics in BT0 is much less than BT10. The plot of BT10 does not show obvious shifting characteristics compared with BT0. Mean value of each metric only differs slightly between the two. However, BT10 clearly has larger standard deviation and coefficient of variation for each metric than BT0. This indicates that shearing induces higher scatter in the distribution of these pore network related metrics. The larger entropy value for BT10 also suggests a shear-induced higher degree of disorder of each distribution. Comparing the results between BT0_Center and BT10_Inside in Figure 5.35, a slight right-shifting of the histogram for BT10_Inside can be observed in the distributions of pore throat size, pore body size, and pore channel length. In Figure 5.36, it becomes more noticeable that shearing shifts the histogram to the right and flattens it for each metric when comparing inside and outside the shear zone for BT10. This is indicative of an increased degree of heterogeneity of the pore structure characteristics due to shearing.

Dilation inside the shear zone leads to fewer but larger pore throats and pore bodies, higher coordination number of pore bodies, and longer pore channels than outside the shear zone. These shearing effects are evident from the statistical parameters for the distributions (see Table 5.11), with mean, standard deviation and entropy always increasing with shearing.

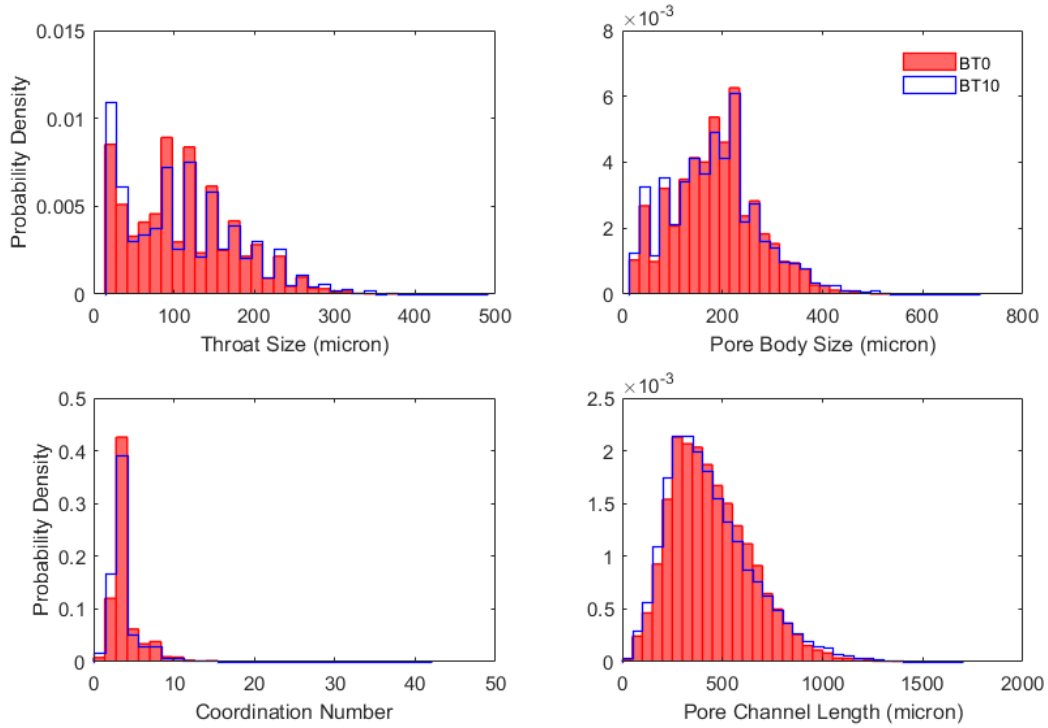

Figure 5.34 Distribution of pore network related metrics for the LAV of BT0 and BT10 based on LS method

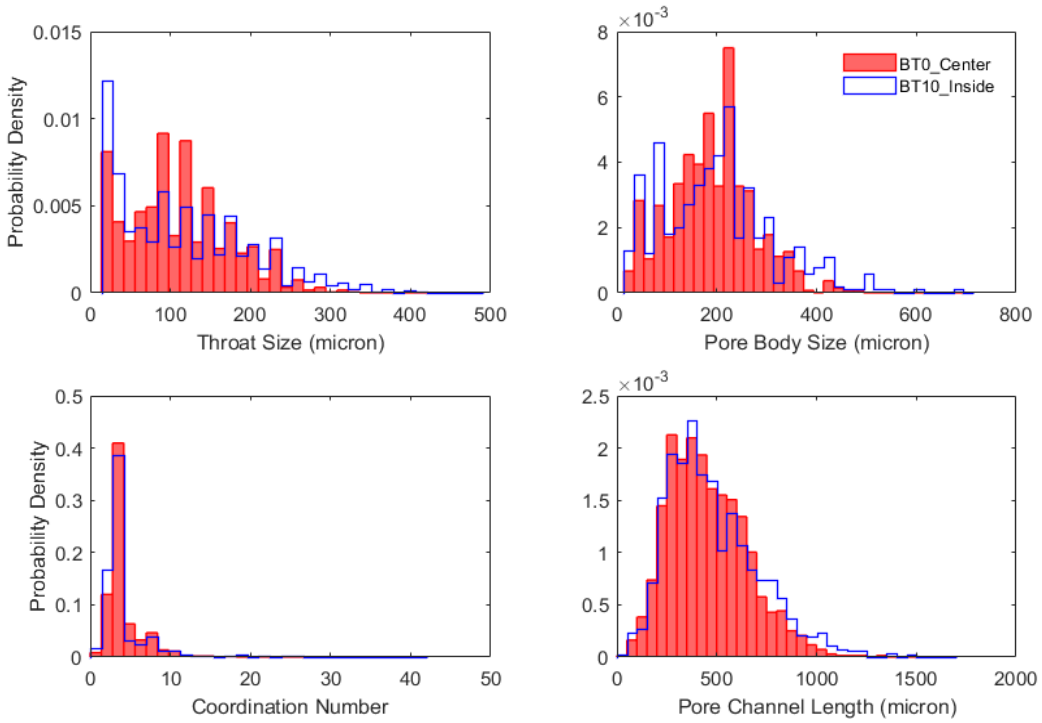

Figure 5.35 Distribution of pore network related metrics for the REV of BT0 and BT10 based on LS Method

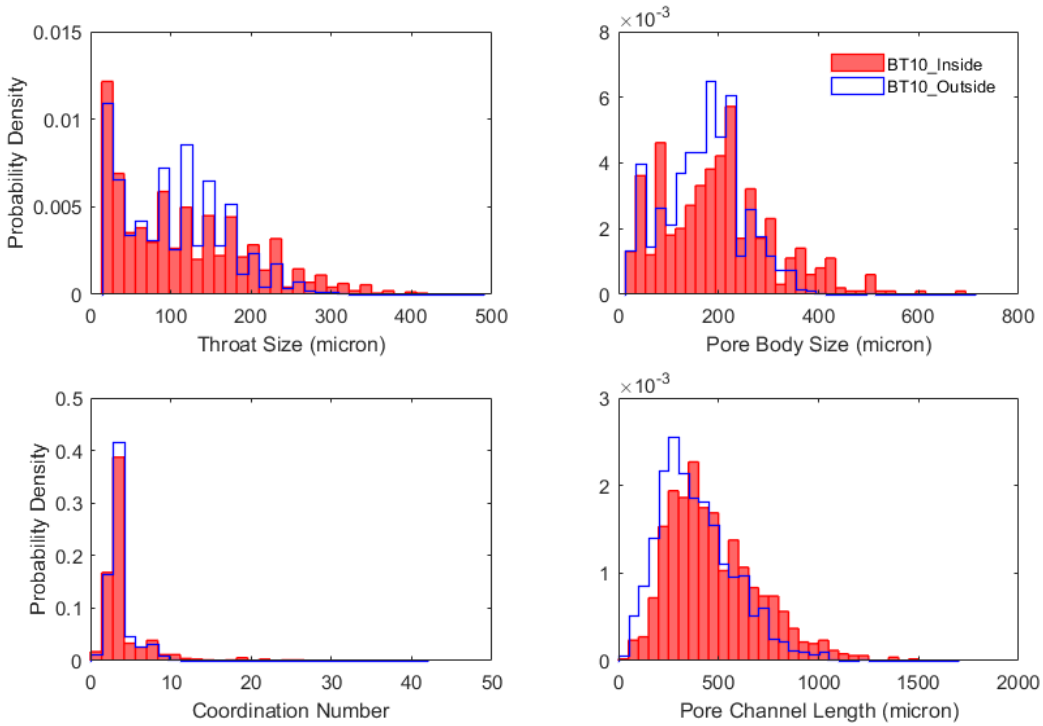

Figure 5.36 Distribution of pore network related metrics inside and outside shear zone for BT10 based on LS method

Table 5.11 Distribution statistics of pore network related metrics for BT0 and BT10 based on LS method

Metrics		LAV		REV		
		BT0	BT10	BT0_Center	BT10_Inside	BT10_Outside
3-D Porosity		33.8%	36.3%	33.6%	38.7%	32.4%
3-D Void Ratio		0.510	0.570	0.506	0.631	0.479
Throat Size (μm)	No.	15924	20983	1349	1034	1486
	μ	108.5	109.7	108.9	114.7	101.8
	σ	65.7	73.5	63.5	84.4	64.5
	CV (%)	60.5	67.0	58.3	73.6	63.4
	H_v	0.777	0.789	0.771	0.812	0.753
Pore Body Size (μm)	No.	7864	10925	673	498	851
	μ	185.7	184.3	190.5	200.5	170.7
	σ	84.9	92.8	84.5	113.6	79.6
	CV (%)	45.7	50.3	44.4	56.7	46.6
	H_v	0.784	0.801	0.775	0.831	0.754
Pore Body-Throat Connectivity	No.	7864	10925	673	498	851
	μ	3.9	3.6	4.0	4.0	3.5
	σ	2.0	2.2	2.1	3.1	1.6
	CV (%)	51.0	60.2	53.0	77.8	47.0
	H_v	0.396	0.410	0.415	0.435	0.372
Pore Channel Length (μm)	No.	15876	20946	1354	1031	1501
	μ	443.9	439.7	455.4	478.9	391.1
	σ	199.3	217.9	195.9	228.2	191.6
	CV (%)	44.9	49.5	43.0	47.7	49.0
	H_v	0.780	0.796	0.776	0.806	0.762

Size correlation between neighboring pore bodies, and between neighboring pore throats and pore bodies are explored in structure BT10. For each counted pore body, the average size of its neighboring pore bodies is plotted against its size. From Figure 5.37, it can be seen that the plot for BT10_Inside is more scattered and covers a wider space. At a specific pore body size, the average size of the neighboring pore bodies can reach a larger

value in BT10_Inside than in BT10_Outside. Similar result is rendered when plotting the average size of the two neighboring pore bodies against the size of a counted throat. Shearing tends to not only induce a wider size range of throats but also a wider size range of neighboring pore bodies for a chosen throat size. Finally, distribution of throat/pore body aspect ratio is presented. The histogram for BT10_Outside shows a slight shift to the right of BT10_Inside, with a larger statistical mean of 0.52 than 0.45 for BT10_Inside.

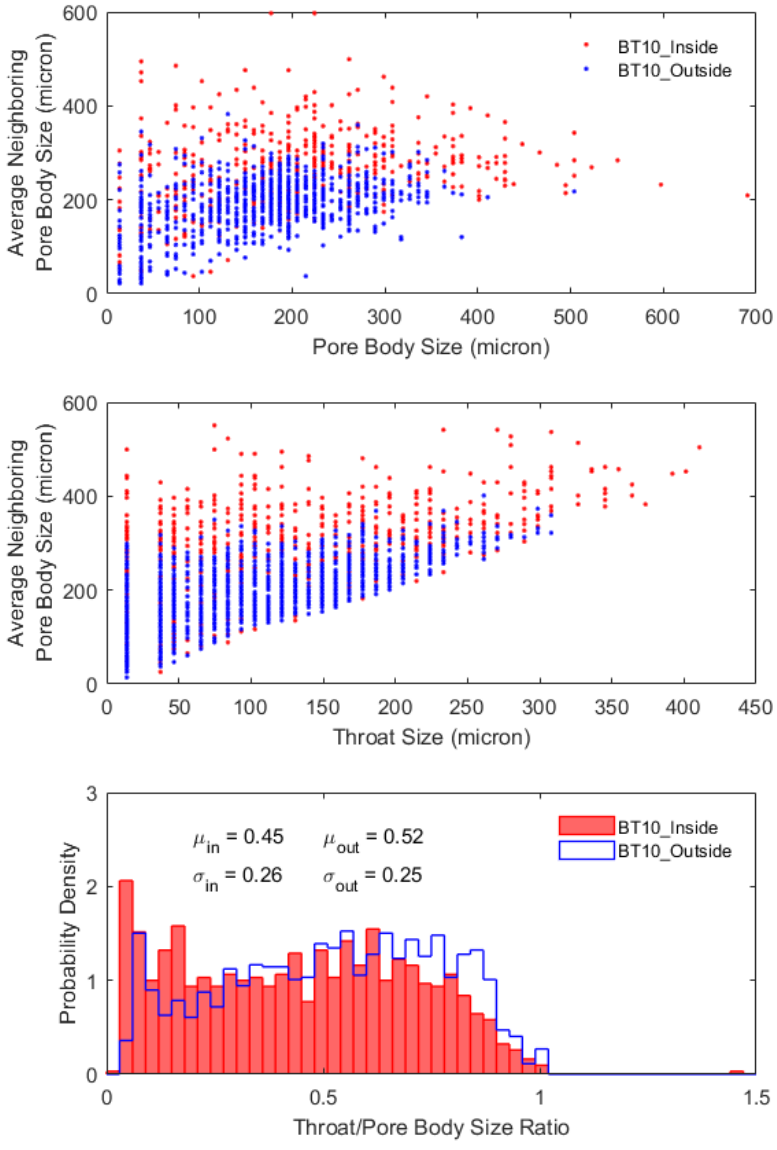

Figure 5.37 Size correlation inside and outside shear zone for BT10

Using the above quantitative information, the pore structure in each volume of interest can be represented by a 3-D pore network model (PNM). A minor distinction between the number of throats counted and the number of pore channels counted can be noticed in Table 5.11. Theoretically, there should be no distinction because every pore channel contains a pore throat. However, the two metrics are counted separately and each counting adheres to the unbiased 3-D quantification rule. Moreover, it is likely for a counted pore body to have no neighboring pore bodies counted such that this pore body is isolated in the PNM. Considering that a PNM is a network of spatially distributed spherical pore bodies being the nodes connected by cylindrical tubes, building the PNM in this study is accomplished through examining the neighborhood of the pore bodies counted. This consists of two steps: (1) identify non-isolated counted pore bodies as nodes; (2) if both of the two pore bodies that a throat connects are counted, this throat and its corresponding pore channel are turned into a tube; otherwise not.

Table 5.12 presents the statistics of the PNM built for BT0_Center, BT10_Inside, and BT10_Outside. For example, the PNM for BT10_Inside consists of 487 spherical pore bodies as the nodes and 770 cylindrical tubes, with a mean tube connectivity per node (coordination number) of 4.0. Mean pore body diameter is 201.0 μm, mean tube diameter is 114.4 μm, and mean tube length is 458.1 μm. Comparative relations of the statistical parameters between BT0_Center and BT10_Inside, as well as between BT10_Inside and BT10_Outside are consistent with that shown in Table 5.11. The derived PNM data can be further employed in the pore network simulation to estimate transport properties such as the hydraulic and electrical conductances.

Table 5.12 Pore Network Model statistics for the REV of BT0 and BT10

Metrics		BT0_Center	BT10_Inside	BT10_Outside
Tube Diameter (μm)	No.	1077	770	1221
	μ	107.2	114.4	101.1
	σ	62.9	83.7	64.0
	CV (%)	58.7	73.1	63.3
	H_v	0.765	0.812	0.749
Pore Body (Node) Size (μm)	No.	641	487	836
	μ	188.0	201.0	170.9
	σ	84.2	113.3	79.5
	CV (%)	44.8	56.4	46.5
	H_v	0.773	0.831	0.753
Tube Connectivity per Node	No.	641	487	836
	μ	3.9	4.0	3.5
	σ	2.0	3.0	1.6
	CV (%)	51.6	76.2	45.6
	H_v	0.402	0.433	0.366
Tube Length (μm)	No.	1077	770	1221
	μ	446.1	458.1	380.8
	σ	194.7	223.8	189.5
	CV (%)	43.6	48.9	49.8
	H_v	0.773	0.795	0.759

5.6.1.3 Pore Topology Based on Planar Surface Construction Method

To characterize pore structure using the planar surface construction (PSC) method, throat finding is executed on the REV instead of the whole microstructure volume. As introduced in Section 3.5.6, relevant *SPP*s to the sub-volume of interest, *R-SPP*s, are selected out of the complete set of *SPP*s to run the algorithm. BT0_Center has been utilized to demonstrate the detailed computational throat-finding procedure, with the result listed in Table 3.1, identified throats visualized in Figure 3.35 (c) and pore bodies visualized in

Figure 3.36. After throat finding, a modification process was proposed in Section 3.5.5.2 to divide throats, partition pore space, and extract network parameters for quantification. Therefore, pore structure characterization using this method is composed of two stages: (1) throat-finding stage; and (2) modification stage. In this section, results for BT0_Center and BT10_Inside at both stages will be presented.

Table 5.13 presents the results for the throat-finding stage and compares that with the results obtained from LS algorithm. With a higher porosity (38.7% versus 33.6%), BT10_Center has fewer *R-SPP*s and a lower throat-finding rate than BT0_Center. This is expected because constructing a throat perimeter made up of connected boundary particle voxels will be more difficult in sheared sand microstructure in which particles are more loosely packed and have insufficient contacts. Percentages of crossing-throats are 17.2% and 15.4% for BT0_Center and BT10_Inside, respectively. As for the same *R-SPP*s, LS algorithm renders noticeably higher throat-finding rates. Identified throats and pore bodies pertaining to BT10_Inside are visualized in Figure 5.38. Compared with Figure 3.37, BT10_Inside has much fewer pore bodies separated out from the remaining pore space.

Table 5.13 Results of throat finding for BT0_Center and BT10_Inside

Items		BT0_Center	BT10_Inside
Information	No. *R-SPP*s	2411	2032
	No. *Points*	58193	53636
	No. *Nodes*/ *Node Clusters*	1484	1217
PSC Algorithm	No. Throats	1548	1099
	Throat-finding Rate	64.2%	54.1%
	No. Crossing-throats	266	169
LS Algorithm	No. Throats	2365	1999
	Throat-finding Rate	98.1%	98.4%

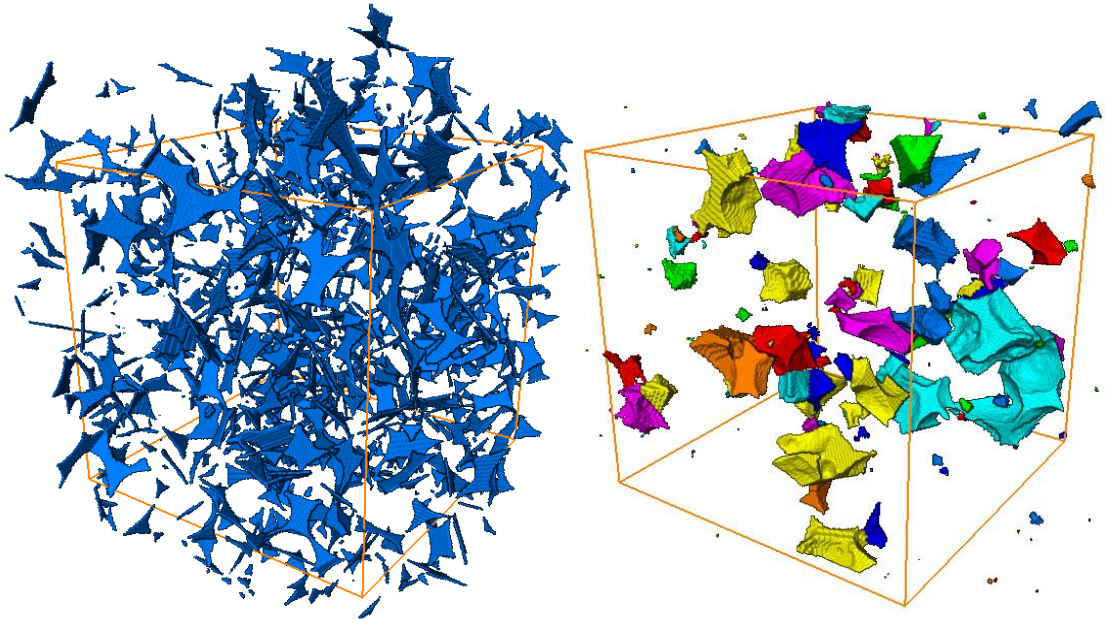

(a) (b)

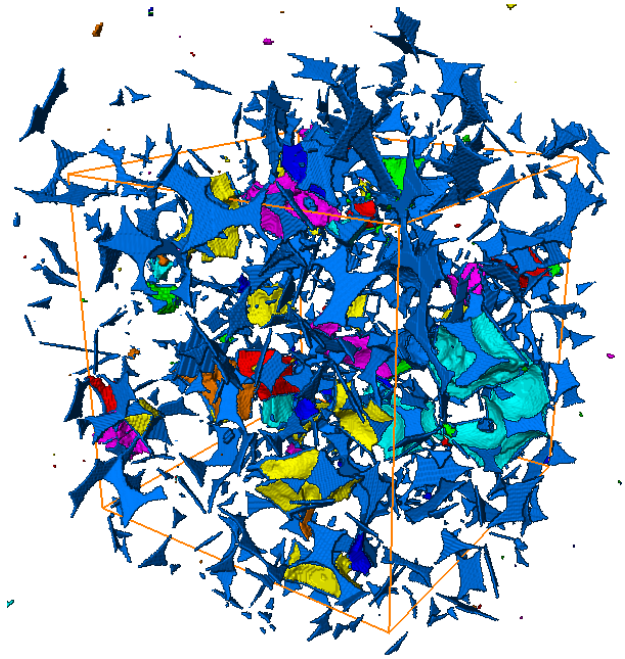

(c)

Figure 5.38 Visualization of throat-finding results for BT10_Inside: (a) pore throat barriers; (b) pore bodies pertaining to the sub-volume; (c) a combined display

Regarding the modification stage, there is an increase in the number of throats through throat division (Table 5.14). 12.6% more throats for BT0_Center and 6.2% more for BT10_Inside can be detected. After that, partitioning the pore space into distinct pore bodies with properly calculated volumes is accomplished. Applying the unbiased 3-D brick counting rule to quantify the major pore network parameters, the numbers of counted throats and pore bodies are also given in Table 5.14, with the 3-D visualization presented in Figure 5.39 and Figure 5.40. As a quite large portion of the pore space surrounding BT10_Inside remains connected, the amount of pore bodies counted is very limited. So, a direct comparison on the size distributions of throats and pore bodies between BT0_Center and BT10_Inside may not be appropriate.

Table 5.14 Results of throats and pore bodies at the two stages for BT0_Center and BT10_Inside

Items	BT0_Center	BT10_Inside
No. Throats[1]	1548	1099
No. Throats[2]	1743	1167
No. Throats Counted[1]	931	604
No. Throats Counted[2]	1096	662
No. Pore Bodies Counted[2]	197	102

Note: 1 - throat-finding stage; 2 - modification stage

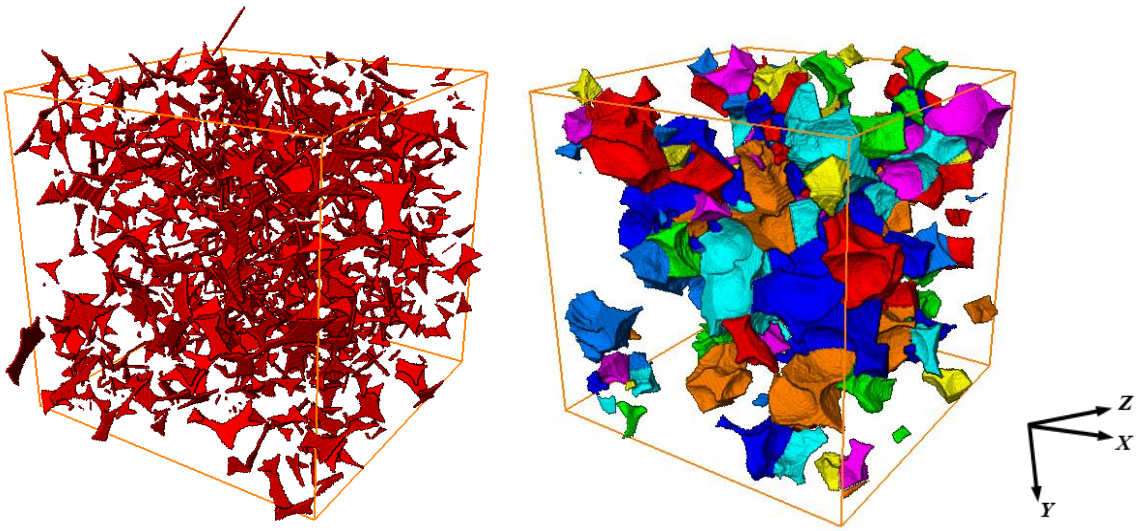

(a) (b)

Figure 5.39 Counted pore network components for BT0_Center from modification stage: (a) pore throat barriers; (b) pore bodies

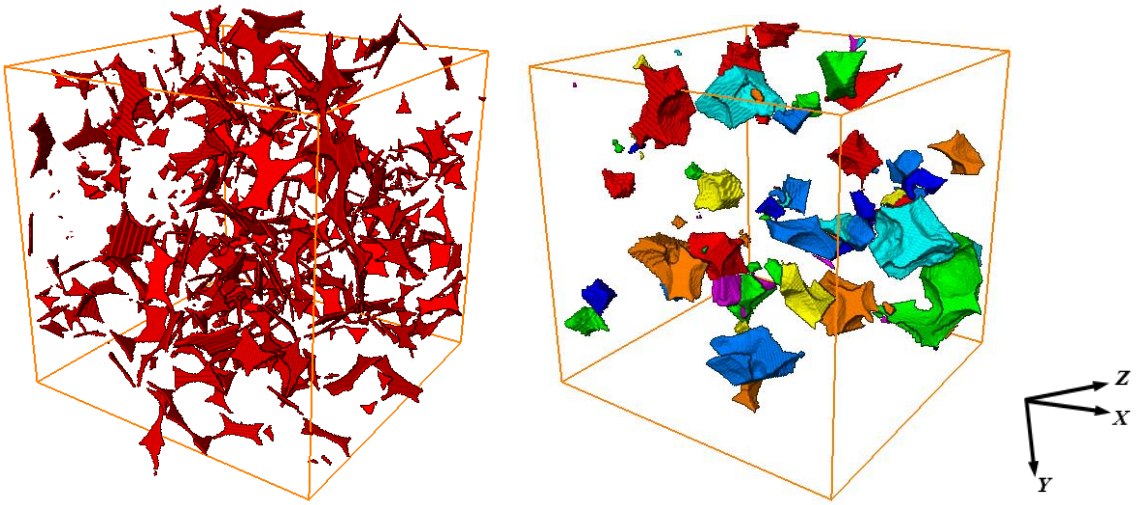

(a) (b)

Figure 5.40 Counted pore network components for BT10_Inside from modification stage: (a) pore throat barriers; (b) pore bodies

5.6.2 Characterization of Triaxial Sand Structures

To characterize pore structures in AP0a, AP14a, MT0a, and MT14a, the defined dimensions of LAV (see Table 5.4) are utilized. Analyses of the spatial distribution of geometrical tortuosity continues to apply the approach of randomly sampling sub-volumes (each 200 × 200 × 200 voxels) from the pore skeleton. On the other hand, in the study of pore network characteristics, a cubic sub-volume with an edge length of 250 voxels is sampled from the center of each microstructure, and designated as AP0a_Center, AP14a_Center, MT0a_Center, and MT14a_Center, respectively. These four sub-volumes will be the focus when implementing the PSC algorithm.

5.6.2.1 Geometrical Tortuosity Distribution

Like was performed in analyzing the biaxial microstructures, the first step is to determine the adequate number of random sub-volumes to be used such that variation of the internal structure can be well captured. For AP0a and AP14a, the results of standard pore metrics for the six groups of datasets are presented in Table 5.15 and Table 5.16, respectively. With respect to either AP0a or AP14a, negligible differences are seen among the estimated values for different groups. The values estimated from the sub-volumes are in accord with that estimated from the whole microstructure, considering that AP0a has a porosity of 0.366, void ratio of 0.578, and specific surface area of 0.0155 μm^{-1}; while the corresponding three numbers for AP14a are 0.419, 0.721, and 0.0136 μm^{-1}. For MT0a and MT14a, the results are shown in Table 5.17 and Table 5.18, and similar observations can be made. Since the microstructure is sufficiently sampled, the comprehensive dataset

containing 300 random sub-volumes is utilized in the tortuosity analyses for both the air-pluviated and the moist-tamped microstructures.

Table 5.15 Standard metrics computed using different groups of sub-volumes in AP0a

No. Sub-volumes	Metrics		
	Porosity	Void Ratio	Specific Surface Area (μm^{-1})
40	0.362±0.014	0.569±0.034	0.0156±0.0005
60	0.362±0.014	0.567±0.034	0.0157±0.0005
80	0.361±0.014	0.565±0.033	0.0157±0.0005
100	0.362±0.013	0.567±0.033	0.0156±0.0005
200	0.362±0.013	0.569±0.033	0.0157±0.0005
300	0.362±0.014	0.569±0.033	0.0157±0.0005

Table 5.16 Standard metrics computed using different groups of sub-volumes in AP14a

No. Sub-volumes	Metrics		
	Porosity	Void Ratio	Specific Surface Area (μm^{-1})
40	0.418±0.011	0.718±0.032	0.0134±0.0004
60	0.417±0.011	0.717±0.033	0.0134±0.0003
80	0.417±0.011	0.716±0.031	0.0134±0.0004
100	0.417±0.010	0.716±0.031	0.0134±0.0004
200	0.416±0.011	0.714±0.032	0.0134±0.0004
300	0.417±0.011	0.715±0.033	0.0134±0.0004

Table 5.17 Standard metrics computed using different groups of sub-volumes in MT0a

No. Sub-volumes	Metrics		
	Porosity	Void Ratio	Specific Surface Area (μm^{-1})
40	0.349±0.012	0.537±0.028	0.0148±0.0004
60	0.351±0.012	0.541±0.027	0.0149±0.0003
80	0.351±0.012	0.541±0.028	0.0149±0.0004
100	0.351±0.011	0.542±0.027	0.0149±0.0004
200	0.351±0.011	0.542±0.027	0.0149±0.0004
300	0.351±0.012	0.541±0.028	0.0149±0.0004

Table 5.18 Standard metrics computed using different groups of sub-volumes in MT14a

No. Sub-volumes	Metrics		
	Porosity	Void Ratio	Specific Surface Area (μm^{-1})
40	0.416±0.012	0.713±0.034	0.0153±0.0006
60	0.416±0.011	0.712±0.032	0.0153±0.0006
80	0.416±0.011	0.713±0.032	0.0154±0.0006
100	0.417±0.011	0.715±0.033	0.0153±0.0006
200	0.417±0.011	0.716±0.033	0.0153±0.0006
300	0.417±0.011	0.716±0.032	0.0153±0.0006

Distribution of tortuosity is computed for each sub-volume along positive *X*, *Y*, and *Z* directions. The overall tortuosity distribution and distribution of average tortuosity for AP0a and AP14a are presented in Figure 5.41, and those for MT0a and MT14a are presented in Figure 5.42. Values including the average, minimum, and maximum tortuosity are evaluated and listed in Table 5.19 - Table 5.22 for AP0a, AP14a, MT0a, and MT14a, respectively. Spatial anisotropy in the tortuous attributes and wide range in the lengths of tortuous paths are obvious in these triaxial microstructures too. When comparing sheared microstructure with its unsheared counterpart, a right-shifted and flattened histogram can be noticed in the overall distribution as well as in the distribution of average tortuosity. Shearing leads to fewer tortuous paths identified, a higher degree of dispersion in the length of those paths, and a larger statistical mean of the distribution, which are all consistent with the findings for the biaxial microstructures. This strengthens the postulate made earlier that the tortuous attribute of pore structure should depend on a combined effect of porosity (or void ratio), size of pore openings and more importantly, connectivity of pore network. In addition, it is found that AP14a has 34.6% ~ 36.4% less amount of computed tortuous paths than AP0a while MT14a has only 5.5% ~ 9.3% less than MT0a. It states that the shear-

induced change is much more evident in AP14a, supporting the fact that a more global dilation was observed in it compared with a more localized dilation occurred in MT14a.

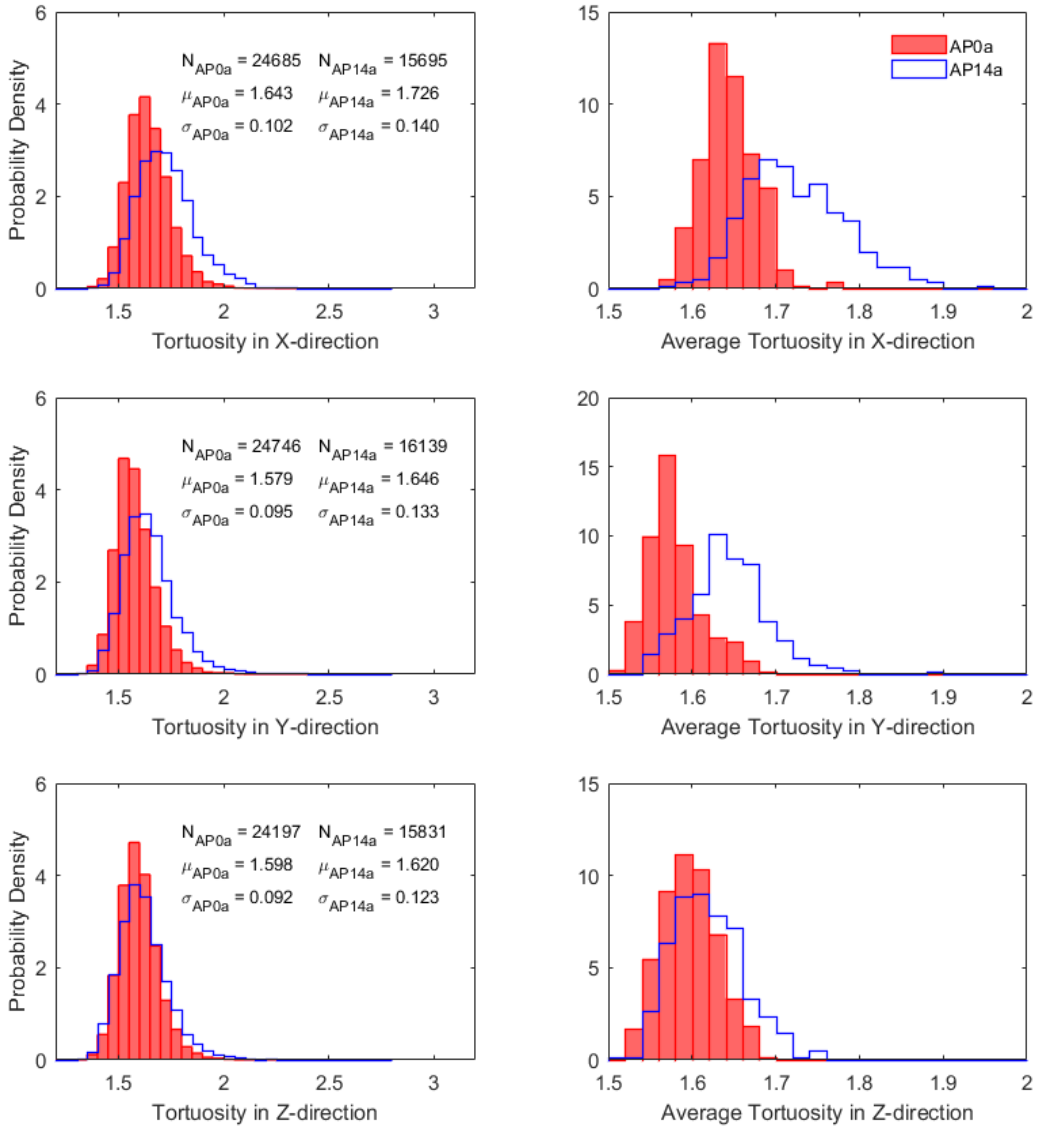

Figure 5.41 Distribution of tortuosity computed from 300 random sub-volumes and comparison between AP0a and AP14a

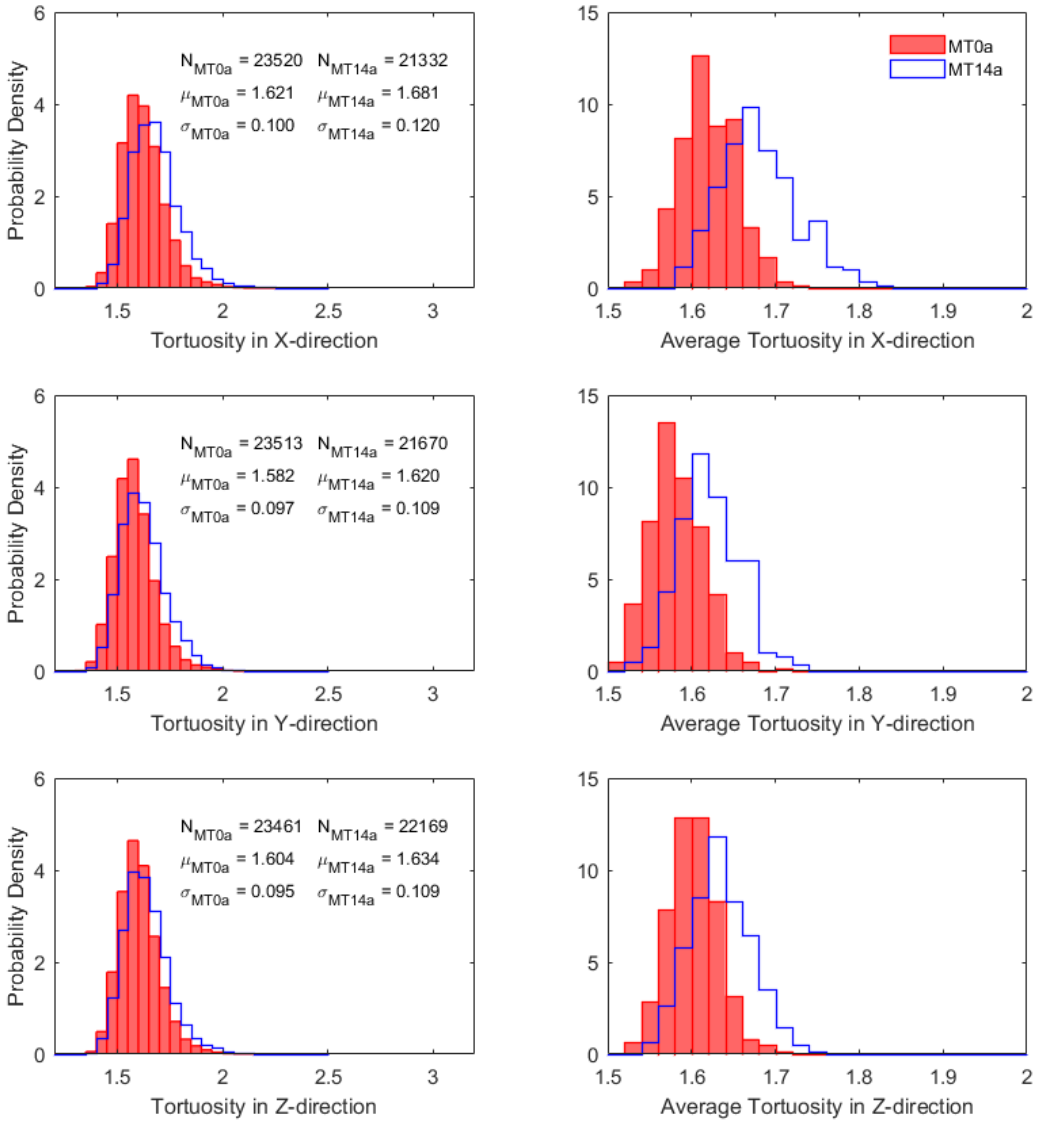

Figure 5.42 Distribution of tortuosity computed from 300 random sub-volumes and comparison between MT0a and MT14a

Table 5.19 Calculated average, minimum, and maximum tortuosity from 300 random sub-volumes for structure AP0a along three orthogonal axes

Metrics	Average	Minimum	Maximum
Tortuosity in *X*-direction	1.644±0.031	1.461±0.042	1.905±0.102
Tortuosity in *Y*-direction	1.579±0.033	1.418±0.034	1.822±0.094
Tortuosity in *Z*-direction	1.597±0.033	1.432±0.043	1.832±0.086

Table 5.20 Calculated average, minimum, and maximum tortuosity from 300 random sub-volumes for structure AP14a along three orthogonal axes

Metrics	Average	Minimum	Maximum
Tortuosity in *X*-direction	1.724±0.060	1.505±0.057	2.031±0.150
Tortuosity in *Y*-direction	1.644±0.048	1.440±0.045	1.951±0.145
Tortuosity in *Z*-direction	1.619±0.042	1.424±0.044	1.897±0.140

Table 5.21 Calculated average, minimum, and maximum tortuosity from 300 random sub-volumes for structure MT0a along three orthogonal axes

Metrics	Average	Minimum	Maximum
Tortuosity in *X*-direction	1.620±0.033	1.446±0.037	1.871±0.095
Tortuosity in *Y*-direction	1.582±0.031	1.412±0.035	1.825±0.096
Tortuosity in *Z*-direction	1.603±0.030	1.436±0.034	1.843±0.094

Table 5.22 Calculated average, minimum, and maximum tortuosity from 300 random sub-volumes for structure MT14a along three orthogonal axes

Metrics	Average	Minimum	Maximum
Tortuosity in *X*-direction	1.680±0.046	1.486±0.043	1.972±0.127
Tortuosity in *Y*-direction	1.620±0.036	1.433±0.040	1.888±0.101
Tortuosity in *Z*-direction	1.634±0.037	1.453±0.042	1.914±0.115

5.6.2.2 Pore Topology Based on Local Sphericity Method

After running the LS algorithm, 64797 throats are identified from the 66398 *SPP*s in structure AP0a, 33279 throats identified from the 34012 *SPP*s in structure AP14a. And in structure MT0a and MT14a, 66267 throats and 52325 throats are identified from the 67757 *SPP*s and the 53640 *SPP*s, respectively.

Distributions of the primary pore network related metrics for the air-pluviated structures are plotted in Figure 5.43 for the LAV and Figure 5.44 for the sub-volumes. It is clearly observed that the histograms of throat size, pore body size, and pore channel length

for both AP14a and AP14a_Center are shifted to the right, and that the histogram of coordination number of pore bodies does not show obvious shifting. Distribution statistics are calculated and listed in Table 5.23. As with sheared versus unsheared microstructures, the amount of each metric quantified by the unbiased counting rule tends to decrease; while the mean values of throat size, pore body size, and pore channel length increase, indicating dilation in the sheared structure. Standard deviation, coefficient of variation, and entropy are seen to increase for each metric in the sheared microstructure, demonstrating an increased variation and disorder with shearing.

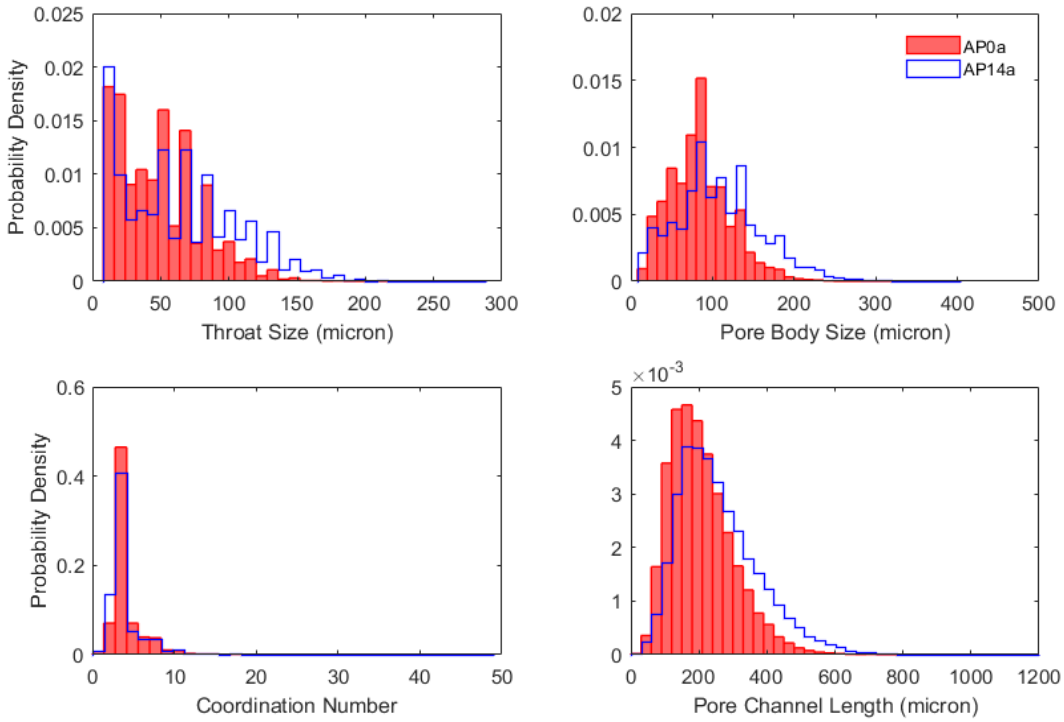

Figure 5.43 Distribution of pore network related metrics for the LAV of AP0a and AP14a based on LS method

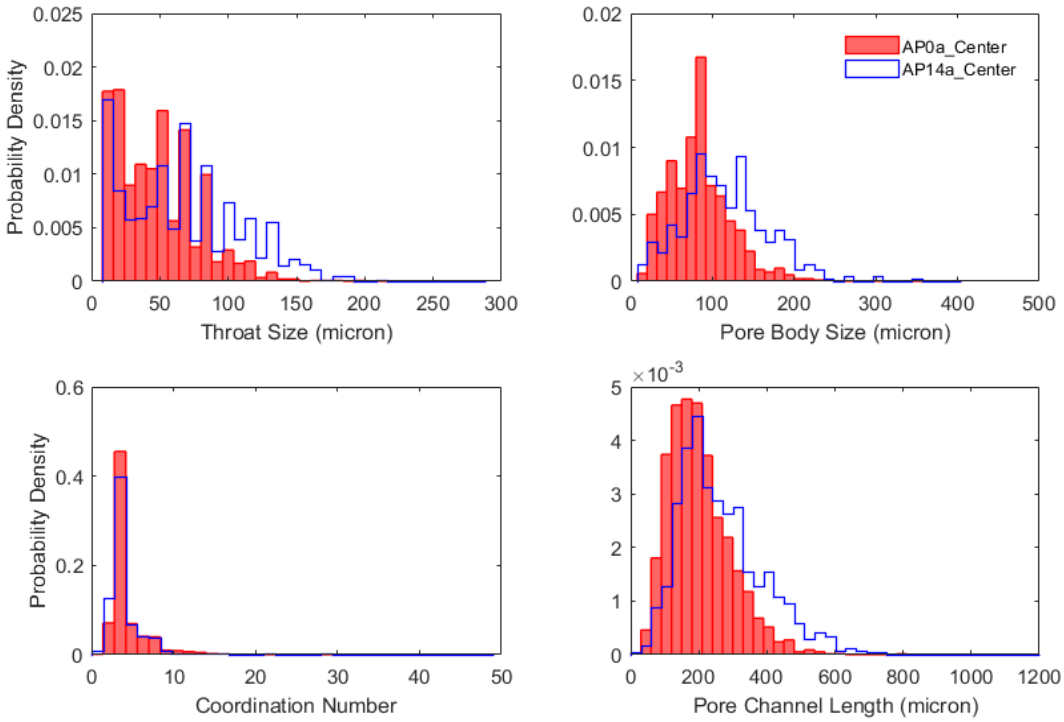

Figure 5.44 Distribution of pore network related metrics for the REV of AP0a and AP14a based on LS method

Comparisons between sheared and unsheared moist-tamped microstructures are presented in Figure 5.45 for the LAV and Figure 5.46 for the REV, with the distribution statistics summarized in Table 5.24. As for throat size, pore body size, and pore channel length, the histograms of MT14a and MT14a_Center are shifted to the right of MT0a and MT0a_Center, though the shifting is much less evident than that for the sheared air-pluviated microstructure. The distribution statistics show similar comparative results to those between AP0a and AP14a as well as between AP0a_Center and AP14a_Center, except that coefficient of variation for the sheared microstructure is not consistently larger than the unsheared one. Dilation, increased variation and increased disorder due to shearing can still be noted. Furthermore, either from the histograms or the calculated statistics including mean, standard deviation and entropy, the extent of shear-induced change is

clearly greater in the air-pluviated microstructure than in the moist-tamped microstructure. This reflects the fact that dilation in the sheared air-pluviated specimen is more global, whereas the sheared moist-tamped specimen shows localized dilation.

Table 5.23 Distribution statistics of pore network related metrics for AP0a and AP14a based on LS method

Metrics		LAV		REV	
		AP0a	AP14a	AP0a_Center	AP14a_Center
3-D Porosity		36.6%	41.8%	36.5%	42.0%
3-D Void Ratio		0.577	0.718	0.575	0.724
Throat Size (μm)	No.	53816	26287	1797	781
	μ	47.7	63.0	46.9	66.2
	σ	30.4	42.8	29.5	42.3
	CV (%)	63.7	68.0	63.0	63.9
	H_v	0.703	0.785	0.694	0.791
Pore Body Size (μm)	No.	25672	12300	852	393
	μ	84.0	107.8	82.5	114.4
	σ	37.7	53.7	37.2	52.7
	CV (%)	44.8	49.8	45.1	46.1
	H_v	0.713	0.811	0.703	0.803
Pore Body-Throat Connectivity	No.	25672	12300	852	393
	μ	4.0	3.9	4.2	4.1
	σ	2.0	2.5	2.2	2.8
	CV (%)	49.3	63.3	53.3	69.0
	H_v	0.355	0.406	0.370	0.412
Pore Channel Length (μm)	No.	53684	26241	1810	800
	μ	207.0	257.4	202.2	264.4
	σ	92.4	118.6	91.2	122.5
	CV (%)	44.6	46.1	45.1	46.3
	H_v	0.669	0.735	0.664	0.740

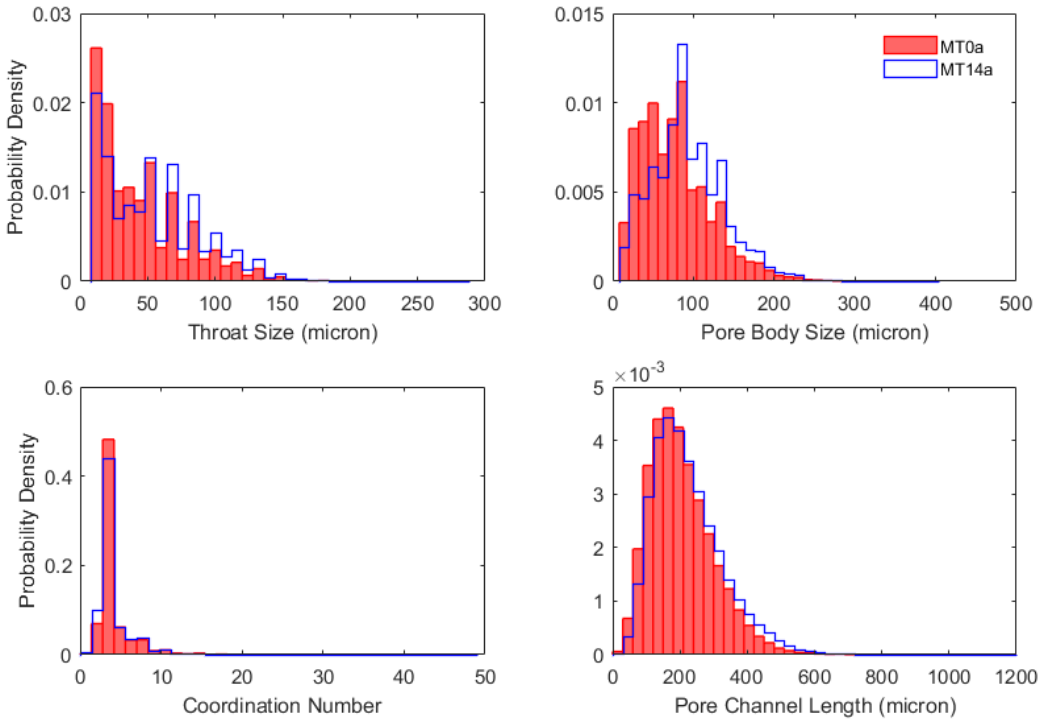

Figure 5.45 Distribution of pore network related metrics for the LAV of MT0a and MT14a based on LS method

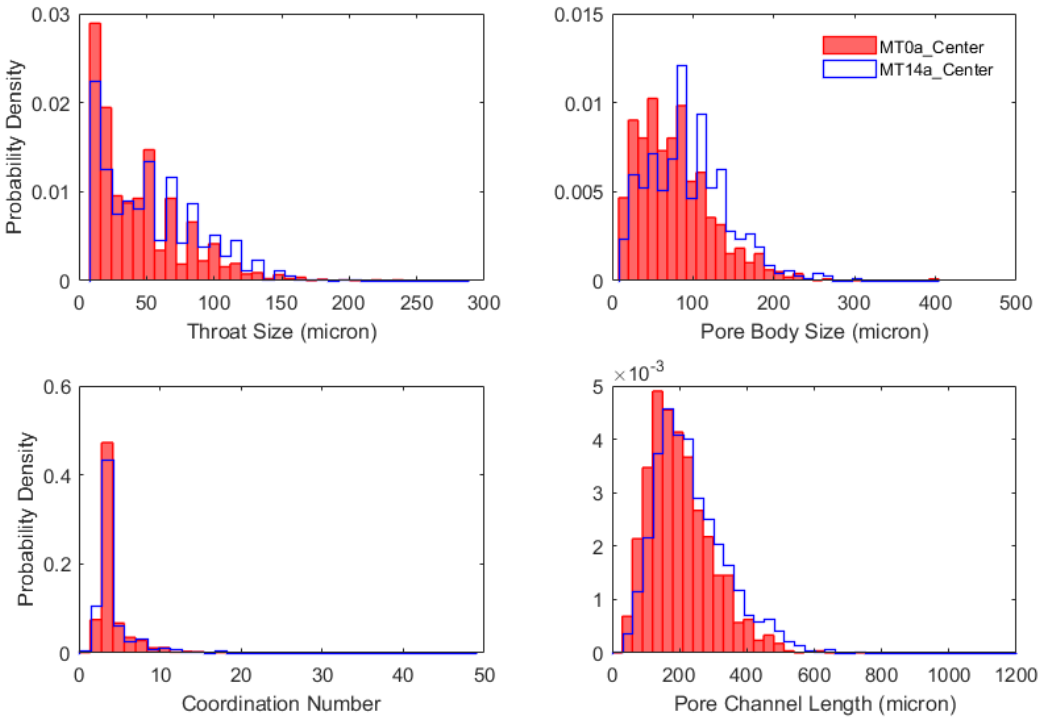

Figure 5.46 Distribution of pore network related metrics for the REV of MT0a and MT14a based on LS method

Table 5.24 Distribution statistics of pore network related metrics for MT0a and MT14a based on LS method

Metrics		LAV		REV	
		MT0a	MT14a	MT0a_Center	MT14a_Center
3-D Porosity		35.3%	41.5%	36.1%	42.2%
3-D Void Ratio		0.546	0.709	0.565	0.730
Throat Size (μm)	No.	54373	43232	1690	1217
	μ	43.4	52.9	42.8	53.3
	σ	32.5	36.1	33.5	37.3
	CV (%)	75.0	68.1	78.2	69.9
	H_v	0.690	0.738	0.681	0.745
Pore Body Size (μm)	No.	25577	20399	822	570
	μ	76.9	92.7	76.7	93.6
	σ	44.0	45.2	47.2	49.7
	CV (%)	57.2	48.7	61.5	53.2
	H_v	0.739	0.762	0.750	0.777
Pore Body-Throat Connectivity	No.	25577	20399	822	570
	μ	4.0	4.0	4.1	4.1
	σ	2.2	2.3	2.6	2.9
	CV (%)	55.7	58.4	62.5	68.9
	H_v	0.346	0.384	0.354	0.397
Pore Channel Length (μm)	No.	54315	43177	1700	1209
	μ	204.4	223.7	201.7	233.1
	σ	94.4	104.3	93.4	106.7
	CV (%)	46.2	46.6	46.3	45.8
	H_v	0.678	0.699	0.671	0.705

Size correlation between neighboring pore bodies, and between neighboring pore throats and pore bodies for AP0a_Center and AP14a_Center are plotted in Figure 5.47, and for MT0a_Center and MT14a_Center are plotted in Figure 5.48. As for AP14a_Center, a wider range and a larger peak value in terms of the sizes of neighboring pore bodies for a chosen pore body size and a chosen throat size than AP0a_Center can be observed, which

are similar to the trend in BT10_Inside compared with BT10_Outside (Figure 5.37). As for MT14a_Center, however, this shearing effect is not discernable. Also, there is only a slight difference but without shifting in the histogram of throat//pore body aspect ratio, as well as negligible differences in statistical mean and standard deviation between the sheared and the unsheared triaxial microstructures.

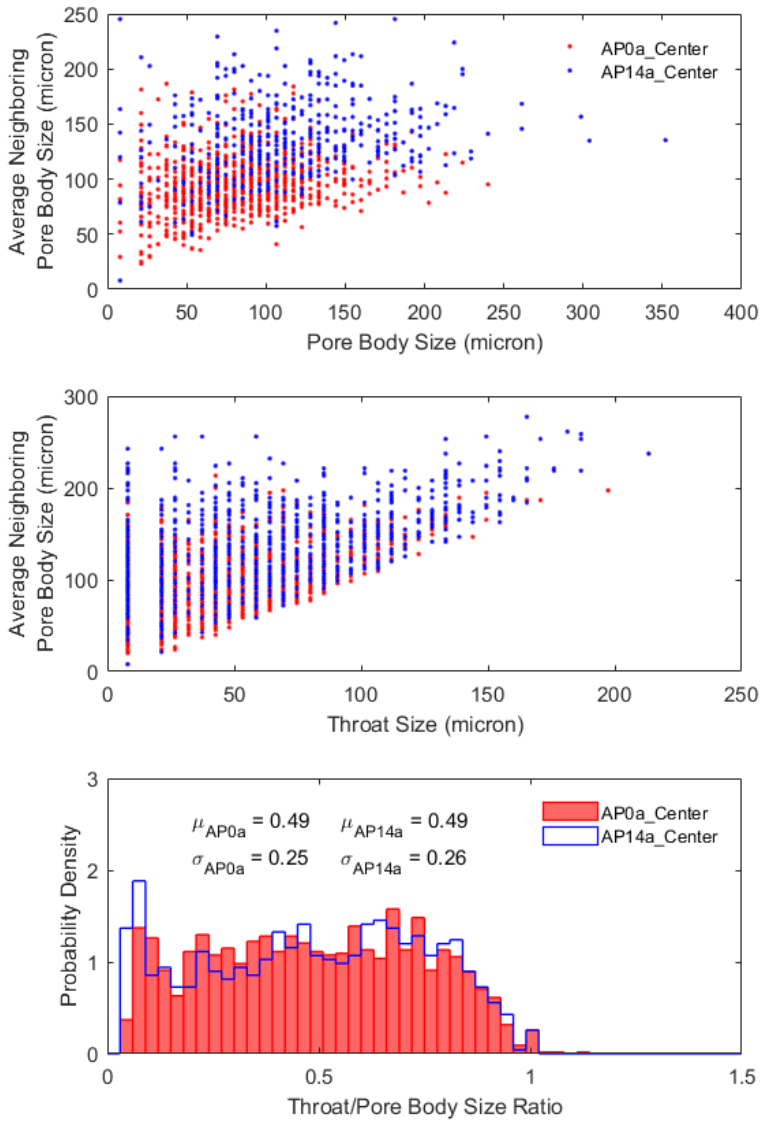

Figure 5.47 Size correlation for the REV of AP0a and AP14a

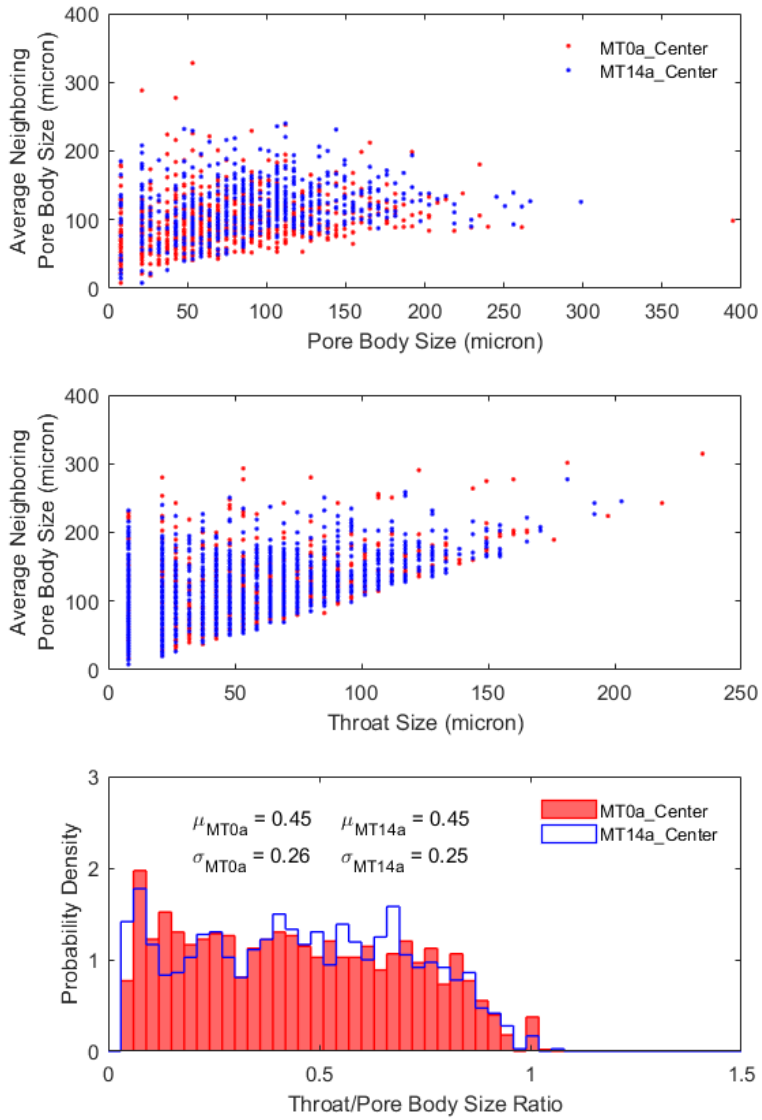

Figure 5.48 Size correlation for the REV of MT0a and MT14a

PNM models are built for AP0a_Center and AP14a_Center with the statistics shown in Table 5.25, and for MT0a_Center and MT14a_Center shown in Table 5.26. The amount of each feature is less than the corresponding number in Table 5.23 and Table 5.24, while the comparative results on the distribution statistics of the sheared microstructures with the unsheared ones remain the same.

Table 5.25 Pore Network Model statistics for the REV of AP0a and AP14a

Metrics		AP0a_Center	AP14a_Center
Tube Diameter (μm)	No.	1450	565
	μ	46.2	63.3
	σ	28.9	39.9
	CV (%)	62.6	63.1
	H_v	0.690	0.771
Pore Body (Node) Size (μm)	No.	841	378
	μ	82.8	115.2
	σ	37.2	52.8
	CV (%)	45.0	45.8
	H_v	0.703	0.803
Tube Connectivity per Node	No.	841	378
	μ	4.2	4.1
	σ	2.2	2.8
	CV (%)	53.3	69.0
	H_v	0.371	0.409
Tube Length (μm)	No.	1450	565
	μ	196.6	247.5
	σ	86.8	115.7
	CV (%)	44.1	46.8
	H_v	0.654	0.722

Table 5.26 Pore Network Model statistics for the REV of MT0a and MT14a

Metrics		MT0a_Center	MT14a_Center
Tube Diameter (μm)	No.	1387	938
	μ	41.6	50.9
	σ	32.8	36.0
	CV (%)	79.0	70.8
	H_v	0.671	0.731
Pore Body (Node) Size (μm)	No.	816	553
	μ	76.6	93.8
	σ	47.3	49.8
	CV (%)	61.8	53.1
	H_v	0.750	0.778
Tube Connectivity per Node	No.	816	553
	μ	4.1	4.2
	σ	2.6	2.8
	CV (%)	62.5	68.6
	H_v	0.354	0.391
Tube Length (μm)	No.	1387	938
	μ	196.9	225.0
	σ	94.1	104.7
	CV (%)	47.8	46.6
	H_v	0.669	0.698

5.6.2.3 Pore Topology Based on Planar Surface Construction Method

Pore topology characterization and analysis from the PSC algorithm for the triaxial microstructures involve the same two stages, throat-finding stage and modification stage.

Throat-finding results for the sub-volumes in the air-pluviated microstructures are shown in Table 5.27. Like the results for the biaxial microstructures, AP14a_Center has a smaller amount of *R-SPP*s engaged in the throat finding and a lower throat-finding rate than AP0a_Center. Among the identified throats, AP0a_Center (porosity of 36.5%) has

20.5% crossing-throats and AP14a_Center (porosity of 42.0%) has 20.8% crossing-throats. The LS algorithm continues to yield high throat-finding rates of around 98.0%. Results are visualized in Figure 5.49 for AP0a_Center and in Figure 5.50 for AP14a_Center. More pore bodies are separated out in the unsheared sub-volume than the sheared one.

Through the modification stage, AP0a_Center has a net gain of 11.3% in the number of throats before the unbiased counting and a net gain of 16.6% after the counting as shown in Table 5.28. AP14a_Center has 6.3% and 8.5% more throats before and after the counting, respectively. Visualizations of counted throats and pore bodies are presented in Figure 5.51 and Figure 5.52, and the Cartesian coordinate system *XYZ* is annotated. In the same manner as for the biaxial microstructures, no quantitative comparisons on the sizes of throats and pore bodies are made here between AP0a_Center and AP14a_Center.

Table 5.27 Results of throat finding for AP0a_Center and AP14a_Center

Items		AP0a_Center	AP14a_Center
Information	No. *R-SPP*s	3102	1673
	No. *Points*	59243	41720
	No. *Nodes*/ *Node Clusters*	1811	1044
PSC Algorithm	No. Throats	1926	851
	Throat-finding Rate	62.1	50.9
	No. Crossing-throats	394	177
LS Algorithm	No. Throats	3034	1650
	Throat-finding Rate	97.8	98.6

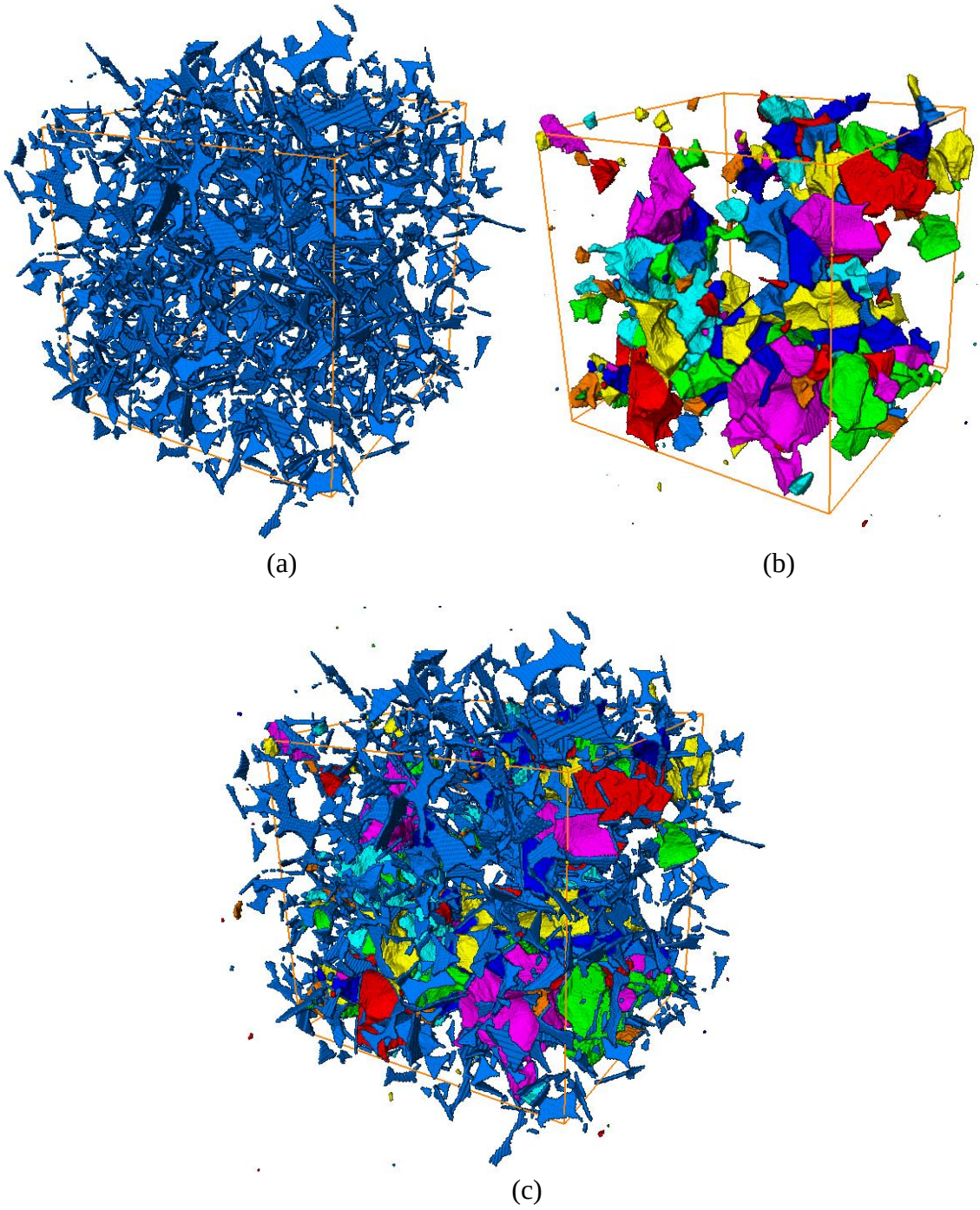

Figure 5.49 Visualization of throat-finding results for AP0a_Center: (a) pore throat barriers; (b) pore bodies pertaining to the sub-volume; (c) a combined display

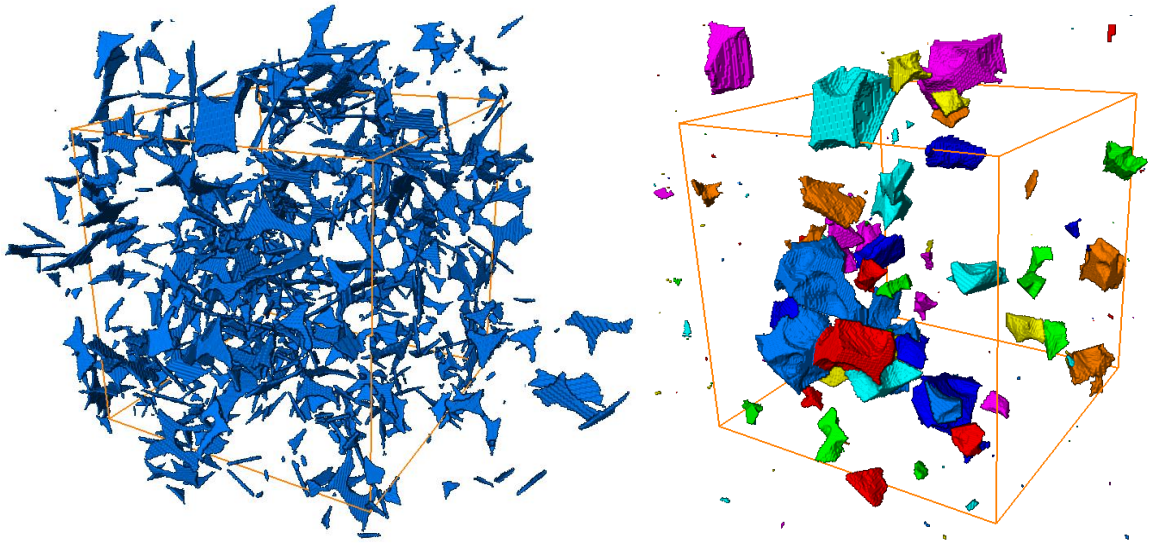

(a) (b)

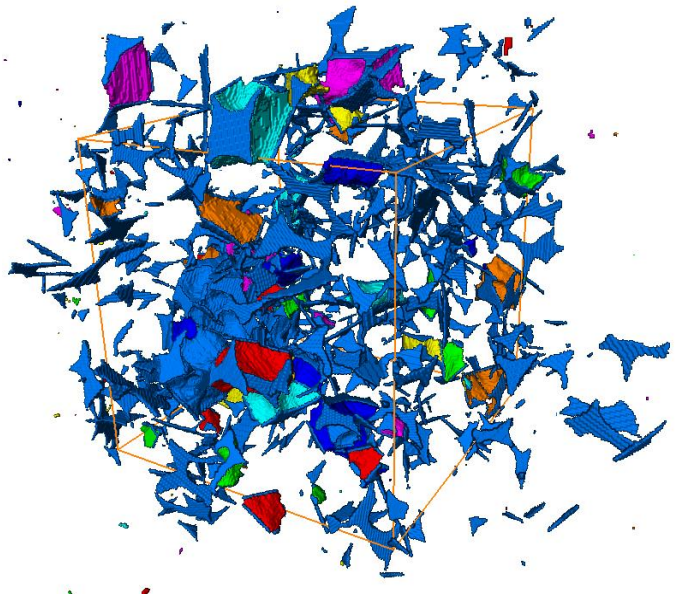

(c)

Figure 5.50 Visualization of throat-finding results for AP14a_Center: (a) pore throat barriers; (b) pore bodies pertaining to the sub-volume; (c) a combined display

Table 5.28 Results of throats and pore bodies at the two stages for AP0a_Center and AP14a_Center

Items	AP0a_Center	AP14a_Center
No. Throats[1]	1926	851
No. Throats[2]	2143	905
No. Throats Counted[1]	1149	401
No. Throats Counted[2]	1340	435
No. Pore Bodies Counted[2]	197	54

Note: 1 - throat-finding stage; 2 - modification stage

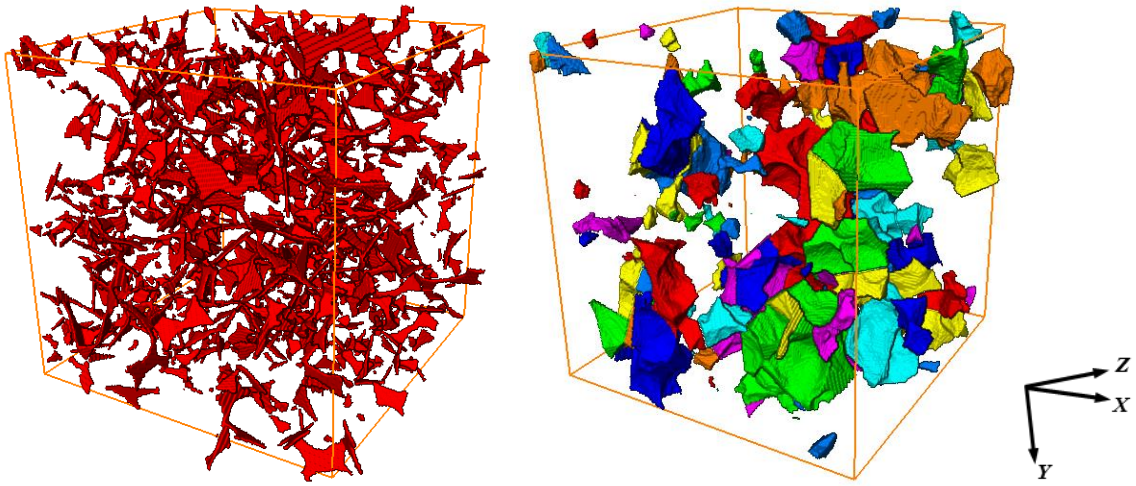

(a) (b)

Figure 5.51 Counted pore network components for AP0a_Center from modification stage: (a) pore throat barriers; (b) pore bodies

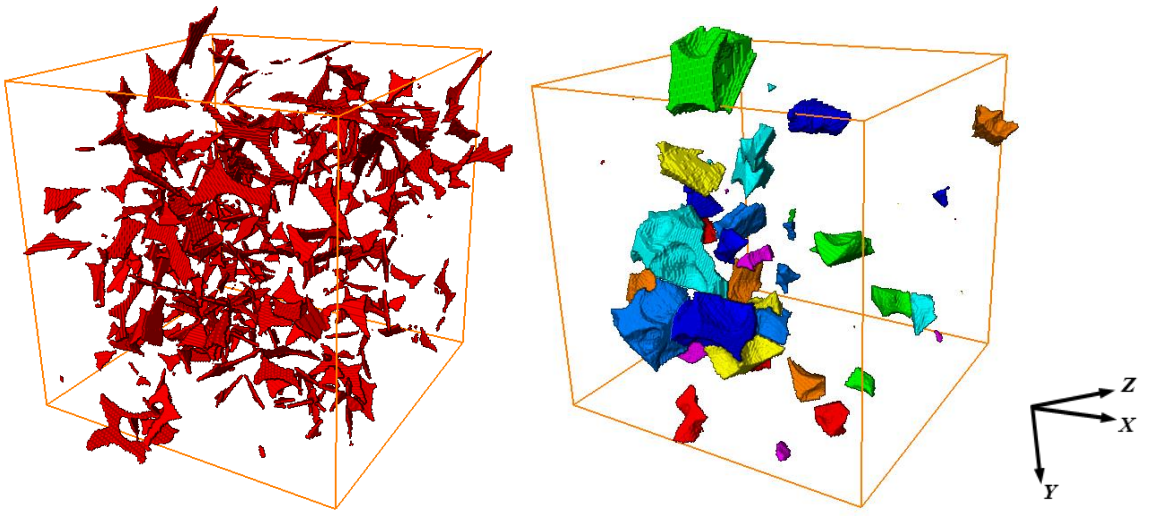

(a) (b)

Figure 5.52 Counted pore network components for AP14a_Center from modification stage: (a) pore throat barriers; (b) pore bodies

As for the sub-volumes of MT0a and MT14a, Table 5.29 gives the throat-finding results. MT0a_Center (porosity of 36.1%) exhibits a 12.0% higher throat-finding rate than MT14a_Center (porosity of 42.2%), while the first one has 14.4% crossing-throats and the latter one has 23.5%. Visualizations for MT0a_Center are displayed in Figure 5.53 and for MT14a_Center in Figure 5.54. Again, the unsheared sub-volume renders apparently larger amount of separated pore bodies than the sheared sub-volume. After the modification stage as shown in Table 5.30, a net gain of 10.4% in the number of throats before the unbiased counting and a net gain of 13.7% after the counting are seen for MT0a_Center; and the corresponding two numbers are 6.4% and 10.1% for MT14a_Center. The counted throats and pore bodies for MT0a_Center and MT14a_Center are visualized in Figure 5.55 and Figure 5.56, respectively.

Table 5.29 Results of throat finding for MT0a_Center and MT14a_Center

Items		MT0a_Center	MT14a_Center
Information	No. *R-SPP*s	2917	2326
	No. *Points*	57167	52524
	No. *Nodes*/ *Node Clusters*	1709	1398
PSC Algorithm	No. Throats	1932	1261
	Throat-finding Rate	66.2	54.2
	No. Crossing-throats	278	296
LS Algorithm	No. Throats	2852	2274
	Throat-finding Rate	97.8	97.8

Table 5.30 Results of throats and pore bodies at the two stages for MT0a_Center and MT14a_Center

Items	MT0a_Center	MT14a_Center
No. Throats[1]	1932	1261
No. Throats[2]	2133	1342
No. Throats Counted[1]	1142	683
No. Throats Counted[2]	1298	752
No. Pore Bodies Counted[2]	253	104

Note: 1 - throat-finding stage; 2 - modification stage

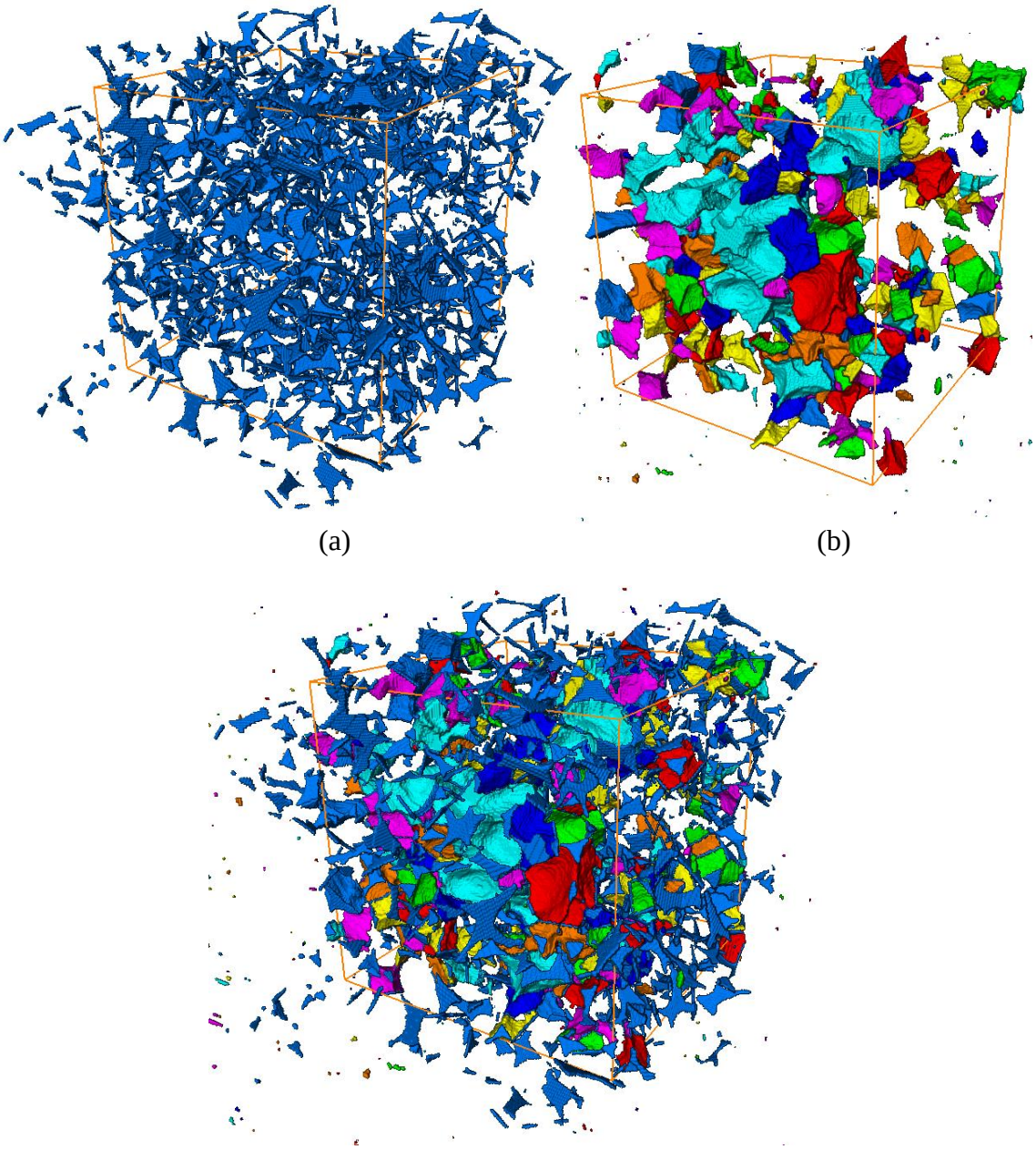

Figure 5.53 Visualization of throat-finding results for MT0a_Center: (a) pore throat barriers; (b) pore bodies pertaining to the sub-volume; (c) a combined display

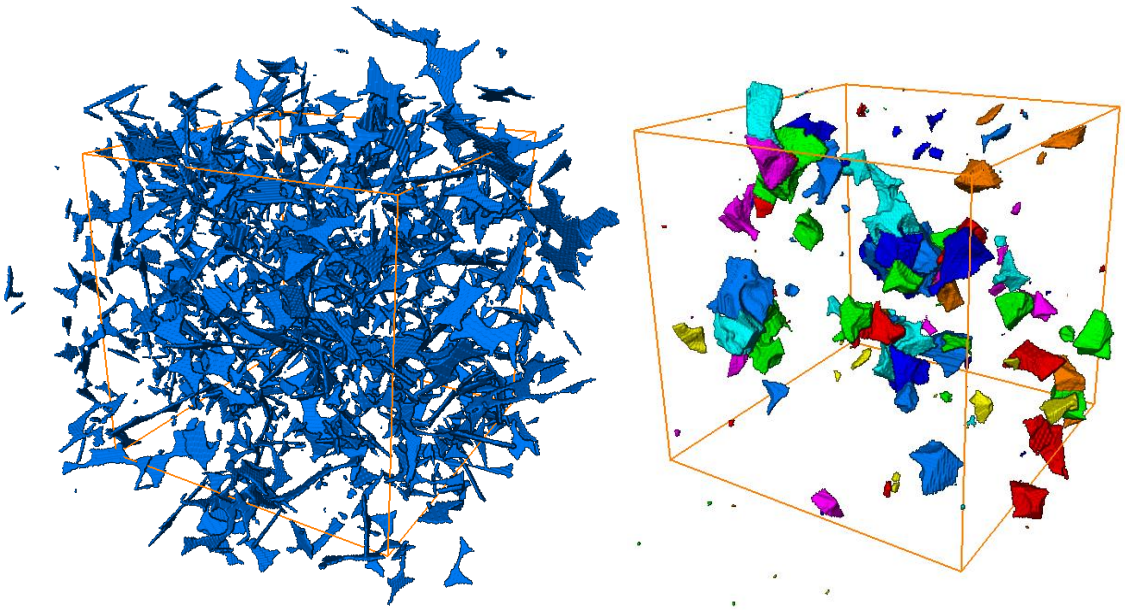

(a) (b)

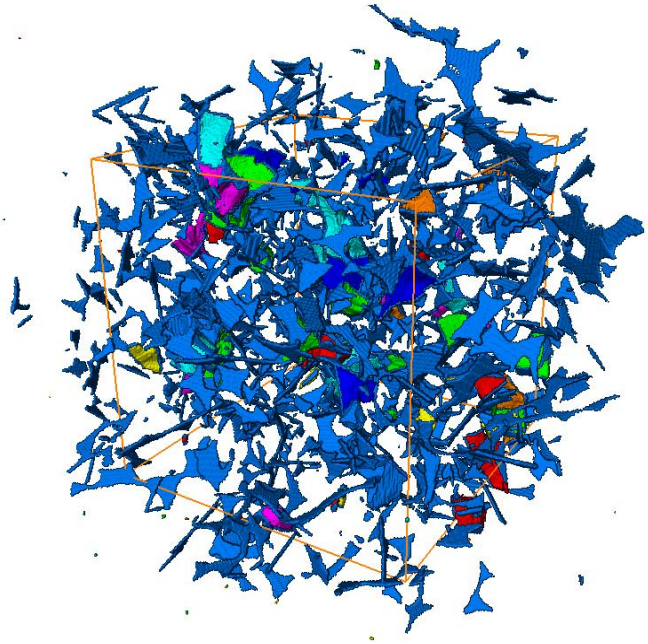

(c)

Figure 5.54 Visualization of throat-finding results for MT14a_Center: (a) pore throat barriers; (b) pore bodies pertaining to the sub-volume; (c) a combined display

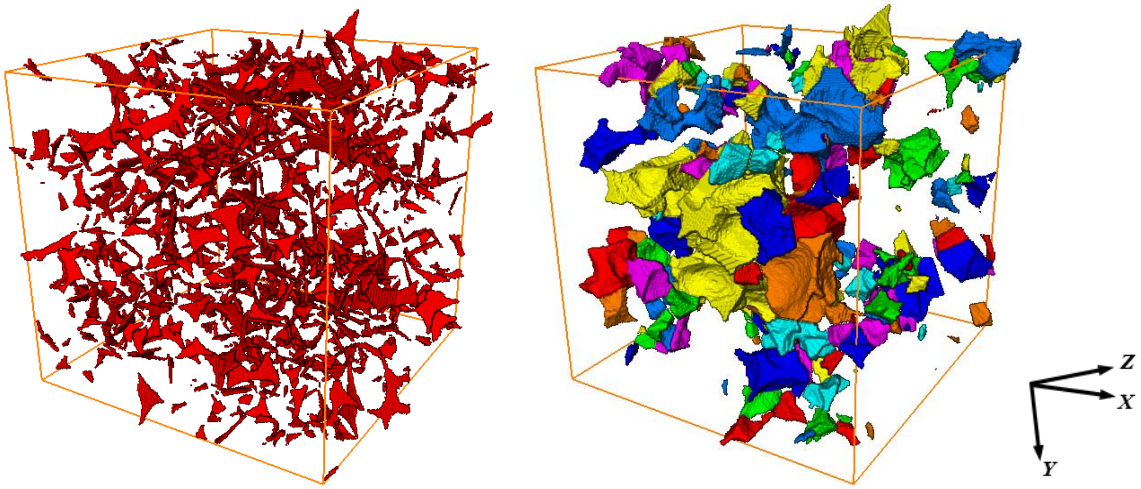

Figure 5.55 Counted pore network components for MT0a_Center from modification stage: (a) pore throat barriers; (b) pore bodies

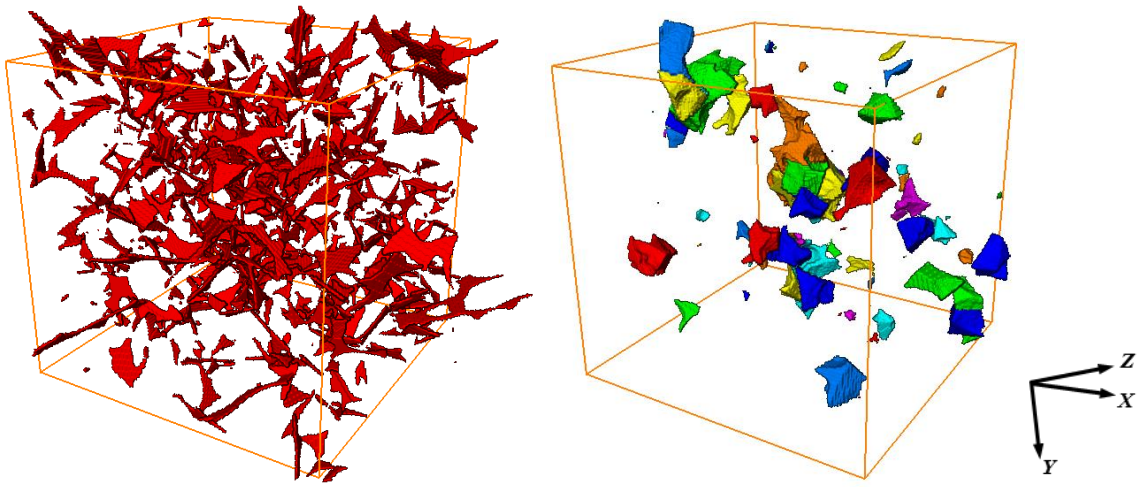

Figure 5.56 Counted pore network components for MT14a_Center from modification stage: (a) pore throat barriers; (b) pore bodies

5.7 Preparation-Induced Pore Structure Variation

To examine the pore-scale discrepancy introduced by different laboratory specimen preparation methods, characterization results of the unsheared air-pluviated and moist-tamped microstructures are presented together for comparison. Tortuous attribute of pore structure will be discussed first, and then pore network characteristics.

As presented in Section 5.6.2.1, tortuosity analysis was conducted on 300 random sub-volumes sampled from each microstructure. Figure 5.57 plots the overall distribution and distribution of average tortuosity for AP0a and MT0a together. Summary of the values of average, minimum, and maximum tortuosity was given in Table 5.19 for AP0a and in Table 5.21 for MT0a. Generally, about 5% more tortuous paths are computed for AP0a than MT0a, but there are no certain comparative relations regarding the statistical mean and standard deviation of the tortuosity distribution along the orthogonal axes. A slightly larger mean and standard deviation is seen for tortuosity along X axis in AP0a for the overall distribution and a right-shifted histogram of average tortuosity. At the same time, mean and standard deviation for both distributions along Y and Z axes are a little bit larger in MT0a. Hence, the two different preparation methods do not induce explicit distinction on the tortuous attribute of pore structure.

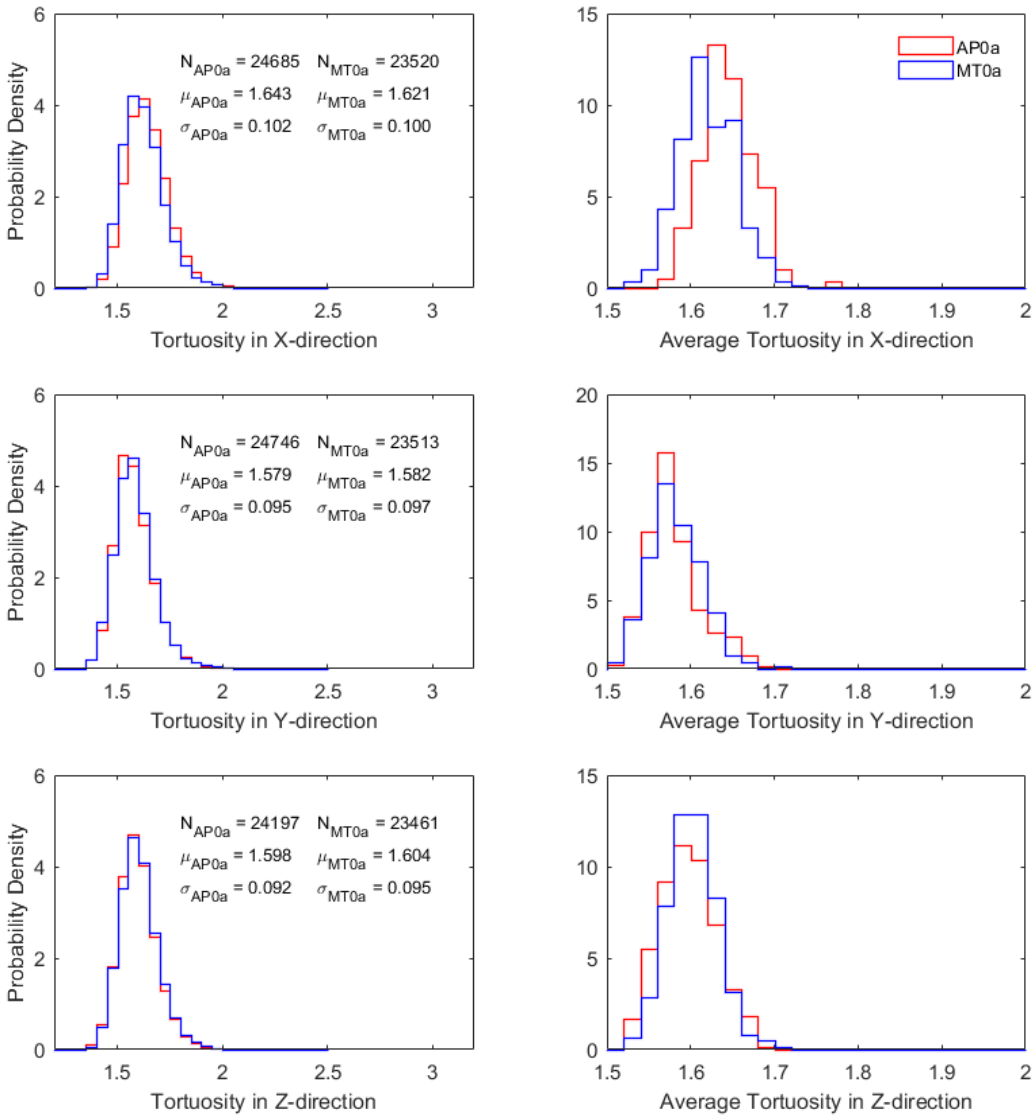

Figure 5.57 Comparison of tortuosity distribution between AP0a and MT0a

Based on the LS method, histograms of pore network related metrics for the LAV and the REV of AP0a and MT0a are plotted in Figure 5.58 and Figure 5.59 with the distribution statistics summarized in Table 5.31. The plots show that MT0a and MT0a_Center have more small throats and pore bodies, pore bodies of low coordination number, and short pore channels than AP0a and AP0a_Center, respectively. This is demonstrated by smaller statistical mean of the distributions for MT0a and MT0a_Center. In addition, a broader distribution range in the histograms of MT0a and MT0a_Center is

seen, with larger values of standard deviation and coefficient of variation which imply a lower degree of uniformity. This suggests that the moist tamping method produced less uniform soil structure than the air pluviation method in terms of throat size, pore body size, pore body-throat connectivity, and pore channel length. The moist-tamped specimens were found to have less uniform structure in terms of local void ratio distribution from the previous study (Yang, 2005). In the matter of distribution entropy, however, the comparative results vary for different metrics. MT0a and MT0a_Center have higher entropy in the distribution of pore body size and pore channel length, while lower entropy in the distribution of throat size and pore body-throat connectivity.

Size correlation are evaluated to study the difference in the initial structures as well. As shown in Figure 5.60, MT0a_Center renders a wider size range and larger maximum size of neighboring pore bodies at a specific throat size and pore body size than AP0_Center. Regarding the distribution of throat/pore body aspect ratio, AP0a_Center has a similar degree of dispersion as MT0a_Center indicated by the value of standard deviation, and a larger mean value. The histogram of MT0a_Center is seen to have a higher frequency of occurrence in the aspect ratio smaller than 0.2 while a lower frequency of occurrence in the aspect ratio between 0.5 and 0.7.

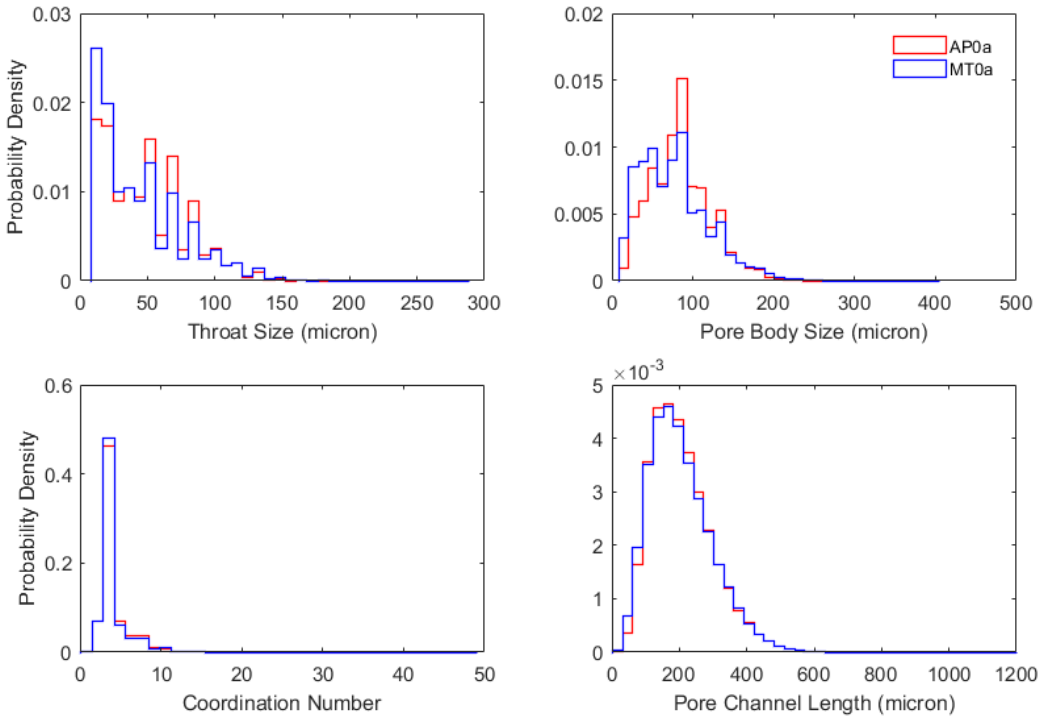

Figure 5.58 Distribution of pore network related metrics for the LAV of AP0a and MT0a based on LS method

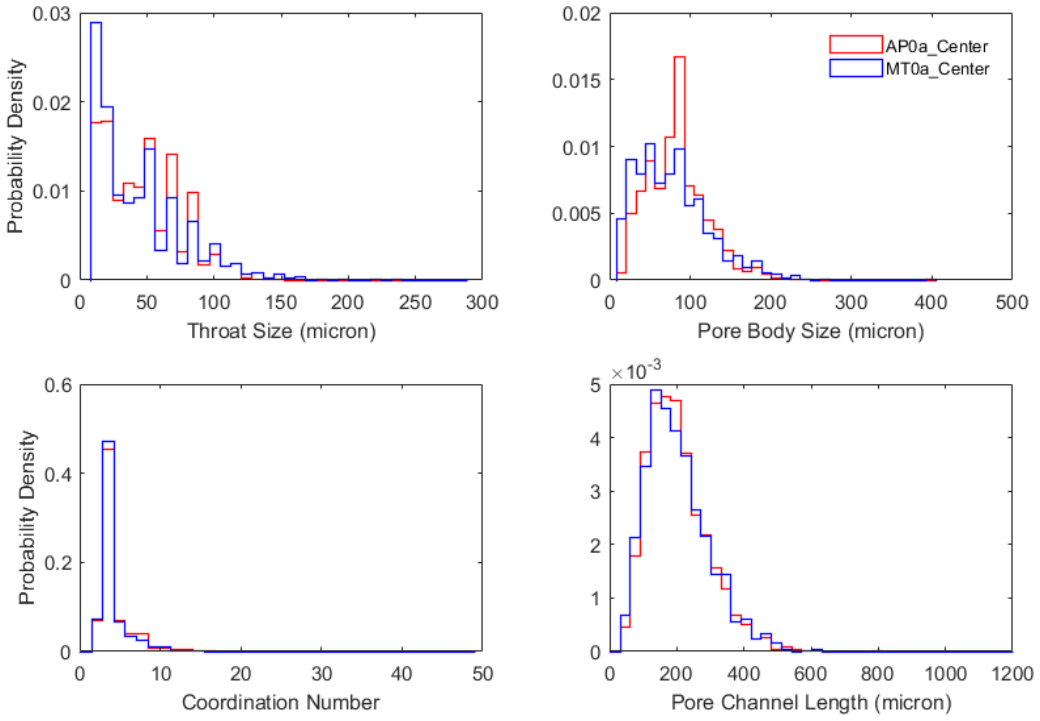

Figure 5.59 Distribution of pore network related metrics for the REV of AP0a and MT0a based on LS method

Table 5.31 Distribution statistics of pore network related metrics for AP0a and MT0a based on LS method

Metrics		LAV		REV	
		AP0a	MT0a	AP0a_Center	MT0a_Center
3-D Porosity		36.6%	35.3%	36.5%	36.1%
3-D Void Ratio		0.577	0.546	0.575	0.565
Throat Size (μm)	No.	53816	54373	1797	1690
	μ	47.7	43.4	46.9	42.8
	σ	30.4	32.5	29.5	33.5
	CV (%)	63.7	75.0	63.0	78.2
	H_v	0.703	0.690	0.694	0.681
Pore Body Size (μm)	No.	25672	25577	852	822
	μ	84.0	76.9	82.5	76.7
	σ	37.7	44.0	37.2	47.2
	CV (%)	44.8	57.2	45.1	61.5
	H_v	0.713	0.739	0.703	0.750
Pore Body-Throat Connectivity	No.	25672	25577	852	822
	μ	4.0	4.0	4.2	4.1
	σ	2.0	2.2	2.2	2.6
	CV (%)	49.3	55.7	53.3	62.5
	H_v	0.355	0.346	0.370	0.354
Pore Channel Length (μm)	No.	53684	54315	1810	1700
	μ	207.0	204.4	202.2	201.7
	σ	92.4	94.4	91.2	93.4
	CV (%)	44.6	46.2	45.1	46.3
	H_v	0.669	0.678	0.664	0.671

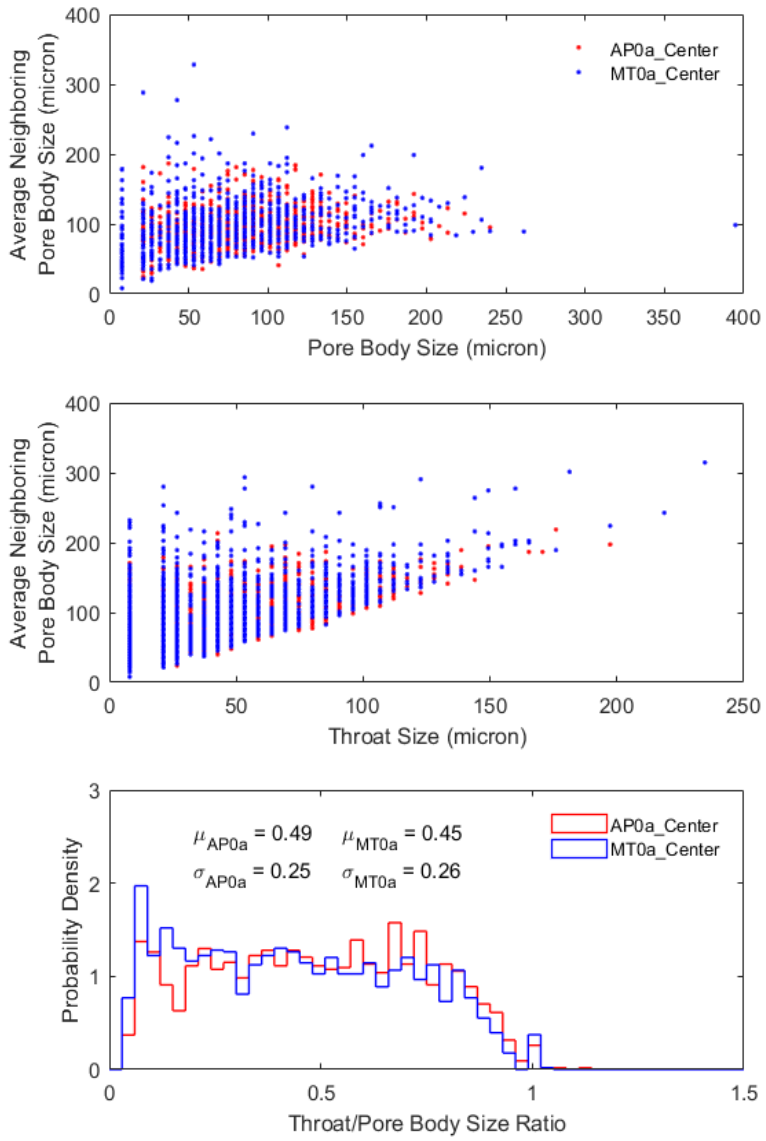

Figure 5.60 Size correlation for the REV of AP0a and MT0a

Regarding the PSC method, a comparison between AP0a_Center and MT0a_Center is conducted in view of the fact that the two have relatively comparable throat-finding rate, quantity of throats counted, and quantity of pore bodies counted (Table 5.27 - Table 5.30). Figure 5.61 presents histograms of the major pore network parameters, and Table 5.32 lists the distribution statistics. The data for throat area (size) corresponds to the item "No. Throats Counted[2]" in Table 5.28 and Table 5.30. The plots demonstrate that MT0a_Center

has a larger quantity of small throats and pore bodies, and pore bodies of low coordination number than AP0a_Center. Specifically, a shifting of throat size and pore body size to smaller values can be noted in the histograms of MT0a_Center. These phenomena agree with the results obtained from the LS method (see Figure 5.59), but the shifting is more evident here. As a result, statistical mean of every distribution for MT0a_Center is smaller than AP0a_Center. In addition, MT0a_Center consistently has a larger coefficient of variation for all the distributions, as well as larger values of standard deviation and entropy for the distribution of throat area and pore body volume. This strengthens the finding that the specimen prepared by moist tamping is less uniform than that prepared by air pluviation with respect to pore network characteristics. Also, it is noteworthy to mention that sizes of throats and pore bodies estimated from the LS method are smaller than those estimated from the PSC method for the same sub-volume (AP0a_Center or MT0a_Center) when comparing their mean values in Table 5.31 and Table 5.32. The reason is the spherical assumptions formulated in the LS method design.

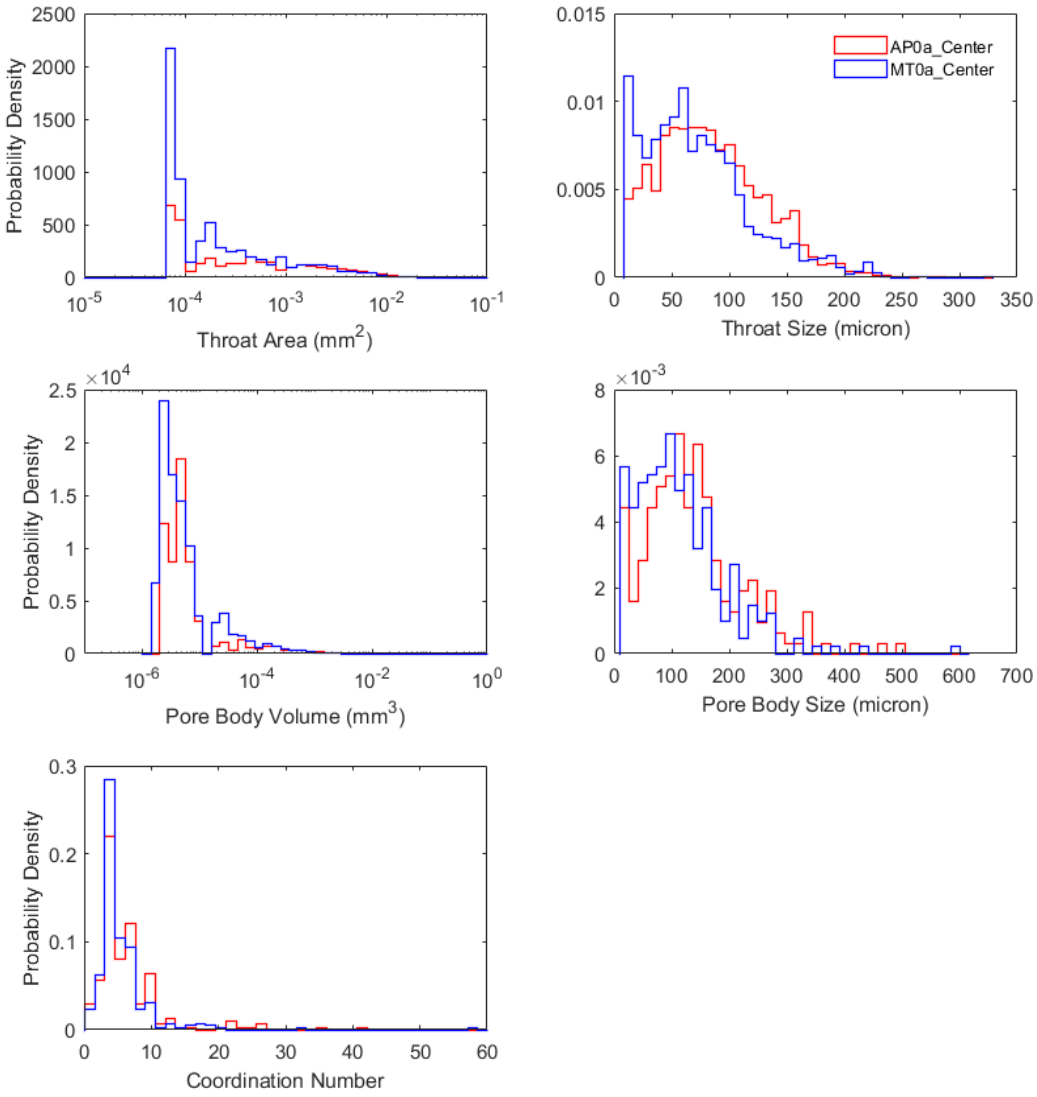

Figure 5.61 Distribution of pore network related metrics for the REV of AP0a and MT0a based on PSC method

Table 5.32 Distribution statistics of pore network related metrics for AP0a and MT0a based on PSC method

Metrics		AP0a_Center	MT0a_Center
Throat Area (mm^2)	μ	0.0073	0.0059
	σ	0.0075	0.0077
	CV (%)	103.7	130.9
	H_v	0.825	0.861
Throat Size (μm)	μ	84.7	72.3
	σ	45.8	47.3
	CV (%)	54.1	65.5
	H_v	0.834	0.813
Pore Body Volume (mm^3)	μ	0.0034	0.0023
	σ	0.0076	0.0082
	CV (%)	222.8	348.5
	H_v	0.833	0.852
Pore Body Size (μm)	μ	138.2	113.8
	σ	86.2	79.2
	CV (%)	62.4	69.5
	H_v	0.790	0.754
Pore Body-Throat Connectivity	μ	6.3	5.3
	σ	5.5	4.9
	CV (%)	87.7	92.8
	H_v	0.563	0.496

5.8 Summary and Conclusions

Unsheared and sheared digital microstructures of biaxial specimens, air-pluviated triaxial specimens, and moist-tamped triaxial specimens were characterized and analyzed in 3-D space. Image-based particle size, especially the "sieve equivalent" size, was in good agreement with the laboratory sieving result. When investigating pore structure by the skeleton-based computational approaches, the largest analysis volume (LAV) established the largest volumetric domain for sub-volume samplings and pore network quantifications.

By integrating analyses for three standard metrics (porosity, void ratio, and specific surface area) and four advanced metrics (throat size, pore body size, pore body-throat connectivity, and pore channel length), an overall REV was determined to be a cubic sub-volume with an edge length of 300 voxels for the biaxial microstructures, and 250 voxels for the triaxial microstructures. Both approximately equaled to 5.70 times D_{50} of the corresponding type of Ottawa sands. Since no adequate REV was identified for geometrical tortuosity, spatial information of the tortuous attributes of pore structure was extracted by randomly sampling 300 sub-volumes from the pore skeleton. Pore topology was explored on the basis of throat finding and pore network construction. For all the REVs involved in the throat computation, throat-finding rates provided by the LS algorithm were around 98.0% while ranged from 50.9% to 66.2% by the PSC algorithm. 3-D pore network models (PNM) were successfully established from the LS algorithm-based pore topology descriptions.

Shear-induced pore structure evolutions were studied by comparing the sheared microstructure with its unsheared counterpart. Sheared microstructures were found to have a smaller amount of computed tortuous paths, higher statistical mean and standard deviation for the tortuosity distribution. The results suggested that shearing tended to produce more scattered distribution of pore skeleton, a higher degree of dispersion in the lengths of tortuous paths, and mostly more longer paths and fewer shorter paths. Tortuosity analyses postulated that porosity (or void ratio) was not the only determinant factor, but instead size of pore openings and connectivity of pore network could also affect the spatial tortuous attribute. From the LS algorithm, the shearing effects were revealed by a higher statistical mean for the distributions of throat size, pore body size, and pore channel length in the sheared microstructures, though the amount of these metrics quantified via the

unbiased counting rule tended to decrease. At the same time, higher standard deviation and entropy were constantly observed for the distribution of every pore network related metric in the sheared microstructures, which indicated an increase of the degree of variation and disorder. From the PSC algorithm, sheared microstructures had throat-finding rates of less than 60.0%, leading to much fewer pore bodies separated out from the continuum pore space. Additionally, it was noticed that shearing induced a greater extent of change in the pore structure for the air-pluviated triaxial microstructure in terms of more significantly reduced number of tortuous paths and right-shifted histograms for the distributions of pore network related metrics. These confirmed the fact that shearing dilation was more global in the air-pluviated specimen whereas more localized in the moist-tamped specimen.

The effects of preparation methods on the pore-scale characteristics were examined by a comparison between the two unsheared triaxial microstructures. The unsheared air-pluviated microstructure had a higher statistical mean, but lower standard deviation and coefficient of variation for the distributions of pore network related metrics. It was noted that the moist-tamped microstructure had a larger quantity of small throats, pore bodies, and pore bodies of low coordination number and most importantly, less uniform pore structure than the air-pluviated microstructure.

CHAPTER 6. EXPLORATION ON TOPOLOGY OF PARTICLE NETWORK

6.1 Introduction

In granular materials, an assembly of particles interact via contacts where external compressive loads are transmitted and a complex network of interconnected force chains emerges (Mueth et al., 1998; Peters et al., 2005; Zhang et al., 2014). Spatial characteristic of the force-chain network is explored by employing the skeleton-based approach originally proposed for the pore structure to the particle phase. Focus is concentrated on the distribution of force-chain tortuosity. Through studying the force-chain network in this image-based manner rather than measuring the actual contact forces between particles, all possible geometrically shortest transmitting paths of forces within the particulate system are evaluated. Inherent variation and shear-induced evolution of the force-chain tortuosity characteristics are analyzed.

6.2 Skeleton Analysis

Using the adapted Distance Ordered Homotopic Thinning (DOHT) method, the homotopic, thin, and centered voxel skeleton of the particle phase can be computed for each microstructure volume. As shown in Figure 6.1 for a 2-D illustration, the force chains always pass through the particle-particle contacts. Particles are shown in white and pore space is in black in the figure, and the force chains are presented in the voxel skeleton format. Because the sand particles in the studied microstructures are irregular in shapes as opposed to being spheres, a force chain extracted locally is a curved line between two

contacted neighboring particles, and those particle-particle contacts are far from smooth sphere-sphere interactions.

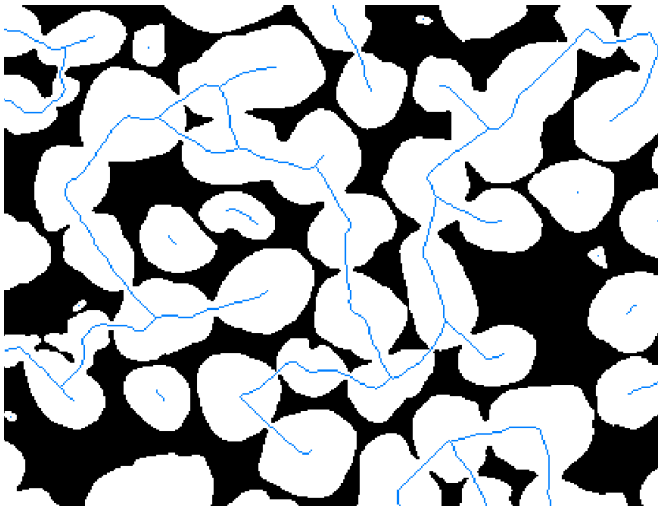

Figure 6.1 A 2-D example of voxel skeleton of the particle phase

Edge effect bias, concerning borders of the microstructure volume, continues to be handled through defining the largest analysis volume (LAV) that is smaller in size and concentric to the whole volume. Step 1 of the proposed skeleton trimming process (see details in Section 3.5.3.2) is needed from which the *Segment*s intersecting the boundary surfaces are identified. Analogous to the role of *SEG_Incomplete* for pore skeleton, these *Segment*s contain incomplete particle information, and average length of them is used to estimate the characteristics length of the "guard volume" (termed as *l_guard*) at each side of the LAV. Spatial graph object is thus created from the voxel skeleton firstly. Table 6.1 presents information of the spatial graph and the LAV for the six microstructures.

Table 6.1 Information of particle skeleton and defined LAV dimension

ID	Spatial Graph			*l_guard* (voxels)	LAV (voxels)
	*Node*s	*Segment*s	*Point*s		
BT0	22473	36918	733590	40	1220 × 720 × 350
BT10	29261	48066	922681	40	1220 × 720 × 520
AP0a	56821	93269	1589644	35	1230 × 730 × 530
AP14a	35760	57536	1061686	40	1220 × 720 × 520
MT0a	63752	107424	1674489	30	1240 × 740 × 540
MT14a	53134	87058	1425792	35	1230 × 730 × 530

Like the geometrical tortuosity of the pore structure, the force-chain tortuosity is calculated by finding the shortest paths from every single voxel on an entry surface of interest to the entire exit surface at the opposite side along the extracted particle skeleton, and the developed pure voxel-based algorithm is implemented. In addition, the analysis is performed on randomly sampled small sub-volumes from the LAV domain. In Section 5.6.1.1 and 5.6.2.1, the suitable set of sub-volumes was decided based on gauging the variations of standard pore metrics with the number of sub-volumes sampled. Considering the particle phase is complementary to the pore phase in the binary microstructures studied, the standard particle metrics are in direct, simple correlations with those standard pore metrics. Therefore, 300 randomly sampled sub-volumes (each 200 × 200 × 200 voxels) containing the voxel skeleton are used in the current force-chain tortuosity characterization.

6.3 Comparison among Digital Sand Microstructures

Distribution of the force-chain tortuosity is computed on each sub-volume along positive *X*, *Y* and *Z* directions. Average, minimum, and maximum values are estimated from each distribution. Combining the results of all the 300 sub-volumes, an overall

distribution as well as distribution of average force-chain tortuosity are generated. Results for the two biaxial microstructures are presented in Table 6.2, Table 6.3, and Figure 6.2, for the two air-pluviated triaxial microstructures are presented in Table 6.4, Table 6.5, and Figure 6.3, and for the moist-tamped triaxial microstructures are in Table 6.6, Table 6.7, and Figure 6.4. Spatial anisotropy of the force-chain tortuosity can be observed, but is less obvious than the anisotropy of geometrical tortuosity for the pore structure with respect to shape of the histogram, statistical mean and standard deviation of the distribution. Besides, the computed force-chain tortuosity has a wide range marked by the difference between the maximum and the minimum values, indicating variations in the lengths of tortuous force-chain paths.

When the force-chain tortuosity is compared between the unsheared and the corresponding sheared microstructure, histogram of the latter one consistently shifts to right of the unsheared one and covers a greater range, exhibiting larger statistical mean and standard deviation. This holds true for both the overall distribution and the distribution of average force-chain tortuosity, which indicates an induced higher dispersion in the lengths of the tortuous force-chain paths with an increasing number of longer paths. Moreover, the sheared microstructure has fewer tortuous paths obtained than the unsheared one, and specifically BT10 has 9.1% ~ 14.5% less than BT0, AP14a has 33.0% ~ 35.5% less than AP0a, and MT14a has 29.3% ~ 33.8% less than MT0a. The reason should be that shearing produces a looser packing of particles, and then shearing dilation reduces the coordination number of particles which strongly influences the formation of force chains. As AP14a underwent a more global dilation, shear-induced reduction in the number of tortuous force-

chain paths is more significant, and the right-shifting trend from the unsheared histogram is more obvious than MT14a.

Figure 6.5 compares the distributions of force-chain tortuosity between the two unsheared triaxial microstructures prepared by air pluviation and moist tamping methods, including the overall distribution and distribution of average values. More tortuous force-chain paths (24.2% ~ 29.3% more) are identified from MT0a along each of the three searching directions. However, statistical mean and standard deviation of AP0a and MT0a are only slightly different, and the comparative relations depend on the searching direction. There seems to be no clear discrepancy in terms of the characteristic of force-chain tortuosity introduced by the two specimen preparation methods.

Table 6.2 Calculated average, minimum, and maximum force-chain tortuosity from 300 random sub-volumes for structure BT0 along three orthogonal axes

Metrics	Average	Minimum	Maximum
Force-Chain Tortuosity in *X*-direction	1.553±0.048	1.389±0.037	1.800±0.111
Force-Chain Tortuosity in *Y*-direction	1.574±0.044	1.411±0.042	1.815±0.105
Force-Chain Tortuosity in *Z*-direction	1.564±0.044	1.389±0.034	1.814±0.124

Table 6.3 Calculated average, minimum, and maximum force-chain tortuosity from 300 random sub-volumes for structure BT10 along three orthogonal axes

Metrics	Average	Minimum	Maximum
Force-Chain Tortuosity in *X*-direction	1.626±0.059	1.433±0.043	1.903±0.136
Force-Chain Tortuosity in *Y*-direction	1.595±0.058	1.422±0.045	1.855±0.138
Force-Chain Tortuosity in *Z*-direction	1.614±0.051	1.424±0.049	1.891±0.135

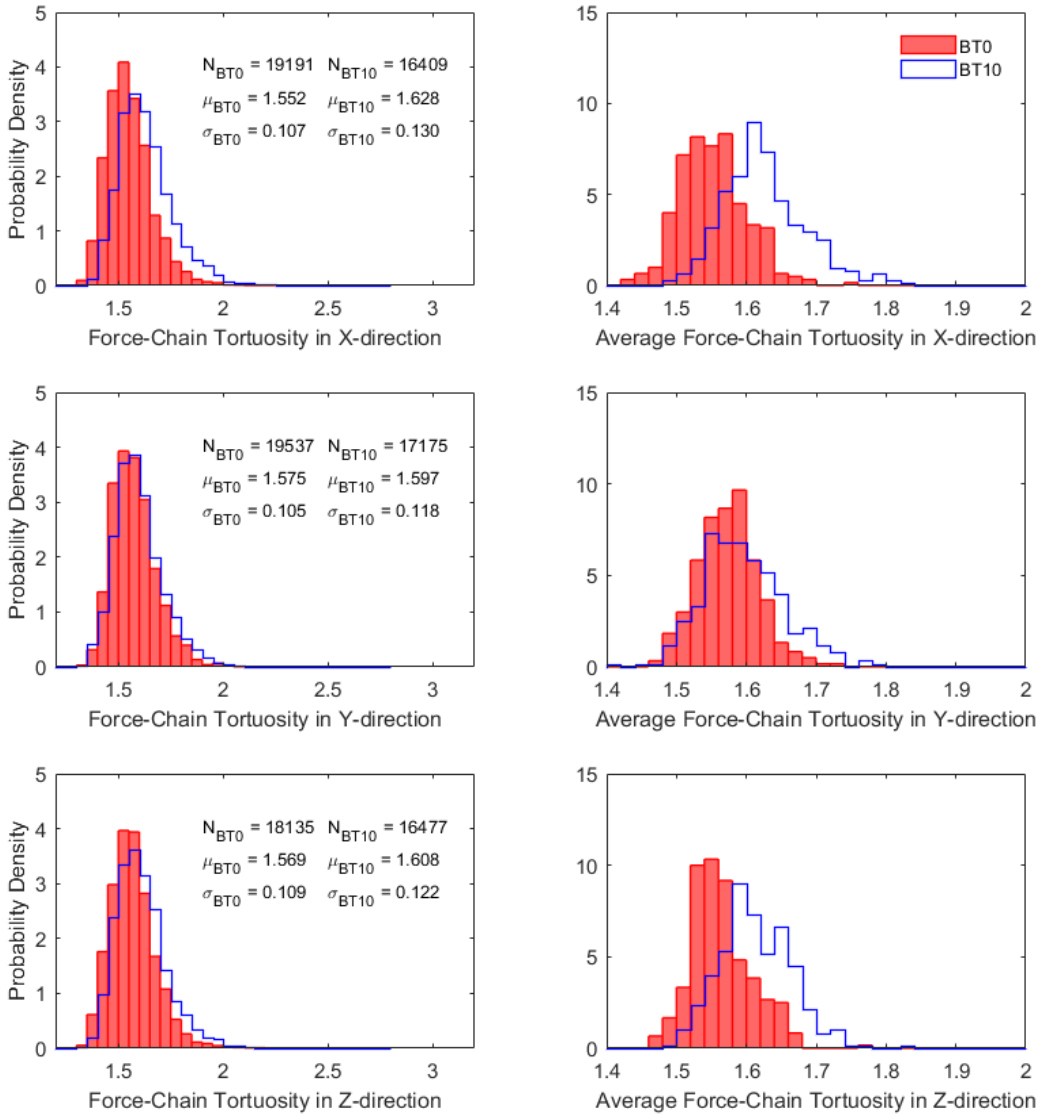

Figure 6.2 Distribution of force-chain tortuosity computed from 300 random sub-volumes and comparison between BT0 and BT10

Table 6.4 Calculated average, minimum, and maximum force-chain tortuosity from 300 random sub-volumes for structure AP0a along three orthogonal axes

Metrics	Average	Minimum	Maximum
Force-Chain Tortuosity in *X*-direction	1.571±0.033	1.411±0.034	1.818±0.095
Force-Chain Tortuosity in *Y*-direction	1.549±0.032	1.401±0.029	1.803±0.099
Force-Chain Tortuosity in *Z*-direction	1.571±0.037	1.409±0.036	1.809±0.087

Table 6.5 Calculated average, minimum, and maximum force-chain tortuosity from 300 random sub-volumes for structure AP14a along three orthogonal axes

Metrics	Average	Minimum	Maximum
Force-Chain Tortuosity in *X*-direction	1.648±0.060	1.466±0.049	1.928±0.136
Force-Chain Tortuosity in *Y*-direction	1.618±0.056	1.432±0.044	1.895±0.131
Force-Chain Tortuosity in *Z*-direction	1.623±0.050	1.440±0.039	1.907±0.129

Table 6.6 Calculated average, minimum, and maximum force-chain tortuosity from 300 random sub-volumes for structure MT0a along three orthogonal axes

Metrics	Average	Minimum	Maximum
Force-Chain Tortuosity in *X*-direction	1.561±0.038	1.398±0.038	1.814±0.098
Force-Chain Tortuosity in *Y*-direction	1.563±0.035	1.402±0.031	1.820±0.103
Force-Chain Tortuosity in *Z*-direction	1.563±0.037	1.410±0.032	1.811±0.092

Table 6.7 Calculated average, minimum, and maximum force-chain tortuosity from 300 random sub-volumes for structure MT14a along three orthogonal axes

Metrics	Average	Minimum	Maximum
Force-Chain Tortuosity in *X*-direction	1.616±0.042	1.440±0.042	1.894±0.126
Force-Chain Tortuosity in *Y*-direction	1.616±0.041	1.441±0.038	1.885±0.111
Force-Chain Tortuosity in *Z*-direction	1.612±0.040	1.440±0.041	1.882±0.115

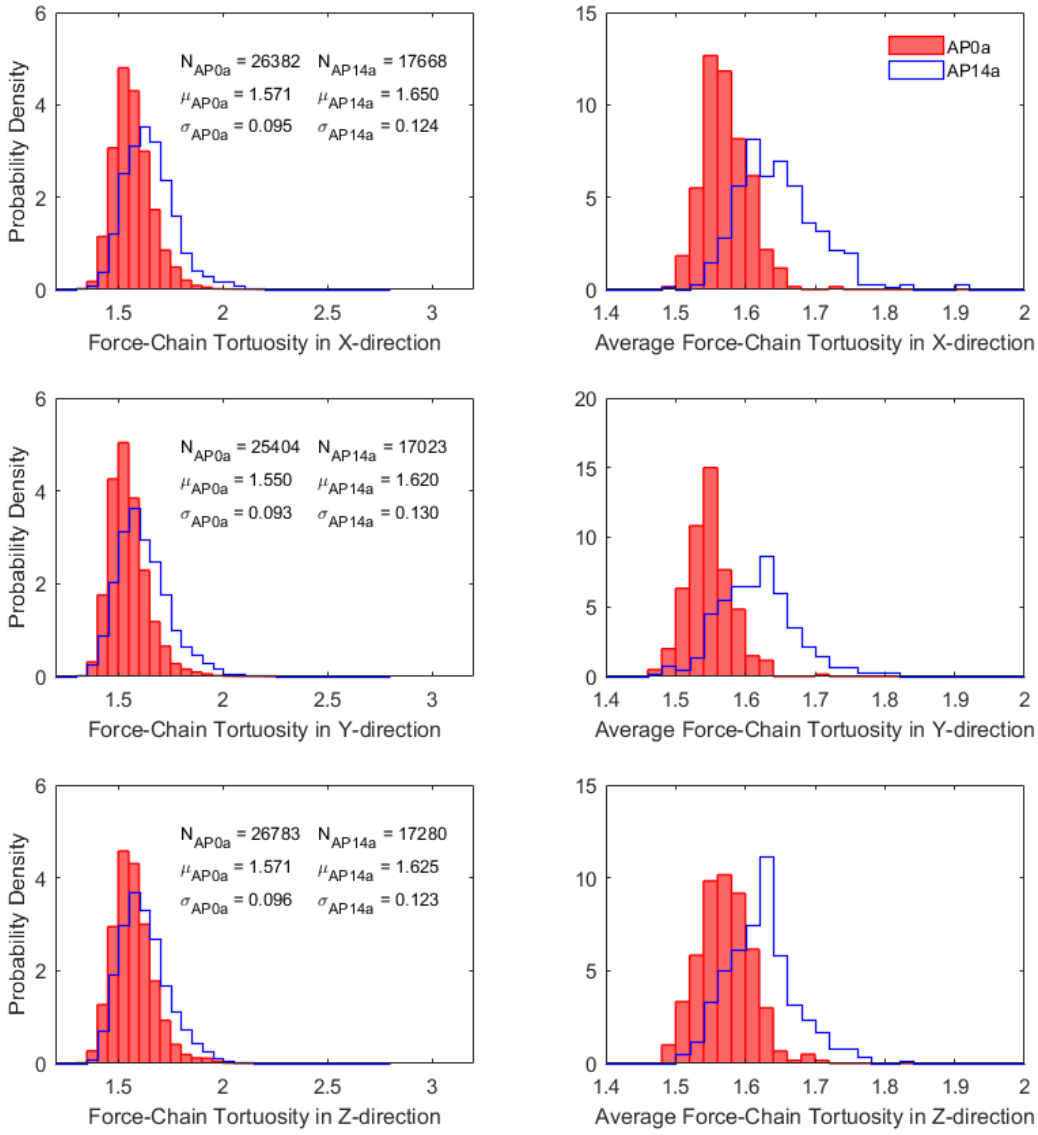

Figure 6.3 Distribution of force-chain tortuosity computed from 300 random sub-volumes and comparison between AP0a and AP14a

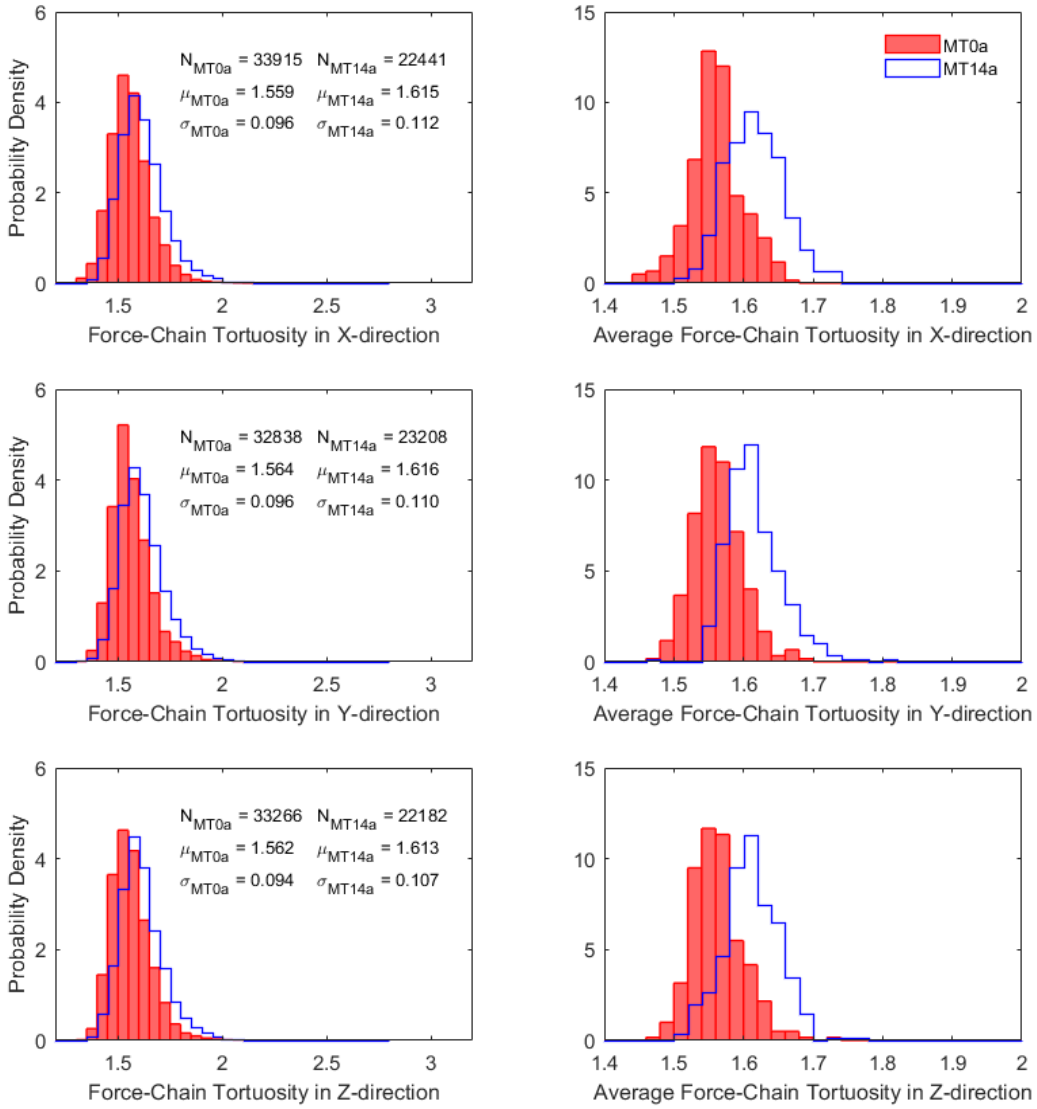

Figure 6.4 Distribution of force-chain tortuosity computed from 300 random sub-volumes and comparison between MT0a and MT14a

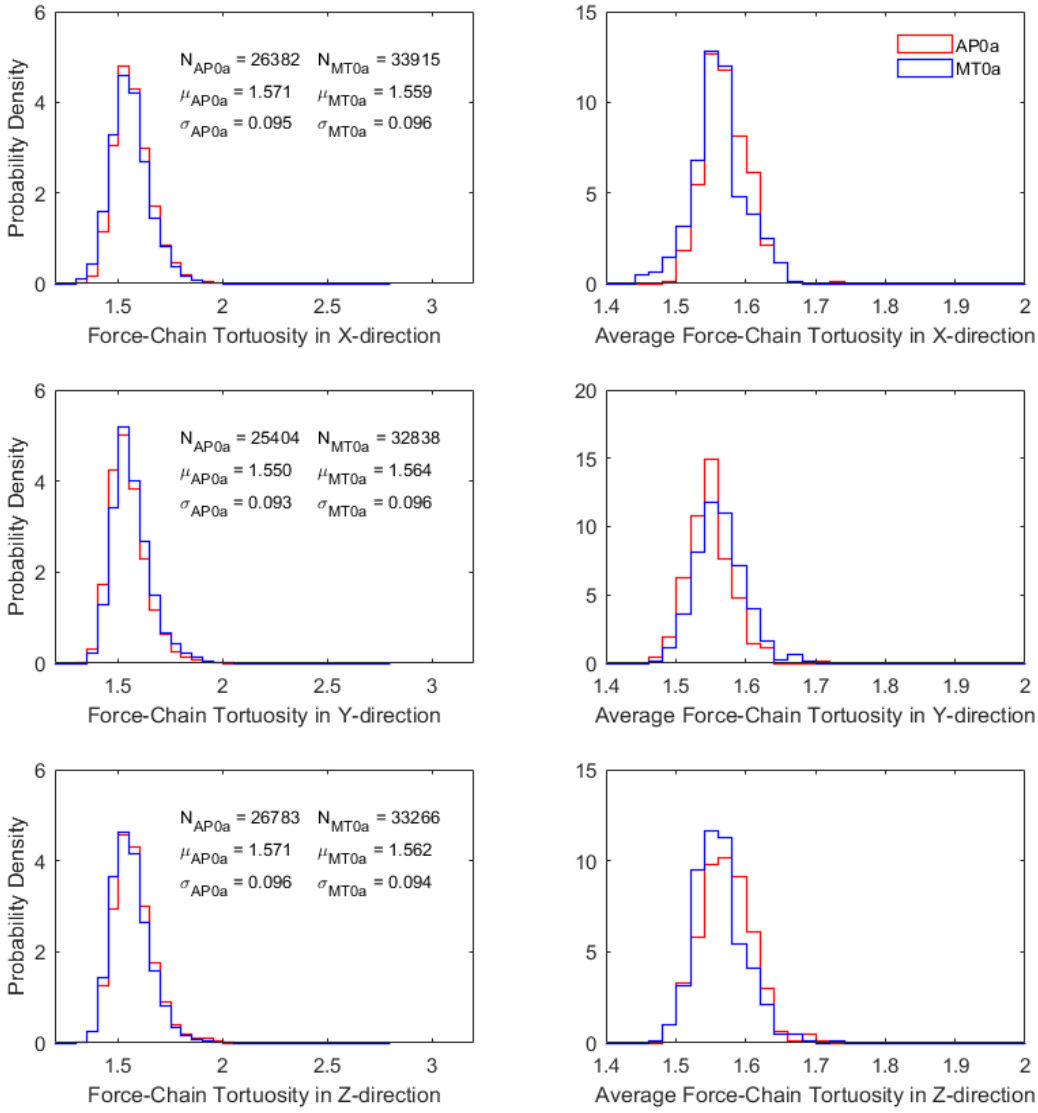

Figure 6.5 Comparison of force-chain tortuosity distribution between AP0a and MT0a

6.4 Summary and Conclusions

Skeleton of the particle phase in the digital sand microstructures was extracted and employed in characterizing the distribution of force-chain tortuosity. Through executing the algorithm on 300 random sub-volumes within each microstructure, spatial anisotropy in the force-chain tortuosity was detected. Shearing was found to result in lower number of computed tortuous force-chain paths but higher statistical mean and standard deviation

in their lengths. A more global shearing dilation in the air-pluviated triaxial specimen manifested itself as having a more notable decrease in the number of the computed paths as well as shifting of the histogram to the right in comparison with the sheared moist-tamped triaxial specimen. The two different specimen preparation methods did not display clear influence on the characteristics of force-chain tortuosity.

CHAPTER 7. CONCLUSIONS AND RECOMMENDATIONS

7.1 Conclusions

To study the behavior of geomaterials through multiscale approaches, performing microstructure analyses at particle-pore scale is critical to improve the understanding of macro-geomechanical phenomena and to predict macroscale performance. In the last two decades, extensive researches have been conducted at Georgia Tech to characterize the microstructural properties of Ottawa sands subjected to laboratory biaxial and triaxial loadings, and to correlate those with the mechanisms of strain localization. As an effort to enhance and complement the previous studies, the current study sought to explore an appropriate workflow for image-based characterization of the digital sand microstructures in 3-D, and to develop efficient computational analysis tools for capturing quantitative knowledge of inherent variation and shear-induced evolution in the microstructures. The focus was placed on characterizing important geometrical and topological attributes of the highly intricate pore space. This study is composed of three components: computational protocols proposal, utility evaluation, and applications. Regarding the first component, a marker-based watershed algorithm was employed for particle separation in 3-D, and a pore skeleton-based framework was developed to represent and quantify pore structure, involving describing the tortuous feature and mapping it onto a network. Subsequently, effectiveness of these pore skeleton-based computational tools was demonstrated on two simulated idealized packing structures, Simple Cubic packing (SCP) and Face-Centered Cubic packing (FCP). Finally, six reconstructed digital Ottawa sand microstructures were characterized and analyzed in 3-D to examine their basic fabrics, representative elementary

volume (REV), geometrical tortuosity, pore topology, and particle network. The following primary developments and conclusions were achieved in the current study:

- Digital images of Ottawa sand microstructures were processed through threshold segmentation, reconstruction and visualization, and post segmentation in software Avizo with a 26-connectivity setting for adjacent voxels. The post segmentation procedure helped resolve unfavorable small irregularities that could harm the pore structure analyses. Basic fabric was captured by standard structure metrics in 3-D including porosity (or void ratio), specific surface area, and connected components.
- Individually accessible particles were acquired with a relatively high fidelity through a marker-based morphological watershed separation. Euclidean distance transform was central for generating markers and separation function. Image-based measurements on the particle sizes, in terms of "volume equivalent" and "sieve equivalent", agreed well with sieve analysis results, with the latter size definition rendering a better match.
- Continuum pore space was transformed into skeleton that preserved its topological information and realized dimensional reduction using an adapted Distance Ordered Homotopic Thinning (DOHT) method. As a binary representation of the pore skeleton, voxel skeleton was analyzed through calculating spatial distribution of geometrical tortuosity. Spatial graph consisting of *Point*, *Node*, and *Segment* was created by converting voxel skeleton into a network of curved lines. It was essential to establish the physically representative pore network architecture and its statistics.
- Geometrical tortuosity characterized the tortuous attribute of pore structure. Its spatial variation was investigated by a novel, generic algorithm developed based on

graph theory and shortest-path searching. This pure voxel-based algorithm contained two steps: (1) transform 3-D skeleton into a 2-D mathematical graph represented by an adjacency matrix; and (2) apply Dijkstra's searching algorithm. It was aimed to comprehensively identify existing convoluted pathways available for transport along a specified direction within the pore space.

- Pore structure was delineated into a network embracing pore bodies as the larger pore space openings and pore throats as the minimum restrictions. To concentrate network analyses on the flow-accessible portion of the pore space, pore skeleton represented by spatial graph was trimmed through a proposed five-step procedure with significant pore paths (*SPP*s) retained.
- A pore throat was defined as the global minimum restriction on a *SPP* and uniquely separated two distinct pore bodies. Two computational algorithms, local sphericity (LS) algorithm and planar surface construction (PSC) algorithm, were developed for throat finding. Both incorporated a qualified throat condition to ensure that a throat would not lie in one single pore body.
- Local sphericity attribute estimated radius of the local maximal sphere centered at a skeleton voxel and completely fit into the pore space. Taking advantage of this measure, the LS algorithm simplified throats and pore bodies as spheres, located a throat as a position with the smallest local sphericity, and identified pore bodies via classifying skeleton into different groups, having the largest local sphericity for each group as the pore body radius. This algorithm was superior for its considerably lower level of computational complexity and computational expense, while higher throat-finding rates for the unconsolidated real sand microstructures under study.

- The PSC algorithm was developed to partition pore space into pore bodies bounded by throat surfaces. A pore throat was simplified as a planar surface having the minimum cross-section area on each *SPP*. The main workflow was to construct an assembly of face-to-face connected pore voxels (barrier) that were passed through by the surface, quantify surface area, and identify crossing-throats and reconstruct throats. Throat construction was particularly challenging in the unconsolidated real sand microstructures under study which had porosities above 30% and insufficient particle-particle contacts, showing the presence of crossing-throats and generally low throat-finding rates. One major advancement was made to realize discrete optimization on the orientations of a throat surface through considering a total of 49 cases. This algorithm characterized the real geometry of pore structure, but demanded markedly higher computational expense. So far, its execution was limited to the REV domain.
- Pore network statistics including size distribution of pore throats and pore bodies, pore body-throat connectivity, distribution of pore channel length, and a few preliminary size correlations (e.g. pore body-pore body correlation, pore body-throat correlation, and throat/pore body aspect ratio) could be derived from the LS algorithm. As for the PSC algorithm, a modification stage was designed to divide those throats bordering more than two distinct pore bodies, and then network parameters were extracted. Spatial distribution (i.e. coordinates) of throats and pore bodies could be acquired from both throat-finding algorithms.
- 3-D pore network model (PNM) consisted of spherical pore bodies connected by cylindrical tubes was able to be built based on the LS algorithm. Accommodating

all the key information of pore structure, the PNM could be utilized in pore network simulations to predict transport properties such as hydraulic conductance.

- Unbiased stereological techniques for sampling and estimation were implemented such that 3-D quantitative characterizations were performed in a scientific manner. Schemes of uniform random sampling and systematic random sampling were used in spatial analysis of geometrical tortuosity, and evaluation of REV, respectively. To address edge effects introduced systematic estimation error, a 3-D unbiased brick containing three "acceptance surfaces" and five "forbidden surfaces" together with a concept of "guard volume" were employed in selecting geometric features for measurements. Especially guided by the unbiased counting rule, a largest analysis volume (LAV) was defined as the largest characterization domain in pore skeleton analyses and relevant significant pore paths (*R-SPP*s) were identified when running the PSC algorithm on the REV.
- Performance of pore skeleton-based microstructure analysis tools was evaluated on simulated SCP and FCP. Geometrical tortuosity was accurately quantified. Both throat-finding algorithms offered a 100% throat-finding rate and exact prediction on pore body-throat connectivity. Comparing with the theoretical values of throat area (size) and pore body volume (size), the PSC algorithm achieved better estimation (< 6% error) while the LS algorithm underestimated them (around 30% ~ 50% error) due to its spherical shape assumptions. Significance and adequacy of the unbiased 3-D quantification techniques were revealed.
- Existence and size of REV were studied based on characterizing several pore-scale properties. Results indicated the dependence of REV on the different properties of

interest. An integrated REV, expressed as the edge length of a cubic sub-volume, for analyzing most pore structure attributes except for geometrical tortuosity was estimated to be 300 voxels in the biaxial microstructures and 250 voxels in the triaxial microstructures, with both approximating to $5.7 \times D_{50}$.

- Distribution of geometrical tortuosity was investigated by sampling 300 random sub-volumes from the voxel skeleton. Results indicated that tortuous attribute of pore structure was spatially anisotropic, and representing it as a distribution could capture various convoluted paths and permitted detailed examinations on transport phenomena inside the pore space.
- Relative to unsheared microstructures, a smaller number of tortuous paths were computed from sheared microstructures. Distribution of geometrical tortuosity in sheared microstructures showed higher mean and standard deviation, even though porosity (or void ratio) was higher too. Shearing tended to produce more scattered distribution of skeleton and a higher degree of dispersion in the lengths of tortuous paths. One implication was that porosity (or void ratio), size of pore openings and more importantly, connectivity of pore network should jointly influence tortuous attributes of pore structure.
- Shear-induced alternations in pore topology were explored relying on throat finding and pore network construction. From the LS algorithm, it was found that shearing dilation led to fewer but larger throats and pore bodies, and longer pore channels. Higher standard deviation and entropy in the distribution of every pore network related metric in sheared microstructures suggested that shearing tended to increase the degree of variation and disorder. These shearing effects were evident as well

when a closer inspection inside the shear zone of the sheared biaxial microstructure was made and compared with that outside. Using the PSC algorithm, identified throats and pore bodies were visualized before and after the unbiased brick counting. Sheared microstructures had throat-finding rates below 60.0%, which were generally 10.0% ~ 12.0% lower than their unsheared counterparts. Much less quantify of pore bodies were separated from the continuum pore space, and thus quantitative comparisons on the sizes of throats and pore bodies were prevented. Percentage of crossing-throats out of identified throats ranged from 14.4% to 23.5% in the analyzed sand microstructures.

- Pore-scale discrepancy induced by different specimen preparation methods was studied by comparing unsheared air-pluviated and unsheared moist-tamped triaxial microstructures. Distributions of major pore network related metric in the latter one presented lower mean but higher standard deviation and coefficient of variation. At a specific throat size and pore body size, sizes of neighboring pore bodies covered a broader range in the unsheared moist-tamped microstructure. These observations were indicative of less uniform pore structure produced by the moist tamping preparation method.
- Exploratory characterization on topology of particle networks was conducted on skeleton of particle phase, and distribution of force-chain tortuosity was quantified. Shearing decreased the number of tortuous force-chain paths, while increased the mean value and dispersion of the path lengths.
- Shear-induced change in air-pluviated triaxial microstructures was greater than moist-tamped triaxial microstructures. It was observed that shearing triggered: (1)

a more notable reduction in the number of searched tortuous pore paths and force-chain paths compared with unsheared microstructures; and (2) more obvious right-shifted histograms as well as bigger changes in the statistical parameters (mean, standard deviation and entropy) for the distributions of throat size, pore body size and pore channel length in sheared air-pluviated microstructure. These adhered to the fact that shearing dilation was more global in sheared air-pluviated specimen whereas localization occurred in sheared moist-tamped specimen.

- Concerning the lack of rigorous definitions for the components and descriptive parameters of pore network, some assumptions for simplification and individual decisions had to be made in developing the above skeleton-based analysis tools in particular the algorithms for throat finding. These may include: merging process in skeleton trimming, shape of throats and pore bodies, condition for qualified throats, throat surface orientation, and crossing-throats checking. This highlighted the difficulty in creating a unique network for the intrinsically complex pore space.

7.2 Recommendations

Although the current work proposed some useful 3-D computational approaches to quantitatively characterize the sand microstructures and shed new insights into the inherent and induced structure properties at micro-to-meso scale, additional work needs to be considered in the future to enhance characterization capability and the understanding of strain localization as well as other macroscale behaviors:

- Regarding throat construction using PSC algorithm, another 24 scenarios ((θ, φ) combinations) or a finer discretization for (θ, φ) can be added into the optimization

on the orientations of a throat surface to possibly increase throat-finding rates. Besides, identification of *R-SPP*s should be improved to facilitate separation of pore bodies that potentially intersect borders of the REV under consideration, and in turn adequately involve them in the quantification conforming to the unbiased counting rule. As discussed in Section 3.5.4.2, one solution may be to iteratively expand the selection of *R-SPP*s.

- Very expensive computation impeded the application of PSC algorithm to a larger microstructure domain, and thus some high performance computing techniques or programming languages are needed. With an improved computational efficiency, constructing non-planar surfaces of throats may become feasible as well.
- An in-depth exploration on the correlations among different pore metrics needs to be performed. Specifically, the combined effects of porosity (or void ratio), size of pore openings and connectivity of pore network on geometrical tortuosity should be elaborated quantitatively.
- Digital Ottawa sand microstructures were preserved and characterized at the initial and final loading states only, which corresponded to the unsheared and the sheared specimens, respectively. To better comprehend shear-induced pore-scale evolution, 3-D microstructures need to be created and analyzed for other loading states. For example, non-destructive imaging techniques (e.g. X-ray micro-CT) can be utilized to capture microstructure data during the whole loading process.
- Existence and identification of an REV for geometrical tortuosity need to be further discussed by involving the sampling and analysis on the sub-volumes of larger sizes.

The current tortuosity algorithm can be optimized on memory usage such that the computations on larger image datasets become applicable and efficient.

- In the future study on the force-chain network formed in an assembly of particles under stress, information of actual contact forces should be supplemented, and then incorporated into the spatial characterization of force-chain tortuosity.
- Pore network simulations can be attempted on the formulated PNMs to investigate transport processes and properties in unconsolidated porous media.

REFERENCES

Al-Kharusi, A. S., & Blunt, M. J. (2007). Network extraction from sandstone and carbonate pore space images. *Journal of Petroleum Science and Engineering*, *56*(4), 219-231.

Al-Raoush, R., & Papadopoulos, A. (2010). Representative elementary volume analysis of porous media using X-ray computed tomography. *Powder technology*, *200*(1), 69-77.

Al-Raoush, R., Thompson, K., & Willson, C. S. (2003). Comparison of network generation techniques for unconsolidated porous media. *Soil Science Society of America Journal*, *67*(6), 1687-1700.

Al-Raoush, R. I., & Willson, C. S. (2005). A pore-scale investigation of a multiphase porous media system. *Journal of Contaminant Hydrology*, *77*(1), 67-89.

Al-Raoush, R. I., & Willson, C. S. (2005). Extraction of physically realistic pore network properties from three-dimensional synchrotron X-ray microtomography images of unconsolidated porous media systems. *Journal of hydrology*, *300*(1), 44-64.

Amunts, K., Lepage, C., Borgeat, L., Mohlberg, H., Dickscheid, T., Rousseau, M. É., ... & Shah, N. J. (2013). BigBrain: an ultrahigh-resolution 3D human brain model. *Science*, *340*(6139), 1472-1475.

Ando, E. (2013). *Experimental investigation of microstructural changes in deforming granular media using x-ray tomography* (Doctoral dissertation, Université Grenoble Alpes).

Baddeley, A. J., Gundersen, H. J. G., & Cruz-Orive, L. M. (1986). Estimation of surface area from vertical sections. *Journal of Microscopy*, *142*(3), 259-276.

Bakke, S., & Øren, P. E. (1997). 3-D pore-scale modelling of sandstones and flow simulations in the pore networks. *Spe Journal*, *2*(02), 136-149.

Baldwin, C. A., Sederman, A. J., Mantle, M. D., Alexander, P., & Gladden, L. F. (1996). Determination and characterization of the structure of a pore space from 3D volume images. *Journal of Colloid and Interface Science*, *181*(1), 79-92.

Beucher, S. (1992). The watershed transformation applied to image segmentation. *SCANNING MICROSCOPY-SUPPLEMENT-*, 299-299.

Borgefors, G. (1984). Distance transformations in arbitrary dimensions. *Computer vision, graphics, and image processing*, *27*(3), 321-345.

Cecen, A., Wargo, E. A., Hanna, A. C., Turner, D. M., Kalidindi, S. R., & Kumbur, E. C. (2012). 3-D microstructure analysis of fuel cell materials: spatial distributions of tortuosity, void size and diffusivity. *Journal of The Electrochemical Society*, *159*(3), B299-B307.

Chen, C. C. (2000). *Shear induced evolution of structure in water-deposited sand specimens* (Doctoral dissertation, Georgia Institute of Technology).

Cormen, T. H. (2009). *Introduction to algorithms*. MIT press.

Dong, H., & Blunt, M. J. (2009). Pore-network extraction from micro-computerized-tomography images. *Physical review E*, *80*(3), 036307.

Dong, H., Fjeldstad, S., Alberts, L., Roth, S., Bakke, S., & Øren, P. E. (2008, October). Pore network modelling on carbonate: a comparative study of different micro-CT Network extraction methods. In *International symposium of the society of core analysts, Society of Core Analysts*.

Evans, T. M. (2005). *Microscale physical and numerical investigations of shear banding in granular soils* (Doctoral dissertation, Georgia Institute of Technology).

Evans, T. M., & Frost, J. D. (2010). Multiscale investigation of shear bands in sand: physical and numerical experiments. *International Journal for Numerical and Analytical Methods in Geomechanics*, *34*(15), 1634-1650.

Fernandes, J. S., Appoloni, C. R., & Fernandes, C. P. (2012). Determination of the representative elementary volume for the study of sandstones and siltstones by X-Ray microtomography. *Materials Research*, *15*(4), 662-670.

Fiala, J. C., & Harris, K. M. (2001). Extending unbiased stereology of brain ultrastructure to three-dimensional volumes. *Journal of the American Medical Informatics Association*, *8*(1), 1-16.

Fouard, C., Malandain, G., Prohaska, S., & Westerhoff, M. (2006). Blockwise processing applied to brain microvascular network study. *IEEE transactions on medical imaging*, *25*(10), 1319-1328.

Frost, J. D., & Kuo, C. Y. (1996). Automated determination of the distribution of local void ratio from digital images. *Geotechnical Testing Journal*, *19*(2), 107-117.

Frost, J. D., Roy, N., Chen, C. C. Park, J. Y., Jang D. J., Lu, Y., & Cao, J. (2018). Quantitative Analysis of Inherent and Induced Variations in Sand Microstructure and their Influence on Shearing Behavior. *KSCE Journal of Civil Engineering*, in review. (Submitted April, 2018).

Gokhale, A. M. (1990). Unbiased estimation of curve length in 3-D using vertical slices. *Journal of Microscopy*, *159*(2), 133-141.

Goldman, R. N. (1991). Area of planar polygons and volume of polyhedra. *Graphics gems II*, *2*, 24-28.

Gundersen, H. J. G. (1977). Notes on the estimation of the numerical density of arbitrary profiles: the edge effect. *Journal of microscopy*, *111*(2), 219-223.

Gundersen, H. J. G. (1986). Stereology of arbitrary particles. *Journal of microscopy*, *143*(1), 3-45.

Gundersen, H. J. G., & Jensen, E. B. (1987). The efficiency of systematic sampling in stereology and its prediction. *Journal of microscopy*, *147*(3), 229-263.

Gusev, A. A. (1997). Representative volume element size for elastic composites: a numerical study. *Journal of the Mechanics and Physics of Solids*, *45*(9), 1449-1459.

Hall, S. A., Bornert, M., Desrues, J., Pannier, Y., Lenoir, N., Viggiani, G., & Bésuelle, P. (2010). Discrete and continuum analysis of localised deformation in sand using X-ray μCT and volumetric digital image correlation. *Géotechnique*, *60*(5), 315-322.

Hasan, A., & Alshibli, K. A. (2010). Experimental assessment of 3D particle-to-particle interaction within sheared sand using synchrotron microtomography. *Géotechnique*, *60*(5), 369.

Haussener, S., Coray, P., LipiĹ, W., Wyss, P., & Steinfeld, A. (2010). Tomography-based heat and mass transfer characterization of reticulate porous ceramics for high-temperature processing. *Journal of Heat Transfer*, *132*(2), 023305.

Higo, Y., Oka, F., Kimoto, S., Sanagawa, T., & Matsushima, Y. (2011). Study of strain localization and microstructural changes in partially saturated sand during triaxial tests using microfocus X-ray CT. *Soils and foundations*, *51*(1), 95-111.

Higo, Y., Oka, F., Sato, T., Matsushima, Y., & Kimoto, S. (2013). Investigation of localized deformation in partially saturated sand under triaxial compression using microfocus X-ray CT with digital image correlation. *Soils and Foundations*, *53*(2), 181-198.

Hill, R. (1963). Elastic properties of reinforced solids: some theoretical principles. *Journal of the Mechanics and Physics of Solids*, *11*(5), 357-372.

Howard, V., & Reed, M. (2004). *Unbiased stereology: three-dimensional measurement in microscopy*. Garland Science.

Howard, V., Reid, S., Baddeley, A., & Boyde, A. (1985). Unbiased estimation of particle density in the tandem scanning reflected light microscope. *Journal of Microscopy*, *138*(2), 203-212.

Iwai, H., Shikazono, N., Matsui, T., Teshima, H., Kishimoto, M., Kishida, R., & Muroyama, H. (2010). Quantification of SOFC anode microstructure based on dual beam FIB-SEM technique. *Journal of Power Sources*, *195*(4), 955-961.

Jang, D. J. (1997). *Quantification of sand structure and its evolution during shearing using image analysis* (Doctoral dissertation, Georgia Institute of Technology).

Jiang, Z., Wu, K., Couples, G., Van Dijke, M. I. J., Sorbie, K. S., & Ma, J. (2007). Efficient extraction of networks from three-dimensional porous media. *Water Resources Research*, *43*(12).

Kanit, T., Forest, S., Galliet, I., Mounoury, V., & Jeulin, D. (2003). Determination of the size of the representative volume element for random composites: statistical and numerical approach. *International Journal of solids and structures*, *40*(13), 3647-3679.

Kim, J. W., Kim, D., & Lindquist, W. B. (2013). A re-examination of throats. *Water resources research*, *49*(11), 7615-7626.

Kuo, C. Y. (1994). *Quantifying the fabric of granular materials an image analysis approach* (Doctoral dissertation, Georgia Institute of Technology).

Kuo, C. Y., Frost, J., Lai, J., & Wang, L. (1996). Three-dimensional image analysis of aggregate particles from orthogonal projections. *Transportation Research Record: Journal of the Transportation Research Board*, (1526), 98-103.

Liang, Z., Ioannidis, M. A., & Chatzis, I. (2000). Geometric and topological analysis of three-dimensional porous media: pore space partitioning based on morphological skeletonization. *Journal of colloid and interface science*, *221*(1), 13-24.

Lindquist, W. B., & Venkatarangan, A. (1999). Investigating 3D geometry of porous media from high resolution images. *Physics and Chemistry of the Earth, Part A: Solid Earth and Geodesy*, *24*(7), 593-599.

Lu, Y. (2010). *Reconstruction, characterization, modeling and visualization of inherent and induced digital sand microstructures* (Doctoral dissertation, Georgia Institute of Technology).

Metzner, R., van Dusschoten, D., Bühler, J., Schurr, U., & Jahnke, S. (2014). Belowground plant development measured with magnetic resonance imaging (MRI): exploiting the potential for non-invasive trait quantification using sugar beet as a proxy. *Frontiers in plant science*, *5*, 469.

Mouton, P. R., Gokhale, A. M., Ward, N. L., & West, M. J. (2002). Stereological length estimation using spherical probes. *Journal of microscopy*, *206*(1), 54-64.

Mueth, D. M., Jaeger, H. M., & Nagel, S. R. (1998). Force distribution in a granular medium. *Physical Review E*, *57*(3), 3164.

Mukunoki, T., Miyata, Y., Mikami, K., & Shiota, E. (2016). X-ray CT analysis of pore structure in sand. *Solid Earth*, *7*(3), 929-942.

Oda, M. (1976). Fabrics and Their Effects on the Deformation Behavior of Sand. *Special Issue*, Department of Foundation Engineering, Faculty of Engineering, Saitama University, Japan.

Oda, M., Takemura, T., & Takahashi, M. (2004). Microstructure in shear band observed by microfocus X-ray computed tomography. *Geotechnique, 54*(8), 539-542.

Ohm, H. S., & Hryciw, R. D. (2013). Translucent segregation table test for sand and gravel particle size distribution. *Geotech. Test. J. 36*(4): 592-605.

Øren, P. E., & Bakke, S. (2002). Process based reconstruction of sandstones and prediction of transport properties. *Transport in Porous Media*, *46*(2), 311-343.

Øren, P. E., & Bakke, S. (2003). Reconstruction of Berea sandstone and pore-scale modelling of wettability effects. *Journal of Petroleum Science and Engineering*, *39*(3), 177-199.

Ostadi, H., Rama, P., Liu, Y., Chen, R., Zhang, X. X., & Jiang, K. (2010). 3D reconstruction of a gas diffusion layer and a microporous layer. *Journal of Membrane Science*, *351*(1), 69-74.

Park, J. Y. (1999). *A critical assessment of moist tamping and its effect on the initial and evolving structure of dilatant triaxial specimens* (Doctoral dissertation, Georgia Institute of Technology).

Peters, J. F., Muthuswamy, M., Wibowo, J., & Tordesillas, A. (2005). Characterization of force chains in granular material. *Physical review E*, *72*(4), 041307.

Prodanović, M., Lindquist, W. B., & Seright, R. S. (2006). Porous structure and fluid partitioning in polyethylene cores from 3D X-ray microtomographic imaging. *Journal of Colloid and Interface Science*, *298*(1), 282-297.

Rabbani, A., Jamshidi, S., & Salehi, S. (2014). An automated simple algorithm for realistic pore network extraction from micro-tomography images. *Journal of Petroleum Science and Engineering*, *123*, 164-171.

Razavi, M. R., Muhunthan, B., & Al Hattamleh, O. (2006). Representative elementary volume analysis of sands using X-ray computed tomography. *ASTM geotechnical testing journal*, *30*(3), 212-219.

Rechenmacher, A. L. & Finno, R. J. (2004). Digital image correlationto evaluate shear banding in dilative sands. *Geotech. Testing J. 27*(1), 13–22.

Rechenmacher, A. L. (2006). Grain-scale processes governing shear band initiation and evolution in sands. *Journal of the Mechanics and Physics of Solids*, *54*(1), 22-45.

Rechenmacher, A., Abedi, S., & Chupin, O. (2010). Evolution of force chains in shear bands in sands. *Geotechnique*, *60*(5), 343-351.

Rozenbaum, O., & du Roscoat, S. R. (2014). Representative elementary volume assessment of three-dimensional x-ray microtomography images of heterogeneous materials: Application to limestones. *Physical Review E*, *89*(5), 053304.

Segal, D., Schmitz, C., & Hof, P. R. (2009). Spatial distribution and density of oligodendrocytes in the cingulum bundle are unaltered in schizophrenia. *Acta neuropathologica*, *117*(4), 385.

Shin, H., Lindquist, W. B., Sahagian, D. L., & Song, S. R. (2005). Analysis of the vesicular structure of basalts. *Computers & geosciences*, *31*(4), 473-487.

Silin, D. B., Jin, G., & Patzek, T. W. (2003, January). Robust determination of the pore space morphology in sedimentary rocks. In *SPE Annual Technical Conference and Exhibition*. Society of Petroleum Engineers.

Silin, D., & Patzek, T. (2006). Pore space morphology analysis using maximal inscribed spheres. *Physica A: Statistical mechanics and its applications*, *371*(2), 336-360.

Sterio, D. C. (1984). The unbiased estimation of number and sizes of arbitrary particles using the disector. *Journal of microscopy*, *134*(2), 127-136.

Tagliaferri, F., Waller, J., Andò, E., Hall, S. A., Viggiani, G., Bésuelle, P., & DeJong, J. T. (2011). Observing strain localisation processes in bio-cemented sand using x-ray imaging. *Granular Matter*, *13*(3), 247-250.

Tewari, A., & Gokhale, A. M. (2000). Efficient estimation of number density in opaque material microstructures: the large-area disector. *Journal of microscopy*, *200*(3), 277-283.

Viggiani, G., & Hall, S. A. (2008). Full-field measurements, a new tool for laboratory experimental geomechanics. In *Fourth symposium on deformation characteristics of geomaterials* (Vol. 1, pp. 3-26). Amsterdam: IOS Press.

Vlahinić, I., Andò, E., Viggiani, G., & Andrade, J. E. (2014). Towards a more accurate characterization of granular media: extracting quantitative descriptors from tomographic images. *Granular Matter*, *16*(1), 9-21.

Weibel, E. R., Hsia, C. C., & Ochs, M. (2007). How much is there really? Why stereology is essential in lung morphometry. *Journal of applied physiology*, *102*(1), 459-467.

Yang, C. T. (2002). *Boundary condition and inherent stratigraphic effects on microstructure evolution in sand specimens* (Doctoral dissertation, Georgia Institute of Technology).

Yang, F., Hingerl, F. F., Xiao, X., Liu, Y., Wu, Z., Benson, S. M., & Toney, M. F. (2015). Extraction of pore-morphology and capillary pressure curves of porous media from synchrotron-based tomography data. *Scientific Reports (Nature Publisher Group)*, *5*, 10635.

Yang, X. (2005). *Three-dimensional characterization of inherent and induced sand microstructure* (Doctoral dissertation, Georgia Institute of Technology).

Youssef, S., Rosenberg, E., Gland, N. F., Kenter, J. A., Skalinski, M., & Vizika, O. (2007, January). High resolution CT and pore-network models to assess petrophysical properties of homogeneous and heterogeneous carbonates. In *SPE/EAGE Reservoir Characterization and Simulation Conference*. Society of Petroleum Engineers.

Zhang, L., Wang, Y., & Zhang, J. (2014). Force-chain distributions in granular systems. *Physical Review E*, *89*(1), 012203.